DIGITAL PARTICLE IMAGE VELOCIMETRY (DPIV): SYSTEMATIC ERROR ANALYSIS

By

Edward R. J. Putman

M.Eng (Hons)

A Doctoral Thesis submitted in partial fulfilment of the requirements for the award of Doctor of Philosophy of Loughborough University

October 2011

Abstract

Digital Particle Image Velocimetry (DPIV) is a flow diagnostic technique that is able to provide velocity measurements within a fluid whilst also offering flow visualisation during analysis. Whole field velocity measurements are calculated by using cross-correlation algorithms to process sequential images of flow tracer particles recorded using a laser-camera system. This technique is capable of calculating velocity fields in both two and three dimensions and is the most widely used whole field measurement technique in flow diagnostics. With the advent of time-resolved DPIV it is now possible to resolve the 3D spatio-temporal dynamics of turbulent and transient flows as they develop over time. Minimising the systematic and random errors associated with the cross-correlation of flow images is essential in providing accurate quantitative results for DPIV.

This research has explored a variety of cross-correlation algorithms and techniques developed to increase the accuracy of DPIV measurements. It is shown that these methods are unable to suppress either the inherent errors associated with the random distribution of particle images within each interrogation region or the background noise of an image. This has been achieved through a combination of both theoretical modelling and experimental verification for a uniform particle image displacement.

The study demonstrates that normalising the correlation field by the signal strength that contributes to each point of the correlation field suppresses both the mean bias and RMS error. A further enhancement to this routine has lead to the development of a robust cross-correlation algorithm that is able to suppress the systematic errors associated to the random distribution of particle images and background noise.

Acknowledgements

Having spent all my university life at Loughborough University I would like to extend my thanks and appreciation to all those people who have made it such an enjoyable experience. In my postgraduate years I would like to especially thank my supervisors Professor Graham Hargrave and Professor Neil Halliwell who have provided continual advice, support and motivation as well as topical conversation throughout my research.

I would also like to extend my gratitude to my parents and to Georgina who have given their resolute support throughout my write-up. I am indebted to you.

Publications

1. Partial Image Error (PIE) in Digital Particle Image Velocimetry (DPIV), E. Putman, G. K. Hargrave and N. A. Halliwell, Proceedings in the 26th AIAA Aerodynamic Measurement Technology and Ground Testing Conference, Seattle, WA, United States of America, 2008

Nomenclature

2D	Two-dimensional
3D	Three-dimensional
Al_2O_3	Aluminium Oxide
CCD	Charge-coupled device
CFD	Computational fluid dynamics
CMOS	Complementary metal oxide semiconductor
DPIV	Digital Particle Image Velocimetry
DWS	Discrete window shifting
FFT	Fast Fourier Transform
FFT_{OA}	Fast Fourier Transform normalised by overlapped area
FFT_{SS}	Fast Fourier Transform normalised by signal strength
$FFT_{w/oZP}$	Fast Fourier Transform without zero padding
Nd:YAG	Neodynium doped Yttrium Aluminium Garnet
NSS	Normalisation by Signal Strength
NSS_{WS}	Normalisation by Signal Strength with window shifting
PIE	Partial image error
PIPM	Particle image pattern matching
PIV	Particle Image Velocimetry
PPR	Particle images per region
PSF	Point Spread Function
RMS	Root mean square
SCC	Standard cross-correlation
SCC_{OA}	Standard cross-correlation normalised by overlapped area
SCC_{SS}	Standard cross-correlation normalised by signal strength
SCC_{WS}	Standard cross-correlation with discrete window shifting
SNR	Signal to noise ratio
TRDPIV	Time-resolved Digital Particle Image Velocimetry
VVD	Valid Vector Detection

β	Total error
μ_1, μ_2	Mean intensity of $I_1(i,j)$ and $I_2(i,j)$ respectively
$A(m,n)$	Overlapped area weighting function
d_a	Actual particle image displacement
d_b	Mean bias error
d_d	Particle image diameter
d_g	Geometric particle diameter
d_i	Measured displacement
$\bar{d}_i$	Mean measured displacement
d_p	Physical particle diameter
d_x	Known distance shift
D	Aperture of camera
f	focal length of lens
$f^{\#}$	f-number of lens
$I(x,y)$	Two-dimensional Gaussian intensity profile
$I(x_p,y_p)$	Two-dimensional digitised particle image
I_{cap}	Threshold value
I_{max}	Maximum attainable intensity value
I_{median}	Median intensity value
I_{new}	New intensity value
$I_{hr}(i,j)$	High resolution interrogation region
I_0	Peak image intensity
$I_1(i,j)$, $I_2(i,j)$	Digitised interrogation regions
$\bar{I}_1, \bar{I}_2$	Spatial mean image intensity of interrogation region
$\hat{I}_1(\xi,\eta)$	Fourier transform of $I_1(i,j)$
$\hat{I}_2^{*}(\xi,\eta)$	Complex conjugate of the Fourier transform of $I_2(i,j)$
$J_1(x)$	First order Bessel function
M	Magnification
$max(I_{kernel})$	maximum intensity within a kernel
$min(I_{kernel})$	minimum intensity within a kernel
$R(m,n)$	Direct digital cross-correlation routine
$R(x,y)$	Correlation field

$R_I(m,n)$	Normalisation of the $R(m,n)$ correlation field by intensity
$R_{OA}(m,n)$	Normalisation of the $R(m,n)$ correlation field by overlapped area
$R_{MS}(m,n)$	Mean subtraction prior to $R(m,n)$ cross-correlation
$R_{MSSS}(m,n)$	Mean subtraction prior to $R(m,n)$ cross-correlation normalised by signal strength
$R_{MSSS}(m,n)_{WS}$	$R_{MSSS}(m,n)$ with window shifting
$R_V(m,n)$	Normalisation of the $R(m,n)$ correlation field by variance
(x_c, y_c)	Pixel location of correlation peak
(x_i, y_i)	Centre co-ordinates of particle images
(x_{pk}, y_{pk})	True centre of the correlation peak
w	Pixel width
z_i	distance between image plane and lens
z_o	distance between object plane and lens
σ	RMS error
λ	wavelength of light source

Contents

List of Figures

Chapter 1

Overview

Digital Particle Image Velocimetry (DPIV) is a non-invasive flow diagnostic technique that quantifies flow dynamics whilst also providing whole field flow visualisations. Velocity vectors are calculated by capturing the motion of micron-sized tracer particles that follow the flow dynamics, using a high-speed camera focussed on a sheet of light produced by a multiple-pulsed laser. Following image capture, analysis requires a velocity map to be calculated by dividing the image into a grid of smaller interrogation regions. In order to quantify local velocities, each region is processed using a cross-correlation algorithm to estimate the average displacement of particle images between sequential pairs of regions.

Developments in digital image processing, image capture, data storage and pulsed laser technology has lead to the advent of time-resolved DPIV (TRDPIV) capable of resolving the spatio-temporal dynamics of transient and turbulent flows. The development of this technique is seen as the foremost advance in DPIV. Although research has been conducted into minimising the experimental errors in TRDPIV, systematic errors associated with the cross-correlation algorithm remains. It is essential therefore to minimise the systematic errors in order to accurately resolve flow field measurements.

The accuracy of measurements is defined by two metrics: the closeness a measured value is to the actual value (mean bias error) and the degree to which further measurements show the same or similar results (RMS error). As will be shown in section 2.5 (p.15), the standard cross-correlation algorithm, which is readily available in DPIV analysis, results in a negative mean bias and an RMS error of approximately 4% for an actual uniform displacement of one pixel. Therefore there is considerable scope to improve the accuracy of measurements with respect to current processing.

Since cross-correlation was first used for quantitative measurements (Willert and Gharib, 1991) there have been many techniques developed to refine the accuracy of results. One of these techniques includes that of discrete window shifting (Westerweel, 1997) and several other techniques were derived from this, including: continuous window shifting (Gui and Wereley, 2002) and iterative window deformations (Scarano, 2002). Another iterative approach developed includes that of particle image pattern matching (Huang et al., 1993a). The first region from a sequential pair is reduced in size and is then cross-correlated with a larger second region which accommodates the initial particle image pattern. Further to this, techniques have included single pixel correlation (Westerweel et al., 2004), correlation spatial averaging (Hart, 1998) and ensemble correlation (Meinhart et al., 2000).

Although significant focus has been made into developing these evaluation algorithms, each routine still requires standard cross-correlation (direct cross-correlation in the spatial domain, $R(m,n)$, or fast Fourier transform, FFT, cross-correlation in the Fourier domain) to provide a displacement evaluation. Therefore the systematic errors caused by the standard cross-correlation of interrogation regions still remains a limiting factor in the accuracy of DPIV measurements.

Cross-correlation normalisation functions were also introduced as a means of improving the accuracy of measurements (see section 2.8, p.24). However, this thesis discusses how various functions are only able to affect mean bias and not RMS errors. This work extends the use of the normalisation by signal strength function (NSS) originally outlined by Huang et al., (1997) for FFT cross-correlation and Anandarajah (2005) who investigated its effects in the spatial domain. It was shown that underestimations in measurements, originally solely attributed to the shape of the correlation weighting function, are in fact contributed to by clipped particle images (Partial Image Error, PIE) at the edge of each interrogation region. These are generated by the random distribution of particle images within each DPIV image. Each image is subsequently divided into smaller regions to obtain local velocity measurements and thereby particle images at the edge of each region are clipped. It

is also shown that variations between measurements are caused by the cross-correlation of unrelated particle images.

This thesis demonstrates that although NSS is able to provide improvements to both accuracy metrics, when using a sub-pixel estimator, it provides the most accurate measurements from the cross-correlation of 'ideal' regions where there is no background noise. The addition of background noise, inherent in experimental images, will increase the amplitude of the mean bias error oscillation, whilst also introducing a 'beating' effect into RMS error results. A robust cross-correlation algorithm is subsequently introduced that is able to compensate for background noise as well as the random distribution of particle images. It is shown that this algorithm is able to maintain measurement accuracy as the background noise intensity increases, minimising the systematic errors within DPIV processing.

Data-sets of artificial DPIV interrogation regions have to be simulated in order to assess the effects systematic errors have on accuracy when using various processing algorithms. Chapter 3 describes a model developed using Visual C++ where the particle image size, seeding density, distribution, known displacement and background noise intensity etc. can be controlled. Data-sets of interrogation region pairs (realisations) describing the same uniform particle image displacement of randomly distributed particle images were generated for a series of known displacements in the x-direction so that the performance of the processing algorithms could be evaluated. This also meant that each artificial region was not subject to any form of experimental error. Assessment of the performance of processing algorithms using artificial regions is a useful method for distinguishing the effects systematic errors have on accuracy. Providing a known displacement between interrogation regions also means that a mean bias error can be quantified. This thesis reports error quantification using both simulated and experimental data.

Although assessment is to be made on the performance of processing algorithms, the accuracy of results is dependent upon the quality of the data recorded in each interrogation region. Huang et al. (1997) and Anandarajah (2005) both stipulated that each interrogation region should be populated with 22 particle images, each with

a diameter of 2.8 pixels. It was stated that this was to avoid errors associated with poor signal-to-noise ratio (SNR) and poor particle image resolution. However, section 3.9 (p.51) addresses the accuracy dependence on image quality by optimising the particle image size and seeding density for regions processed using the standard cross-correlation algorithm. The optimised interrogation regions without background noise were then used to assess the accuracy of various processing algorithms studied in Chapter 4. This shows that NSS is a normalisation function that is able to satisfy reductions in both accuracy metrics, when compared to standard cross-correlation results, by compensating for the random distribution of particle images.

Section 4.5 highlights that with the addition of background noise NSS is not able to maintain the level of accuracy that is quantified with 'ideal' images. From this, Chapter 5 assesses the techniques that can be used to compensate for the presence of background noise in each interrogation region. This leads to the development of a new robust processing algorithm that compensates for the random distribution of particle images as well as the additional background noise. Results show that processing artificial regions, with additional background noise, using the new robust processing algorithm produces accuracy metrics comparable to those generated by the NSS algorithm using 'ideal' images. Comparable results are generated for equal-sized region cross-correlation as well as with iterative techniques for moderate background noise intensities.

Chapter 6 assesses the accuracy of two iterative techniques developed to refine measurements using standard cross-correlation; these techniques are discrete window shifting and particle image pattern matching. The standard cross-correlation results are compared to those generated using NSS as well as the new robust processing algorithm using these iterative techniques. It is shown that these techniques with standard cross-correlation do not compensate for the systematic errors associated to the random distribution of particle images although both techniques provide an improvement in mean bias error regardless of the cross-correlation algorithm used.

Errors predicted by the analysis of artificial images are verified in a controlled experiment described in Chapter 7. The original images were captured by

Anandarajah (2005) and processing with NSS. However, the issues associated with background noise were not addressed. Experimental verifications of the new robust processing algorithm are also in good agreement with their artificial image predictions. This algorithm minimises both accuracy metrics on analysis of equal-sized interrogation regions and the iterative techniques over that of standard cross-correlation results.

Chapter 2

Digital Particle Image Velocimetry Analysis

2.1 Introduction

Over the past 25 years Digital Particle Image Velocimetry (DPIV) has evolved and matured into a versatile and well used fluid flow measurement technique (Adrian, 2005). It is able to provide velocity vector measurements whilst also offering flow visualisation during analysis. Although the technique is the most widely used whole field measurement method in flow diagnostics some fundamental limitations associated with the technique are still apparent. With the development of time-resolved DPIV it is possible to quantify velocities within a turbulent or transient flow field as it develops over time. Although being able to provide high spatio-temporal flow statistics is of high importance in flow diagnostics, it is necessary to quantify and reduce the systematic errors which ultimately arise from image processing.

This chapter firstly outlines the errors quantified using the fast Fourier transform (FFT) and the direct digital cross-correlation ($R(m,n)$) algorithms, collectively referred to as the standard cross-correlation algorithms (SCC), on data-sets of realisations describing a uniform particle image displacement. These algorithms, together with the Gaussian sub-pixel estimator, are widely used to evaluate sub-pixel displacements and as such form a benchmark for error analysis. This highlights the systematic issues associated with SCC analysis.

The next section introduces some of the iterative techniques that have been developed to improve the accuracy of measurements when analysing with SCC. Quantifying the error statistics using discrete window shifting shows that both the mean bias and RMS errors are described over sub-pixel displacements but the

systematic errors causing inaccuracies in measurements remain, thus neither metric is truly reduced using this method. On the application of the particle image pattern matching technique with SCC it is shown that the mean bias error is suppressed but this in turn leads to an increase in RMS error. Implementing these techniques further highlights the inadequacies of the SCC algorithms with regards to suppressing the systematic errors within DPIV.

Thirdly, this chapter reviews some of the image enhancement techniques that can be used if the initial analysis of interrogation regions does not result in a recognisable correlation peak. The next section provides a comprehensive assessment of five normalisation functions that were originally intended to improve the accuracy of measurements. This section extends previous analysis to investigate the effects each normalisation function has on the correlation noise floor before their accuracy metrics are quantified in Chapter 4.

The final section discusses some of the averaging techniques that have been developed with the intention of improving the accuracy of measurements using the standard cross-correlation algorithms.

2.2 Standard processing algorithms

2.2.1 Fast Fourier transform cross-correlation, FFT

The Fast Fourier Transform (FFT) algorithm allows for quick cross-correlation of interrogation region pairs. The computational efficiency of the FFT algorithm makes it the cross-correlation technique favoured by most commercial systems (Fore, 2010) as it requires $M^2 log_2 M^2$ calculations to complete (where M is the size of the square interrogation region) (El-Bakry and Hamada, 2008). To cross-correlate two regions using FFT, the Fourier transformed region $I_1(i, j)$ and the complex conjugate of the Fourier transformed region $I_2(i, j)$ are multiplied together; the resultant FFT array is inverted to compute a correlation field such that:

$$I_1(i, j) \otimes I_2(i, j) \Leftrightarrow FFT^{-1}\left(\hat{I}_1(\xi,\eta) \times \hat{I}_2^{*}(\xi,\eta) \right) \qquad \textbf{2.1}$$

where $\hat{I}_1(\xi,\eta)$ denotes the Fourier transform of $I_1(i, j)$ and $\hat{I}_2^{*}(\xi,\eta)$ represents the complex conjugate of the Fourier transform of $I_2(i, j)$. The pixel position during correlation is denoted by (i, j).

While the FFT algorithm is computationally efficient, analysis requires square interrogation regions that are a power-of-two in dimension (i.e. 16 x 16, 32 x 32…2^n x 2^n pixels etc). However, non-square regions may also be processed if regions are zero-padded before FFT cross-correlation (McKenna and McGillis, 2002). For example, a region that is n x m pixels is padded with zeros so that it is located at the centre of a region that is 2^n x 2^n pixels without the loss of any particle image data; after which the correlation field can be computed using equation 2.1. When processing regions that are already 2^n x 2^n pixels in size (prior to zero-padding) with the FFT algorithm, aliasing will introduce errors into analysis. Thus, aliasing is present because the sampling frequency is not high enough to sample the signal. This causes the correlation signal to overlap forming a ‘wrap-around' due to the assumed periodicity of the signal when the FFT algorithm is used (Gonzales and Wintz, 1987). Issues associated with ‘wrap-around’ can be avoided if interrogation regions are again zero-padded before FFT cross-correlation.

2.2.2 Spatial domain cross-correlation, *R(m,n)*

Alternatively, cross-correlation can be evaluated directly in the spatial domain using the digital direct cross-correlation algorithm, *R(m,n)* which is described by equation 2.2:

$$R(m,n) = \sum_{i=0}^{M}\sum_{j=0}^{N} I_1(i,j)\, I_2(i-m, j-n) \qquad \textbf{2.2}$$

For an interrogation region size of length, *M* and width, *N* and *m* and *n* is the shift in the *x* and *y*-directions as the first region $I_1(i,j)$ shifts over the second $I_2(i,j)$ to calculate each point in the correlation field (Figure 2.1).

Although this cross-correlation method is simple to implement it is computationally intensive. Each correlation field requires $(M\times N)^4$ calculations to complete and this is the main (and only reason) why FFT was introduced as a cross-correlation algorithm (Pust, 2000). However, unlike FFT cross-correlation, regions processed this way are not required to have 2^n x 2^n dimensions and as a result do not have to be zero-padded.

For equal size interrogation regions, the *R(m,n)* routine works by passing the first interrogation region $I_1(i,j)$ of size $M\times N$ across the second region $I_2(i,j)$ as is illustrated in Figure 2.1. Correlation produces a $[(2M-1)\times(2N-1)]$ field so therefore for the correlation of two equal 32 x 32 pixel regions will generate a 63 × 63 pixel correlation field.

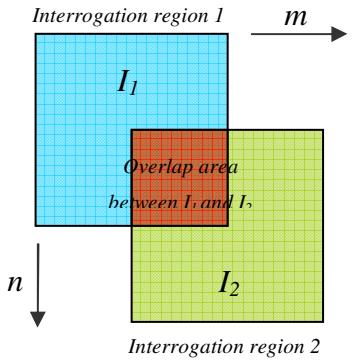

Figure 2.1 *R(m,n)* cross-correlation

During cross-correlation, the point at which there is a maximum particle image correlation corresponds to the location of the correlation or signal peak as is

illustrated in Figure 2.2. The position of the peak relative to the centre of the correlation field corresponds to the average displacement within the realisation and, after digitisation, is twice the width of the particle images being analysed. Its position within the correlation field can be described to within a fraction of a pixel using a sub-pixel estimator (section 2.3). As the displacement between two regions increases, the correlation peak will decrease in height and broaden. This is caused by a decreasing number of particle images that can contribute to the correlation peak. This is known as the out-of-pattern (or in-plane loss-of-pairs) effect (Adrian, 1991 and Huang et al., 1993b).

It is also noted that when calculating velocity vectors, interrogation regions that are zero-padded before FFT cross-correlation will produce identical results to regions processed using *R(m,n)* cross-correlation (Eckstein, 2007). Since both algorithms provide identical results they are referred to as the standard cross-correlation algorithms, SCC.

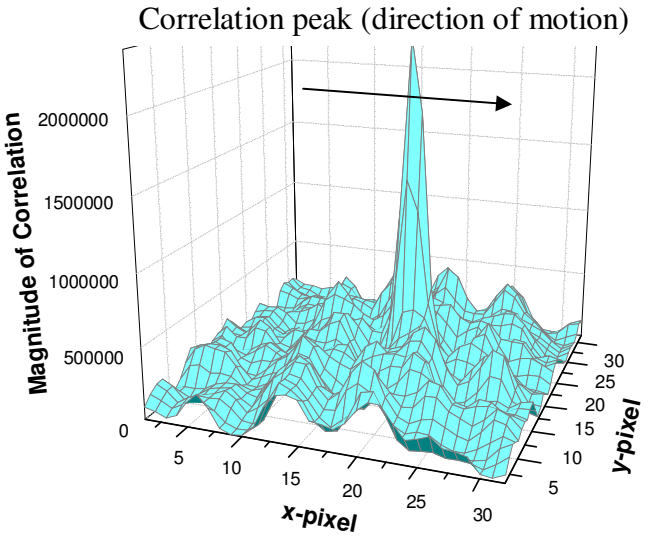

Figure 2.2 A standard cross-correlation field

2.3 Sub-pixel estimators

The development of interpolation algorithms to obtain the sub-pixel location of the correlation peak was the crucial step in the advance of DPIV. The measurement resolution of displacement estimations changed from ±½ pixel to ±1/100th of a pixel upon the implementation of a sub-pixel estimator. In commercial codes, the sub-pixel location of the correlation peak in both the *x*- and *y*-directions is determined using the five central points of the correlation peak (Fore, 2010); the four adjacent points in the *x*- and *y*-directions and the central correlation peak value. Although many sub-pixel estimators are available the three most commonly used are the centroid estimator, the parabolic estimator and the Gaussian estimator (Willert and Gharib, 1991). For a two-dimensional correlation field, $R(x,y)$ the location of the correlation peak found to within ±½ pixel is given as (x_c, y_c) and the sub-pixel peak centre (x_{pk}, y_{pk}) is defined using the three estimators as:

Centroid estimator:

$$x_{pk} = \frac{(x_c-1)R(x_c-1,y_c)+x_cR(x_c,y_c)+(x_c+1)R(x_c+1,y_c)}{R(x_c-1,y_c)+R(x_c,y_c)+R(x_c+1,y_c)}$$
$$y_{pk} = \frac{(y_c-1)R(x_c,y_c-1)+x_cR(x_c,y_c)+(y_c+1)R(x_c,y_c+1)}{R(x_c,y_c-1)+R(x_c,y_c)+R(x_c,y_c+1)} \quad \textbf{2.3}$$

Parabolic estimator:

$$x_{pk} = x_c + \frac{R(x_c-1,y_c)-R(x_c+1,y_c)}{2R(x_c-1,y_c)-4R(x_c,y_c)+2R(x_c+1,y_c)}$$
$$y_{pk} = y_c + \frac{R(x_c,y_c-1)-R(x_c,y_c+1)}{2R(x_c,y_c-1)-4R(x_c,y_c)+2R(x_c,y_c+1)} \quad \textbf{2.4}$$

Gaussian estimator:

$$x_{pk} = x_c + \frac{\ln R(x_c-1,y_c)-\ln R(x_c+1,y_c)}{2(\ln R(x_c-1,y_c)-2\ln R(x_c,y_c)+\ln R(x_c+1,y_c))}$$
$$y_{pk} = y_c + \frac{\ln R(x_c,y_c-1)-\ln R(x_c,y_c+1)}{2(\ln R(x_c,y_c-1)-2\ln R(x_c,y_c)+\ln R(x_c,y_c+1))} \quad \textbf{2.5}$$

Quantifying both accuracy metrics requires particle images to be displaced in only one direction. Since a displacement in the *x*-direction is to be modelled then only the three points defining sub-pixel displacement of the correlation peak in the *x*-direction have to be considered for this analysis. With this is mind, the central point is common to both the *x*- and *y*-direction and so in two dimensions the interpolation functions can be referred to as being five point estimators.

Westerweel (1993a) stated that the Gaussian estimator is superior to both the centroid and parabolic estimators as it produces the lowest measurement errors of the three sub-pixel estimators examined. The Gaussian estimator is generally accepted as being the standard estimator when processing with the standard cross-correlation algorithms. This is due to digitised particle images approximating two-dimensional Gaussian distributions; when two Gaussian distributions are cross-correlated the resulting signal also has a Gaussian distribution. For this reason, the Gaussian sub-pixel estimator is used as the benchmark estimator when quantifying the accuracy of measurements.

2.4 Error quantification

Once the sub-pixel displacement has been calculated the performance of the processing algorithm can then be assessed. Quantifying the accuracy of a DPIV processing algorithm is achieved using two metrics, these are: the mean bias and RMS (random) errors. The mean bias error, d_b is a measure of the difference between the mean measured displacement, $\bar{d}_i$ over N realisations and the actual displacement, d_a. This is defined as:

$$\bar{d}_i = \frac{1}{N}\sum_{i=1}^{N} d_i$$
$$d_b = \bar{d}_i - d_a \qquad \textbf{2.6}$$

Where d_i is the measured displacement from a single measurement where i = 1, 2, 3…N and N is the total number of realisations.

The random error is used to determine the deviation of measured displacements for each realisation from the mean measured displacement. This is termed the root mean square (RMS) error or σ, and is defined as:

$$\sigma = \sqrt{\frac{1}{N}\sum_{i=1}^{N}\left(d_i - \bar{d}_i\right)^2} \qquad \textbf{2.7}$$

By being able to calculate the average measured displacement and the variation in individual measurements from the mean for each data-set means that the systematic errors within DPIV can be analysed and quantified. A mean bias and RMS error point is calculated for each data-set where the actual displacement is known.

A reduction in both accuracy metrics is required to show that a cross-correlation algorithm provides an improvement in accuracy. Therefore both metrics can be given an equal weighting and if it is assumed that they are independent variables, a reasonable definition of total error, β can be defined as:

$$\beta = \sqrt{{d_b}^2 + \sigma^2} \qquad \textbf{2.8}$$

where d_b is the mean bias error and σ the RMS error.

Valid vector detection (VVD) can also be used to measure the validity and subsequently the accuracy of measurements because it quantifies the number of valid vectors that have been processed (Wernet, 2005). The validity of a vector is user defined (i.e. a measurement should be within a defined range) and should give a detection probability of between 90-100% to provide a reasonable representation of the flow (Westerweel et al., 2005). For example, the average displacement is calculated across an image and if an individual vector is outside ±½ pixel of the average then these are referred to as invalid or erroneous vectors and are removed from analysis during validation. Once all vectors have been validated a new average is calculated and the process is repeated until there is no change in the average displacement value between two successive validation processes. A second approach to remove invalid vectors is to identify the condition of the correlation peak and the magnitude of the correlation noise floor. Therefore, the signal-to-noise ratio (SNR) can be used as a measure to validate measurements further. This is defined as:

$$SNR = \frac{\text{Height of signal peak}}{\text{Height of highest noise peak}} \qquad \textbf{2.9}$$

For a measurement to be valid, the signal peak must be greater than the highest noise peak (i.e. SNR > 1). Values below 1 are achieved if the processed images are dominated by noise or when the signal is too low for a correlation peak to be detected. It is therefore essential to maintain a high VVD rate when conducting an experimental analysis or theoretical quantifications of images using robust processing algorithms that can withstand the rigours of changing image quality.

The next section reviews the accuracy metrics quantified with the standard cross-correlation algorithms using artificially generated particle images experiencing a uniform particle image displacement in the *x*-direction.

2.5 Standard cross-correlation error quantification

Figure 2.3 shows the typical error plots that are generated when the standard cross-correlation routines (SCC: either *R(m,n)* or FFT with zero padding, and FFT without zero padding) are used calculate a correlation peak and the Gaussian sub-pixel estimator used to evaluate each displacement. These error plots are generated from a series of artificially generated interrogation regions (32 x 32 pixels) each of which contain 22 particle images with a diameter of 2.8 pixels that describe a known uniform particle image displacement in the *x*-direction.

(a) mean bias error

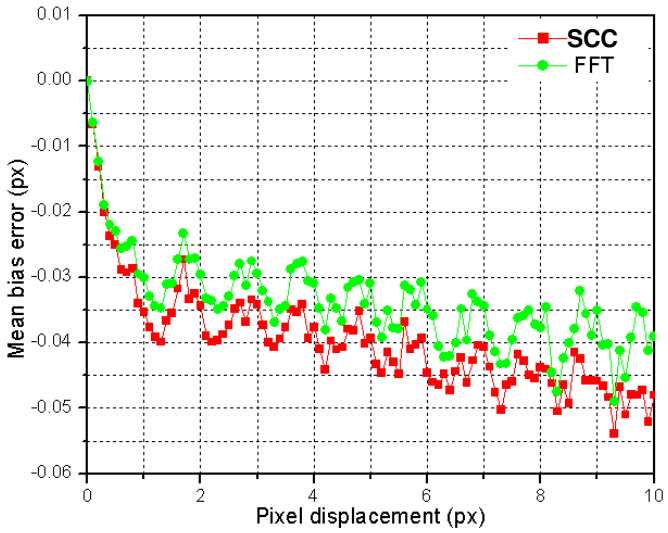

(b) RMS error

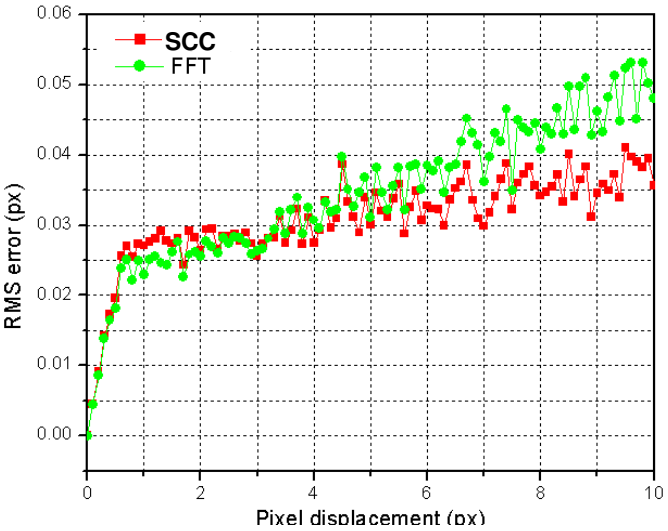

Figure 2.3 Error plots for SCC and FFT without zero padding (Anandarajah, 2005)

Figure 2.3(a) clearly highlights that both SCC and FFT without zero padding generates a negative mean bias error for each displacement that also contains a characteristic oscillation; this is often referred to as the peak-locking effect (Raffel et al., 1998). When examining the RMS error plot (Figure 2.3(b)) is it clear that both routines generate a sharp increase in RMS error at sub-pixel displacements, after which this rate of increase diminishes.

Previous studies of error quantifications using SCC ($R(m,n)$ or FFT with zero padding) associated the negative mean bias to the non-uniform weighting of the correlation function. This weighting is inherent to the SCC functions and is caused by the cross-correlation of unrelated particle images (or more generally, pixel intensities) contributing to the correlation field. As the displacement increases between interrogation regions, the correlation peak shifts away from the centre of the correlation field. It was stated (Raffel, 1998) that since the correlation peak is located on a pyramid shaped correlation field then it is this that biases the peak away from the actual displacement value. As such the correlation field has to be corrected to account for the bias in peak position. These underestimations, assumed to be associated to the non-uniform weighting of the correlation function, have been well documented and methods for its removal include using appriopriate weighting functions (e.g. Raffel et al., 1998) or subtraction of the mean intensity from within each interrogation region before cross-correlation (Westerweel, 1997).

Anandarajah (2005) extended this investigation by studying the average correlation noise floor for both the SCC and FFT (without zero padding) routines as are shown in Figure 2.4.

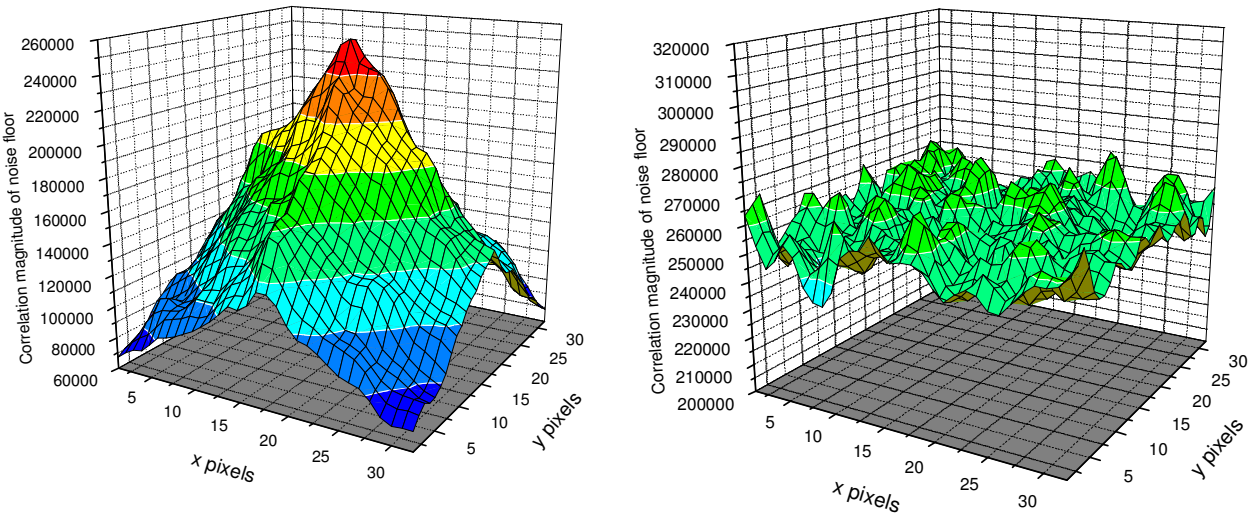

(a) SCC correlation noise floor **(b) FFT correlation noise floor**

Figure 2.4 Typical correlation noise floors for SCC and FFT cross-correlation

On evaluation of the FFT routine, a flat correlation field is produced; caused by the circular convolution effect. Following the original assumption that the shape of the correlation field biases the peak away from the actual value then it is intuitive to assume that results from FFT correlation will not be biased as the correlation field is flat. However, as Figure 2.3(a) shows, FFT cross-correlation still results in negatively biased displacements. It was therefore stated by Andandarajah (2005) that the correlation field characteristics are not the sole cause of biases in measurements.

2.6 Iterative correlation methods

As the displacement between regions increases, the number of particle images that contribute to the correlation peak decreases and is referred to as the out-of-pattern effect. Concerns were raised that the loss of signal would increase measurement errors and therefore investigations proceeded to minimise this effect.

The proposed solution for increasing the measurement accuracy for standard cross-correlation was the iterative correlation method. This process was developed to maintain a high and constant SNR whist also taking advantage of low sub-pixel displacement errors (Raffel et al., 1998). One of the simplest iterative methods is discrete window shifting (DWS) (Westerweel et al., 1997). This method estimates the shift required by the first region by estimating the displacement from an initial cross-correlation. After the shift, a second cross-correlation provides a sub-pixel displacement where the out-of-pattern effect has less of an influence on measurements.

Figure 2.5 shows the typical error plots generated when applying window shifting with SCC and using the Gaussian sub-pixel estimator to evaluate displacements of regions experiencing a uniform displacement in the *x*-direction. The use of window shifting as a means of error reduction is further discussed in Chapter 6.

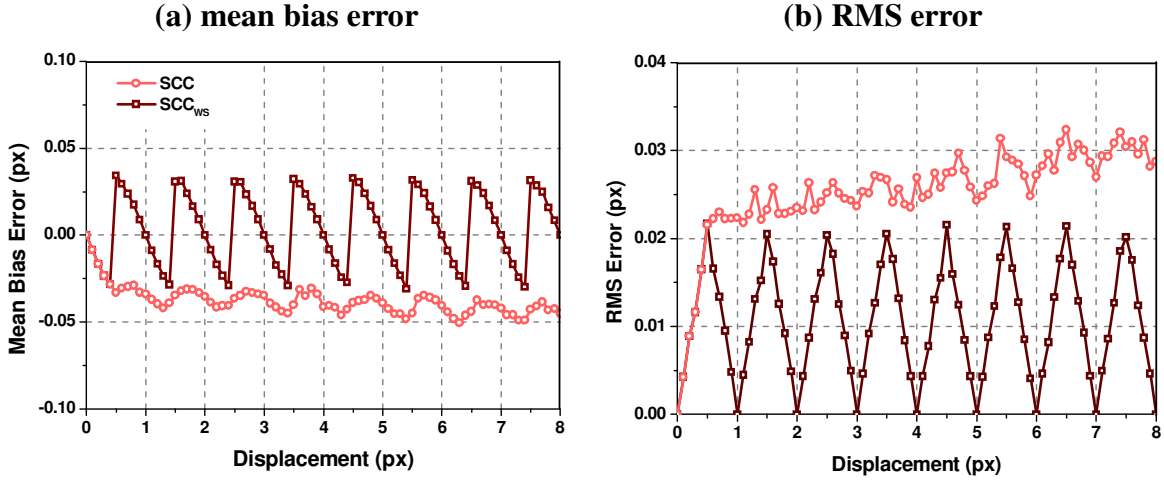

Figure 2.5 Error plots for SCC_{WS} compared with SCC

The figure illustrates that for sub-pixel displacements the errors generated for SCC and SCC_{WS} are identical. Once the first window shift is implemented, as is described

in section 6.2 (p.150), the errors generated for each displacement are described over a single pixel and therefore each error is composed solely of the sub-pixel displacement error. This generates the distinctive oscillation in the accuracy metric plots shown in Figure 2.5.

An extension to the DWS is continuous window shifting. After an initial displacement estimation this process uses bi-linear image interpolation before a second cross-correlation provides the sub-pixel displacement. Advances in this technique have lead to the development of higher order interpolation functions being developed including the sinc function (Lourenco and Krothapalli, 1995 and Roesgen, 2003) and a Gaussian function (Nobach et al., 2004) and also the Particle Image Distortion (PID) technique (Huang et al., 1993a). This process manipulates the interrogation region shape before a final displacement estimate is determined.

The window deformation techniques were subsequently enhanced by Nogueira et al. (1999) and Scarano and Riethmuller (2000). These techniques are best when analysing flows experiencing strong velocity gradients (Keane and Adrian, 1992) since loss of image pairs will cause the correlation peak to reduce in height and adverse gradients will cause the peak to eventually splinter, resulting in the generation of spurious velocity vectors. Scarano (2002) stated that the cause of the demise of measurement accuracy from flows experiencing gradients could also be minimised if the size of the interrogation regions under investigation were reduced; this will also inherently increase the velocity vector resolution. As will be shown in section 5.4 (p.144), processing smaller interrogation regions can preclude meaningful and accurate velocity vectors from being extracted compared to larger region analysis. Huang et al. (1997) also introduced a technique that would allow a smaller first region to be cross-correlated with a larger second increasing the likelihood of particle image pair correlation. This is known as particle image pattern matching (PIPM).

Figure 2.6 provides typical error plots for when the second region is decreased in size and is cross-correlated with a first region that is 32 x 32 pixels in size. Each displacement is evaluated using the Gaussian sub-pixel estimator on data-sets of regions that are experiencing a known uniform particle image displacement in the *x*-direction. The use of PIPM with SCC as a means of reducing the accuracy metrics is discussed further in Chapter 6.

(a) mean bias error **(b) RMS error**

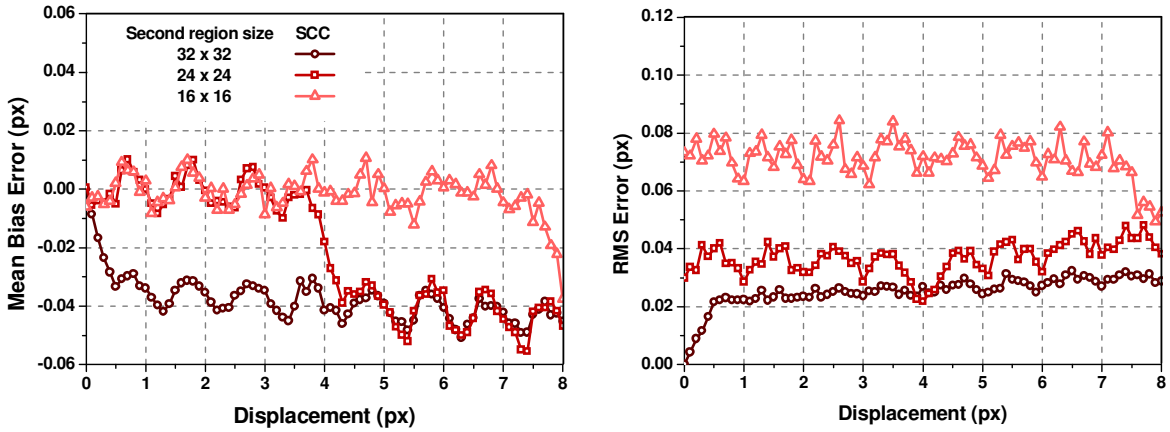

Figure 2.6 Error plots for PIPM of 16 x 16, 24 x 24 and 32 x 32 pixel regions with 32 x 32 pixel regions using SCC

The figure clearly shows that as the second region size is decreased there is an improvement to the mean bias error. However, this is coupled with an increase in RMS error. The reasons for this decrease in mean bias error with subsequent increase in RMS error as the second region size decreases is explained in section 6.3 (p.156).

Adaptive iterative schemes have also been developed as a means of increasing accuracy (e.g. Jambunathan et al., 1995; Takumara and Dimotakis, 1995 and Scarano, 2002) but each of these algorithms are numerically and computationally intensive and result in heavy image manipulation in order to generate a second region identical to that of the first. Image manipulation may unintentionally cause vital information in the second frame to be lost and therefore detract from the validity of the velocity vector generated. Although these algorithms are useful in their own right their development has continued despite neglecting the systematic errors that occurs within DPIV analysis. All these iterative correlation techniques typically use SCC to calculate displacements. Although these methods have been shown to

improve the mean bias error over the classic SCC approach, Chapter 6 shows that neither DWS nor PIPM improves the RMS error when processing with SCC.

Another factor affecting the accuracy of measurements is caused by variations in image intensities across and between interrogation regions. This can result from the heterogeneous illumination of particle image intensities due to light sheet non-uniformities including pulse-to-pulse variations. The cross-correlation of background noise intensities, including out-of-plane motion, irregular shaped particle images and unrelated particle images will also affect measurements. Two approaches are often implemented to restore the accuracy lost through intensity variations, these are: image enhancements prior to cross-correlation and the development of normalisation functions designed to improve measurement accuracy. These two methods are reviewed in section 2.7 and section 2.8 respectively.

2.7 Image enhancement

Image enhancement techniques are designed to reduce the variation in particle image intensity across and between interrogation region pairs. Fore et al. (2005) proposed subtracting an average background noise image, obtained by averaging a series of images that do not contain particle image intensities, from each interrogation region. As intensity subtraction reduces the pixel intensity range from cross-correlation the technique also requires the grey-scale intensities to be linearly stretched. Dellenback et al. (2000) evaluated measurements by applying a threshold, contrast enhancement and histogram hyperbolisation to their low quality images before cross-correlation to improve accuracy. These techniques were enhanced by Roth and Katz (2001) who developed a modified histogram equalization technique that combines thresholding with histogram stretching.

Image enhancement through intensity capping was developed by Shavit et al. (2006) and was reported to be effective and easy to implement. The technique relies upon setting intensities that exceed a certain threshold value to the threshold value and those below maintain their original value. The threshold value I_{cap} defined in equation 2.10 is calculated by determining the median grey-scale intensity across a region I_{median} and the standard deviation σ. Raffel et al. (2007) noted that although optimal threshold values vary with the image content, it may be calculated for the entire image from the grey-scale median intensity value I_{median}.

$$I_{cap} = I_{median} + n\sigma \qquad \textbf{2.10}$$

The scaling factor n is user defined and is in the range $0.5<n<2$. Once the intensity distribution has been capped displacements are determined using standard cross-correlation.

Additionally, Westerweel (1993b) suggested a *min/max* filter intended to adjust intensity values across an image. Rather than adjusting intensities using global statistics, as was proposed with the other methods, this technique requires local statistics obtained from within a given region (or kernel) centred on each point within the image. A new pixel intensity value is then calculated using equation 2.11:

$$I_{new}(x,y) = I_{\max}\left[\frac{I(x,y) - \min(I_{kernel})}{\max(I_{Kernel}) - \min(I_{kernel})}\right] \qquad \textbf{2.11}$$

where I_{max} is the maximum intensity value attainable in the image (i.e. 8-bit image = 2^8 = 256 or 12-bit image = 2^{12} = 4096 etc.), $I(x,y)$ is the original pixel value and the min/max values are obtained from within a local region around each pixel value. Raffel et al. (2007) stated that each local region should be larger than the particle image diameter yet small enough to eliminate spatial variations in the background and therefore sizes of 7 x 7 to 15 x 15 pixels are generally used. Using the same principles as Westerweel's *min/max* filter, image enhancements can also be made by subtracting a mean intensity calculated over a local region centred on each point within the image to remove background noise before analysis.

In brief, this section has introduced some image enhancement techniques used prior to cross-correlation; these limit the variation in pixel intensity across and between each interrogation region pair to maintain the accuracy of DPIV results. Each technique calculates a new pixel value for each point within an interrogation region using the original intensities and as such care must be taken to avoid manipulations that will overtly affect accuracy.

2.8 Normalisation of the correlation field

When processing interrogation regions using standard cross-correlation, the height and shape of the correlation peak will vary from one realisation to the next and therefore will affect the accuracy metrics. This is caused by variations in illumination across and between two interrogation regions (Gonzales and Wintz, 1987), variations in particle seeding density (Anandarajah, 2005) and also electronic image noise (Raffel et al., 1998). These uncertainties were a major concern for researchers who regarded limiting changes in the variation of the correlation peak height as a critical enhancement of DPIV processing. It can be concluded (e.g. Gonzales and Wintz, 1987 and Raffel, 1998) that the accuracy metrics were affected by correlation peak height, and to account for these variations each correlation field should be normalised to improve accuracy. Once normalised, a comparison between two independent correlation fields can be made. This section introduces five normalisation functions that are commonly used in DPIV processing and their effect on measurement accuracy is discussed further in Chapter 4.

2.8.1 Normalisation by overlapped area

It has previously been assumed (Raffel et al., 1998) that when cross-correlating equal-sized regions, the non-uniform weighting of the correlation function results in underestimated measurements. This bias was assumed to be caused by the cross-correlation of unrelated particle images contributing to a pyramid shaped correlation noise floor (Figure 2.4(a)). It was therefore concluded that the bias could be reduced if each correlation field were normalised by the unit area used to calculate each point of the field. Normalisation of the SCC field with overlapped area, SCC_{OA}, is expressed as:

$$SCC_{OA} = \frac{SCC}{A(m,n)} \qquad \textbf{2.12}$$

$A(m,n)$ can be calculated by generating two interrogation regions; each pixel within both regions assume a value of one. These two regions can then be cross-correlated using equation 2.2 to generate the overlapped area weighting function illustrated in Figure 2.7.

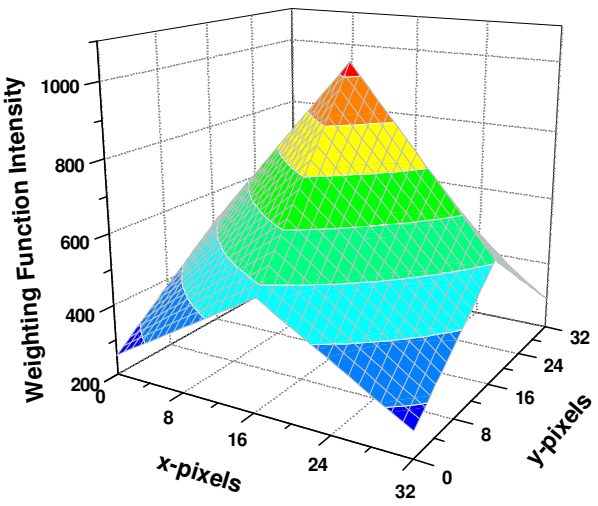

Figure 2.7 Overlapped area weighting function (32 x 32 pixel regions)

When normalising by area, each point of the correlation field is normalised by a local constant value. This normalisation function remains the same regardless of changes in the condition of individual interrogation regions. When the SCC correlation noise floor (Figure 2.4(a)) is normalised by area (Figure 2.7) the resulting normalised correlation noise floor is flat, as is shown in Figure 2.8(a). However, when the FFT (without zero-padding) correlation noise floor (Figure 2.4(b)) is normalised by area, a 'valley' shaped correlation noise floor is generated as is shown in Figure 2.8(b).

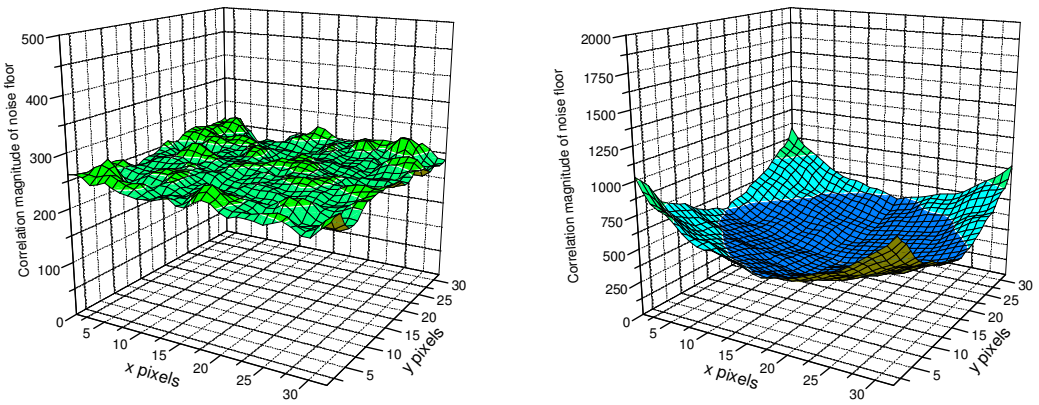

(a) SCC_{OA} correlation noise floor **(b) FFT_{OA} correlation noise floor**

Figure 2.8 SCC and FFT correlation noise floors normalised by area

As section 4.3.1 (p.73) explains, when both correlation functions are normalised by area there is an improvement to the mean bias error metric, albeit measurements are overestimated for FFT_{OA}. However, when normalising by area neither function will account for the uncertainties in measurements. Therefore, the RMS error results are equivalent to the results produced from their respective SCC routines.

2.8.2 Normalisation by signal strength

One of the main issues of normalising the correlation field before determining the measured displacement is that some weighting functions are able to reduce mean bias error, but fail to affect the RMS error. Huang et al. (1997) originally proposed normalising the FFT correlation field by the pixel intensities within the overlapped area, referred to as the signal strength. It was known that the intensity distribution across each interrogation region affects the asymmetry of each correlation peak; therefore normalising by the pixel intensities that contribute to each point of the correlation field will inherently reduce the uncertainties in measurements to improve both accuracy metrics.

Normalisation by signal strength (NSS) is defined as:

$$NSS = \frac{SCC}{\left[\sum_{i,j\in A} I_1^2(i,j) \times \sum_{i,j\in A} I_2^2(i,j)\right]^{1/2}} \qquad \textbf{2.13}$$

where A denotes the overlapping area between regions $I_1(i,j)$ and $I_2(i,j)$. The signal strength is defined as the product of the summed squared intensities within the overlapped area and is calculated in the spatial domain.

A typical signal strength weighting function is illustrated in Figure 2.9. Its shape is dictated by the variations in intensity content within each realisation

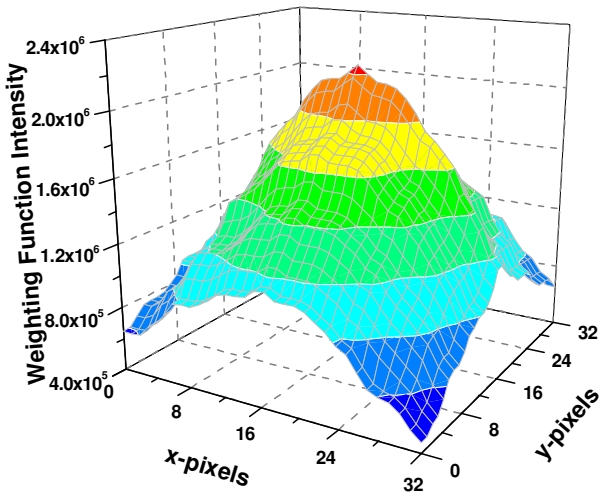

Figure 2.9 A typical signal strength weighting function

In the original investigation by Huang (1997) each interrogation region was not zero-padded prior to FFT cross-correlation. Therefore normalisation of the FFT correlation field (Figure 2.4(b)) by a typical signal strength function will generate a 'valley' shaped normalised correlation field similar to that generated for the normalisation of the FFT correlation field by area (Figure 2.8(b)). As Figure 4.5 (p.75) verifies, FFT_{SS} will also overestimate measurements. As section 4.3.1 (p.73) describes, this overestimation results from the 'valley' shape of the normalised correlation field.

The study of the signal strength function was further enhanced by Anandarajah (2005) who stated that this normalisation function could compensate for the random distribution of particle images within each interrogation region and thereby reduce both accuracy metrics. This would be achieved if zero-padding prior to FFT cross-correlation or applying *R(m,n)* cross-correlation before normalising the correlation field by the signal strength. On the normalisation of the SCC correlation field (Figure 2.4(a)) by a typical signal strength weighting function the resulting normalised correlation field will be flat. As is identified in both section 4.3.1 (p.73) and section 4.3.2 (p.75), generating a flat correlation noise floor through normalisation suppresses the mean bias error. Anandarajah (2005) also stated that accounting for the variations in intensity distribution across each region through normalisation by signal strength will inherently provide an improvement to both accuracy metrics; this is verified by the error plots generated in Figure 4.5 (p.75).

2.8.3 Normalisation by intensity

Willert and Ghirib (1991) introduced normalising the correlation field by intensity as a means of accounting for variations in correlation peak height per realisation. This is defined as:

$$SCC_I = \frac{SCC}{\sum_{i=0}^{M}\sum_{j=0}^{N} I_1(i,j) \times \sum_{i=0}^{M}\sum_{j=0}^{N} I_2(i,j)} \qquad \textbf{2.14}$$

where the normalisation function is defined as the product of total intensities across both interrogation regions, $I_1(i,j)$ and $I_2(i,j)$ that have dimensions $M \times N$. This therefore normalises each correlation field by a global constant. This normalisation function will vary between each realisation within a flow field image to account for variations in intensity content across each region. However, if each correlation field is normalised by a global constant there is no effect on the shape of the correlation functions thus there will be no changes in either the mean bias or RMS error results.

2.8.4 Mean image intensity subtraction prior to cross-correlation

Another method proposed to reduce measurement error is that of subtracting the mean image intensity from the first and second interrogation region prior to *R(m,n)* cross-correlation. The $R_{MS}(m,n)$ method was originally presented by Westerweel (1997) and is defined as:

$$R_{MS}(m,n) = \sum_{i=0}^{M}\sum_{j=0}^{N}\left[I_1(i,j) - \bar{I}_1\right]\left[I_2(i-m, j-n) - \bar{I}_2\right] \qquad \textbf{2.15}$$

where $\bar{I}_1$ and $\bar{I}_2$ are defined as the mean image intensity across the entire first and second interrogation regions respectively.

Pust (2000) discussed the calculations for this technique further by stating that the average global intensities for each interrogation region $\bar{I}_1$ and $\bar{I}_2$ are computed and subtracted from each individual intensity values. If the individual intensity values are smaller than the average intensity they are set equal to zero.

In the original investigations by Westerweel (1997) it was stated that this technique would provide improvements to the accuracy of measurements. It was reported that this method reduced the mean bias error by suppressing the 'pyramid' noise floor. Anandarajah (2005) did identify that $R_{MS}(m,n)$ generates a flat correlation noise floor by removing the non-uniform weighting of the *R(m,n)* correlation function, as is shown in Figure 2.10.

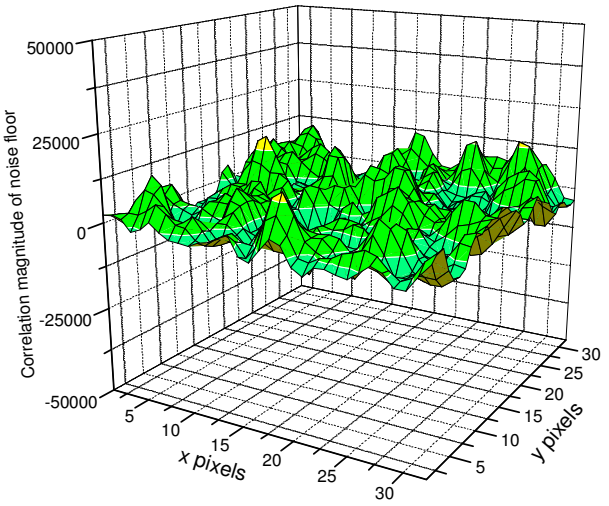

Figure 2.10 $R_{MS}(m,n)$ correlation noise floor

However, as section 4.3.3 (p.77) identifies, there are only negligible improvements to the accuracy metrics when analysing 'ideal' artificial interrogation regions and are comparable to SCC results. This procedure does however improve accuracy over that of SCC when quantifying measurements from regions that contain background noise. This is because this method effectively thresholds (at zero) to remove a substantial part of the background noise intensities from each individual realisation. This method is addressed further in section 5.2.5 (p.120).

2.8.5 Normalisation by variance

One of the first normalisation functions that could compensate for changes in brightness across a flow field due to changes in lighting and exposure conditions was proposed by Burt et al. (1982). This was termed the variance normalised cross-correlation routine, $R_V(m,n)$ and is defined as:

$$R_V(m,n) = \frac{\sum_{i=0}^{M}\sum_{j=0}^{N}\left[I_1(i,j)-\bar{I}_1\right]\left[I_2(i-m,j-n)-\bar{I}_2\right]}{\left[\sum_{i=0}^{M}\sum_{j=0}^{N}\left[I_1(i,j)-\bar{I}_1\right]^2 \times \sum_{i=0}^{M}\sum_{j=0}^{N}\left[I_2(i,j)-\bar{I}_2\right]^2\right]^{1/2}} \qquad \textbf{2.16}$$

where $\bar{I}_1$ and $\bar{I}_2$ represent the mean intensities across the first and second interrogation region respectively. As the flow field image is divided into interrogation regions a mean intensity is calculated across each region. On cross-correlation the mean intensity value is subtracted from the pixel values from their respective interrogation regions. This is then normalised by the variance of both interrogation regions. This is intended to account for variations in flow field illuminations as a velocity map is calculated. This point was further highlighted by Willert (1996) who stated that the mean image intensity was subtracted to avoid changes in the maximum correlation peak height produced from variations in illumination across each interrogation regions.

As the function describes a global variance across the interrogation region a global constant is provided for normalisation. As with the normalisation by intensity function, described in section 2.8.3, the global variance within each realisation (which is directly related to the intensity content) will vary between interrogation region pairs, as such this global constant value will change accordingly. However, this consequently provides error plots that are comparable to those generated by normalisation by intensity and as such this normalisation function does not provide an improvement to either accuracy metric.

The essence of the variance normalised cross-correlation routine proposed by Burt et al. (1982) was further enhanced by Fincham and Spedding (1997) and Raffel et al. (1998). Both proposed normalising the correlation field in a similar way but instead

of calculating a mean intensity over each region this routine provides a varying average for the second region. This varying mean intensity value is calculated from the intensity values that contribute to the correlation and therefore will change for each correlation field value. The mean intensity value for the first region is calculated in the same way as the Burt et al. (1982) method. Raffel et al. (1998) reasoned that this normalisation routine should be used because "regions that contain more particle images will produce much higher correlation values than regions that contain fewer particles. This makes a comparison of the degree of correlation between individual interrogation regions impossible". The mathematical definition of the variance normalised cross-correlation routine proposed by Fincham and Spedding (1997) and Raffel et al. (1998) is defined as:

$$R_V(m,n) = \frac{\sum_{i=0}^{M}\sum_{j=0}^{N}[I_1(i,j)-\mu_1][I_2(i-m,j-n)-\mu_2(m,n)]}{\sqrt{\sum_{i=0}^{M}\sum_{j=0}^{N}[I_1(i,j)-\mu_1]^2 \times \sum_{i=0}^{M}\sum_{j=0}^{N}[I_2(i,j)-\mu_2(m,n)]^2}} \qquad \textbf{2.17}$$

where μ_1 is the mean intensity of the first interrogation region and is calculated only once for each realisation analysis and $\mu_2(m,n)$ is the mean intensity of $I_2(i,j)$ that is coincident with $I_1(i,j)$ at position (m,n) (i.e. the mean intensity of the second region's contribution to the correlation field.) and is calculated each time the coincident area changes. Mathematically, $\mu_2(m,n)$ is defined as:

$$\mu_2(m,n) = \frac{\sum_{i=0}^{M}\sum_{j=0}^{N} I_2(i-m,j-n)}{A(m,n)} \qquad \textbf{2.18}$$

where *A(m,n)* is defined in section 2.8.1. Raffel et al. (1998) further stated that this normalisation routine is considerably more difficult to implement using an FFT-based approach and therefore is subsequently computed directly in the spatial domain.

Lewis (1995) also proposed a similar normalisation routine to the Fincham and Spedding (1997) and Raffel et al. (1998) approach described in equation 2.17. This routine was formulated to track features within an image. The normalisation routine is defined as:

$$R_V(m,n) = \frac{\sum_{i=0}^{M}\sum_{j=0}^{N}[I_1(i,j)-\mu_1(m,n)][I_2(i-m,j-n)-\mu_2]}{\sqrt{\sum_{i=0}^{M}\sum_{j=0}^{N}[I_1(i,j)-\mu_1(m,n)]^2 \times \sum_{i=0}^{M}\sum_{j=0}^{N}[I_2(i-m,j-n)-\mu_2]^2}} \qquad \textbf{2.19}$$

where each term has the same meaning as defined by equation 2.17 with the exception of the average intensities calculated for the first and second interrogation region. For this routine $\mu_1(m,n)$ is the mean intensity of $I_1(i,j)$ that contributes to the correlation field and is calculated for each point during cross-correlation and μ_2 is the mean intensity of $I_2(i,j)$ and is calculated once per realisation analysis. Figure 2.11 illustrates typical weighting functions for the normalisation procedures described in equations 2.17 (Figure 2.11(a)) and equation 2.19 (Figure 2.11(b)).

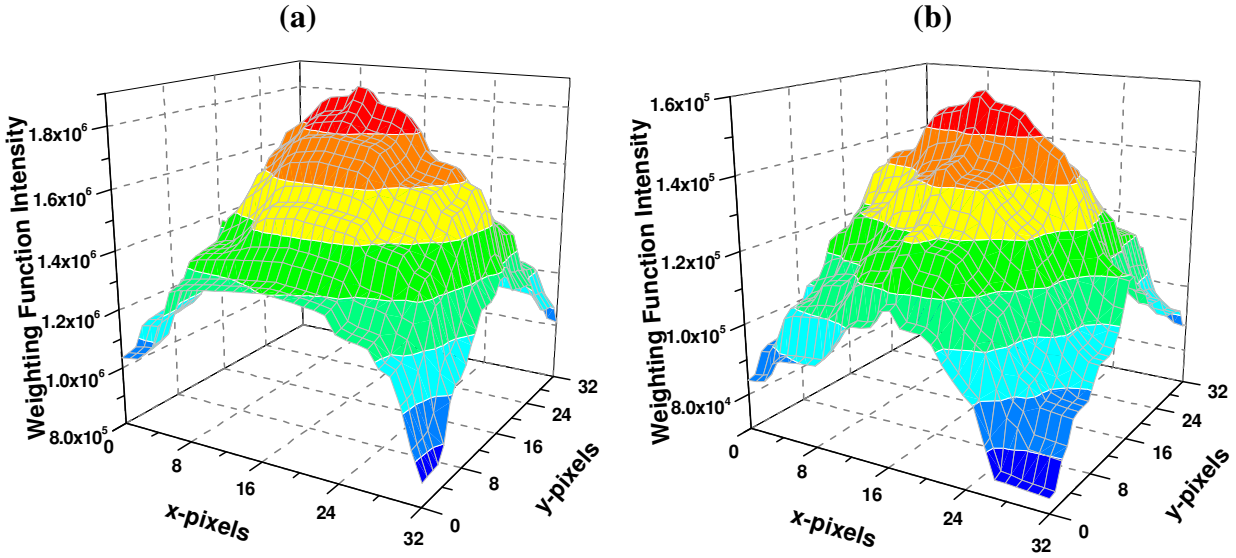

Figure 2.11 A typical $R_V(m,n)$ weighting function for (a) eq. 2.17 and (b) eq. 2.19

The shape of these two normalisation functions is dictated by the intensity distribution across each realisation. Since each realisation contains a random distribution of particle images then this distribution is unique to each realisation. This variation in the shape of the weighting function per realisation however only

provides a small improvement to both accuracy metrics over that of SCC as is demonstrated in section 4.3.4 (p.78).

2.9 Averaging techniques

Another proposed solution for improving the accuracy of measurements using SCC was the development of the averaging techniques. These improve the SNR and thereby can provide high VVD rates but will cause the loss of either the spatial or temporal resolution of a flow. The Hart correlation was one such averaging technique (Hart, 1998) whereby at least two correlation fields, generated by the cross-correlation of realisations separated by an offset typically of between a quarter to half a region width, are multiplied together. Provided that the location of the correlation peak in both fields is the same then multiplication will enhance the signal peak over the surrounding noise peaks. A similar method generates an average correlation field from several realisations; this averaging technique is more robust than Hart correlation as it is more robust when more realisations are used.

While the Hart correlation improves the SNR within an image the technique was extended to generate an average between sequential images; this is known as ensemble (temporal) averaging. This method was designed to reduce the effect of background noise from a single PIV image and thereby improve the SNR. Ensemble averaging calculates an average correlation field from the SCC of coincident interrogation regions from a series of sequential images. Although this averaging technique provides a mean displacement for a series of sequential interrogation regions it is at the detriment of the temporal resolution. A simple extension to ensemble averaging is the single pixel averaging technique (Westerweel et al., 2004). Since the SNR for ensemble averaging can be increased by increasing the number of images acquired (e.g. increasing the frame rate of acquisition) then it was stated that the size of each interrogation region can be subsequently reduced maintaining the SNR whilst also retaining the accuracy and improving the spatial resolution. In some instances the size of each region can be reduced to a single pixel yet as is shown in section 5.4 (p.144) decreasing the size of an interrogation region has an adverse affect on the accuracy of SCC measurements.

Although the averaging techniques are commonly used in DPIV results generated this way assume a similarity between interrogation regions. The averaging of particle image motion including displacement gradients across and between interrogation regions can preclude a meaningful displacement from being obtained since noise peaks can unintentionally influence measurements. Therefore, to quantify the systematic errors within DPIV, accuracy metrics are provided from the cross-correlation of individual realisations.

2.10 Summary

In summary, this chapter has identified that when processing with SCC and evaluating displacements with the Gaussian sub-pixel estimator, which are typical in DPIV analysis, there is an underestimation in measurements (Figure 2.3(a)) and large uncertainties in measurements that results in large RMS errors (Figure 2.3(b)). These errors were originally attributed to the non-uniform weighting of the correlation noise floor that is generated during cross-correlation. However, as section 2.5 identifies, the shape of the noise floor is not the sole contributor to errors within measurements. When applying iterative correlation methods, also originally designed to improve accuracy with SCC, it is shown that these do not improve accuracy. Errors associated to these techniques whilst processing with various cross-correlation algorithms are reviewed in Chapter 6.

This chapter has introduced several image enhancement techniques and weighting functions originally proposed to improve the accuracy of measurements over that of SCC by accounting for the shape of the noise floor. Assessment of the errors quantified with these functions is made in Chapter 4.

Chapter 3

Artificial Image Generation

3.1 Introduction

Digital Particle Image Velocimetry (DPIV) is an optical diagnostic tool that can provide quantitative velocity statistics over an entire flow field. Being able to generate measurement statistics helps in a wide variety of applications as it allows researchers to quantify flow field phenomena, validate and refine Computational Fluid Dynamics (CFD) flow models whilst also providing direct engineering design solutions. However, as with all experimental processes, the flow statistics will be subjected to the effects of systematic errors that have to be analysed, quantified and minimised before any comparison with CFD predictions are made. Processing artificial interrogation regions, or Monte Carlo simulations, provides these measurement statistics on a theoretical basis and are used to evaluate the systematic errors within DPIV.

Within a simulation all aspects of the artificial regions are controlled. Each pair of artificial regions contains randomly distributed particle images of a known size at a specified seeding density. In order to quantify the systematic errors within DPIV evaluation these particle images are subjected to a prescribed uniform displacement in the x-direction; this is so that no form of experimental error is present during analysis. The background noise level within each image can also be controlled. From this, when realisations are processed, the systematic errors associated with cross-correlation can be quantified. Ultimately, the performance of any processing algorithm must be evaluated against actual DPIV data. However, a theoretical understanding provides a good basis for the quantification of the systematic errors within DPIV.

This chapter provides details of the model developed to generate data-sets of artificial interrogation regions. This describes the geometry of each artificial particle

image, how they are randomly distributed across the first region, the prescribed uniform displacement to generate the second region, and then the digitisation of both regions. This chapter also identifies the optimum interrogation region parameters with respect to the intensity contain to provide the the most accurate measurement statistics from SCC.

3.2 Principles of digital particle image velocimetry

Since its inception, Digital Particle Image Velocimetry (DPIV) has matured into a well-established and widely used flow diagnostic technique that is able to provide velocity measurements within a two-dimensional flow field. In a typical DPIV experiment, a flow is seeded with a large number of micron-sized tracer particles that are assumed to follow the flow dynamics. The area of flow under examination is illuminated with a sheet of light produced by a high-frequency laser. The light sheet is formed using a combination of spherical and cylindrical lenses. A series of exposures are then captured over a known time period using a high-speed camera focused on the laser plane. The flow dynamics are calculated using these particle image exposures. The average local velocity within the flow is determined by dividing the series of images into a grid of smaller interrogation regions. Each pair of regions from sequential images are processed using cross-correlation to estimate the average particle image displacement and hence a local velocity. Velocity vectors are extracted from each pair of regions to build up a flow field velocity map.

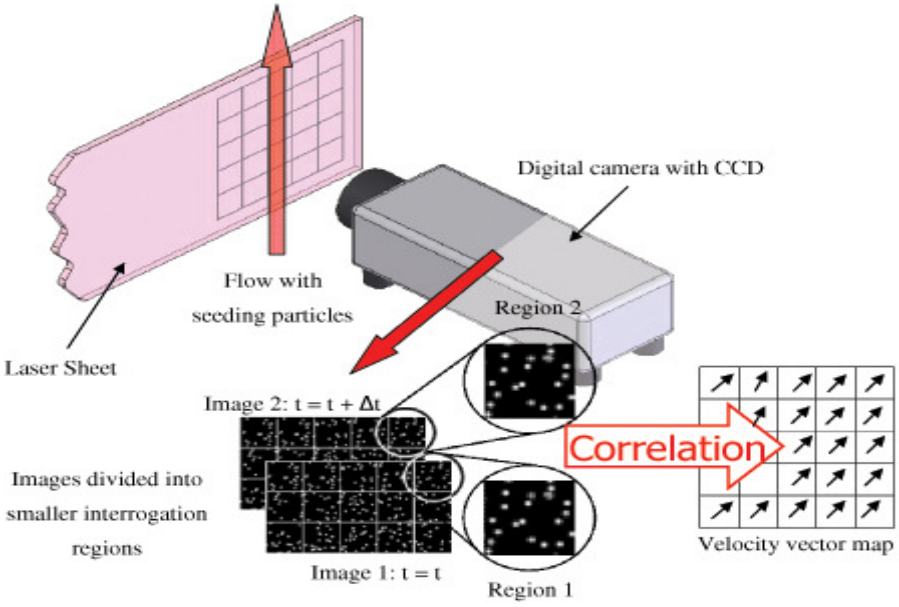

Figure 3.1 A typical DPIV experimental setup

Careful consideration should be given to experimental design and practice. Although considerable effort should be taken to minimise experimental errors, results from the utmost designed experiment performed by experienced PIV users will still contain systematic errors associated with the standard cross-correlation algorithm. As such a robust processing algorithm is required to compensate for their effects.

3.3 Seeding particles

The most critical aspect in the design of a DPIV experiment is the selection of the particles used to seed the flow. Since the flow dynamics are indirectly measured by cross-correlating regions of particle images, it is critical to select the correct tracer particles. From a physical perspective a tracer particle should be chosen that is small enough to follow the flow dynamics yet not interfere with flow characteristics (Durst et al., 1976) but also be large enough to scatter sufficient light for detection (Drain, 1980). Specifically, a particle should be chosen where there is a minimum response time between particle motion and velocity fluctuations in the flow; these properties are governed by the Stokes drag law. Typically, tracer particles have diameters of between 1 and 50μm depending on the fluid properties. Their size also dictates the type of laser that can be used to scatter sufficient light for detection. Pulsed Nd:YAG lasers with a wavelength of 532nm are generally used as these lasers are able to deliver high light energy within a short time interval.

From an imaging perspective the particle image size is ultimately determined by the magnification of the optical system and this therefore dictates the resolution detail within the flow field. Therefore when exposures of particles within the flow are captured, typically using a high-speed CCD camera, the size of each particle image is a critical factor in determining accurate measurements. If the particle image is too small digitisation will no longer preserve the true particle image shape. Cross-correlation will then bias measurements towards integer pixel displacements. This is referred to as peak-locking (Westerweel, 1997 and Raffel et al., 1998). Increasing the particle image size will increase the intensity content of each particle image yet image truncation will generate significant partial image errors (Nogueira et al., 2001 and Anandarajah, 2005) with standard cross-correlation which subsequently causes larger measurement errors. As a consequence of this, the optimum diameter is between 2 to 3 pixels (Raffel et al., 1998) when evaluating with standard cross-correlation and using a Gaussian sub-pixel estimator to access displacements. However, when selecting a tracer particle a balance must be struck between the physical and imaging requirement. Usually the physical criteria are maintained to the detriment of the imaging requirements which subsequently affects accuracy.

The resolution detail of a flow field is also dictated by the size of the interrogation region and by the seeding density of the particle images. To maximise correlation, each region should contain sufficient numbers of well defined particle images. If there are insufficient numbers particle images errors will be incurred from an inadequate signal-to-noise ratio. Conversely, if there are too many particle images within a region the magnitude of the correlation noise floor will increase; this also affects measurements and is discussed in section 3.9.2.

3.4 Image processing techniques

In the early development of PIV, photographic film was used as a means of recording flow images. This was generally regarded as being the best approach due to its high spatial resolution capabilities which are typically between 70 to 100 lines/mm. Although film is able to yield a high spatial resolution it suffered from two significant drawbacks: firstly a time constraint needed to develop the film for velocity extraction. This can be especially time consuming if large amounts of flow data has to be collected and analysed. Secondly, without the use of high-specification cameras and equipment (Williams et al., 2000) a low frame rate is typical, limiting high speed flows to multi-pulsed PIV systems which rely upon autocorrelation of single images.

A significant advance in the development of the PIV technique was the shift away from photographic film towards digital image capture. The development of full-frame charged-couple device (CCD) sensors, complementary metal oxide semiconductor (CMOS) arrays and intensified CMOS cameras has transformed the accessibility of PIV. These sensors provide the added advantage of being able to process digital images directly in a computer removing developing issues caused by film. A comparison between these three sensory arrays is reviewed by Hain et al. (2007). This gave rise to the term Digital Particle Image Velocimetry (DPIV) that is capable of instantaneously quantifying velocity vectors within a flow field.

Although some researchers had been using digital imaging in preference to film for years before it gained popularity, many had their reservations over the accuracy of using lower resolution exposures produced this way. Willert and Gharib (1991) and Westerweel (1993a) produced results to show that low resolution digital images were still capable of producing accurate velocity estimates using digital processing algorithms.

As an initial basis, the model was developed to simulate digitised interrogation regions that would be typically generated by a CCD or CMOS camera. The first stage is to model a high resolution particle image (section 3.5) and then randomly

distribute these high-resolution particle images within each interrogation region to simulate particle images within a flow (section 3.6); these are then displaced by a known amount to generate the second region before each high-resolution image is digitised to simulate typical DPIV images (section 3.7).

Preliminary analysis was conducted using interrogation regions that were 32 x 32 pixels in size. This size of region is commonly used in DPIV analysis. These dimensions result from a legacy of FFT processing that constrain interrogations regions to have equal dimensions of 2^n pixels (i.e. 16 x 16, 32 x 32… etc.). In papers by Huang et al. (1997) and Anandarajah (2005) it was stated that each region should be seeded with 22 particle images each with a diameter of 2.8 pixels. It was stated that using these values avoids errors associated with poor signal-to-noise ratio with standard cross-correlation and an inadequate image resolution. Therefore, for preliminary analysis, each interrogation region is seeded with 22 particle images each with diameters of 2.8 pixels. Although assessment is to be made on the accuracy performance of processing algorithms each result is dependent on the quality of the data used to calculate each displacement. Therefore section 3.9 evaluates the particle image size and seeding density to provide optimum imaging parameters and thereby minimise the accuracy metrics using the standard cross-correlation algorithms.

3.5 Particle image geometry

The most critical aspect of artificial image generation is the simulation of each particle image. In an actual DPIV experiment tracer particles that seed the flow are typically in the order of microns in size. These particles are resolved using imaging optics and thus each particle image is diffraction limited. The shape of the diffraction limited particle image is commonly referred to as a point spread function (PSF) (Goodman, 1968). As an imaging camera has a circular aperture the PSF is observed to have a bright central spot surrounded by much fainter concentric rings that spread out indefinitely. The bright central spot of referred to has the Poisson's ring with the pattern referred to as the Airy distribution.

In order to model each particle image, Airy distribution (in the absence of lens aberrations) acquired from a point source has to be considered. This can be mathematically represented by the square of the first order Bessel function:

$$I(x) = I_0\left[\frac{2J_1(x)}{x}\right]^2 \qquad \textbf{3.1}$$

Where I_0 is the peak light intensity and $J_1(x)$ is the first order Bessel function. The first minima of this function corresponds to the diffraction limited particle image diameter (Meinhart et al., 2003) which, for a simple lens system is defined as:

$$d_{diff} = 2.44(M+1)f^{\#}\lambda \qquad \textbf{3.2}$$

This gives the minimum resolvable size of an image for a given magnification, M, f-number, $f^{\#}$, and wavelength, λ.

For an aberration free lens with a focal length f, the image of a small particle at a distance z_i between the image plane and the lens and a distance z_o between the lens and the object plane has a magnification factor that is given by:

$$M = \frac{z_i}{z_o} \qquad \textbf{3.3}$$

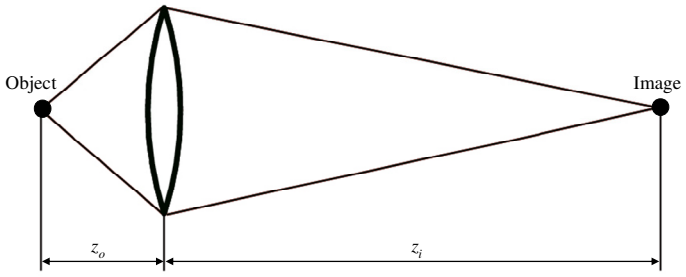

Figure 3.2 An optical arrangement

Where the focal length *f*, is defined as:

$$f = \frac{1}{z_i} + \frac{1}{z_o} \qquad \textbf{3.4}$$

For clarity, the *f*-number, is defined as the ratio of the focal length *f*, to the aperture diameter of the camera *D*.

$$f^{\#} = \frac{f}{D} \qquad \textbf{3.5}$$

When imaging a spherical particle, the diameter can be approximated using the geometric particle diameter (Adrian, 1995).

$$d_i = \sqrt{\left(Md_p\right)^2 + \left(2.44(M+1)f^{\#}\lambda\right)^2} \qquad \textbf{3.6}$$

where d_p is the physical size of the tracer particle.

When generating artificial particle images the Fraunhofer diffraction pattern that governs the particle image intensity distribution can be approximated as a high resolution two-dimensional Gaussian intensity profile $I(x, y)$ (Hart, 1998, Huang et al., 1997 and Prasad et al., 1992). This is mathematically expressed by equation 3.7.

$$I(x, y) = I_0 \exp\left[\frac{(x - x_0)^2 - (y - y_0)^2}{\sigma_i^2}\right] \qquad \textbf{3.7}$$

where the centre of the pixel is located at point $I(x_0, y_0)$ and has a maximum intensity of I_0 and the particles are randomly distributed over the interrogation region (Huang et al., 1997). σ_i is related to the particle image diameter d_i where $\sigma_i = d_i / \sqrt{2}$. The diameter d_i being defined at $e^{-1/2}$ of the peak intensity value of the Gaussian function applied. This means that, by definition, the diameter of the particle image contains 61% of the total intensity of the Gaussian intensity profile within the defined envelope (Willert and Gharib, 1991).

Figure 3.3 shows that the two-dimensional Gaussian intensity profile gives a good approximation of the Airy distribution: represented by the square of the first order Bessel function. As such, an artificial particle image which describes a two-dimensional Gaussian profile can be assumed to be a reasonable approximation with regards to the actual case.

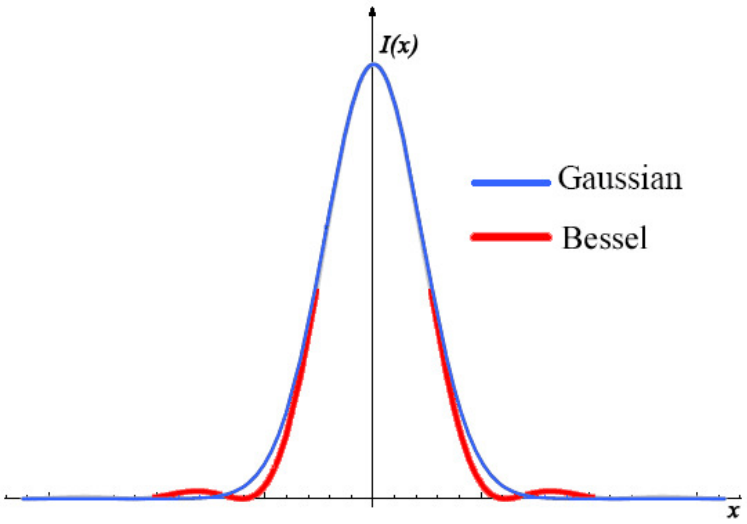

Figure 3.3 Approximating the Airy disc with a Gaussian function

3.6 Artificial interrogation regions

Now that the geometry of the particle images has been established (equation 3.7) the next stage of artificial interrogation region generation is to randomly distribute high resolution particle images throughout an initial 3200 x 3200 pixel region. For a random distribution, the coordinates of each particle image was acquired using a random number generator and a high resolution particle image was mapped onto each location. Each particle image location was documented and used to generate the second region.

When generating realistic artificial interrogation regions particle image overlap also has to be taken into account. Goodman (1996) and Marxen et al. (2000) stated that when this occurs it is a good approximation to assume that the interaction of overlapping particle images is additive and therefore the particle image intensities can be added together. Figure 3.4 shows the overlap interaction of two Gaussian profiles.

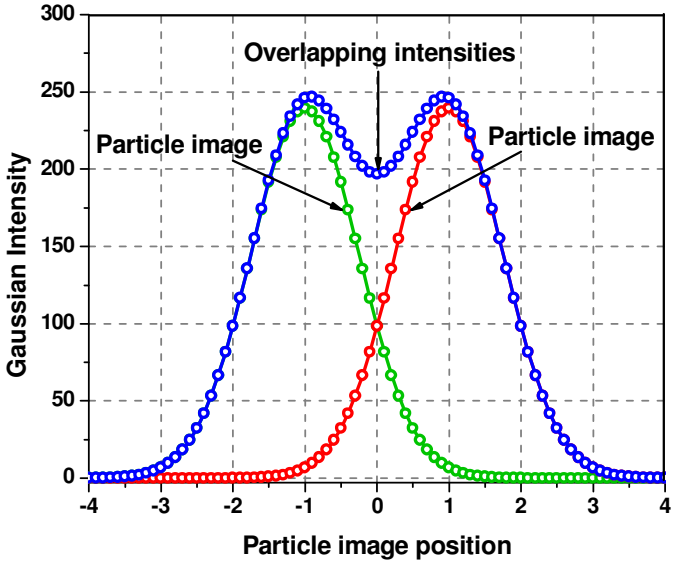

Figure 3.4 Intensity levels of overlapping particle images

3.6.1 Uniform particle image displacement

Having created an initial high resolution interrogation region, where each particle image position is known, then a second region is required where the particle image locations have been shifted by a prescribed displacement. This generates the second interrogation region of the pair, or realisation. This was achieved by taking the coordinate locations of each high resolution particle image from the first region and uniformly shifting them in the *x*-direction by a prescribed amount to generate a second set of coordinate locations. The particle images from the first region were displaced by a known distance $d_x = 10n$ where n = 0, 1, 2, 3…80 to provide the particle image coordinates for the second region. This was to simulate a uniform particle image displacement across each realisation and data-sets containing a series of realisations were modelled for each displacement. Using the new coordinate positions the high resolution particle images were mapped onto a new 3200 x 3200 pixel interrogation region. Therefore, when each region is digitised, as detailed in section 3.7, displacements describing a resolution of one-tenth of a pixel are achieved. A displacement of one pixel in the high resolution region equates to a displacement of one-hundredth of a pixel after digitisation; this is the minimum permissible displacement attainable with this model.

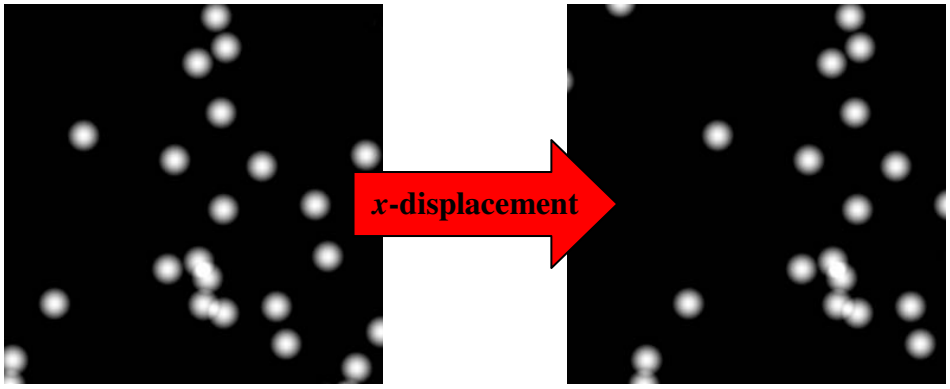

(a) Initial 3200 x 3200 pixel region (b) Final 3200 x 3200 pixel region

Figure 3.5 High resolution interrogation regions experiencing a prescribed displacement

3.7 Digitisation

When experimental DPIV images are captured, particle images are recorded onto a CCD or a CMOS sensor generating a digitised version of the image. Therefore to fully simulate artificial regions the model must be able to replicate images captured by a digital imaging sensor.

To achieve this, each high resolution interrogation region $I_{hr}(x, y)$, described in section 3.6, has to be digitised by integrating the light intensity over one pixel width *w*, to produce a digitised interrogation region $I_n(i, j)$. The digitisation of a high resolution interrogation region is mathematically defined as:

$$I_n(i,j) = \int_{i-\frac{w}{2}}^{i+\frac{w}{2}} \int_{j-\frac{w}{2}}^{j+\frac{w}{2}} I_{hr}(x,y)\, dxdy \qquad \textbf{3.8}$$

The first interrogation region of the pair is referred to as $I_1(i, j)$ and the second as $I_2(i, j)$. (*n* refers to the sequential digitised interrogation region and *hr* refers to the high resolution interrogation region) Therefore each high resolution 3200 x 3200 pixel interrogation region was digitised to produce a 32 x 32 pixel region. For initial investigations the digitisation was generated using an 8-bit (256 grey-scale) output because this format is commonly used in CCD cameras for DPIV experiments.

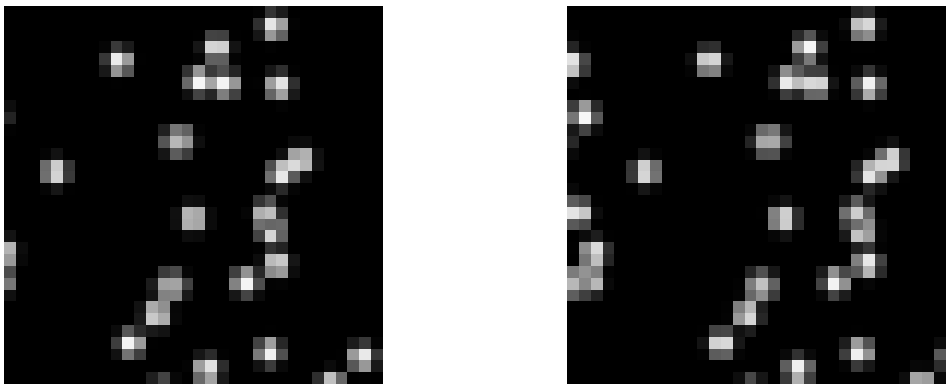

(a) Initial 32 x 32 pixel region (b) Final 32 x 32 pixel region

Figure 3.6 Digitised interrogation region pair displaced by a known amount

3.8 Background noise

In ideal conditions the light scattered from tracer particles are captured on a perfectly black background. However, as with any electronic device, imaging sensors are subject to electronic noise which will result in random errors during analysis. A major source of this noise considered in this analysis is due to thermal effects and is referred to as thermal noise, or dark current noise (Raffel et al., 1998). Thermal noise is caused by the random motion of electrons within the energy wells of the imaging device which cannot be separated from those generated by the photoelectric effect. In some instances this can result in weak particle images being indistinguishable from noise. Thermal noise is highly dependent upon the temperature of the imaging device to the extent where the rate of generation will double for every 6-7^{o}C increase in temperature. This has lead to the development of intercooled cameras that minimise the thermal noise output (Raffel et al., 1998). However, typical imaging devices remain without intercooling and this noise remains as a significant source of random error within DPIV images.

Therefore in order to generate more realistic artificial regions, background noise has to be considered and added into each artificial interrogation region. To provide a realistic approach to background noise levels the electronic noise from a high-resolution CCD camera (PIVCAM 10-30) was measured and then used to compute noise statistics. The electronic background noise measured from the experimental image had a mean pixel intensity of 39 and followed the distribution shown in Figure 3.7. This noise distribution was then artificially generated and added to each artificial interrogation region as Gaussian white noise (GWN) using MATLAB. Both the experimental and artificial noise distributions have been normalised by their respective maximum values. This is to ensure that a direct comparison can be made between the two distributions.

The mean pixel intensity of 39 equates to a background noise level of approximately 15% of the total 8-bit output (i.e. 256 grey-scale). Further to this, other mean background noise intensities are calculated for 2%, 5% and 10% of the total 8-bit

output while maintaining the variance described in Figure 3.7 and are distributed within each data-set.

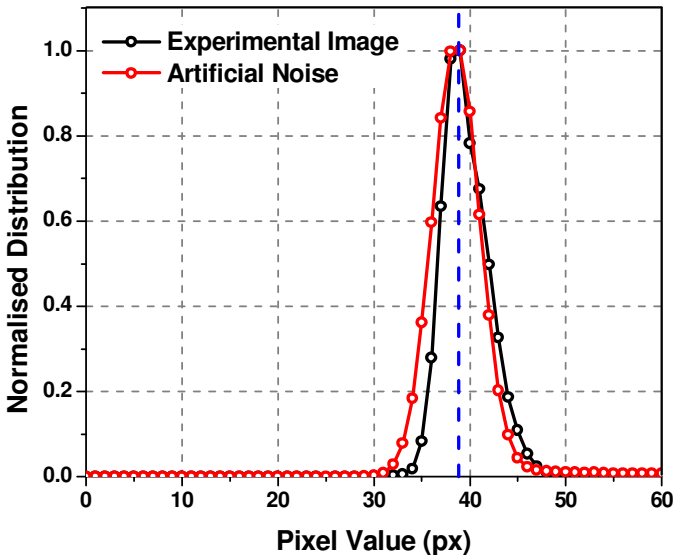

Figure 3.7 Distribution of experimental and artificially generated background noise

The noise distribution generated by the experimental images provides a foundation for the background noise intensity for experimental verifications discussed in Chapter 7[1].

[1] Accuracy metrics generated for various noise distributions whilst maintaining the mean intensity at 39 pixels (i.e. 15% of the 8-bit output) is given in Appendix I.

3.9 Artificial image optimisation

Huang et al. (1997) and Anandarajah (2005) both stated that each 32 x 32 pixel interrogation region should be populated with 22 particle images each with diameters of 2.8 pixels. It was stated that this was to avoid error associated with an insufficient signal-to-noise ratio (SNR) and inadequate particle image resolutions resulting in peak-locking but gave no basis for these findings. These values can be used as an initial basis for error quantification, but in order to produce the most accurate measurement statistics generated by the cross-correlation algorithms with the Gaussian sub-pixel estimator, the size and number of particle images in each interrogation region must be optimised.

This section evaluates the optimum number of realisations that are required for each displacement data-set to provide meaningful error quantifications. It also details the performance of SCC measurement statistics which are used to evaluate the optimum particle image size and seeding density for Monte Carlo simulations.

3.9.1 Optimum number of realisations

Using the preliminary size and seeding density values, displacement data-sets containing 500 realisations were generated for each uniform displacement ranging from zero to 8 pixels at a resolution of one-tenth of a pixel. Each displacement data-set was processed using a standard cross-correlation algorithm (FFT with zero padding or *R(m,n)* shown in equation 2.1 and 2.2, p.8-9) and the measured displacement determined to sub-pixel accuracy using a three point Gaussian estimator (equation 2.3, p.11). To determine the optimum number of realisations required for meaningful error quantification different sized data-sets (e.g. 10, 25, 50, 100 etc. realisations) were randomly taken from the cohort of each displacement data-set containing 500 realisations and the mean bias and RMS error were calculated for each sample. Both quantification metrics were then averaged over the 8 pixel displacement range from which a total error was calculated for each sample size and is presented in Figure 3.8.

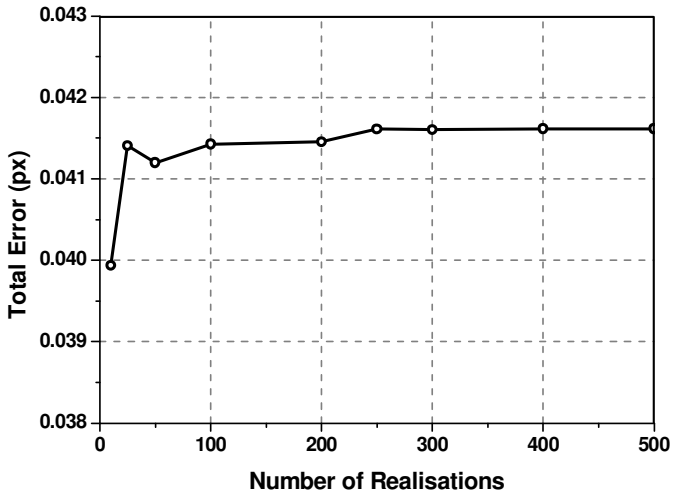

Figure 3.8 Optimising the number of realisations

Figure 3.8 shows that the total error settles when the sample size is 300 realisations or greater. For smaller sample sizes there are fluctuations in the total error. This indicates that each displacement data-set requires at least 300 realisations to provide adequate error statistics.

3.9.2 Optimum particle image size

Now that the number of realisations per displacement data-set is known for meaningful error quantification the next stage is to optimise the particle image size. This was achieved by altering the model so that each artificial interrogation region contained a different sized particle image from the preliminary 2.8 pixel diameter example. As before, displacement data-sets containing 300 realisations were generated for each uniform displacement ranging from zero to 8 pixels at a resolution of one-tenth of a pixel for each particle image size examined. These realisations were processed using SCC and the measured displacement determined using a three point Gaussian sub-pixel estimator. The total errors for each data-set containing different particle image sizes were calculated, as described in section 3.9.1, and the results presented in Figure 3.9.

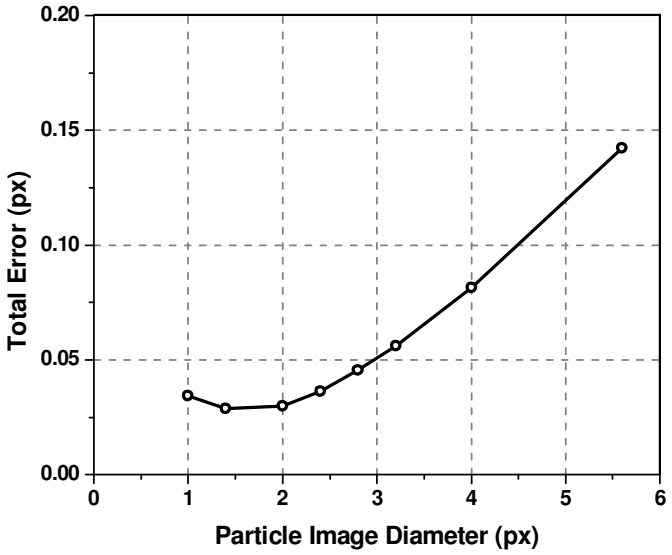

Figure 3.9 The optimum particle image diameter

It is clear that Figure 3.9 indicates that when each realisation contains particle images that are between 1.4 and 2 pixels in diameter then the total error is at a minimum. This corresponds to the results provided by Raffel et al. (1998). However, if the particle images become too small the measured displacement tends towards integer values. This effect is known as peak-locking and it increases when the particle image size decreases; this is highlighted in Figure 3.10(b) which shows the RMS error generated when the particle image size is varied. When the particle image size increases this error reduces but consequently measurements are negatively biased

away from their actual value (Figure 3.10(a)). This is covered in more detail in the next chapter.

(a) mean bias error

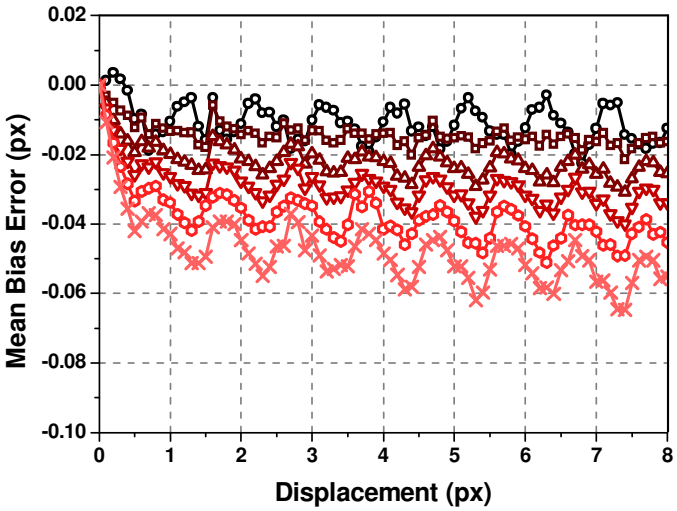

(b) RMS error

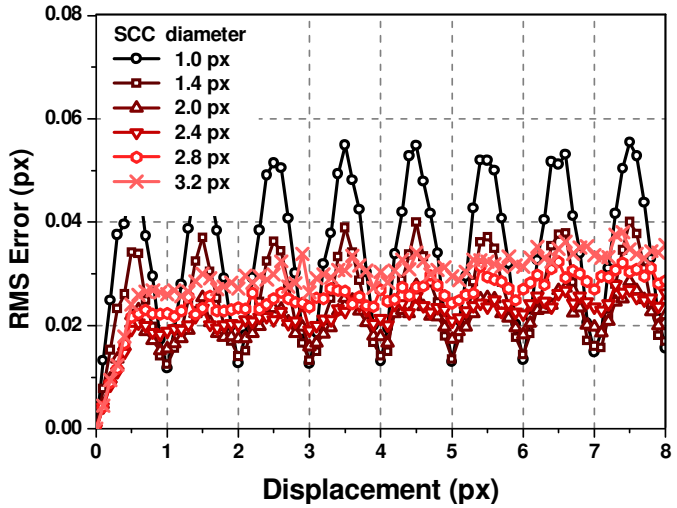

Figure 3.10 Error plots for various particle image diameters

Figure 3.10 clearly indicates that calculating the measured displacement using the Gaussian sub-pixel estimator is unsuitable for small particle image diameters but is more appropriate as the size increases. Figure 3.10(a) shows that as the particle image diameter increases measurements are negatively biased away from their actual values. For smaller particle images the RMS error plot (Figure 3.10(b)) shows a distinctive bias towards integer values with smaller particle images which diminishes as the particle image size increases. This is obvious when the particle image diameter is less than 2.0 pixels but RMS values still tend towards integer values at a particle image diameter of 2.4 pixels. This bias towards integer values does not arise

when the particle image diameter is 2.8 pixels as the Gaussian sub-pixel estimator is able to resolve each displacement. Since there has to be a compromise between the two error metrics to provide accurate measurements then small particle images cause a peak-locking error and increasing the particle image size increases the underestimation in measurements. From this it is concluded that each artificial interrogation region should contain particle images that have a diameter of 2.8 pixels as peak-locking errors are not an issue and the resulting mean bias error can be tolerated using SCC.

Figure 3.10(a) also identifies a cyclic pattern in the mean bias error that increases in amplitude as the particle image size increases. This cyclic pattern will be discussed further in section 4.4 (p.80).

3.9.3 Optimum seeding density

Having established the optimum number of realisation and particle image size the final stage is to obtain the optimum particle image seeding density per realisation. To achieve this, the model was altered to randomly distribute 2.8 pixel diameter particle images at different seeding densities for each data-set. As with the previous sections, displacement data-sets containing 300 realisations were generated for each uniform displacement ranging from zero to 8 pixels at a resolution of one-tenth of a pixel and the seeding density was varied between data-sets as shown in Figure 3.11. Realisations within each data-set were processed using standard cross-correlation and the measured displacement determined using a Gaussian sub-pixel estimator. The total errors for each data-set with varying seeding density were calculated, as described in section 3.9.1, and the results presented in Figure 3.11.

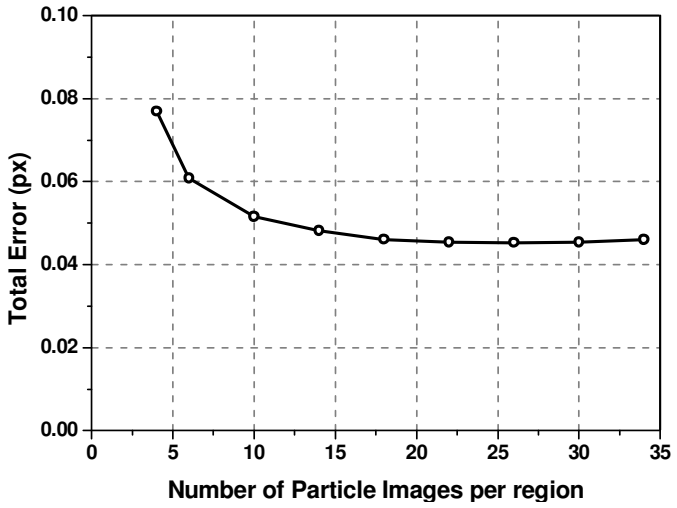

Figure 3.11 Optimising the particle image seeding density

The figure shows that at low seeding densities the total error is higher than when the seeding density is increased. When the seeding density is between 22 and 30 particles per region the total error calculated is at a minimum. This starts to increase again when the density reaches 34 particles per region. Decomposing the total error into its constituent metrics (Figure 3.12) reveals the foundations for the increased total error at low seeding densities that declines as the density is increased.

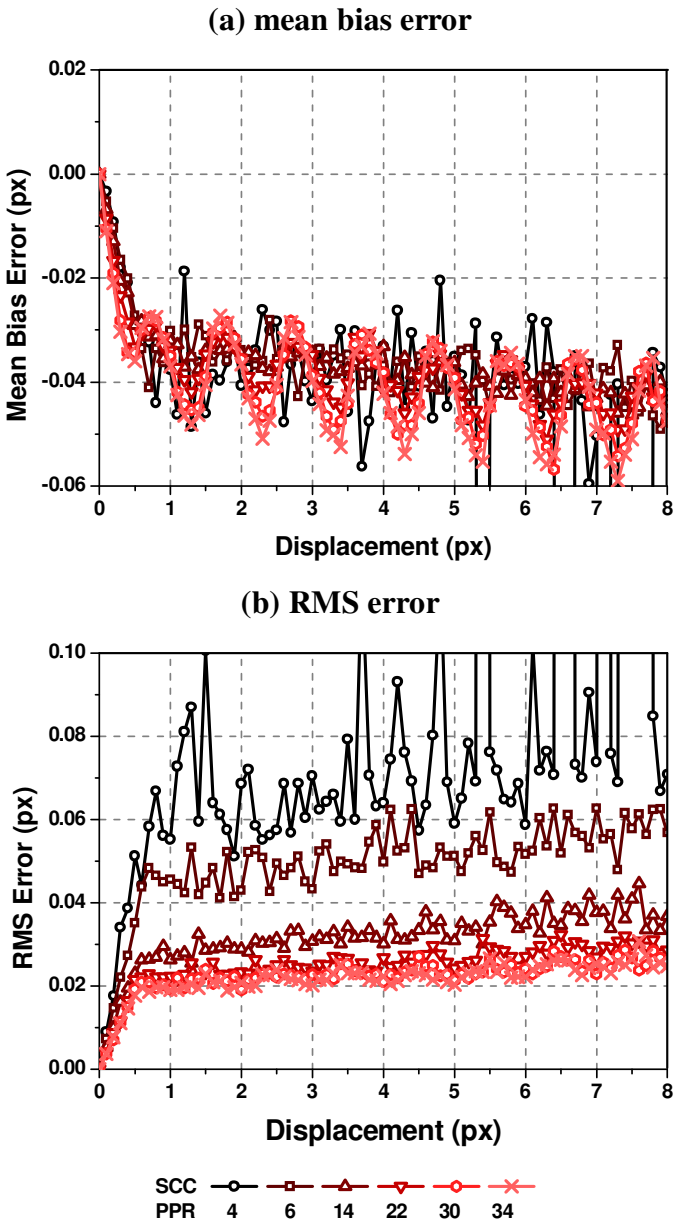

Figure 3.12 Error plots for SCC for various particle image seeding densities

The figure clearly shows that the mean bias error generated for each seeding density level follows the same trend yet fluctuations are more prevalent when the seeding density is low. However, when the RMS error plot is investigated the variations between measurements declines with increasing densities.

In previous studies (Huang et al. 1997 and Anandarajah, 2005) it was stated that each region should be populated with 22 particle images to avoid errors from a poor signal-to-noise ratio (SNR). When the SNR (equation 2.9, p.14) is calculated for each data-set over the 8 pixel displacement range (Figure 3.13) a seeding density of 4

particles per region provides the lowest SNR of the seeding densities examined. This is to be expected using the previous assumptions. However, the highest SNR over the 8 pixel range is provided by regions containing 6 particle images. This then declines with increasing seeding density.

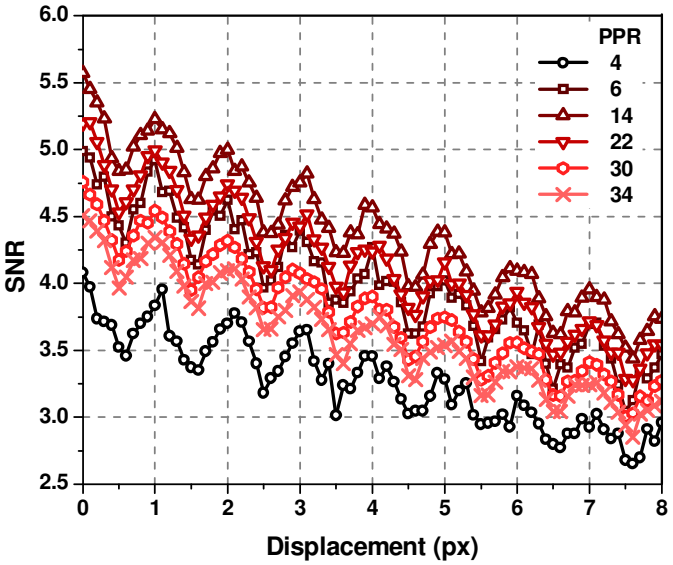

Figure 3.13 SNR for SCC for various particle image seeding densities

This is explained by separately considering the average signal and noise levels generated during cross-correlation as shown in Figure 3.14. When regions with low seeding densities are cross-correlated few particle images contribute to the correlation peak, therefore the peak remains low. Since the seeding density is low, cross-correlation of unrelated particle image pairs will generate a low correlation noise floor. As the seeding density increases the number of particle images contributing to the correlation peak increases resulting in a higher correlation peak. However, since there are a greater number of particle images in each region the correlation noise floor will also increase. As the seeding density increases the noise floor increases at a faster rate than the height of the correlation peak; this causes the SNR to decrease at higher densities.

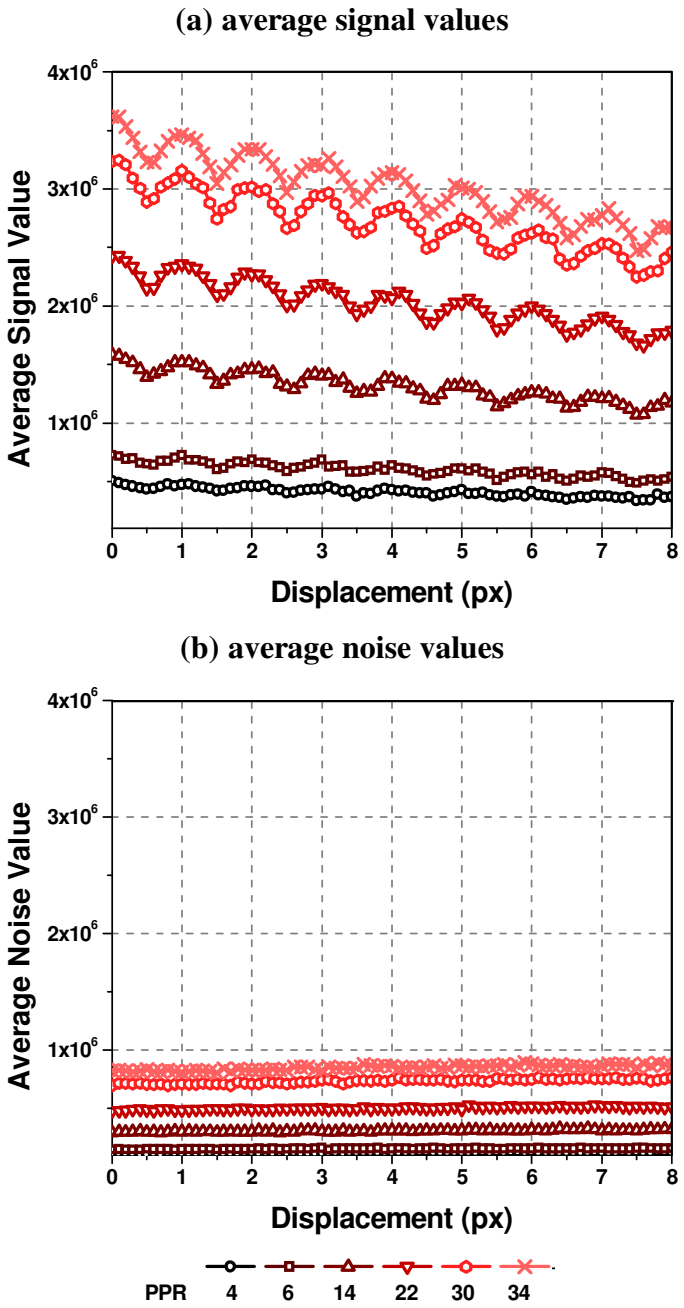

Figure 3.14 (a) average SCC signal value and (b) average SCC noise value for various particle image seeding densities

This is further highlighted by Figure 3.15 which shows the number of particle images that contribute to the correlation peak averaged over the 300 realisation of each displacement data-set. This follows the relationship:

$$N - \frac{N}{width} \times x_{disp} \qquad \textbf{3.9}$$

where N is the seeding density, *width* is the width of the interrogation region and x_{disp} is the displacement in the x-direction. Each point in Figure 3.15 is calculated using

the locations of each particle image within the artificial regions. Assessment can be made as to the number of particle images present in either region; this is then averaged over each displacement data-set.

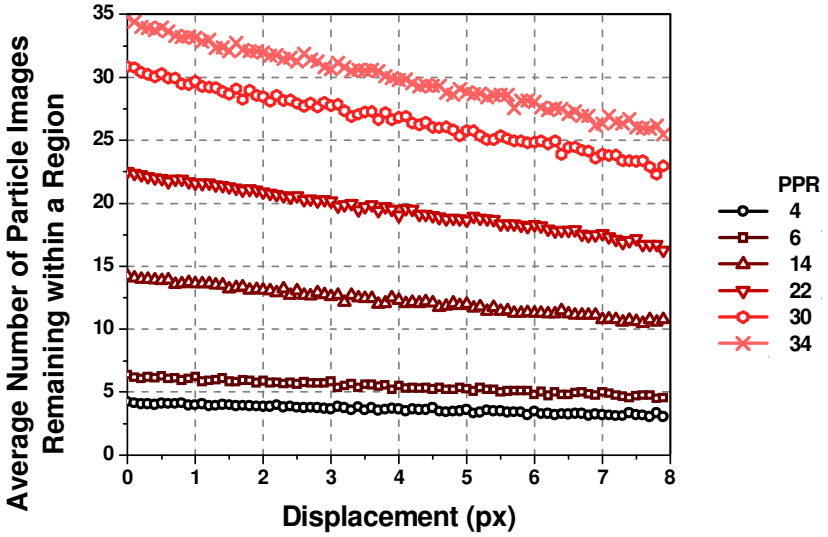

Figure 3.15 Average number of complete particle image pairs

The figure shows that, with increasing displacement, the number of particle images that contribute to the correlation peak decreases at a higher rate when the seeding density is high. Therefore, in order to provide a constant number of particle images per region the number of unrelated particle images has to increase proportionally. This will inherently increase the correlation noise floor and hence generate the results shown in Figure 3.13.

At low seeding densities, the cross-correlation of randomly distributed particle images will cause significant variations in the shape of the correlation peak compared to high density regions. This is illustrated in Figure 3.16 which shows the cross-sectional view of the correlation field through the correlation peak to show the displacement in the *x*-direction for regions containing (a) 6 and (b) 22 particles per region experiencing an actual uniform displacement of 4.3 pixels. Each correlation field is averaged over results from 300 realisations.

(a) 6 particle images per region

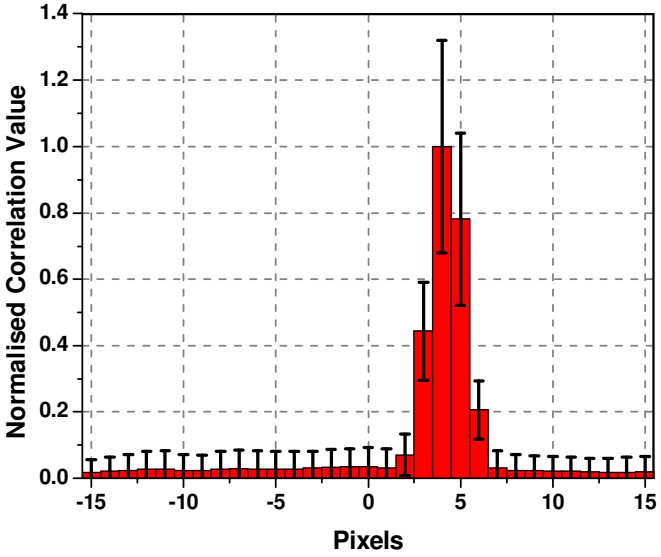

(b) 22 particle images per region

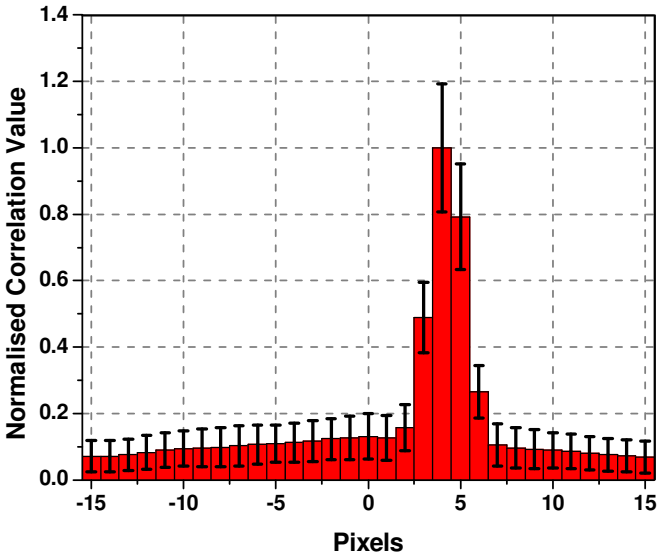

Figure 3.16 Average correlation fields for (a) 6 and (b) 22 particle images per region

The average correlation field is calculated over 300 realisations and then normalised against the maximum correlation peak value. This is so that a direct comparison between 6 and 22 particle images per region can be made. The error bars are calculated by normalising each individual correlation peak by the average correlation peak value and then determining the standard deviation of the correlation fields.

The figure highlights there is significantly more variation between individual correlation fields when the seeding density is low compared to when 22 particle

images seed each region. This is further emphasised in Figure 3.17 which shows the distribution of the measured displacements determined using a Gaussian sub-pixel estimator for an actual displacement of 4.3 pixels.

(a) 6 particle images per region

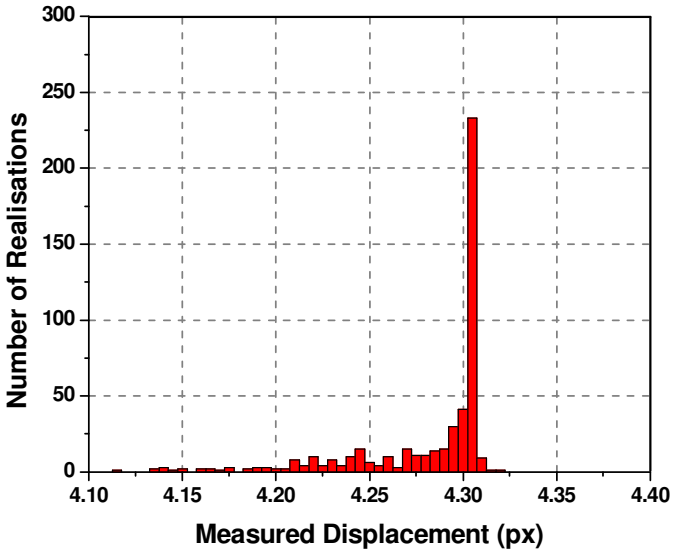

(b) 22 particle images per region

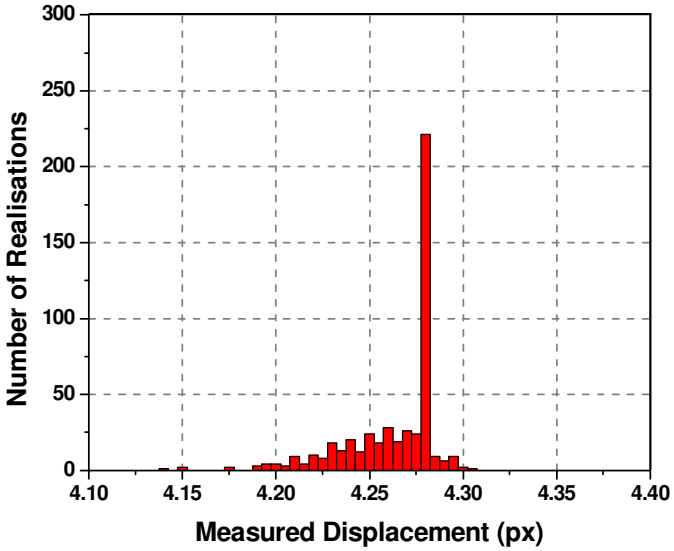

Figure 3.17 SCC measured displacement distribution for SCC from regions with (a) 6 and (b) 22 particle images per region for an actual displacement of 4.3 pixels

The figure highlights that at the low seeding density (Figure 3.16(a)) the measured displacement distribution is high therefore the RMS error is high (Figure 3.12(b)). In comparison, as the seeding density increases (Figure 3.16(b)) the measured displacement distribution decreases generating a lower RMS error.

Therefore ideally each region should be populated with 22 particle images as stated by Huang et al. 1997 and Anandarajah (2005). Rather than assuming this is to avoid errors associated with a poor SNR, it is to avoid variations to the correlation peak shape caused by a low seeding density.

3.10 Summary

This chapter has described the model developed to generate data-sets of artificial interrogation regions that are used to quantify the systematic errors within DPIV analysis. The same displacement is maintained across each realisation of a data-set but the intensity content is varied between each realisation whilst maintaining the optimum imaging content criteria. The model randomly distributes high resolution particle images across the first interrogation region; these are then displaced by a prescribed amount to generate the second region. To simulate particle images captured on a digital imaging sensor (CCD or CMOS), the high resolution regions are digitised to generate artificial region pairs (realisations) whose particle image locations can be defined to within one-hundredth of a pixel. These regions can then be used to verify and quantify the systematic errors in DPIV processing.

This chapter has also outlined the optimum parameters needed in order to minimise the measurement errors generated by the random distribution of particle images using standard cross-correlation. This has included optimising the number of realisations necessary to provide reliable measurement error statistics, the size of particle image that should be used and the seeding density. The following parameters will therefore be used when calculating measurement errors.

- Number of realisations per displacement data-set = **300**
  On average, equal numbers of particle images enter into and exit each region within a displacement data-set.
- Particle image diameter = **2.8 pixels**
  Avoids errors associated with particle image resolution.
- Particle seeding density = **22**
  Avoids errors caused by low seeding densities causing variations to the correlation peak.

Each of these parameters were calculated using 32 x 32 pixel interrogation regions which is a typical size of region used in DPIV analysis. However, to increase vector resolution and avoid errors associated with strong velocity gradients the size of each region is reduced. Therefore in the following chapters, measurement errors are calculated using regions that are 32 x 32 pixels in size and smaller.

Chapter 4

Inherent Error Quantification

4.1 Introduction

This chapter assesses the systematic errors associated to DPIV processing using the typical processing approach of SCC with a Gaussian sub-pixel estimator to quantify measurements. This extends the original findings of Anandarajah (2005) to show that when processing 'ideal' artificial interrogation regions (i.e. no background noise) the cross-correlation of partial images affects the mean bias error whilst the cross-correlation of unrelated particle images affects the RMS error. Following this, the next section provides a comprehensive review of the error quantified using four weighting functions that were originally developed to suppress errors and were initially introduced in section 2.8 (p.24). The section identifies that the signal strength function is the only weighting function that is able to suppressing both accuracy metrics when processing 'ideal' artificial regions.

Having established which normalisation function provides the most accurate measurements, the third section discusses the accuracy of the Gaussian sub-pixel estimator to highlight the effect image quality has on measurement statistics. Here it is it is identified that the cross-correlation of regions affects the magnitude of the correlation noise floor; this is turn affects the accuracy of measurements.

The final section assesses the accuracy of measurements when background noise intensities are added into each interrogation region to generate more realistic artificial interrogation regions. It is shown that the addition of these intensities affects both accuracy metrics when processing with SCC yet just the mean bias when processing with NSS. This highlights that background noise leads to a systematic error and its presence affects measurements with the current processing algorithms.

4.2 Inherent error quantification

Having established the optimum particle image size and seeding density, data-sets of 300 realisations containing particle images at the optimum parameters summarised in section 3.10 were generated for each actual uniform displacement extending from zero to 8 pixels as explained in section 3.6 (p.46).

As a benchmark for error quantification, the mean bias and RMS error were evaluated for each uniform displacement using the standard cross-correlation routines. Figure 4.1 shows the mean bias and RMS error plots for FFT without zero padding and for the standard cross-correlation routines, SCC (FFT with zero padding (eq. 2.1, p.8) or digital direct cross-correlation, *R(m,n)* (eq. 2.2, p.9) provides identical results).

(a) mean bias error

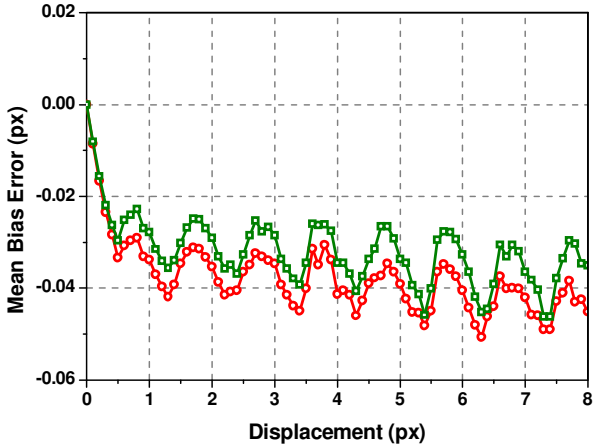

(b) RMS error

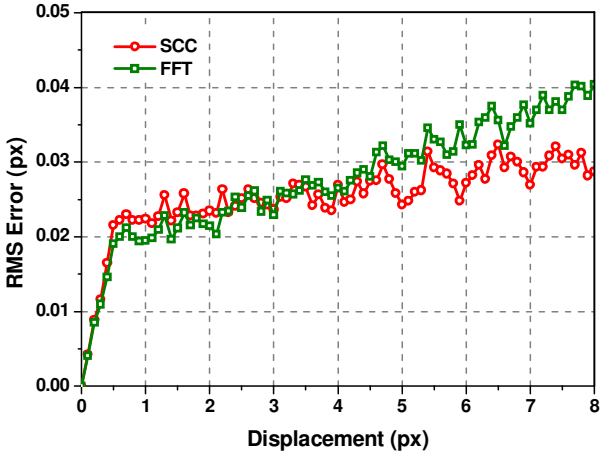

Figure 4.1 Error plots for SCC and FFT without zero padding

As section 2.5 (p.15) showed, previous studies into displacement underestimations had concluded that the correlation noise floor had contributed to the biases in measurements (Raffel et al., 1998). However, Figure 2.4 revealed that SCC and FFT without zero padding resulted in different shaped correlation noise floors yet both resulted in negatively biased displacements. It was therefore stated by Anandarajah (2005) that the correlation field characteristics are not the sole contributor to measurement biases.

Anandarajah (2005) went on to show that the cross-correlation of partial images present at the edge of interrogation regions are a major source of error and it is their presence that cause underestimations. In the original investigation that shows this (Anandarajah, 2005), only the mean bias error plot was calculated for *R(m,n)* cross-correlation, overlooking the RMS errors and the error plots from cross-correlation via FFT without zero-padding. Therefore in order to quantify these results the original investigation was repeated and extended to include these findings.

As with the original investigation, the model was configured so that only complete particle images appear in the first region. After a displacement, these complete images also appear in the second region. On cross-correlation, a symmetric correlation peak will be generated since the two regions will be identical albeit for the second region being a shifted version of the first.

To show that the non-uniform weighting of the correlation function has little effect on bias the next stage of the investigation introduced a noise floor to the correlation field. This was achieved by distributing an extra 6 unrelated particle images into the first and second regions. This number of additional unrelated particle images was chosen because when particle images in the first region are shifted by a quarter of a 32 x 32 pixel region there are approximately 6 unrelated particle images contained in the second region. It is equivalent to a turbulent flow which introduces a third velocity component of unrelated particle images into analysis.

As with the original analysis, displacement data-sets of 300 realisations containing complete particle images and also with the additional 6 particle images were

generated for a series of uniform displacements as shown in Figure 4.2. These realisations were then processed using SCC and FFT without zero-padding and the measured displacement determined using the Gaussian sub-pixel estimator, to evaluate the mean bias and RMS errors. These results are compared to the 'real' case where artificial regions contain both partial and unrelated particle images, (Figure 4.1) and are shown in Figure 4.2.

(a) mean bias error

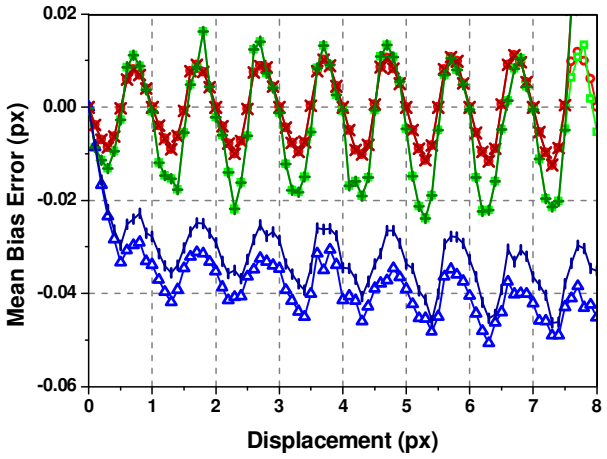

(b) RMS error

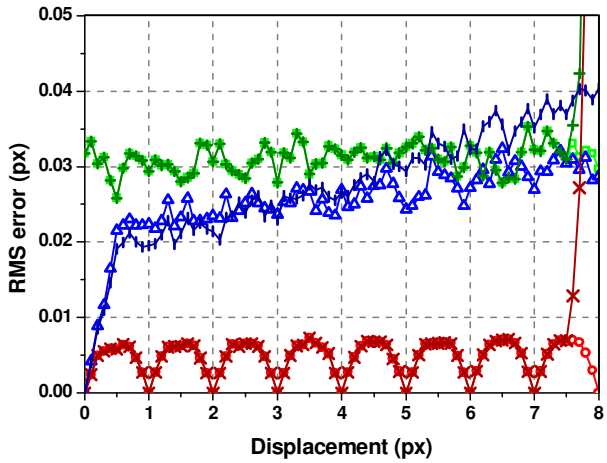

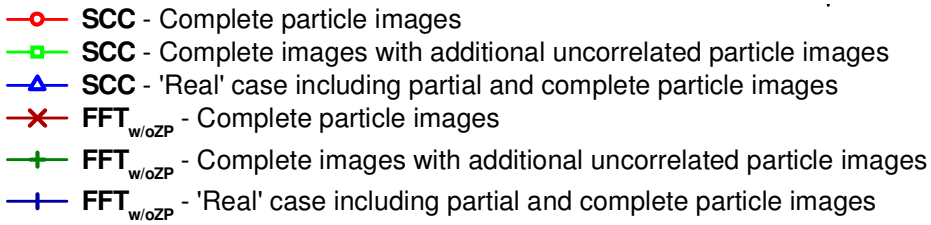

Figure 4.2 Error plots for SCC and FFT without zero-padding for complete and partial images

The mean bias and RMS error results for the cross-correlation of complete particle images and with the addition of 6 extra particle images are identical when processed with either SCC or FFT without zero-padding. This occurs because in these cases there are no partial images, therefore when processing using FFT, without zero-padding, there will be no wrap-around error due to aliasing. Figure 4.2(a) highlights that when only complete particle images are cross-correlated there is a cyclic pattern in the mean bias. This is caused by the cross-correlation of digitised particle images and is investigated further in section 4.4. Figure 4.2(b) shows there is no variation in measurements at integer pixel displacements since the particle images in both interrogation regions for each realisation are identical and therefore will generate a symmetric correlation peak. Anandarajah (2005) stated that FFT cross-correlation fails beyond a displacement of 7 pixels due to the loss of the correlation peak in the correlation field. This is caused by the large particle image displacement within a field that is only N x N pixels in size, where N is the size of the interrogation region. For FFT cross-correlation: correlation peak detection is limited to displacements of less than N/4 pixels (Raffel et al., 1998) and hence a loss of signal starts to occur as this displacement limit is approached. The loss of signal consequently introduces erroneous vectors into measurements and therefore causes a significant increase in error measurements. When using *R(m,n)* cross-correlation this effect is negated because the correlation field is (2N-1) x (2N-1) pixels in size. Thereby, a correlation peak can be located and therefore a displacement estimation can be determined.

It is clear that when complete and unrelated particle images are added into each realisation there is little effect on mean bias error. However the cross-correlation of unrelated particle images results in a significant increase in RMS error. On the inclusion of partial images both SCC and FFT without zero-padding produce an underestimation in measurements. This shows that partial imaging rather than the weighting of the correlation field affects mean bias error. The sharp increase in RMS error from 0 to ½ pixel displacement for the 'real' case is caused by the cross-correlation of partial images at the edge of each region. This is followed by a gentle increase in RMS error as the number of unrelated particle images within each realisation increases but the number of partial images remains constant. This is further illustrated in Figure 4.3 which shows that with increasing displacement the

number of particle image pairs, averaged over each displacement data-set, declines yet the average number of particle images clipped at the edge of each interrogation region remains constant at approximately 2.8 clipped particle images per realisation when populated with 22 particle images.

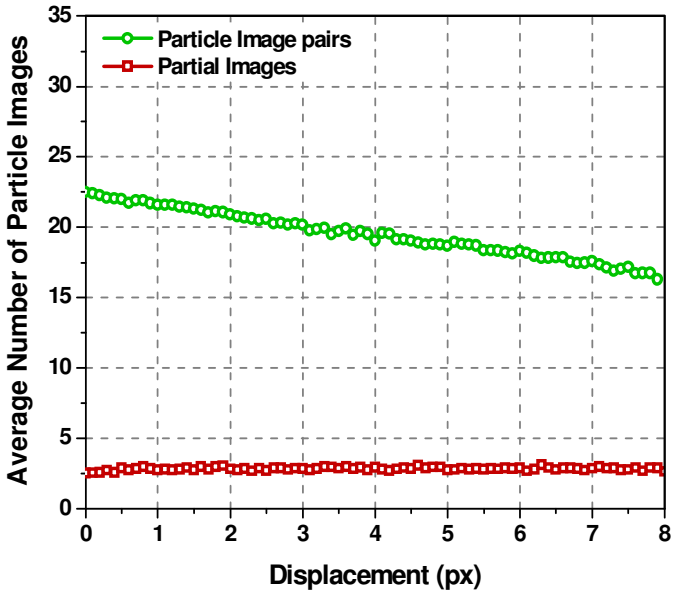

Figure 4.3 Average number of complete particle images and clipped particle images per realisation with increasing displacement

The number of particle images that are present in both regions is calculated using the randomly generated coordinate locations used to map the position of each particle image onto the first interrogation region (see section 3.6.1, p.47). Since the actual displacement is known then the addition of this to each coordinate location determines whether a particle image will be present in both regions. The number of partial images is determined in the same way but only coordinates located around the parameter, at a distance of less than a particle image diameter from the edge of each interrogation region are considered. The average number of particle and partial images is calculated over 300 realisations for each displacement data-set.

As has been shown, the random distribution of particle images within an interrogation region will result in partial images at the edge of each region. On the cross-correlation of equal-sized regions these partial images will cause an underestimation in measurements. Furthermore, the cross-correlation of unrelated particle images will cause an asymmetry in each correlation peak. As particle images are randomly distributed throughout each region then variations in the

correlation peak asymmetry within a displacement data-set will result in RMS errors. It is therefore necessary to correct for the random distribution of particle images which cause underestimations and variations in measurements.

4.3 Normalisation of the correlation field

Each correlation field that is calculated will yield a correlation peak that varies in height and shape even when the actual displacement of particle images per realisation are equal. These variations are caused by uneven illuminations across and between a pair of interrogation regions (Gonzales and Wintz, 1987), the random distribution of particle images per realisation (Anandarajah, 2005) and the addition of electronic noise (Raffel et al., 1998) all of which are systematic to flow field images. These uncertainties were a major concern for researchers who regarded limiting the variations as an essential part in improving the accuracy of DPIV measurements. It was previously assumed that variations in correlation peak height was critical in providing accurate measurements (Raffel et al., 1998), this is incorrect as Figure 4.2 identifies, the cross-correlation of interrogation regions that include partial images affects the accuracy of results. However, in order to limit height variations using the previous assumptions several normalisation functions were devised; the typical shape of each weighting function was examined in section 2.8 (p.24). This section evaluates the measurement errors obtained by processing 'ideal' and optimised interrogation regions (see section 3.9, p.51) experiencing a known, uniform particle image displacement, in the x-direction at a resolution of one-tenth of a pixel, using these normalisation functions. This is to establish whether a function is able to compensate for the systematic variations caused by the random distribution of particle images which is an inherent source of error in DPIV analysis.

4.3.1 Normalisation by overlapped area

The error plots provided in Figure 4.4 are calculated using the SCC_{OA} and FFT_{OA} algorithms (equation 2.12, p.24) on artificial interrogation regions that contain the optimum particle image content. The displacement from each normalised correlation field is evaluated using a Gaussian sub-pixel estimator. These results are compared to those computed by SCC and FFT (without zero-padding) of the same data-sets experiencing a uniform particle image displacement in the *x*-direction.

(a) mean bias error

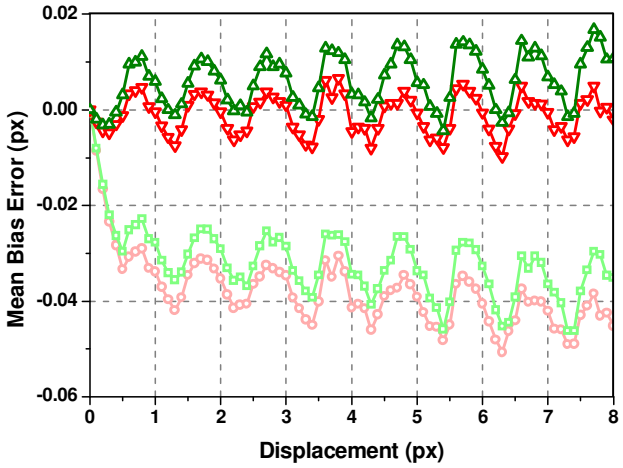

(b) RMS error

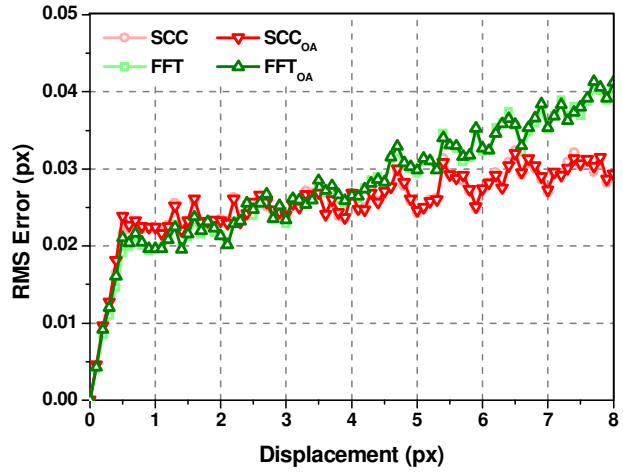

Figure 4.4 Error plots for SCC_{OA} and FFT_{OA} compared with SCC and FFT

As was discussed in section 2.8.1 (p.24) the overlapped area function is identical for every realisation analysed. Figure 4.4(a) shows that when normalising by overlapped area there is a reduction in mean bias error in comparison to SCC results. Anandarajah (2005) reasoned that this reduction was caused by the weighting of the normalisation function. The SCC fields are pyramid shaped functions, therefore

when normalised by overlapped area, that is also a pyramid shape, the resultant normalised correlation field will be flat, as was shown in Figure 2.8(a) (p.25). The correlation peak is therefore skewed towards the actual displacement to reduce mean bias. The normalisation of the FFT correlation field without prior zero padding performs similarly to SCC. However, results are biased towards larger values. As Figure 2.8(b) (p.25) showed, since the FFT correlation field is flat then normalising by overlapped area will generate a 'valley' shaped normalised correlation field. As the displacement increases the shape of this correlation noise floor will skew the correlation peak towards larger values and hence produce a positive mean bias error.

Although normalising by overlapped area provides an improvement to mean bias it offers no reduction in RMS error as Figure 4.4(b) shows. Anandarajah (2005) stated that normalising by overlapped area effectively normalises each point of the correlation field by a local constant, hence reduces the mean bias error by compensating for the shape of the correlation noise floor. This assumes a uniform distribution of particle images across an interrogation region, which in reality there is not. Normalising by area also does not account for the asymmetry of the correlation peak caused by the random distribution of particle images hence the normalised results are identical to those produced from their respective SCC routines.

4.3.2 Normalisation by signal strength

This comparative study provided by Figure 4.5 shows error plots for NSS and FFT_{SS} (equation 2.13, p.26), using the optimum artificial interrogation regions that describe a uniform particle image displacement. These results are compared with their respective standard cross-correlation routines.

(a) mean bias error

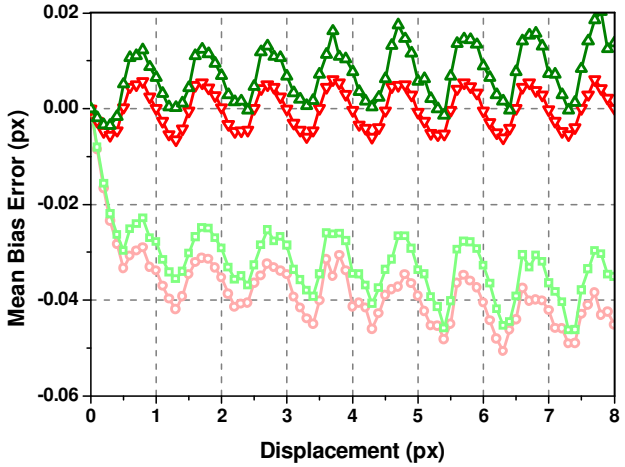

(b) RMS error

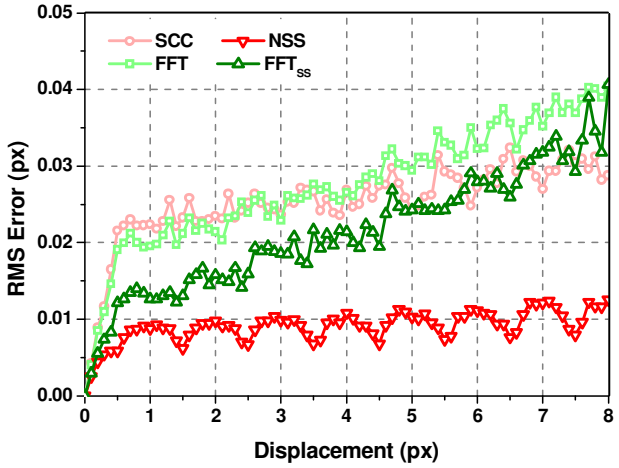

Figure 4.5 Error plots for NSS compared with SCC

The mean bias plot of Figure 4.5(a) shows that normalising the correlation field by the signal strength is able to compensate for the presence of partial images and hence reduce mean bias error. The normalisation of the FFT correlation field without prior zero padding performs similarly to the other two routines but as with normalisation by overlapped area results are biased towards larger values. An explanation for this is given in section 2.8.1 (p.24) concerning the shape of the FFT correlation field

(Figure 2.4(b), p.17) and the shape of the signal strength weighting function (Figure 2.9, p.26).

As well as providing an improvement to mean bias, this normalisation function also provides a reduction in RMS error. In effect, this function is able to correct for the random distribution of particle images within each interrogation region that causes measurement variations and hence suppress RMS errors. The signal strength function is unique to a realisation because it is calculated as the sum of the pixel intensities in the overlapped area which is different for each realisation. This means that NSS is able to compensate for the presence of partial images to reduce mean bias. It is also able to account for the asymmetry of the correlation peak caused by the cross-correlation of unrelated, randomly distributed particle images to reduce RMS error.

4.3.3 Mean image intensity subtraction prior to cross-correlation

Figure 4.6 compares the error plots generated through $R_{MS}(m,n)$ (section 2.8.4, p.29) with that of SCC using the optimised artificial interrogation regions detailed in section 3.9 (p.51) where each displacement data-set describes a uniform particle image displacement.

(a) mean bias error

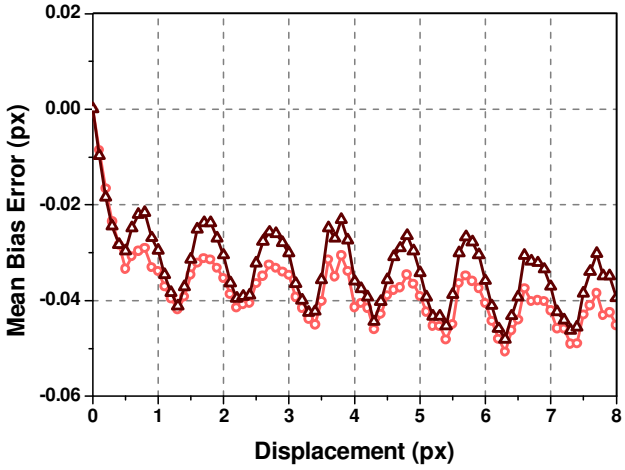

(b) RMS error

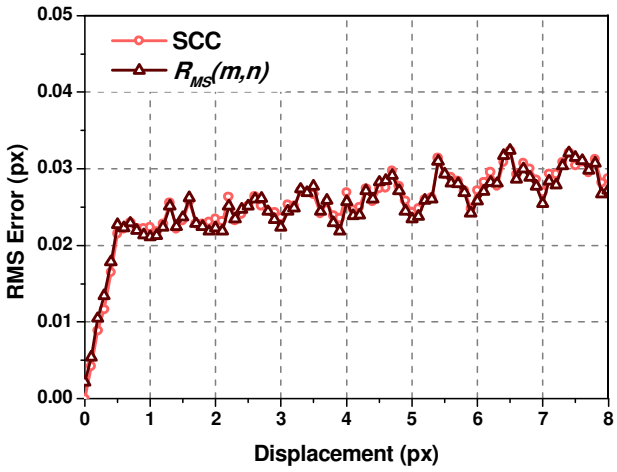

Figure 4.6 Error plots for $R_{MS}(m,n)$ compared with $R(m,n)$

Although $R_{MS}(m,n)$ generates a flat correlation noise floor (Figure 2.10, p.29) it is clear from Figure 4.6 that $R_{MS}(m,n)$ is unable to significantly reduce either the mean bias or RMS error results when compared to results generated through SCC. Subtracting the mean intensity of the interrogation regions prior to cross-correlation is therefore unable to account for the random distribution of particle images and hence does not reduce measurement errors when analysing 'ideal' artificial interrogation regions.

4.3.4 Normalisation by variance

The mean bias and RMS error plots shown in Figure 4.7 have been calculated using the normalisation by variance functions described in section 4.3.4 (p.78). These are compared to SCC and $R_{MS}(m,n)$ results generated in section 4.3.3.

(a) mean bias error

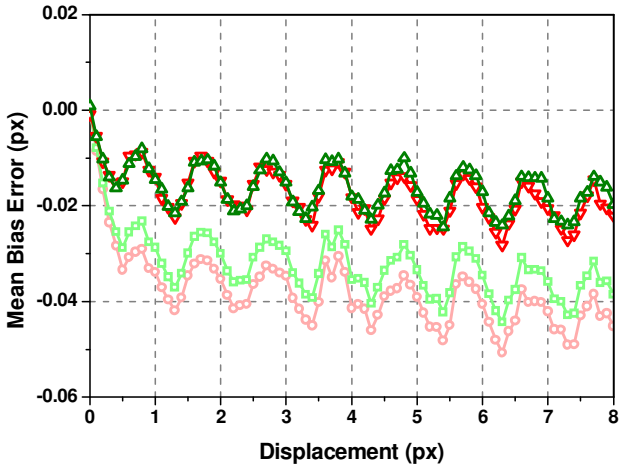

(b) RMS error

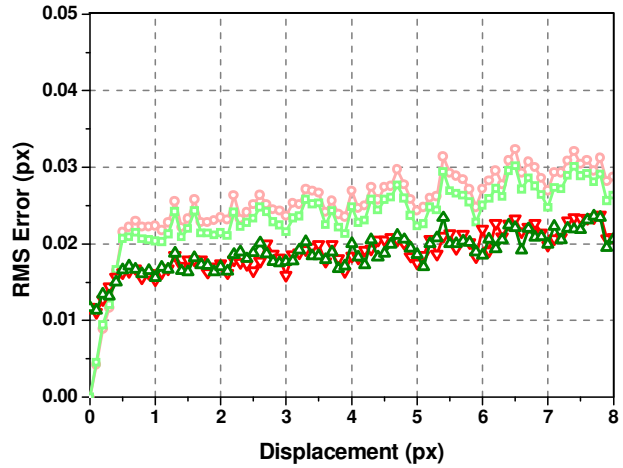

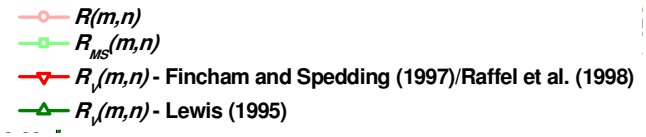

Figure 4.7 Error plots for normalisation by variance

Figure 4.7 highlights that each of the normalisation by variance functions outlined in section 4.3.4 (p.78) outperforms the standard $R(m,n)$ cross-correlation algorithm to produce improved mean bias and RMS errors. The normalisation algorithms suggested by Fincham and Spedding (1997) and Raffel et al. (1998) as well as the one devised by Lewis (1995) do go some way to improving both the mean bias and RMS error but not to the same extent as NSS (Figure 4.5). If the variance functions

expressed in equations 2.17 and 2.19 are compared to the signal strength function of equation 2.13 it can be seen that both functions make use of the intensities within each interrogation region. The variance functions calculate a global variance for one of the regions with the other one being used to calculate a local variance for the area that contributes to each point of the correlation field. Signal strength is calculated as a local summation of intensities from within the area that contributes to each point of the correlation field from both regions. This means that the signal strength function is able to compensate for the random distribution of particle images across an interrogation region as they are the only source of intensities within 'ideal' regions and hence improves both accuracy metrics. As functions described by equations 2.17 and 2.19 calculate a global variance from one of the region they are only able to partially compensate for the random distribution of particle images, thereby are unable to provide the same level of accuracy as shown by the NSS function in Figure 4.5.

In summary, it is clear that NSS provides the greatest improvement to accuracy for all of the normalisation functions that have been reviewed in this section. This function is able to compensate for the presence of partial images as well as the cross-correlation of unrelated particle images to reduce both the mean bias and RMS error metrics to a greater extent than the other routines.

4.4 Digitisation and the accuracy of the Gaussian sub-pixel estimator

Figure 4.1(a) shows a cyclic pattern in the mean bias error with increasing particle image displacement. This cyclic pattern is produced by the cross-correlation of digitised particle images. To identify this, Figure 4.8 shows the average correlation magnitudes for the correlation peak (maximum value) and the magnitudes of the values to the left and to the right of the peak; these values are used by the sub-pixel estimators to calculate the position of the correlation peak as the uniform particle image displacement increases in the *x*-direction. The values are calculated by averaging the magnitudes from each correlation field within each displacement data-set generated from the SCC of regions containing only complete particle images, thereby negating errors associated with partial images. When regions containing only complete particle images are cross-correlated a symmetric Gaussian correlation peak will be generated; each interrogation region pair are identical albeit for the second region being a shifted version of the first.

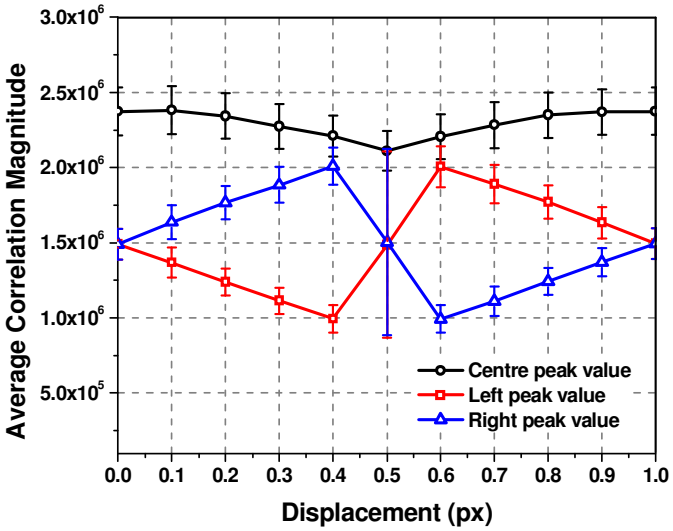

Figure 4.8 Average correlation values for the three central correlation peak points from the cross-correlation of complete particle images (seeding density: 22)

Error bars are included in Figure 4.8 to quantify the variations in individual correlation peaks used to calculate the average correlation peak values. The variation in individual correlation peaks in this instance is caused by the random distribution of particle images within each interrogation region. At integer pixel displacements

both regions within each pair are identical therefore SCC of these 'ideal' artificial regions will produce a symmetric correlation peak. Figure 4.8 shows this as the values to the right and left of the correlation peak are of equal magnitude; this corresponds to points of zero mean bias error at integer pixel displacements as shown in Figure 4.2(a). Over a pixel displacement there is a second point where zero mean bias error occurs; this is at half-pixel displacements. Figure 4.8 shows that at half-pixel displacements, on average, the two values either side of the correlation peak have equal magnitude; this results in a symmetric correlation peak and hence a point of zero mean bias error. However, when considering an individual correlation field for half-pixel displacements the peak is generated over two points. For this to occur the magnitude of one of the neighbouring values (either the right or left point) will be equal to or slightly less than the correlation peak value. This variation is dependent on the cross-correlation of randomly located particle images and results in individual correlation peaks being either positively or negatively skewed at half-pixel displacements. This corresponds to the point of maximum RMS error in Figure 4.2(b) (complete particle images) but, on average, will result in zero mean bias error when all measurements within the displacement data-set are considered.

Although Figure 4.2(a) shows that measurements are underestimated for sub-half pixel displacements and overestimated thereafter (until integer pixel displacements), Figure 4.8 indicates that the cyclic mean bias error pattern should be inverted. The results for Figure 4.8 are independent of the Gaussian sub-pixel estimator yet the figure clearly shows that as the displacement increases towards the half-pixel displacement the value to the right of the correlation peak is greater than the value to the left. Therefore there should be a positive skew in displacements yet when using the Gaussian estimator a negative skew is shown. After the half-pixel displacement point the value to the left of the correlation peak is greater than the value to the right and therefore the correlation peak is negatively skewed. Again, when using the Gaussian estimator a positive skew is shown. This shows that the cross-correlation of unrelated particle images not only affects RMS errors but also the direction of the mean bias error oscillation when measurements are calculated using the Gaussian sub-pixel estimator.

To demonstrate that the cross-correlation of unrelated particle images affects the mean bias oscillation a new data-set of artificial realisations were generated; each containing just one complete particle image with a diameter of 2.8 pixels. The position of the particle image was randomly varied between realisations and particle image clipping was avoided from each region. Displacement data-sets containing 300 realisations were generated for each displacement from zero to 1 pixel at a resolution of one-tenth of a pixel. The measured displacement was then evaluated with SCC and a Gaussian sub-pixel estimator used to calculate the sub-pixel location of each correlation peak. Figure 4.9(a) shows the mean bias error plot generated from the cross-correlation of a single particle image and Figure 4.9(b) shows the corresponding average peak intensity value plot over the one pixel displacement range.

(a) mean bias error

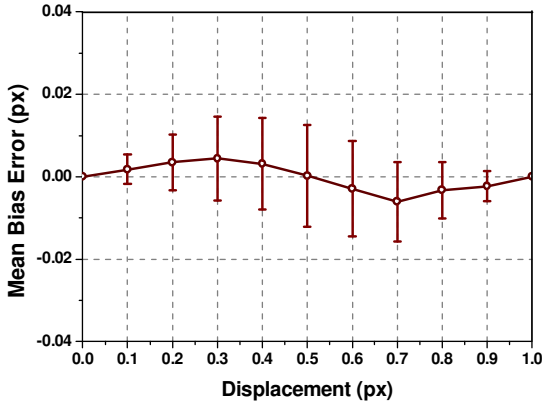

(b) Average correlation point values

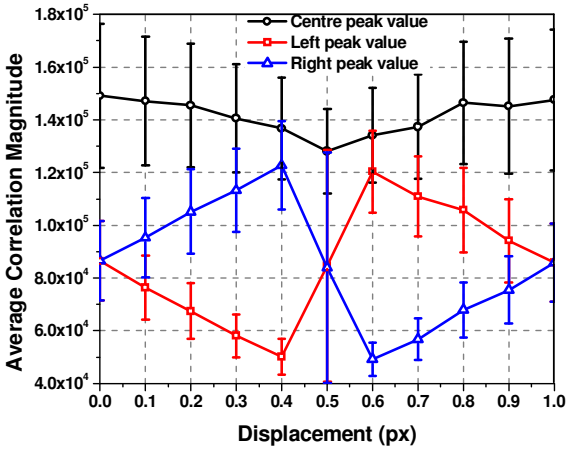

Figure 4.9 (a) mean bias error and (b) average correlation values for the three central correlation peak points from the cross-correlation of single particle images

The error bars are included in these plots to quantify the variations between individual correlation peaks; this dictates the variation in individual displacement values used to calculate the mean bias error. It is evident that on the cross-correlation of realisations that contain single particle images the direction of the mean bias error oscillation (Figure 4.9(a)) corresponds to the correlation peak intensity plot (Figure 4.9(b)). As has previously been stated, the cross-correlation of unrelated particle images introduces a correlation noise floor into each correlation field. This is attributed to an increase in the pixel intensities contributing to each point of the correlation field, thereby increasing the correlation peak height but also the surrounding correlation noise floor.

To show that the correlation noise floor affects the mean bias error oscillation Figure 4.10 presents the error plots generated from the SCC of data-sets containing varying particle image densities per realisation. The particle image densities used in this analysis are 1, 6, 14, 22 and 30 particle images per 32 x 32 pixel interrogation region and each region is modelled so that it only contains complete particle images. Displacement data-sets containing 300 realisations were generated for each displacement from zero to 1 pixel at a resolution of one-tenth of a pixel for each of the particle image densities.

(a) mean bias error

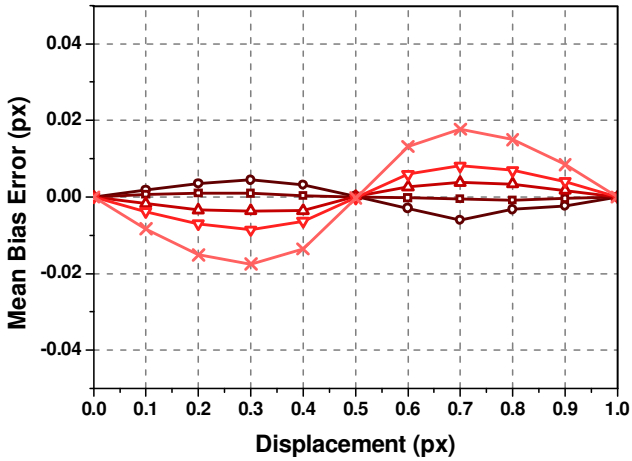

(b) RMS error

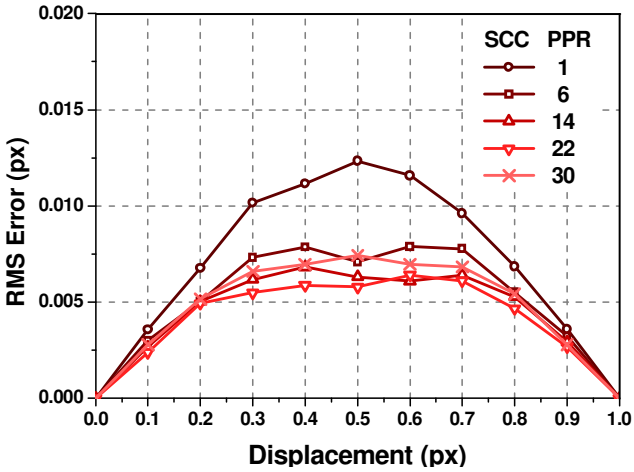

Figure 4.10 Error plots for SCC of complete particle images with varying particle image density (Interrogation region: 32 x 32 pixels)

Figure 4.10(a) clearly shows that as the particle image density increases between data-sets there is an inversion of the mean bias error oscillation. A particle image density of 6 particle images per interrogation region provides a negligible mean bias error across the one pixel displacement range. As the particle image density increases passed 6 particle images per realisation then there is an increase in the amplitude of the mean bias error oscillation. Figure 4.10(b) shows there is zero RMS error at integer pixel displacements. In both instances the intensity content of both regions are identical although at 1 pixel displacement the second region is a shifted version of the first. As the particle image density increases there is little discernable difference in RMS error with increasing displacement. However, as is expected the maximum RMS error occurs at the half-pixel displacement point. As has been

previously stated, the point of maximum RMS error at this displacement is caused by the sensitivity of the Gaussian sub-pixel estimator resulting from minor variations in the correlation peak shape at this displacement.

Figure 4.11 provides (a) an average SCC signal plot and (b) average SCC noise plot for each displacement data-set over a one pixel displacement range for each of the particle image densities.

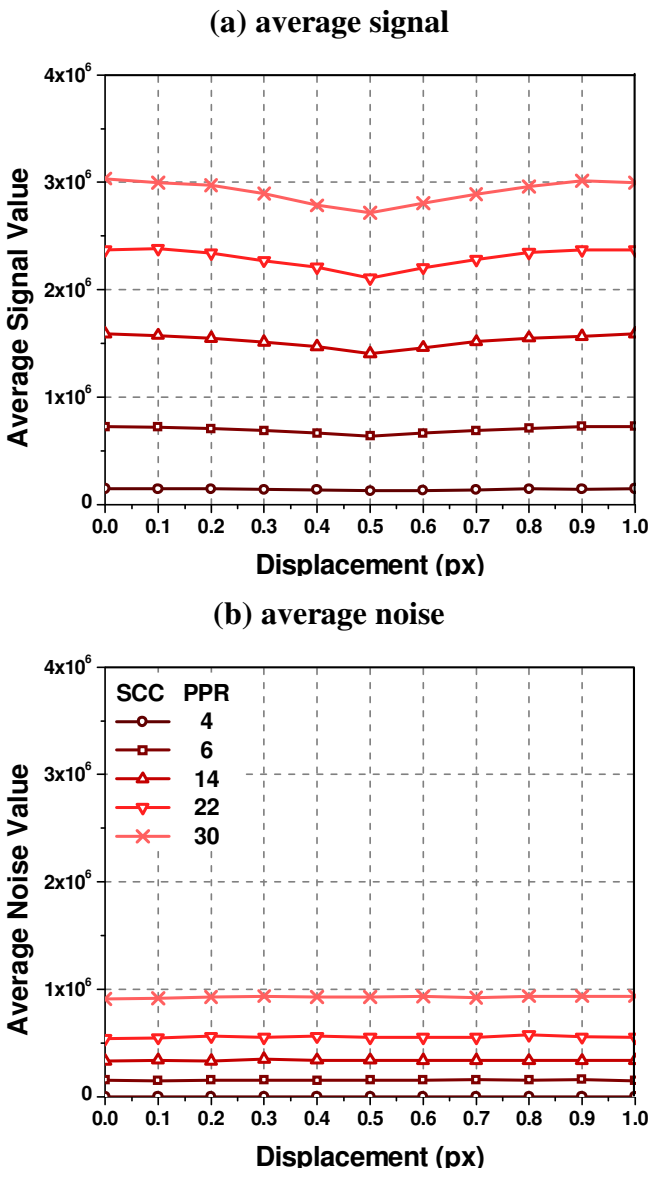

Figure 4.11 (a) average signal value and (b) average noise value for various complete particle image seeding densities

The figure shows that as the particle image density increases between data-sets the average signal value per data-set increases and this is coupled with an increase in the average correlation noise value. This is to be expected since increasing the particle

image density increases the number of particle image intensities that can contribute to the correlation field. This increases both the correlation peak magnitude and the correlation noise floor generated by the cross-correlation of unrelated particle images. Although previous assumptions have stated that maximising the SNR will improve accuracy (Raffel et al., 1998) Figure 4.10 and Figure 4.12 clearly show that this is not the case.

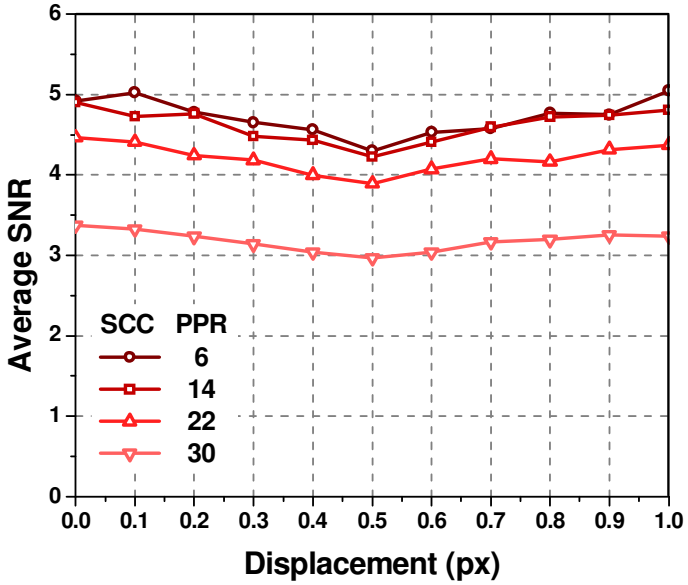

Figure 4.12 Average SNR for various complete particle image seeding densities

As the particle image density is increased there is a decline in the average SNR; this coincides with an inversion and an increase in the amplitude of the mean bias error oscillation.

The inversion and increase in the amplitude of the mean bias error oscillation is credited to a decrease in the ratio between the three central values of the correlation peak. This is caused by an increase in the magnitude of the correlation noise floor generated by the cross-correlation of unrelated particle images as the seeding density increases. Figure 4.13 demonstrates that as the magnitude of the correlation noise floor increases, the ratios between the three central correlation peak values declines thereby affecting accuracy. The figure shows a cross-sectional view through the correlation peak as it displaces in the x-direction. These fields are averaged over 300 realisations for a displacement of 0.3 pixels in the x-direction as the number of complete particle images per region is increased.

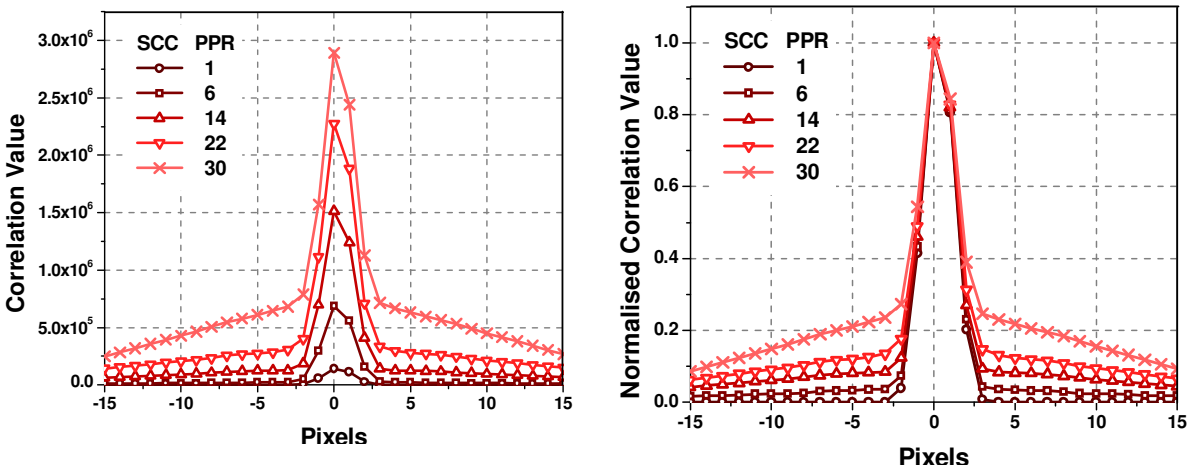

(a) Cross-section of the correlation field **(b) Normalised correlation field**

Figure 4.13 Cross-sectional correlation fields describing an *x*-direction displacement of 0.3 pixels using SCC for various particle image seeding densities

Figure 4.13(a) shows that the magnitude of the correlation field increases as more pixel intensities contribute in cross-correlation. So that each correlation peak can be compared, Figure 4.13(b) shows the normalised correlation values calculated from the correlation values provided in Figure 4.13(a). The normalised correlation values are calculated by normalising each point from each average correlation field by its maximum value.

From Figure 4.13(b) it is clear that as the magnitude of the correlation noise floor increases the ratios between the three central correlation peak values decreases; when evaluating displacements with the Gaussian sub-pixel estimation this causes the mean bias error oscillation to invert and then increase in amplitude. In reality the number of particle images within each region changes and therefore the magnitude of the noise floor will vary; consequently the oscillation in mean bias error will increase or decrease accordingly.

The same principle applies when evaluating the accuracy of measurements using interrogation regions populated with particle images of various sizes. To show this, data-sets of realisations containing 22 complete particle images were generated for each displacement between zero and one pixel at a resolution of one-tenth of a pixel. The particle image diameter for each data-set is varied so that particle images with

diameters of 2.4, 2.8, 3.2, 4.2 and 5.6 pixels are used per data-set. Figure 4.14 shows the error plots generated from the SCC of these data-sets.

(a) mean bias error

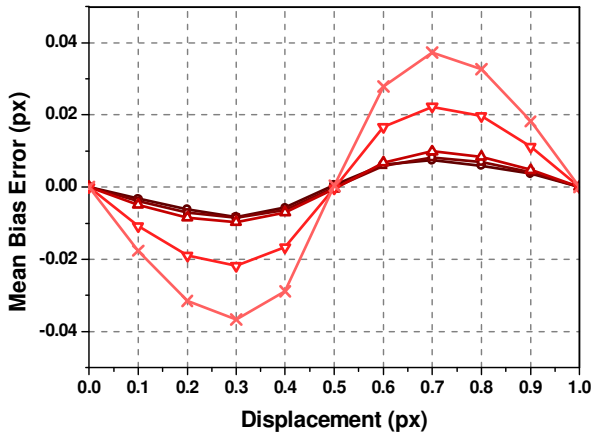

(b) RMS error

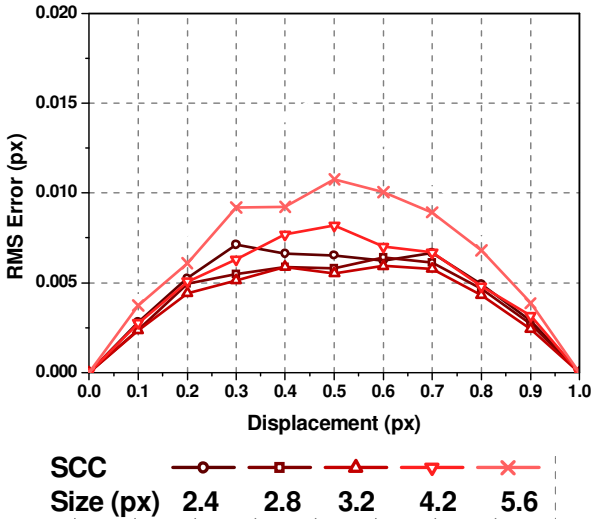

Figure 4.14 Error plots for SCC of complete particle images for various particle image sizes (32 x 32 pixels)

Figure 4.14(a) highlights that as the particle image size increases the mean bias error oscillation also increases in amplitude. This corresponds to the results shown in Figure 4.10(a) where the oscillation increases as the cross-correlation of unrelated particle images increases, adding to the correlation noise floor. The increase in the oscillation amplitude in this instance is due to increasing the intensity content of each particle image. Therefore, cross-correlation of unrelated particle images will provide an additional contribution to the correlation noise floor. As the particle image size increases the correlation peak will subsequently broaden. This will result in the correlation peak being described over more points on the correlation field and

consequently the ratios between the three correlation peak values used to evaluate the sub-pixel displacement will decline and thereby affect accuracy.

As with the previous example of Figure 4.13, Figure 4.15 also shows that as the magnitude of the correlation noise floor increases, the ratios between the three central correlation peak values used to evaluate the sub-pixel displacement in the *x*-direction declines, this subsequently effects accuracy using the Gaussian estimator. The figure describes the cross-sectional view through the correlation peak to show the *x*-direction displacement; each field is averaged over 300 realisations for a displacement of 0.3 pixels in the *x*-direction as the particle image size per region is increased, whilst maintaining the seeding density at 22 particles per region

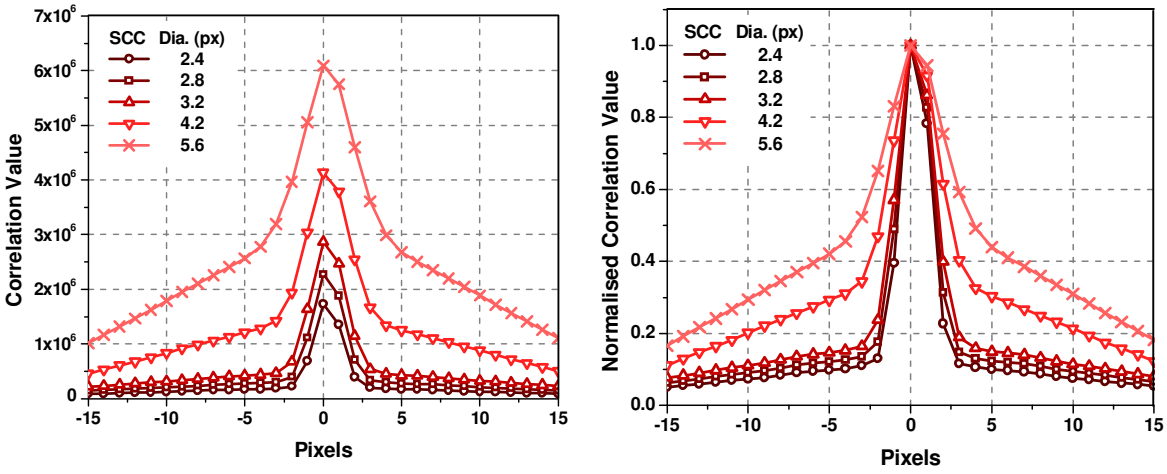

(a) Cross-section of the correlation field **(b) Normalised correlation field**

Figure 4.15 Cross-sectional correlation fields describing an *x*-direction displacement of 0.3 pixels using SCC for various particle image sizes

It is clear from Figure 4.15, when increasing the particle image size more pixel intensities will contribute to the correlation peak and hence as was previously discussed this decreases the ratios between the three central correlation peak values used to evaluate displacements and subsequently effects the amplitude of the mean bias error oscillation as is shown in Figure 4.14(a).

As Figure 4.10 and Figure 4.14 show, increasing the intensity content of each interrogation region increases the amplitude of the mean bias error oscillation. If the background noise distribution discussed in section 3.8 (p.49) is approximated as a uniform distribution (e.g. a 15% background noise equates to a global addition of 39

to each pixel value provided the total intensity does not exceed 255) then the same effect on the mean bias error oscillation occurs, as is shown in Figure 4.16.

Figure 4.16 provides the mean bias and RMS error plots generated from the SCC of data-sets containing 22 complete particle images per realisation whilst increasing the background noise intensity between data-sets. The uniform background noise intensity added to each data-set is 0%, 2%, 5%, 10% and 15% of the maximum 8-bit output. Displacement data-sets containing 300 realisations were generated for each displacement from zero to 1 pixel at a resolution of one-tenth of a pixel for each background noise intensity.

(a) mean bias error

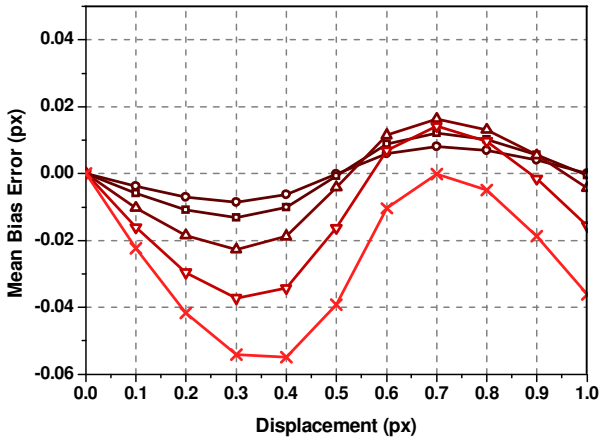

(b) RMS error

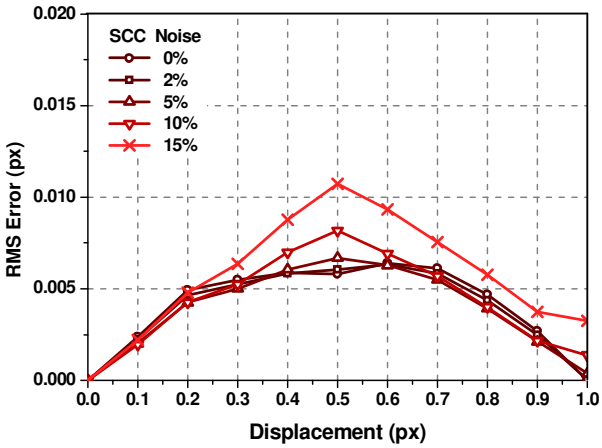

Figure 4.16 Error plots for SCC of complete particle images for various background noise intensities (32 x 32 pixels)

Figure 4.16(a) identifies that although the amplitude of the mean bias error oscillation increases as the background noise intensity increases, it also introduces a

negative bias into measurements. This addition of underestimations to measurements can be explained through comparing the correlation peaks generated in Figure 4.13 and Figure 4.15 with those generated as the background noise intensity increases as shown in Figure 4.17.

Figure 4.17(a) shows the cross-sectional view through the correlation peak to show the *x*-direction displacement. Each field is averaged over 300 realisations for a displacement of 0.3 pixels in the *x*-direction and the background noise intensity is increased up to 15% of the total 8-bit output. So that a comparison can be made between these correlation fields, Figure 4.17(b) provides the normalised correlation field values.

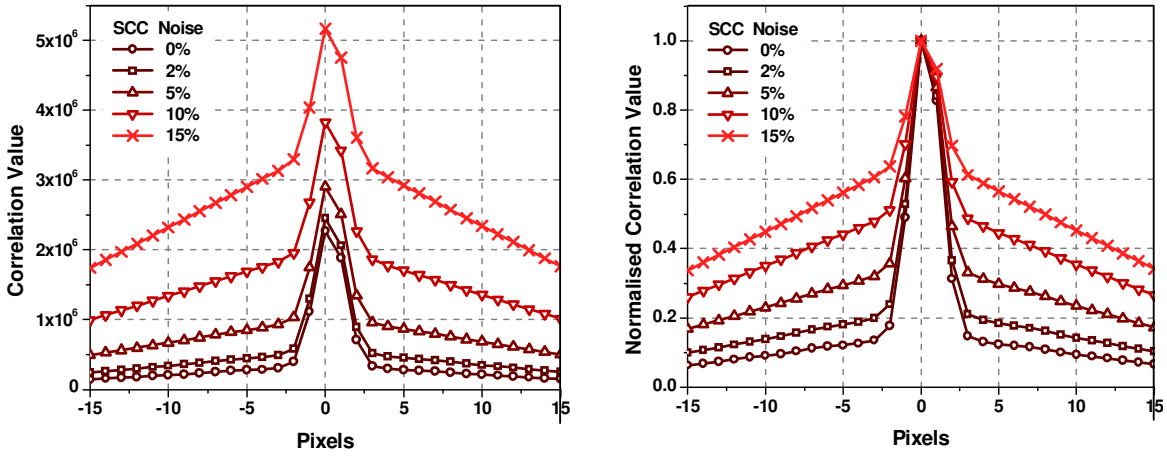

(a) Cross-section of the correlation field **(b) Normalised correlation field**

Figure 4.17 Cross-sectional correlation fields describing an *x*-direction displacement of 0.3 pixels using SCC for various background noise intensities

Comparing the normalised correlation fields generated in Figure 4.13(b), Figure 4.15(b) and Figure 4.17(b) with their respective mean bias error plots, it is evident that the addition of background noise increases the magnitude of the correlation noise floor to a greater extent than increasing the seeding density (Figure 4.13(b)) or increasing the particle image diameter (Figure 4.15(b)). Although increasing the seeding density and the particle image diameter generates a pyramid shaped correlation noise floor its presence in these cases does not cause measurements to be underestimated. The addition of background noise generates a significant pyramid correlation noise floor therefore when a correlation peak is added it will be biased away from the actual measurement as is shown in Figure 4.17(a).

In summary, this section has shown that the Gaussian sub-pixel estimator is capable of providing accurate measurements when applying the estimator to symmetric Gaussian correlation peaks from regions that contain 6 complete 2.8 pixel diameter particle images. However, since each interrogation region contains randomly distributed particle images, this means that the cross-correlation of partial images results in measurement underestimations (Figure 4.2(a)) and the cross-correlation of unrelated particle images results in measurement variations (Figure 4.2(b)). The cross-correlation of unrelated particle images also introduces a correlation noise floor into each correlation field; it is this that affects the ratios between the three correlation peak values used to define the sub-pixel location of the correlation peak.

As the intensity content per realisation increases the magnitude of the correlation noise floor will increase (Figure 4.11(b)), this decreases the ratio between the three central correlation peak values (Figure 4.13 and Figure 4.15). As the ratios decrease, firstly there is an inversion of the mean bias error oscillation, this subsequently increases in amplitude as the correlation noise floor increases (Figure 4.10) which therefore affects accuracy. The presence of a correlation noise floor generated by the cross-correlation of unrelated particle images is inherent to each correlation field. Therefore its effect on accuracy cannot be removed without affecting other aspects such as impeding the particle image size or resolution. The same effect also occurs when regions containing larger particle images are cross-correlated. This will cause the correlation peak to broaden decreasing the ratio between the three central points of the correlation peak and therefore increasing the amplitude of the mean bias error oscillation. When partial images are included in analysis, larger particle images will generate greater PIE caused by the cross-correlation of partial images that have a more significant contribution to the total intensity values, as is shown in Figure 3.12 (p.57). This will increase measurement underestimations and a decrease in the ratio between the three central values will increase the amplitude of the mean bias error oscillation. Each region should therefore contain particle images of optimum size.

Underestimations will also arise when background noise intensities are added into each region. As Figure 4.16(a) shows, when analysing regions that contain only complete particle images the addition of background noise will also negatively bias

measurements because the cross-correlation of background noise intensities contribute to the pyramid-shaped correlation noise floor. Therefore when analysing realistic artificial interrogation regions, the cross-correlation of partial images will cause underestimations which will subsequently be compounded by background noise.

4.5 Evaluation of artificial regions containing background noise

As was shown in section 4.2, partial images at the edge of an interrogation region will negatively skew the correlation peak to underestimate measured displacements. The cross-correlation of unrelated particle images will also cause variations in the shape of each correlation peak resulting in RMS errors. The cross-correlation of background noise in each interrogation region was also shown to affect measurements resulting in underestimations (Figure 4.16(a)).

Huang et al. (1997) and Anandarajah (2005) proposed normalising each correlation field by the signal strength that contributes to each point of the correlation field to account for the random distribution of particle images within each realisation. Figure 4.5 showed that this approach provided an improvement to both the mean bias and RMS errors over other normalisation techniques. However, these results were generated by analysing 'ideal' artificial regions that do not contain background noise which is inherent to real DPIV images. This section identifies that the addition of background noise affects the accuracy of measurements when processing with either SCC or NSS.

To highlight the effect of background noise on the performance of SCC and NSS, artificially generated Gaussian white noise (GWN), as described in section 3.8 (p.49), was added into each artificial interrogation region using MATLAB. Data-sets of realisations containing background noise with mean intensities of 2%, 5%, 10% and 15% of the total 8-bit output were generated for a series of prescribed uniform particle image displacements using the optimum realisation parameters outlined in section 3.9 (p.51) whilst maintaining the distribution described in Figure 3.7 (p.50)[2].

[2] Appendix I shows that it is the mean and not the variance that affects results.

Figure 4.18 shows the error plots generated for SCC and NSS from the data-sets containing background noise at different intensities.

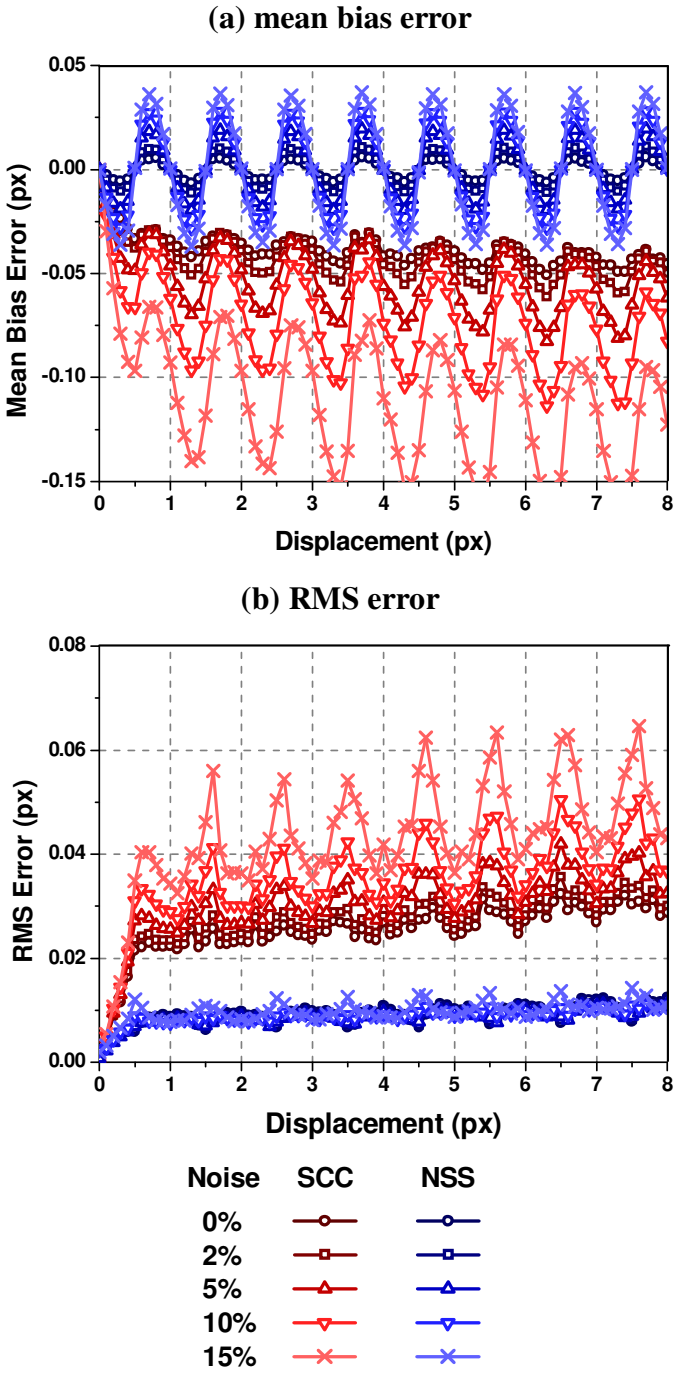

Figure 4.18 Error plots for SCC and NSS with increasing background noise intensities (32 x 32 pixels)

It is clear from Figure 4.18(a) that as the mean background noise intensity increases the amplitude of the mean bias error oscillation increases for both SCC and NSS. However, Figure 4.18(b) shows that although SCC generates larger RMS errors with increasing background noise, variations remain relatively constant when the same

data-sets are analysed with the NSS algorithm. The next section provides an explanation as to why there is an increase in the mean bias error amplitude for the two processing algorithms but only SCC provides a significant increase in RMS errors with increasing background noise intensity.

4.5.1 SCC and NSS with background noise

Figure 4.19 shows the cross-sectional view through the correlation peak to show the *x*-direction. Each correlation field is averaged over 300 realisations using (a) SCC and (b) NSS for each of the mean background noise intensities. The displacement data-set is experiencing a uniform particle image displacement of 4.3 pixels in the *x*-direction. The figure clearly shows that increasing the background noise intensity increases the height of the correlation field noise floor for both SCC and NSS.

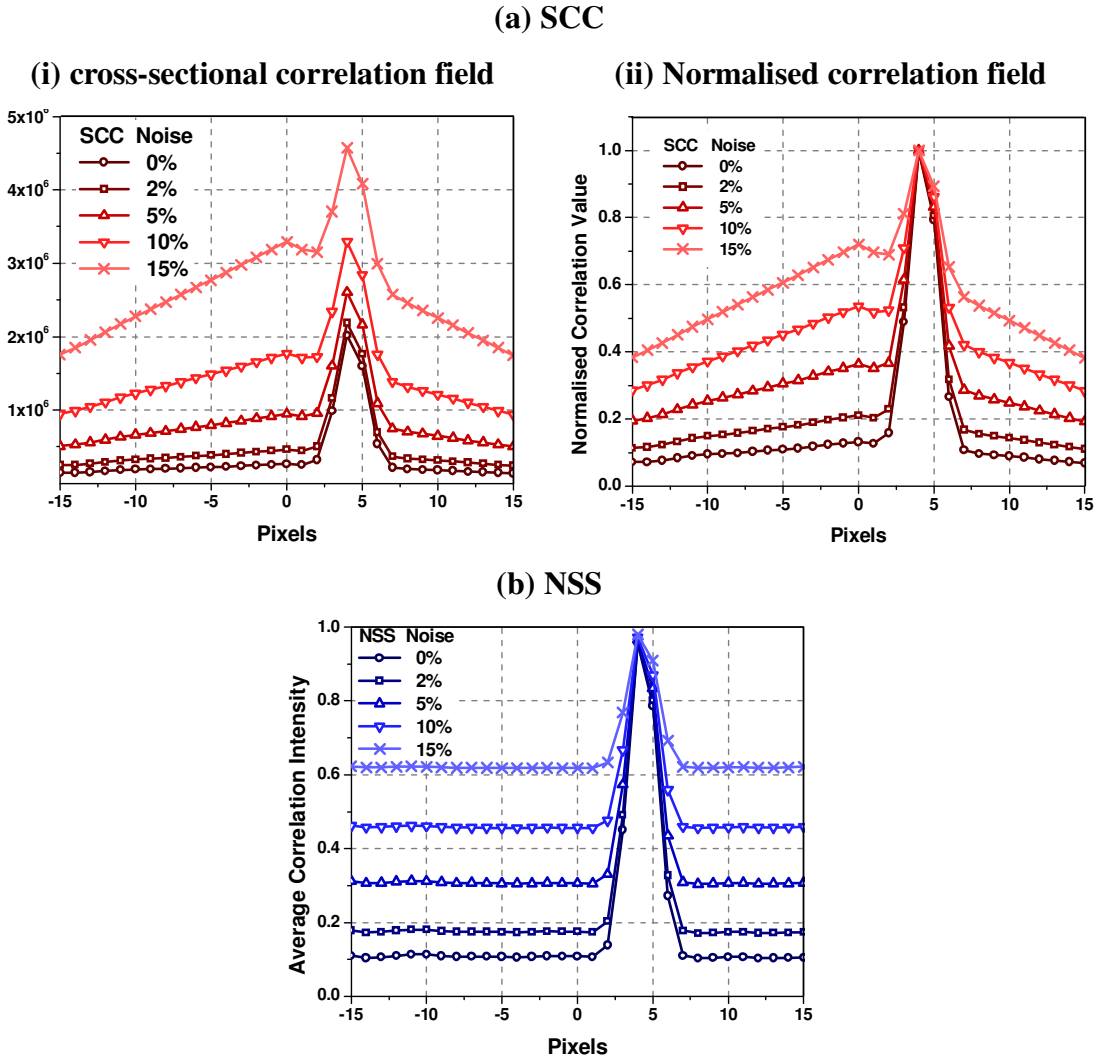

Figure 4.19 Average correlation fields with varying background noise describing an *x*-direction displacement of 4.3 pixels for SCC and NSS

Figure 4.19(ai) also shows there is an increase in correlation peak height with increasing background noise intensity. This is attributed to an increase in pixel intensity values contributing to each point of the correlation field; this thereby increases the correlation peak height and the surrounding noise floor values. The increase in the mean bias error amplitude (Figure 4.18(a)) can be credited to a decrease in the ratios between the three central values of the correlation peak; this is clearly shown in Figure 4.19(aii) which shows the normalised cross-section of the correlation field through the correlation peak. An increase in the correlation noise floor will also negatively bias measurements away from their actual values; this further contributes to the underestimations also caused by partial images. On the application of NSS the random distribution of particle image intensities across each interrogation region are compensated for thereby removing the effects of partial images that cause underestimations. However, background noise intensities remain within analysis which affects the ratios between the three central points of the correlation peak Figure 4.19(bi); this results in an increase to the mean bias error oscillation amplitude.

On examining Figure 4.19(a) and Figure 4.19(b) with Figure 4.18(a) decreasing the ratios between the three correlation peak values causes the mean bias error oscillation amplitude to increase. As was stated in section 4.4 this is ultimately caused by an increase in the magnitude of the correlation noise floor initially generated by the cross-correlation of unrelated particle images but this is added to by increasing the background noise intensity.

The decrease in the ratio between correlation peak values with increasing background noise intensity will also increase measurement uncertainties (RMS errors) for SCC as is highlighted in Figure 4.18(b). This is further illustrated in Figure 4.20 which shows the cross-sectional view through the correlation peak in the x-direction and is averaged over 300 realisations for regions containing (a) no background noise and (b) a mean background noise intensity at 15% of the total 8-bit output whilst experiencing an actual uniform displacement of 4.3 pixels in the x-direction and processed using SCC. The variations between individual correlation

peaks over the 300 realisation data-set are also shown in Figure 4.20 as deviation error bars.

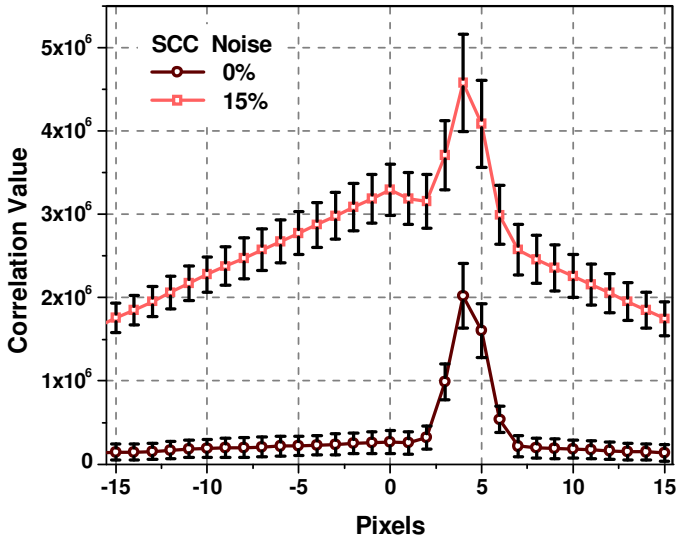

Figure 4.20 Average SCC correlation fields for a 4.3 pixels displacement with error bars

The error bars indicate there is significant deviation in the shape of individual correlation peaks; the decrease in the ratio between adjacent correlation peak values with increasing background noise intensity amplifies this variation. Therefore any sub-pixel estimator used to measure displacement will generate significant RMS errors. This is typical of all displacements processed using SCC. As the background noise intensity increases Figure 4.18(b) shows that SCC provides greater RMS errors; this is coupled with a cyclic 'beating' pattern that provides errors that are smaller at integer pixel displacements and higher at half-pixel values. This cyclic pattern was identified by Huang et al. (1997) and Anandarajah (2005) where it was reasoned that this occurs because at half-pixel displacements the correlation peak is centred between two points on the correlation field. The cross-correlation of the additional background noise will skew the correlation peak either positively or negatively from the mean displacement, thereby generating the cyclic 'beating' pattern. This is evident in Figure 4.21 which compares the measured displacement distribution generated using SCC for an actual displacement of 1 pixel with the distribution generated for an actual displacement of 1.5 pixels when the mean background noise intensity is (a) zero and (b) at 15% of the total 8-bit output.

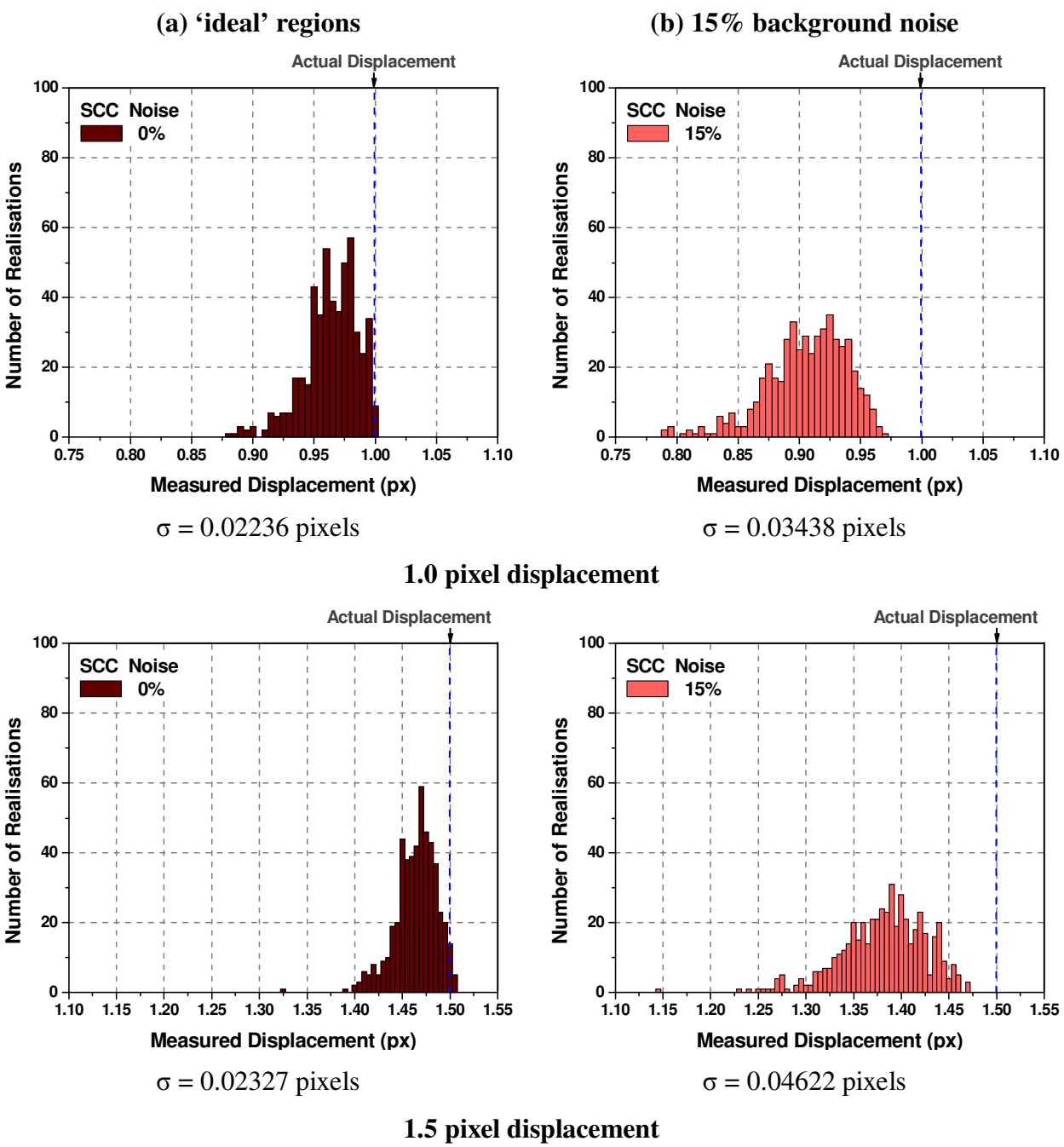

Figure 4.21 SCC measured displacement distribution for actual displacements of 1.0 pixel and 1.5 pixels (bin size: 0.05 pixels)

The figure identifies that as the displacement increases from 1 to 1.5 pixels the RMS error increases regardless of background noise intensity; this is to be expected since there is an increase in the number of unrelated particle images per realisation with increasing displacement. With the addition of background noise the RMS error increases. When each region is cross-correlated the background noise skews each correlation peak generating large variations in measurements. This coincides with the measured displacement distribution shown in Figure 4.21 and the RMS error plot

of Figure 4.18(b). At a displacement of 1.5 pixels (and for each half-pixel displacement thereafter) the RMS error is at a cyclic peak which corresponds to results from Figure 4.18(b). Since the correlation peak is situated between two points on the correlation field then the additional background noise has an added influence on the magnitude of variations. Correlation fields experiencing half-pixel displacements will have peaks that are subjected to the greatest deviations generating the measurement variations; this is highlighted in Figure 5.7 which results from the additional background noise intensities. At half-pixel displacements the correlation peak is defined over two points; this inherently skews the correlation peak either positively or negatively and results are exacerbated by the cross-correlation of the additional background noise.

As was stated previously, normalising the SCC field by the signal strength compensates for the random distribution of particle images across each interrogation region to reduce underestimations and variations between measurements. As Figure 4.18(b) shows, NSS also compensates for the addition of background noise to maintain a consistent RMS error with increasing noise intensity. This is because the technique normalises by the pixel intensities that contribute to each point of the correlation field thereby compensating for both particle image distribution and the additional background noise. Although increasing the magnitude of the correlation noise floor subsequently increases the mean bias error oscillation, the variations between measurements remains small when compared to the SCC results.

This is illustrated in Figure 4.22 which shows the cross-sectional slice through the correlation peak in the *x*-direction that is averaged over 300 realisations and contains (a) no background noise and (b) a mean background noise intensity of 15% of the total 8-bit output whilst experiencing an actual uniform displacement of 4.3 pixels in the *x*-direction and processed using NSS. The variations between individual correlation peaks over the 300 realisation displacement data-set are also shown in Figure 4.22 as deviation error bars.

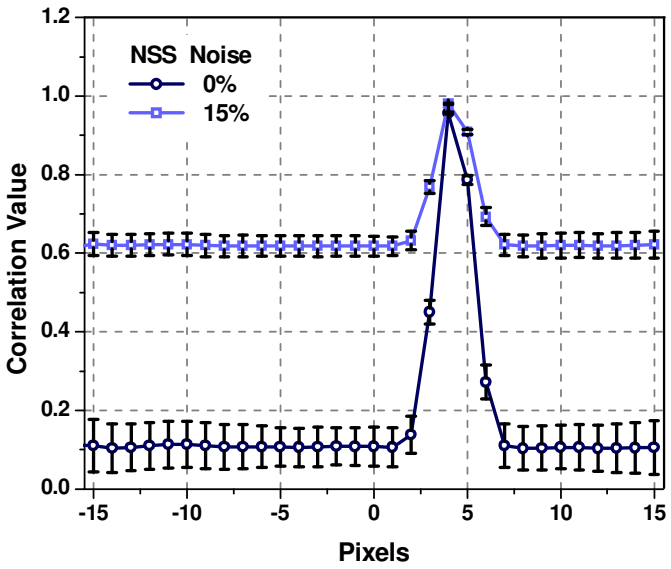

Figure 4.22 Average NSS correlation fields for a 4.3 pixels displacement with error bars

The figure highlights that when processing with NSS, variations between measurements will remain small thereby suppressing RMS error. This confirms the findings of Figure 4.18(b). The cyclic RMS error pattern shown with SCC processing is also evident for NSS when the mean background noise intensity reaches 15% of the total 8-bit output. As with SCC at half-pixel displacements the NSS correlation peak is centred between two points on the correlation field therefore measurements are skewed either positively or negatively generating greater RMS errors at these points. However, since NSS accounts for changes in pixel intensity across each interrogation region to suppress RMS error then the cyclic pattern is less prevalent.

In summary, processing regions that contain background noise will increase the amplitude of the mean bias error oscillation. This is caused by an increase in the magnitude of the correlation noise floor that decreases the ratios between correlation peak values. The decrease in the ratio between the three correlation peak points will also increase measurement variations when processing with SCC. NSS provides an improvement in RMS error because this normalisation function accounts for variations in the pixel intensities across an interrogation region that contributes to the correlation field. Processing this way is therefore able to compensate for the random distribution of particle images as well as background noise to reduce measurement variations. However, at higher mean background noise intensities (i.e. 15% of the

total 8-bit output) the cyclic RMS error pattern shown with SCC is also apparent with NSS processing but to a much lesser extent. Although NSS is able to account for measurement variations the amplitude of the mean bias error oscillation increases as the background noise intensity increases. A robust processing algorithm that compensates for this is discussed in the next chapter.

4.6 Summary

This chapter has outlined that the cross-correlation of partial images causes measurement underestimations and the cross-correlation of unrelated particle images cause measurement variations. It has also been demonstrated that the mean bias error oscillation is caused by a decline in the ratio of the three central points of the correlation peak used by the Gaussian sub-pixel estimator to define the location of the correlation peak. This decline is caused by an increase in the intensity average of each interrogation region which increases the magnitude of the correlation noise floor.

The performance of several processing algorithms designed to improve measurement error statistics have also been reviewed and assessed. The accuracy metrics for each algorithm is provided by processing data-sets of 'ideal' artificial regions experiencing a known uniform particle image displacement. With the previous assumption that the non-uniform weighting of the correlation function causes measurement uncertainties (Raffel et al., 1998) it was shown that normalisation by overlapped area reduces mean bias error by skewing the correlation peak back towards the actual displacement yet was unable to suppress RMS errors. Normalising by a global constant (i.e. by intensity), to account for variations in correlation peak height provides no improvement to either accuracy metric over SCC results. Mean subtraction prior to $R(m,n)$ cross-correlation ($R_{MS}(m,n)$) is also shown not to be able to suppress measurement error statistics. It was also established that normalisation by variance was able to only partially compensate for the systematic errors resulting in improvement to both metrics over SCC results yet underestimations in measurements remain. It was identified that NSS is the preferred normalisation function when quantifying errors using 'ideal' artificial regions. This normalisation function compensates for changes the in seeding density across an interrogation region to account for the partial images that cause measurement underestimation and the cross-correlation of unrelated particle image that cause RMS errors.

Section 4.4 identified that increasing the particle image seeding density and particle image size affects the magnitude of the mean bias error oscillation and therefore the optimum interrogation region properties (summarised in section 3.10) must remain. The addition of background noise intensities (Figure 4.16) increases the mean bias error oscillation but also contributes to the underestimations in measurements.

When processing 'realistic' interrogation regions (i.e. those that contain partial images and background noise) SCC provided worse accuracy metrics (Figure 4.18) yet NSS processing only affected the mean bias error oscillation. It is proposed that the increase in mean bias error oscillation is caused by a decrease in the ratios between the three central points of the correlation peak used to determine measurements in the x-direction. An increase in measurement uncertainties are contributed to the ratio decline in conjunction with the variations in the asymmetry of the correlation peak when processing with SCC. Since NSS accounts for the asymmetry of the correlation peak to suppress RMS error then only an increase in the magnitude of the mean bias error will remain.

The next chapter examines image enhancement techniques that can be used to remove background intensities prior to cross-correlation. From this, a new robust processing algorithm is proposed that accounts for the systematic errors that cause measurement uncertainties with other algorithms without prior knowledge of the region's quality or mean intensity.

Chapter 5

A New Robust Processing Algorithm

5.1 Introduction

The detailed review of each processing algorithm provided in the previous chapter identified that NSS is able to suppress both accuracy metrics to the greatest extent of the normalisation functions over SCC when processing 'ideal' regions. This algorithm compensates for the random distribution of particle images across each region to skew the correlation peak back towards the actual displacement whilst also reducing the variation in the asymmetry of each peak caused by the cross-correlation of unrelated particle images. On the addition of background noise intensities, to model more realistic regions, it was shown that this unfavourably affects the accuracy metrics when processing with either SCC or NSS.

This chapter assesses the accuracy metrics generated through SCC and NSS processing whilst using image enhancement techniques, which are proposed to suppress the presence of background noise intensities. It is shown that these methods do suppress background noise yet prior knowledge of the quality of each region is required before accuracy metrics can be quantified. Following this, a new robust processing algorithm has been developed that accounts for the systematic errors that cause measurement uncertainties with other cross-correlation algorithms, and does not require prior knowledge of each region to provide accurate measurements. This novel approach is called: mean intensity subtraction prior to $R(m,n)$ cross-correlation normalised by signal strength, $R_{MSSS}(m,n)$ and is calculated in the spatial domain. This algorithm takes advantage of the signal strength function to account for the random distribution of particle images and also the subtraction of mean intensities within the overlapped area which accounts for the background image noise.

The error statistics for the processing algorithms are presented for a series of uniform particle image displacements. Data-sets of realisations are generated using the

optimum region criteria outline in section 3.9 (p.51) whilst varying the background noise intensity. In addition, error plots are also generated from processing 16 x 16 pixels interrogation regions maintaining the same seeding density, particle image size and background noise intensity levels as used for the larger region analysis.

5.2 Compensating for the correlation noise floor

In the previous chapter it was revealed that the addition of background noise increased the amplitude of the mean bias error oscillation whilst also affecting the RMS error when processing with SCC. Although NSS also generated mean bias error results with an increased amplitude compared to the 'ideal' case, RMS error results are suppressed since the weighting function suppresses the variations in the asymmetry of the correlation peak. It was shown that increasing the background noise increased the correlation noise floor and subsequently reduced the ratio between correlation peak values which are used to evaluate displacements. Section 2.7 (p.22) identified some image enhancement techniques that can be applied to regions prior to cross-correlation. This section evaluates the accuracy of SCC and NSS by subtracting the average background noise across each region, applying a pixel threshold value to regions and subtracting a local average intensity from within a kernel of varying size. Measurements are evaluated using regions that contain a mean background noise intensity of 15% of the total 8-bit output. These enhancement techniques were developed to reduce variations between measurements yet it is also apparent that these three processes reduce background noise through subtraction. A robust processing algorithm is subsequently introduced that is able to compensate for mean background noise intensities of up to 15% of the total 8-bit output as well as the random distribution of particle images to provide accurate results without prior knowledge of the background noise intensity.

5.2.1 Average background noise subtraction

Fore et al. (2005) proposed subtracting an average background noise image to account for background noise intensities that affect measurements. This is obtained by averaging the background noise intensities over series of images that do not contain particle images. Although the background noise intensities from an individual image

can be used for subtraction an average background noise intensity function is usually calculated. This is because although the background noise distribution across each region may be the same, individual pixel values within each region will be different. The average background noise intensity function can be calculated spatially from each interrogation region across an image or temporally between sequential interrogation regions. Spatial average background subtraction can be used in image enhancement if there is uniform background noise across an image. When background noise intensities are spatially averaged, provided that the average is calculated over a sufficient number of regions, each pixel value of each interrogation region is subtracted by a global constant. Fore et al. (2005) stated that at least 50 interrogation regions should be used for averaging. If there is a large differential in the background noise intensity across an image then temporal averaging of the background noise should take precedence. This means that an average background noise intensity function is calculated over sequential regions. If there is a differential in the background noise intensity across an interrogation region then temporal averaging will also compensate for this by subtracting local average background intensity values from each point as is highlighted in section 5.2.4.

Figure 5.1 provides the mean bias error and RMS error plots for SCC and NSS when the average background noise is subtracted from each region within prior to analysis. The average background noise is calculated over 50 interrogation regions; each of which contain a mean background noise intensity of 15% of the total 8-bit output and describe the distribution illustrated in Figure 3.7 (p.50). This provides an average background noise field which can be simply subtracted from each region prior to cross-correlation. Average background noise subtraction results are compared to the accuracy metrics generated by processing 'ideal' regions and regions that contain a mean background noise intensity at 15% of the 8-bit output.

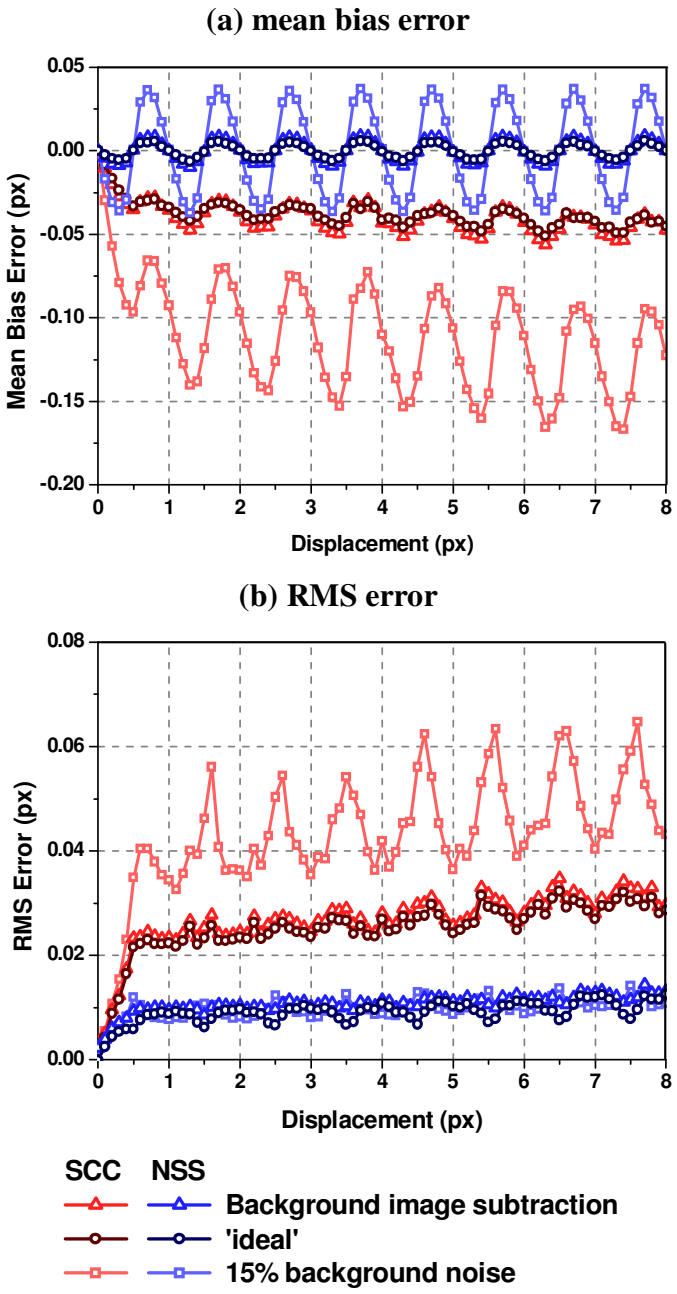

Figure 5.1 Error plots comparing 'ideal' region and 15% background noise results with mean background image subtraction for SCC and NSS (32 x 32 pixels)

The results from Figure 5.1 show that for artificially generated realisations, average background noise subtraction prior to cross-correlation suppresses the background noise intensities to generate accuracy metrics that are comparable to the 'ideal' results.

5.2.2 Image thresholding

One of the simplest ways to remove background noise is to apply a global threshold across an interrogation region (Dellenback et al., 2000). To apply a relevant threshold, region pre-processing is required to obtain a background noise intensity value for both the first and second region. This can be achieved by calculating the distribution of the pixel intensities within each respective region. As with average background noise subtraction, a threshold value can be calculated either individually, per interrogation region, or averaged spatially across an image or temporally, between sequential interrogation regions.

Since background noise follows a Gaussian distribution, an initial threshold should approximate the maximum value of the noise distribution of the region. Figure 5.2 presents the average error plots as the global threshold value is increased from an initial pixel intensity of 40 to an intensity of 70 when each region has a mean background noise intensity of 15% of the total 8-bit output. The resulting interrogation regions are processed with SCC and NSS.

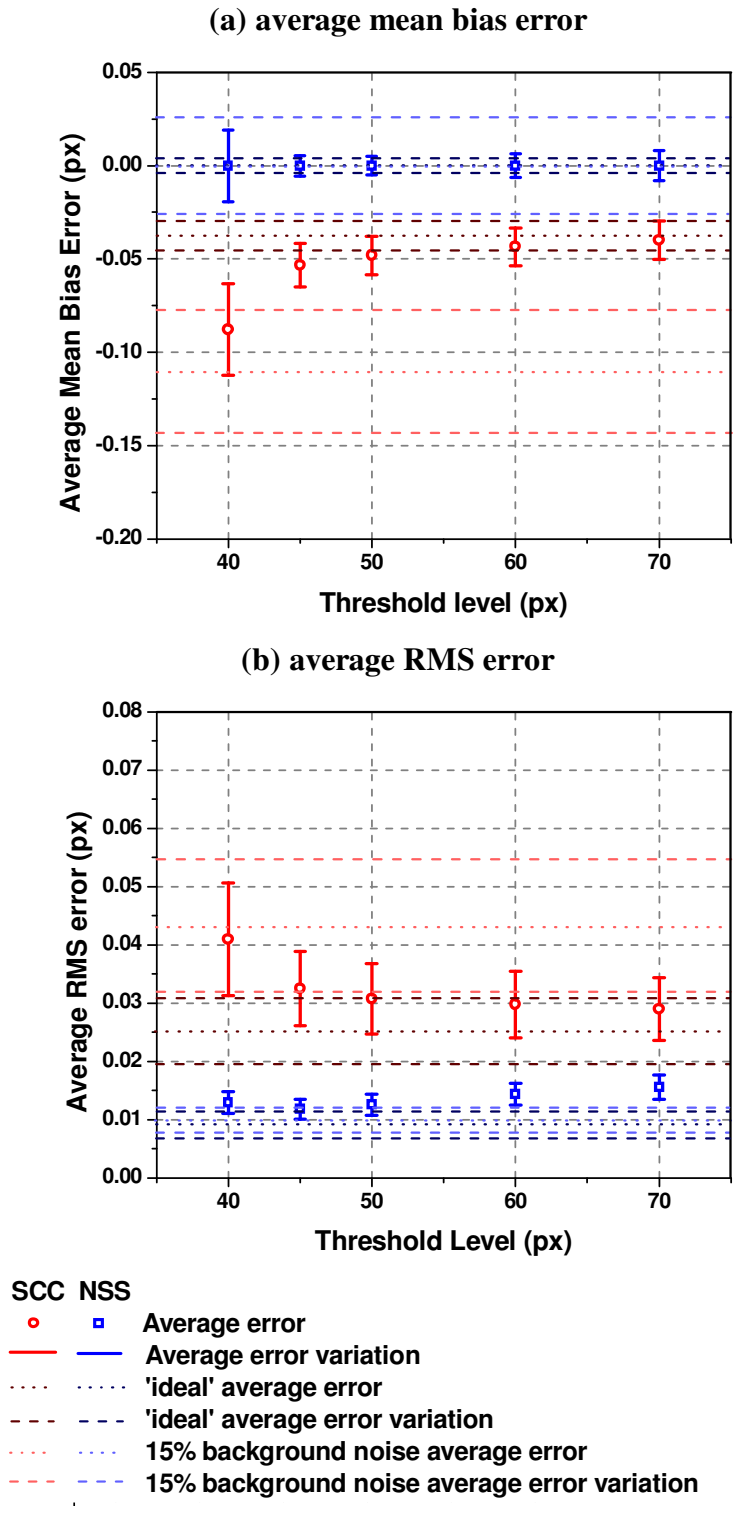

Figure 5.2 Average error plots for thresholded images comparing SCC and NSS results

The average error plots are calculated by averaging the respective accuracy metrics over the 8 pixel displacement range. The error bars provided with each averaged metric represents the variation in measurements (standard deviation) over the 8 pixel

range. The dashed lines represent the extent the average errors deviate by for when 'ideal' regions and regions containing a mean background noise at 15% of the 8-bit output are processed with SCC and NSS.

The average error plots shown in Figure 5.2 shows that by applying a threshold to regions containing background noise does not return the accuracy metrics to levels quantified when processing 'ideal' regions. When providing analysis with a threshold for regions that contain mean background noise intensities at 15% of the total 8-bit output it is reasonable to assume that a pixel value of 50 will be adequate to remove all background noise prior to analysis. The distribution of the background noise is shown in Figure 3.7 (p.50); this figure identifies that over 300 realisations the background noise distribution does not exceed a pixel value of 50. Although applying a threshold to regions prior to analysis does improve the accuracy over regions where no threshold is applied, a definitive threshold level that suppresses errors cannot be achieved in a single-pass (i.e. in one cross-correlation process). At least two or more passes are required to identify the threshold level that will provide the best accuracy. If the threshold level is too low significant levels of background noise will remain to detract from the accuracy of measurements. If the level is too high the threshold will start to impinge on the intensity content of particle images and thereby introduce peak-locking from inadequate particle image resolution.

In brief, the accuracy of measurements can be improved if a threshold is applied to each region to account for the presence of background noise. However, the optimum threshold level has to be iterated towards to obtain the most accurate measurements. For experimental analysis this is not possible without calibration.

5.2.3 Kernel subtraction

Rather than adjusting pixel intensities within each interrogation region using global statistics, as was proposed with other enhancement methods, kernel subtraction prior to cross-correlation obtains local statistics from within a given region (kernel) centred around each point of each interrogation region. The average intensity value, calculated within each kernel, is subtracted from the region pixel value around which the kernel is centred. Therefore this method does not require spatial or temporal averaging statistics, rather local intensity statistics across each region are calculated. Raffel et al. (2007) stated that each local region should be larger than the particle image diameter yet small enough to eliminate spatial variations in background noise. Therefore Figure 5.3 presents the average error plots when the average intensities are subtracted using kernels that are 5 x 5, 9 x 9, 13 x 13, 17 x 17 and 25 x 25 pixels in size when each region has a mean background noise intensity of 15% of the total 8-bit output. The resulting interrogation regions are processed with SCC and NSS. Each value is calculated in accordance with the average error plot of Figure 5.2.

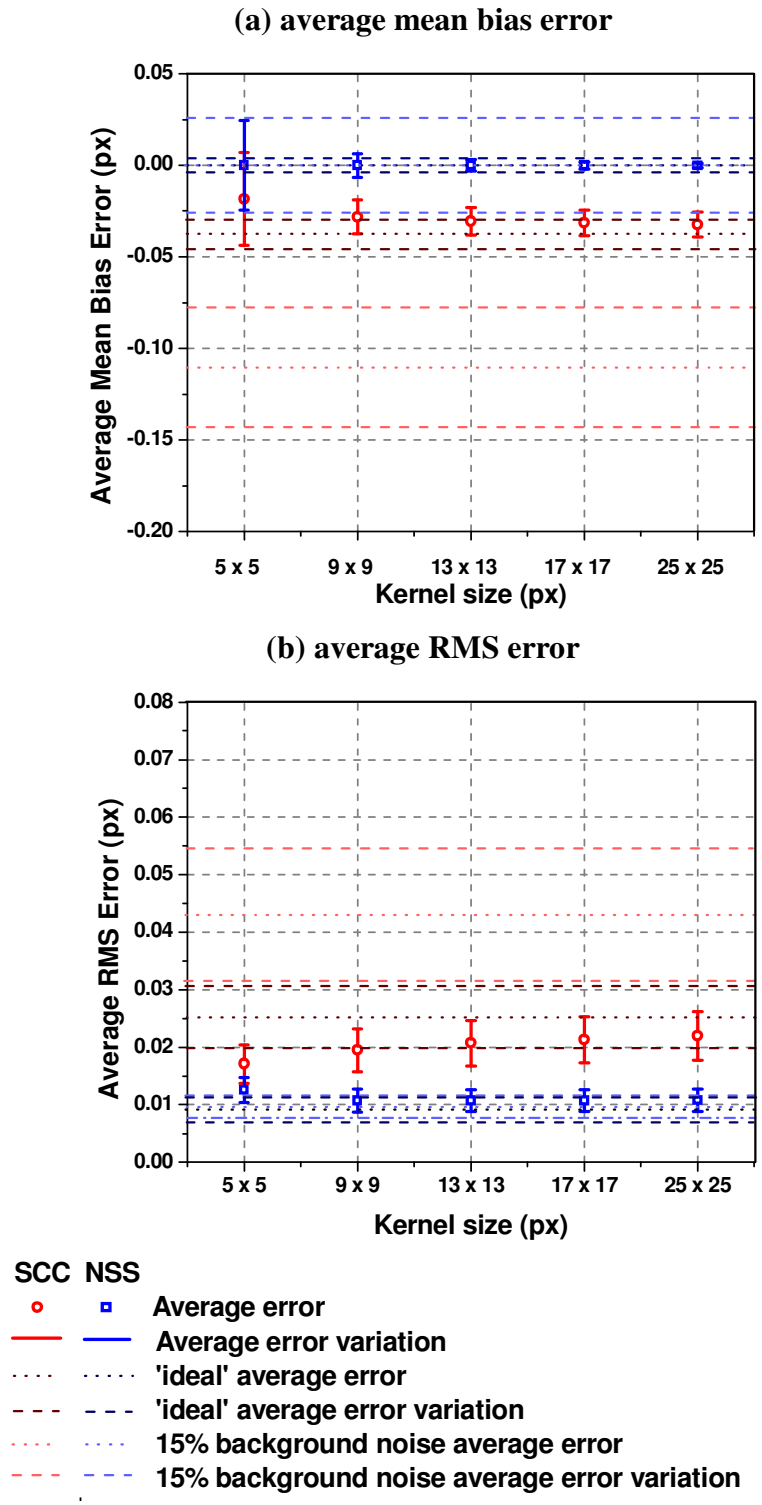

Figure 5.3 Average error plots for kernel subtraction comparing SCC and NSS results

The average error plots of Figure 5.3 identifies that as the kernel size increases the average mean bias error plot improves and provides mean bias errors that are comparable to those achieved through 'ideal' region processing when 25 x 25 pixel

kernels are used. However this is at the detriment of RMS error that deteriorates with increasing kernel size regardless of which processing algorithm is used.

The next section examines the effect a background noise differential across each interrogation region has on errors quantified using these image enhancement techniques whilst processing with SCC and NSS.

5.2.4 Image enhancements with background noise variations

The previous section provided errors quantified through image enhancement of regions that were processed with SCC and NSS to measure displacement. Each region contained a mean background noise distribution described by Figure 3.7 (p.50) that equates to 15% of the total 8-bit output. It was shown that each technique goes some way towards improving accuracy of results by removing background noise intensities. It was also identified that NSS provided better measurement statistics than SCC when background noise is suppressed because the algorithm compensates for the random distribution of particle images across each region including the presence of partial images that have an adverse effect on measurements. Errors quantified in this section are generated from artificial regions that have a step increase in the mean background noise intensity from 2% to 15% of the total 8-bit output as is illustrated in Figure 5.4. Displacement data-sets of artificial regions experiencing a uniform particle image displacement of up to 8 pixels are populated with the optimum imaging parameters are generated to contain this background noise intensity. Half of each region contains a mean background noise intensity of 2% with the other half containing a mean background noise at 15% of the total 8-bit output and describing the distribution provided in Figure 3.7 (p.50). This models a background noise differential across each interrogation region and therefore temporal average is required.

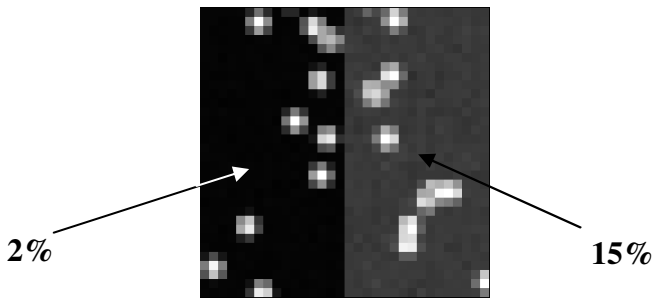

Figure 5.4 An interrogation region containing a step change in background noise from 2% to 15%

Figure 5.5 provides the mean bias error and RMS error plots generated by processing with SCC and NSS over a series of uniform particle image displacements for when an average background noise region is subtracted from each region within each displacement data-set. The average background noise region is calculated over 50 interrogation regions, which represents a temporal average across each region and between sequential regions. Average background noise subtraction results are compared to the SCC and NSS accuracy metrics generated by processing 'ideal' regions and regions that mean background noise intensities at 15% of the total 8-bit output.

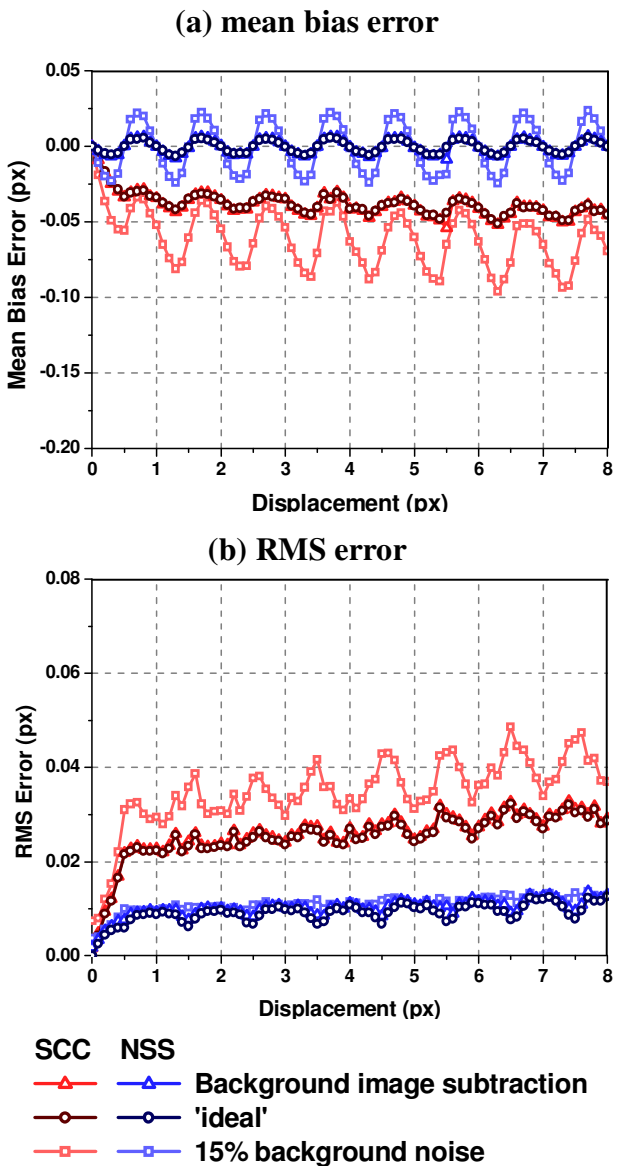

Figure 5.5 Error plots comparing 'ideal' region results and variations in background noise intensity across each region (2% and 15%) with mean background image subtraction for SCC and NSS (32 x 32 pixels)

The error plots generated in Figure 5.5 show that for artificially generated images, average background noise subtraction prior to cross-correlation suppresses the background noise intensities even when there is a background noise step increase across each interrogation region. Therefore the image enhanced error plots generate accuracy metrics that are comparable to their respective 'ideal' results for both processing algorithms. When there is a background noise differential across regions the average background noise intensity function compensates for this by subtracting local average background intensity values from each point across the region thereby suppressing background noise.

Although these error plots show a significant improvement from the background noise accuracy metrics toward the 'ideal' results it is noted that this image enhancement technique is dependent upon the background noise intensity being identical between and across images containing only background noise and those including particle images. The distributions can be controlled during artificial region generation and analysis but experimentally this is a lot harder to achieve. Variations in light intensity from each laser pulse, as well as misalignment, will affect the average background intensity function. This subsequently results in some background noise intensities being present in each region and consequently detracts from the accuracy of measurements.

Figure 5.6 presents the average error plots as the global threshold value is increased from an initial pixel intensity of 40 to an intensity of 70 when each region has a mean background noise step increase from 2% to 15% of the total 8-bit output. The resulting interrogation regions are processed with SCC and NSS.

(a) mean bias error

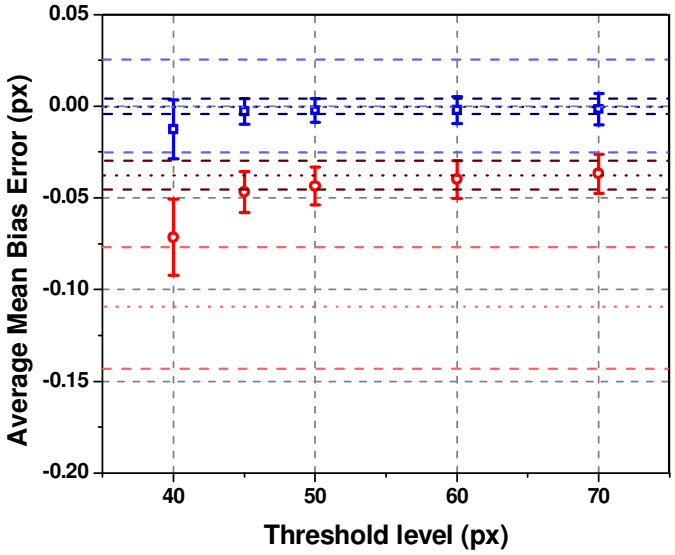

(b) RMS error

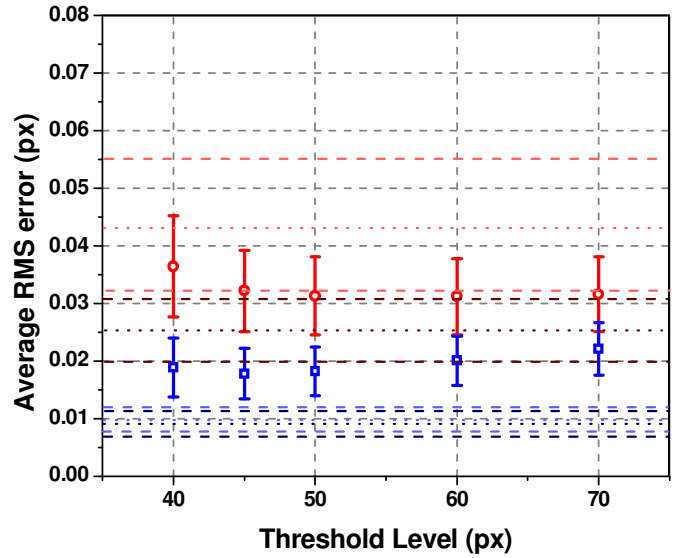

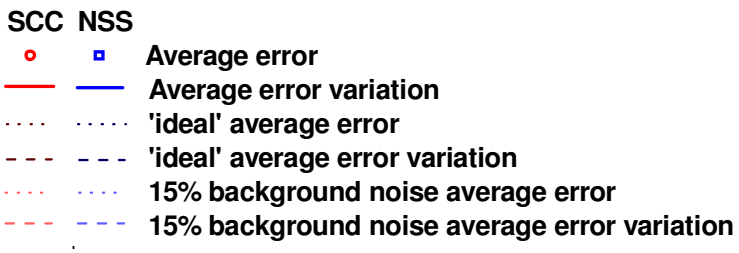

Figure 5.6 Average error plots for thresholded images with varying the background noise across each region (2% and 15%) comparing SCC and NSS results

The average error plots provided by Figure 5.6 shows that by applying a threshold to regions containing background noise does not return the accuracy metrics to levels

quantified with 'ideal' regions. Since thresholding in its simplest form is a global image enhancement technique then this, as with the average error plots generated from thresholding regions that contain a mean background noise intensity of 15% of the total 8-bit output (Figure 5.2), will require an initial threshold value of 50 to remove all background noise prior to analysis. As was stated when uniform background noise distributions were analysis, applying a threshold to regions prior to analysis does improve the accuracy over regions where no threshold is applied. However, applying a threshold of 50 to the area of the region experiencing a mean background noise intensity of 2% will introduce peak-locking into analysis. The threshold level will start to impinge on the intensity content of each particle image. This will therefore generate a significantly larger RMS error than when a mean background noise intensity of 15% of the total 8-bit output is distributed across each region as is shown by comparing Figure 5.2(b) with Figure 5.6(b).

Figure 5.7 presents the average error plots when the average intensities are subtracted using kernels that are 5 x 5, 9 x 9, 13 x 13, 17 x 17 and 25 x 25 pixels in size when each region has a mean background noise intensity increase from 2% to 15% of the total 8-bit output. The resulting interrogation regions are processed with SCC and NSS.

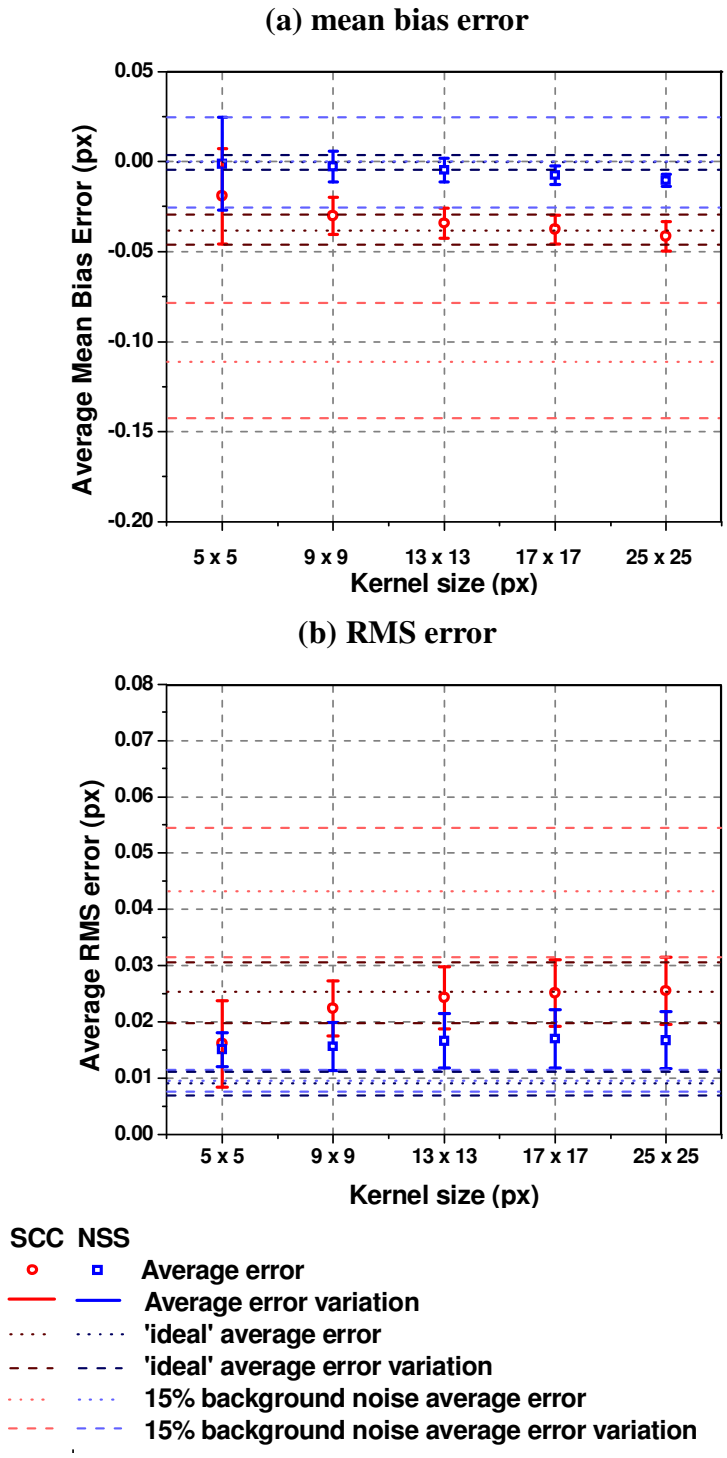

Figure 5.7 Average error plots for kernel subtraction with varying the mean background noise across each region (2% and 15%) comparing SCC and NSS results

Figure 5.7(a) identifies that as the kernel size is increased from 5 x 5 pixels towards 25 x 25 pixels there is an underlying underestimation in measurements. This shows that kernel subtraction prior to cross-correlation is not the preferred technique when there is

a background noise step increase across each interrogation region. This is also evident in Figure 5.7(b) which shows a deviation away from 'ideal' RMS error results and a deterioration in results presented in Figure 5.3 when each region contains a mean background noise intensity of 15% of the 8-bit output.

In summary, this section has examined the effect three image enhancement techniques have on the quantification of error statistics when processing with SCC and NSS. It has been shown that average background noise subtraction and global thresholding provide accuracy metrics that are comparable to 'ideal' results. However, background noise image subtraction is dependent on the background noise regions having an identical background noise as the regions that contain particle images. When applying an image threshold, a definitive threshold level that minimises errors cannot be achieved in a single-pass. Although kernel subtraction is not dependent on these relationships the enhancement technique is able to suppress uniformly distributed background noise across each interrogation region. However, there is an underlying underestimation in measurements when a step increase in the background noise intensity is present across an interrogation region; therefore this is not a preferred image enhancement technique for DPIV prior to processing each interrogation region.

The next section will identify and examine a new, robust processing algorithm that is able to compensate for background noise intensities, including noise differentials (step increases), to provide error plots that are comparable to those generated through NSS processing of 'ideal' artificial regions without requiring prior knowledge of the image quality.

5.2.5 Mean intensity subtraction prior to cross-correlation, $R_{MS}(m,n)$

Westerweel (1997) initially introduced the processing algorithm 'mean intensity subtraction prior to cross-correlation' (expressed in equation 5.1) as a method of providing accurate measurements over that of SCC. Section 2.8.4 (p.29) identified that this processing algorithm did not significantly improve either accuracy metric when analysing 'ideal' artificial interrogation regions.

$$R_{MS}(m,n) = \sum_{i=0}^{M}\sum_{j=0}^{N}\left[I_1(i,j) - \bar{I}_1 \right]\left[I_2(i-m, j-n) - \bar{I}_2 \right] \qquad \textbf{5.1}$$

This processing algorithm subtracts a global mean intensity value from each point within an interrogation region; if an individual intensity value within an interrogation region is smaller than the average intensity the point is set to zero (Pust, 2000). Provided that the background noise intensity is less than the average value the background noise can be regarded as being zero and therefore does not contribute to the correlation field. Figure 5.8 shows the error plots generated when processing interrogation regions with varying levels of background noise per data-set for a series of uniform particle image displacements using $R_{MS}(m,n)$. These results are compared to those generated using SCC.

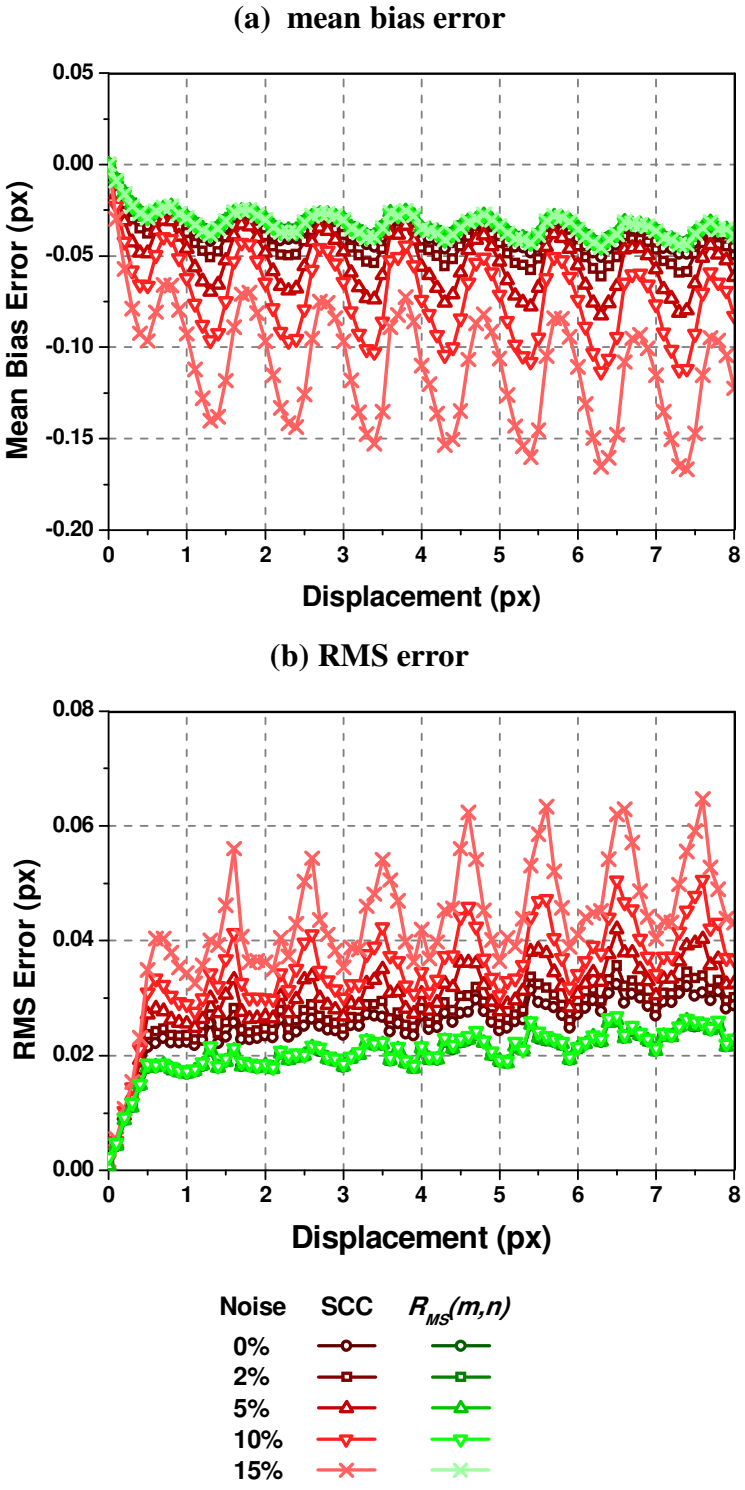

Figure 5.8 Error plots comparing SCC with $R_{MS}(m,n)$ with increasing background noise intensities (32 x 32 pixels)

The figure clearly shows an improvement to both accuracy metrics on the application of $R_{MS}(m,n)$ when analysing artificial regions that contain background noise. The algorithm successfully compensates for background noise to provide an accuracy that is

consistent with the results generated through SCC of 'ideal' regions. Therefore subtracting the mean intensity prior to cross-correlation is a more robust approach to DPIV processing over the standard procedures as it is able to compensate for the inclusion of background noise intensities in interrogation regions.

$R_{MS}(m,n)$ calculated by subtracting a global mean intensity from each point of across an interrogation region assumes that the background noise is uniformly distributed over each region. In reality there are variations in the distribution of background noise across each region that affects the quality of the image being analysed. Therefore, rather than subtracting a global mean intensity from each region an alternative solution is proposed. This involves calculating a local mean intensity from within the overlapped area as each point of the $R_{MS}(m,n)$ correlation field is computed. This means that any local variations in intensity are accounted for and then subtracted from each pixel that contributes to each point of the correlation field. The approach of calculating a local mean intensity within the overlapped area is also consistent with the computation of the signal strength function; this calculates the signal intensity within the overlapped area to account for variations in pixel intensities across an interrogation region and has been shown to improve both accuracy metrics. The method of normalising the $R_{MS}(m,n)$ correlation field with signal strength is studied further in section 5.2.6. Figure 5.9 shows the error plots generated from regions containing a mean background noise intensity at 15% of the total 8-bit output processed with $R_{MS}(m,n)_{\text{global}}$ (global mean intensity subtraction) and $R_{MS}(m,n)_{\text{local}}$ (subtraction of the mean intensity within the overlapped area) and are compared to SCC results from 'ideal' artificial regions.

(a) mean bias error

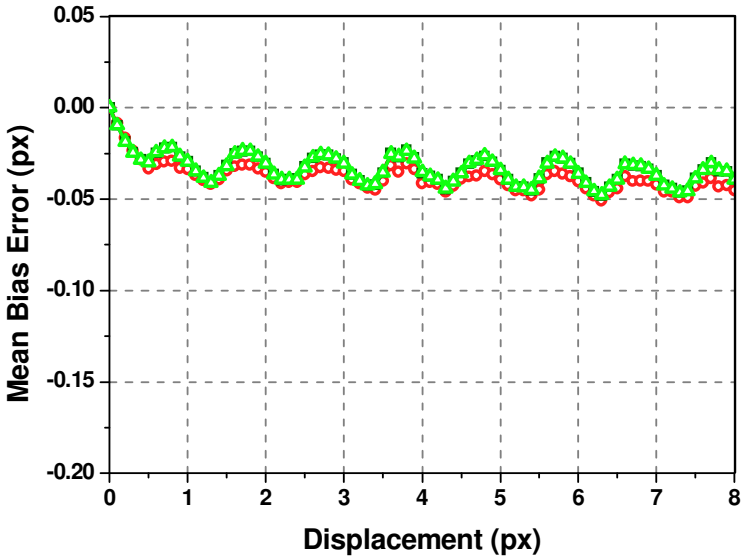

(b) RMS error

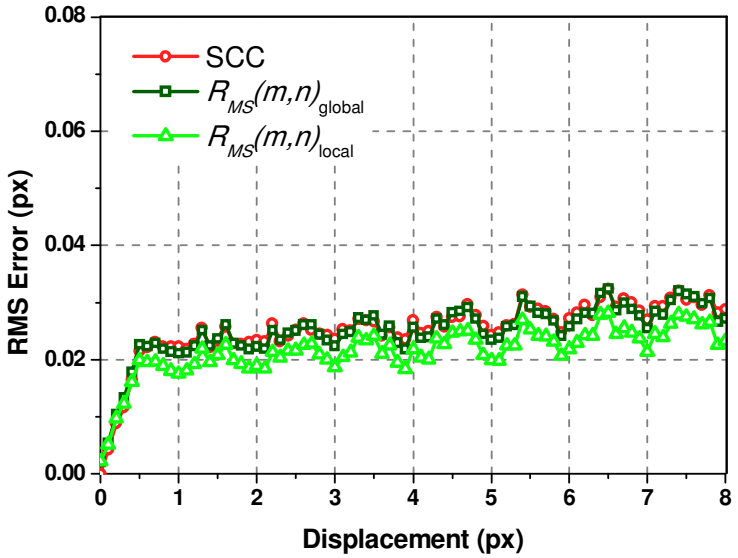

Figure 5.9 Error plots comparing SCC (0% background noise) with $R_{MS}(m,n)_{global}$ and $R_{MS}(m,n)_{local}$ (15% background noise) (32 x 32 pixels)

The figure clearly shows that a mean background noise intensity of 15% of the total 8-bit output is suppressed using both $R_{MS}(m,n)$ methods to provide error plots that are consistent with the SCC results from 'ideal' artificial regions. Figure 5.9(b) also highlights that RMS error is marginally improved if the local mean subtraction approach is used. For this reason and because calculating a local mean intensity within the overlapped area is justified by the computation of the signal strength function (also calculated within the overlapped area) then this method is used here on in. Nevertheless, although $R_{MS}(m,n)$ is able to suppress background noise to provide error

plots consistent with the SCC of 'ideal' regions this algorithm is not able to compensate for the random distribution of particle images. This is shown in Figure 5.9(a); all displacements are underestimated indicating that partial images are not accounted for when using $R_{MS}(m,n)$. Figure 5.9(b) provides a higher RMS error than that of Figure 4.5 (p.75) where the variations caused by the cross-correlation of unrelated particle images are accounted for by the signal strength function. The next section introduces an improved and robust processing algorithm able to suppress both the background noise and the random distribution of particle images across each interrogation region. It is shown that this new technique is able to provide accuracy metrics that are comparable to NSS results computed using 'ideal' interrogation regions (Figure 4.5) for regions that contain various background noise intensities.

5.2.6 Normalising the $R_{MS}(m,n)$ correlation field by signal strength

The previous section proposed that mean intensity subtraction prior to cross-correlation could compensate for background noise within each interrogation region. This routine however could not compensate for the random distribution of particle images that also affects the accuracy metrics. However, their presence is compensated for if the correlation field is normalised by the signal strength that contributes to each point of the correlation field. Therefore this section introduces an improved and robust processing algorithm that is able to compensate for both background noise and the random distribution of particle images. This routine is termed mean intensity subtraction prior to $R(m,n)$ cross-correlation normalised by signal strength, $R_{MSSS}(m,n)$ and is defined as:

$$R_{MSSS}(m,n) = \frac{\sum_{i=0}^{M}\sum_{j=0}^{N}\left[I_1(i,j)-\bar{I}_1(m,n)\right]\left[I_2(i-m,j-n)-\bar{I}_2(m,n)\right]}{\left[\sum_{i,j\in A} I_1^2(i,j)\times\sum_{i,j\in A} I_2^2(i,j)\right]^{1/2}} \qquad \textbf{5.2}$$

where A denotes the overlapped area between I_1 and I_2 as the correlation field is generated. The mean intensity values $\bar{I}_1(m,n)$ and $\bar{I}_2(m,n)$ are defined as the mean intensities from regions $I_1(i,j)$ and $I_2(i,j)$. These mean intensity values are calculated for each point that contributes to the correlation field (i.e. within the overlapped area). If, on subtraction of the mean intensity from each individual value results in an intensity that is less than zero then the intensity for that point is set to zero (Pust, 2000). As with section 4.3.2 (p.75), the signal strength function is defined as the sum of the particle image intensities within the overlapped area between regions $I_1(i,j)$ and $I_2(i,j)$ as cross-correlation commences in the spatial domain.

Figure 5.10 compares the error plots generated when 'ideal' artificial interrogation regions (no background noise) are processed using SCC, NSS and $R_{MSSS}(m,n)$ for a series of uniform particle image displacements.

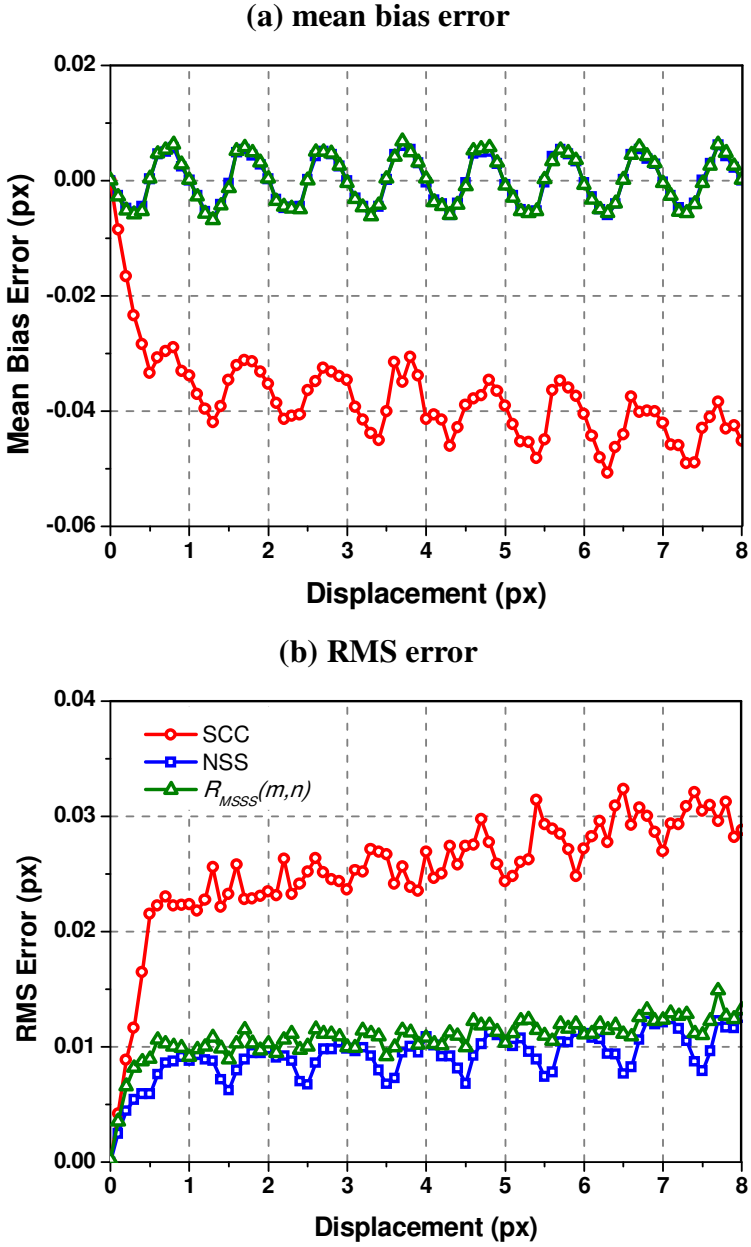

Figure 5.10 Error plots comparing SCC, NSS and $R_{MSSS}(m,n)$ (32 x 32 pixels)

The error plots show that NSS and $R_{MSSS}(m,n)$ have comparable mean bias error results. This occurs because the signal strength function, in both instances, compensates for the presence of partial images that cause the underestimation in measurements. When investigating the RMS error plots for each routine it is clear that NSS fractionally outperforms $R_{MSSS}(m,n)$ to generate lower RMS errors. However both techniques correct for the random distribution of particle images that causes measurement

variations. The slight increase in RMS error when processing with $R_{MSSS}(m,n)$ is caused by the subtraction of the local mean intensity value from within the overlapped area. This affects the Gaussian intensity distribution of each particle image which subsequently causes a slight increase in RMS error.

The advantage of analysing with $R_{MSSS}(m,n)$ becomes apparent when processing artificial regions that contain various intensities of background noise as described in section 3.8 (p.49). The mean bias and RMS error plots for this analysis are presented in Figure 5.11. As was discussed in section 4.5 (p.93), the addition of background noise causes large deviations in the mean bias cyclic pattern for both SCC and NSS, yet $R_{MSSS}(m,n)$ does not provoke such a response.

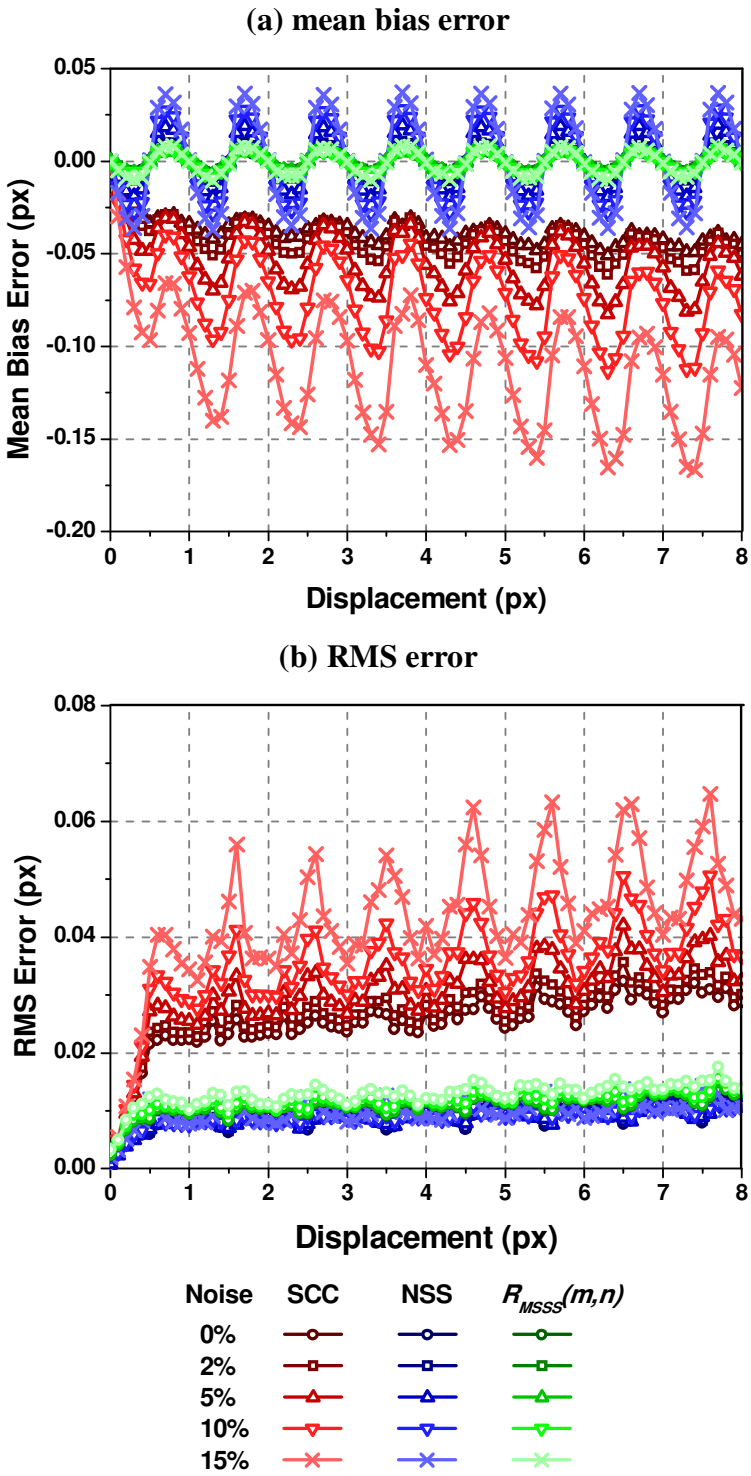

Figure 5.11 Error plots comparing SCC, NSS and $R_{MSSS}(m,n)$ with increasing background noise intensities (32 x 32 pixels)

The next section identifies why $R_{MSSS}(m,n)$ is a robust processing algorithm able to provide accuracy metrics that are comparable to those generated through NSS processing of 'ideal' regions when background noise intensities are introduced.

5.2.7 $R_{MSSS}(m,n)$ with background noise

Figure 5.12 shows the cross-sectional view through the $R_{MSSS}(m,n)$ correlation peak in the x-direction and is averaged over 300 realisations for when the mean background noise intensity is increased. The displacement data-set is experiencing a uniform particle image displacement of 4.3 pixels in the x-direction. Unlike the average correlation peaks processed using SCC and NSS (Figure 4.19, p.95) which showed an increase in the magnitude of the correlation noise floor with increasing background noise intensity, this processing algorithm suppresses the correlation noise floor as the background noise intensity increases.

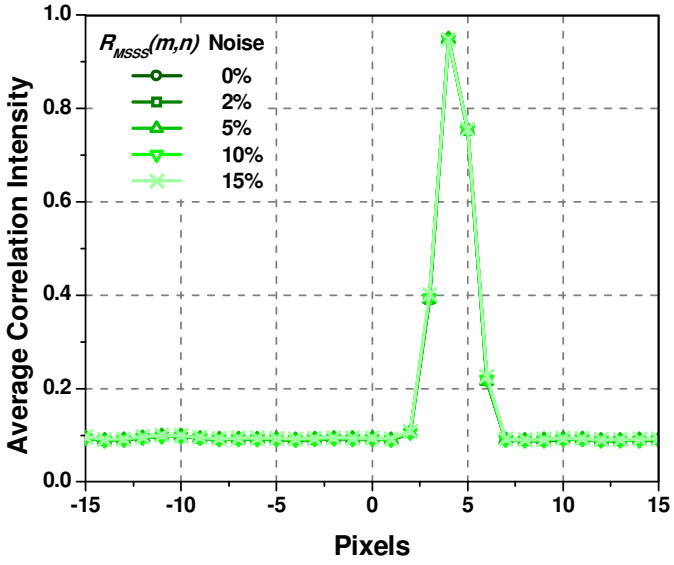

Figure 5.12 Average $R_{MSSS}(m,n)$ correlation field with varying background noise

When using $R_{MSSS}(m,n)$, the average correlation energy has the same magnitude regardless of the background noise. This is shown in Figure 5.12 as both the noise floor and the correlation peak magnitude are maintained at approximately the same level as the background noise intensity increases. This is typical for all x-direction displacements since the error plot in Figure 5.11 shows negligible mean bias oscillation.

As was stated previously, normalising the SCC field by the signal strength compensates for the random distribution of particle images across each interrogation region to reduce variations between measurements. As Figure 5.11(b) shows, NSS also compensates for the addition of background noise with respect to the RMS error results. This is because the technique normalises the correlation field by the pixel intensities that contribute to

the field, therefore compensating for both particle image distribution and the additional background noise. Although the addition of a correlation noise floor subsequently increases the mean bias error oscillation, the variations between measurements remains small when compared to SCC results.

This is illustrated in Figure 5.13; this shows the cross-sectional view through the correlation peak to show the *x*-direction displacement and is averaged over 300 realisations for (a) no background noise and (b) a mean background noise intensity at 15% of the total 8-bit output whilst experiencing an actual uniform displacement of 4.3 pixels in the *x*-direction and processed using $R_{MSSS}(m,n)$. The variations between individual correlation peaks over the 300 realisation data-set are also shown in Figure 5.13 as deviation error bars.

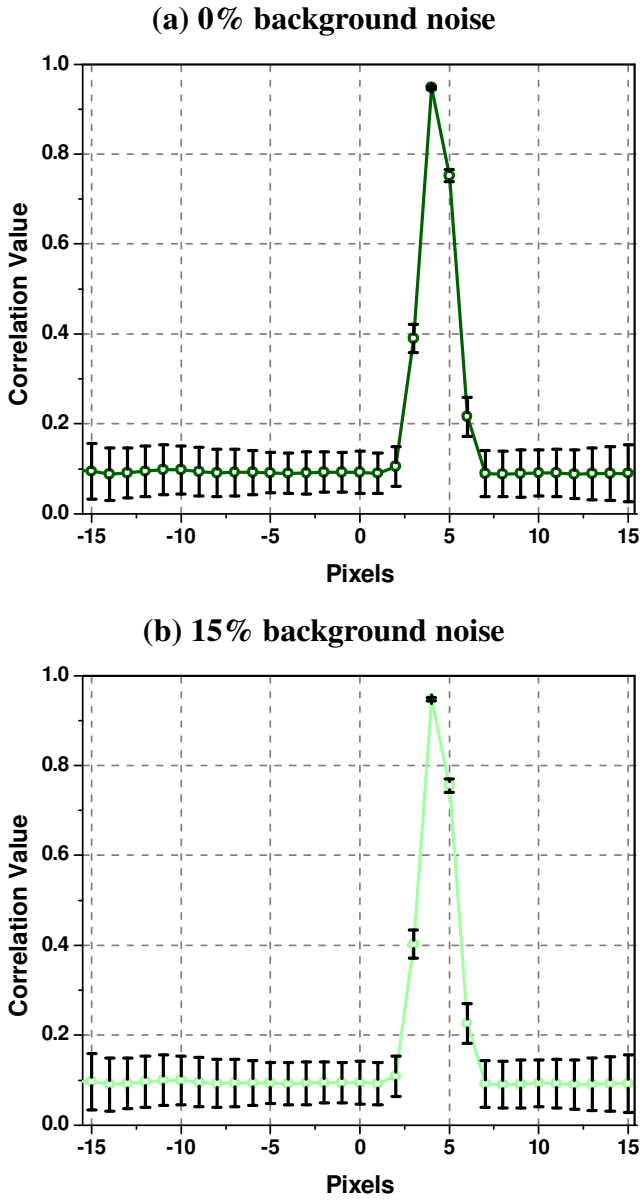

Figure 5.13 Average $R_{MSSS}(m,n)$ correlation fields for a 4.3 pixels displacement with error bars

The figure highlights that with increasing noise intensity the magnitudes of the correlation peak and the noise floor are maintained. This thereby maintains the ratios between the three correlation peak values used to calculate the sub-pixel location of the correlation peak. The figure also illustrates that the variation in correlation peak shape remains similar with increasing displacement. This is demonstrated by the similar magnitudes of the error bars used to describe the deviation in correlation field values over the 300 realisations. The consistent variation between data-sets with increasing background noise intensity is shown across all displacements in Figure 5.11(b) as an

RMS error comparable to that generated by the NSS algorithm. Also, since the $R_{MSSS}(m,n)$ algorithm compensates for background noise, the cyclic RMS error 'beating' pattern identified with SCC and NSS with increasing background noise intensity is now negligible.

In summary, this section has shown that $R_{MSSS}(m,n)$ is a robust algorithm able to provide accuracy metrics for a series of mean background noise intensities of up to 15% of the total 8-bit output, that are comparable to processing 'ideal' artificial regions using NSS. The algorithm suppresses the increase in the correlation noise floor that, in this instance, is caused by the addition of the background noise within each region. This thereby maintains the ratios between the three correlation peak values used to define the sub-pixel location of the correlation peak. Following mean intensity subtraction, normalising by signal strength suppresses both accuracy metrics by accounting for the random distribution of particle images across each interrogation region that causes RMS errors and partial images that cause measurement underestimations.

Having shown that $R_{MSSS}(m,n)$ provides robust accuracy metrics up to a mean background noise intensity at 15% of the total 8-bit output, Figure 5.14 shows the error plots generated when each region within the data-set is saturated with mean background noise intensities of up to 30% of the total 8-bit output.

(a) mean bias error

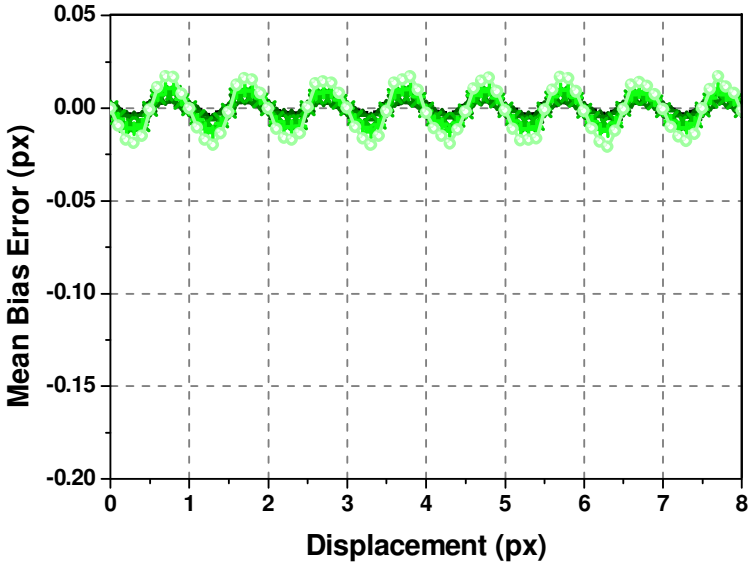

(b) RMS error

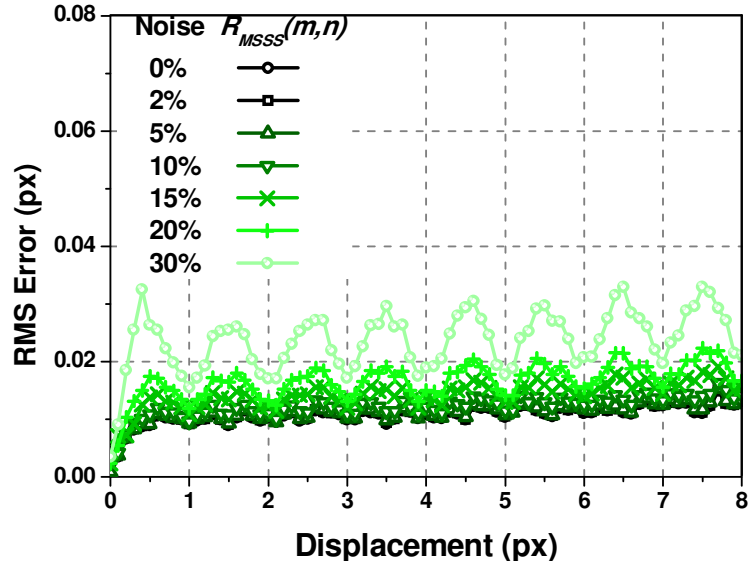

Figure 5.14 $R_{MSSS}(m,n)$ error plots for background intensities up to 30% (32 x 32 pixels)

From the figure it is evident that as the mean background noise increases further to 30% of the 8-bit output there is an increase in both the mean bias error oscillation and the cyclic pattern is present in the RMS error results. At this high level of background noise the particle images become fully saturated (i.e. each point of a particle image has a grey-scale value approaching 256). Therefore as the image quality deteriorates subtraction of the mean intensity within the overlapped area cannot properly reconstruct the Gaussian intensity distribution of each particle image resulting in an increase of both accuracy metrics. Also with a high background noise intensity the

$R_{MSSS}(m,n)$ algorithm is not able to fully suppress the background noise to leave just the particle images for processing; therefore the correlation noise floor will increase in magnitude. This subsequently affects the ratios between the three central correlation peak values used to evaluate the *x*-displacement and thereby increases the magnitude of the mean bias error oscillation.

Quantifying the systematic errors within DPIV processing requires data-sets of artificial interrogation regions experiencing a series of known uniform displacements. This ignores particle images moving through the laser sheet and out-of-focus particle images that will still contribute to the correlation field. Figure 5.15 quantifies the accuracy metrics provided by data-sets of interrogation regions describing a known uniform displacement that includes 6 extra in-focus, but unrelated, particle images. Each data-set is processed using SCC, NSS and $R_{MSSS}(m,n)$. The addition of these unrelated particle images is equivalent to a turbulent flow which introduces a third velocity component into analysis. Furthermore, each data-set contains increasing mean background noise intensities. Since the background noise introduces unrelated pixel intensities into each correlation field this can be assumed to be the contribution from out-of-focus particle images in addition to electronic noise to describe the overall background noise.

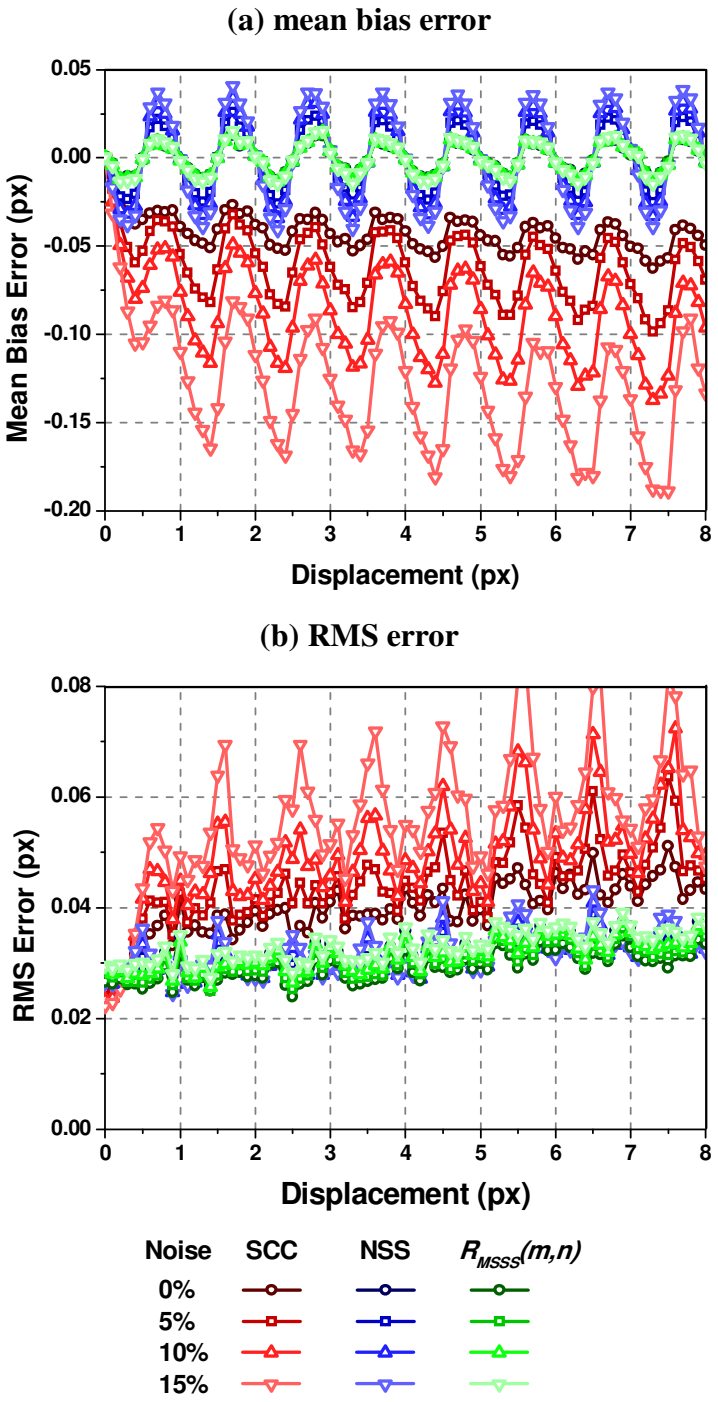

Figure 5.15 Error plots comparing SCC, NSS and $R_{MSSS}(m,n)$ with 6 additional unrelated particle images and increasing background noise intensities (32 x 32 pixels)

When comparing this figure with Figure 5.11 it is clear that the addition of 6 extra, but unrelated, particle images into each realisation affects both accuracy metrics. When describing the influences on mean bias error the underestimation of measurements shown with SCC processing results from the cross-correlation of partial images. This is

subsequently suppressed when the processing function is normalised by signal strength. Figure 5.15(a) shows that on processing with SCC and NSS the mean bias error oscillation increases in amplitude as the background noise intensity increases between data-sets. This is to be expected since the cross-correlation of unrelated particle images introduces a correlation noise floor; the cross-correlation of background noise will subsequently increase its magnitude. As there is an additional 6 unrelated particle images per region then this will inherently increase the magnitude of the correlation noise floor and thereby affect the ratio between the three central correlation peak values used to define its sub-pixel location. When processing with $R_{MSSS}(m,n)$ the effects of background noise are suppressed. This therefore provides a mean bias error comparable to that generated through NSS processing of 'ideal' regions for each data-set that contains regions with increasing background noise intensity.

The cross-correlation of unrelated particle images causes an asymmetry in the correlation peak. As each region contains an extra 6 unrelated particle images then this will increase the RMS error for each of the processing algorithms. As the background noise intensity increases SCC generates RMS error plots that contain the background noise cyclic 'beating' pattern. Peak values occur at half-pixel displacements because each correlation peak is located between two points on the correlation peak. The addition of background noise causes large variations at these points skewing the correlation peak either positively or negatively. As the correlation noise floor magnitude increases the ratios between the three central correlation peak values decreases; this amplifies measurement variations resulting in large RMS errors. As both the NSS and $R_{MSSS}(m,n)$ algorithm use the signal strength function to compensate for the random distribution of pixel intensities across each interrogation region (i.e. particle images and background noise) then the variation in correlation peak shape is reduced thereby providing measurements with less variations for each displacement data-set to suppress RMS error.

This section has demonstrated the performance of $R_{MSSS}(m,n)$ in comparison with SCC and NSS for commonly used interrogation regions of 32 x 32 pixels in size. It illustrates that this is a robust algorithm that is able to account for mean background noise intensities of up to 15% of the total 8-bit output. It has been highlighted that

$R_{MSSS}(m,n)$ is able to provide mean bias and RMS errors that are comparable to processing 'ideal' artificial region using NSS, without prior knowledge of the image and background noise quality. The next section will investigates the effect of introducing a step increase in background noise intensity across each interrogation region on the accuracy of measurements when processing with $R_{MSSS}(m,n)$.

5.2.8 Background noise variations with $R_{MSSS}(m,n)$

Section 5.2.1 to 5.2.4 investigated the effect three image enhancement techniques had on the accuracy metrics for artificial interrogation regions containing a mean background noise intensity of 15% and regions with a step increase in background noise from 2% to 15% of the 8-bit output. It was identified that average background image subtraction and global thresholding provided accuracy metrics that were comparable to 'ideal' NSS results when the mean background noise is uniformly distributed throughout each interrogation region. However, it was highlighted that the average background noise subtraction method was dependent upon identical background noise distributions between regions used to calculate the average background function and regions used to extract velocity statistics. It was also noted that the optimal threshold value used to minimise errors requires two or more passes before the best solution can be obtained.

The error plots provided in Figure 5.16 is generated through $R_{MSSS}(m,n)$ analysis of data-sets of regions that contain step increases in the mean background noise intensity (half the area of a region containing one distribution) whilst particle images within each displacement data-set are experiencing a series of uniform displacements up to 8 pixels at a resolution of one-tenth of a pixel. The step increases in the mean background noise intensity include: 2% with 15%, 5% with 15% and 10% with 15% of the maximum value intensity. These results are compared to the $R_{MSSS}(m,n)$ processing of 'ideal' regions and regions that contain a mean background noise intensity at 15% of the total 8-bit output across each interrogation region.

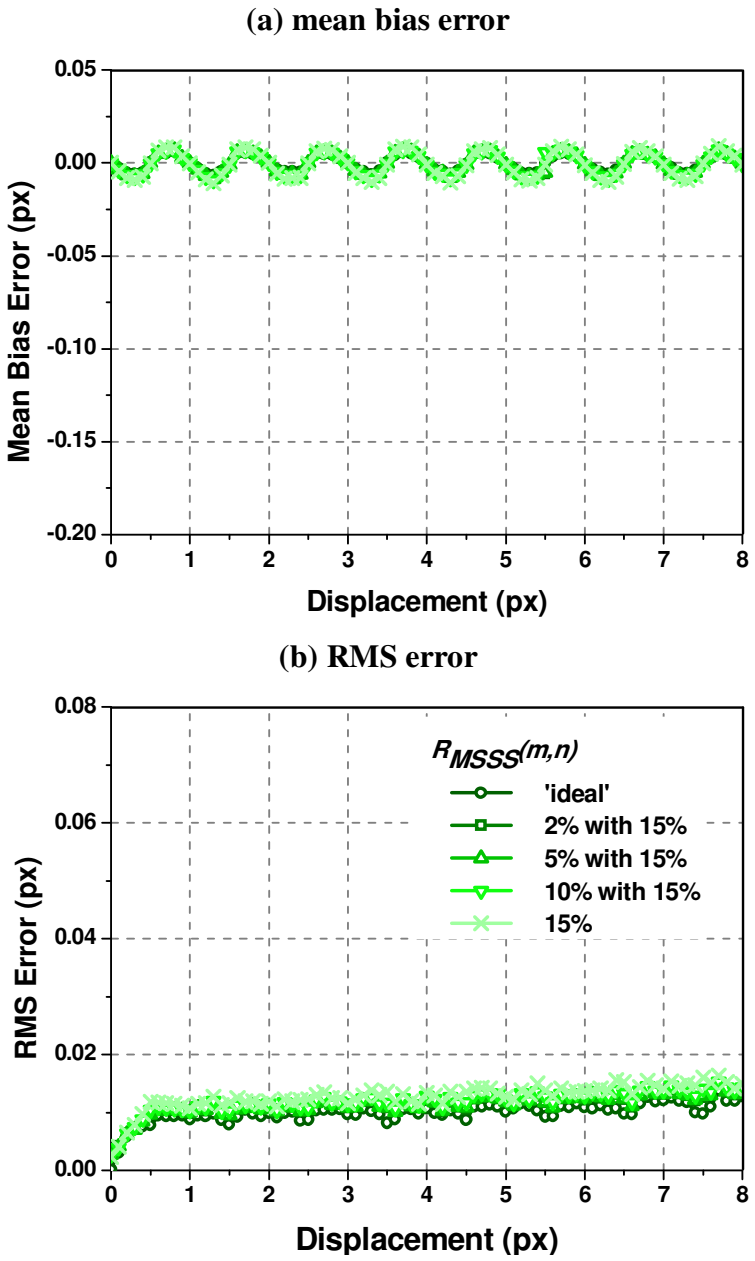

Figure 5.16 $R_{MSSS}(m,n)$ error plots for varying background intensities across each interrogation region (2% and 15%) (32 x 32 pixels)

The figure highlights that the $R_{MSSS}(m,n)$ algorithm is able to account for the step increase in background noise intensity to provide accuracy metrics that are comparable to those generated through 'ideal' region processing using NSS. Therefore $R_{MSSS}(m,n)$ should be the preferred algorithm used for DPIV processing since subtracting the background noise within the overlapped area during cross-correlation accounts for variations in background noise across each interrogation region and the signal strength function compensates for the random distribution of particle images across each region, including partial images to thereby suppress both mean bias and RMS error.

5.3 Alternative sub-pixel estimators

Although the previous sections have identified that the accuracy of measurements are dependent on the cross-correlation algorithm used for analysis, the sub-pixel estimator also plays a pivotal role in error quantifications. Westerweel (1993a) stated that the Gaussian estimator is superior to both the centroid (equation 2.3) and parabolic estimators (equation 2.4) as it produces the lowest measurement errors of the three sub-pixel estimators examined. This section presents the error plots from SCC, NSS and $R_{MSSS}(m,n)$ processing of artificial realisations experiencing a uniform displacement while approximating measurements using the centroid (Figure 5.17) and parabolic estimators (Figure 5.18). Results are also provided for when each displacement data-set experiences mean background noise intensities of up to 15% of the 8-bit output.

(a) mean bias error

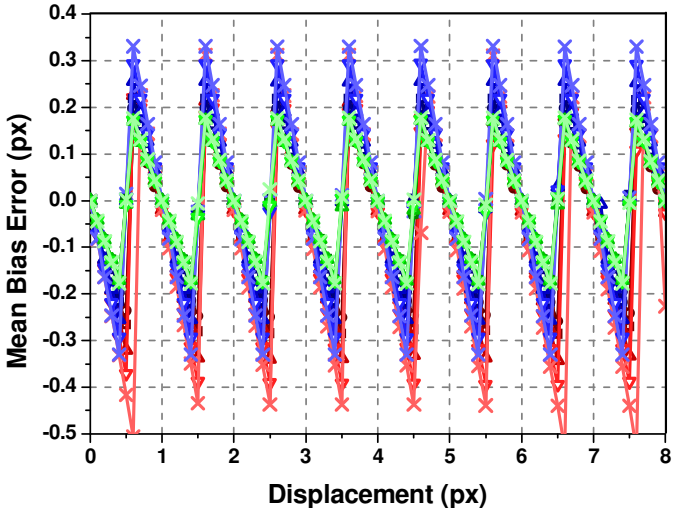

(b) RMS error

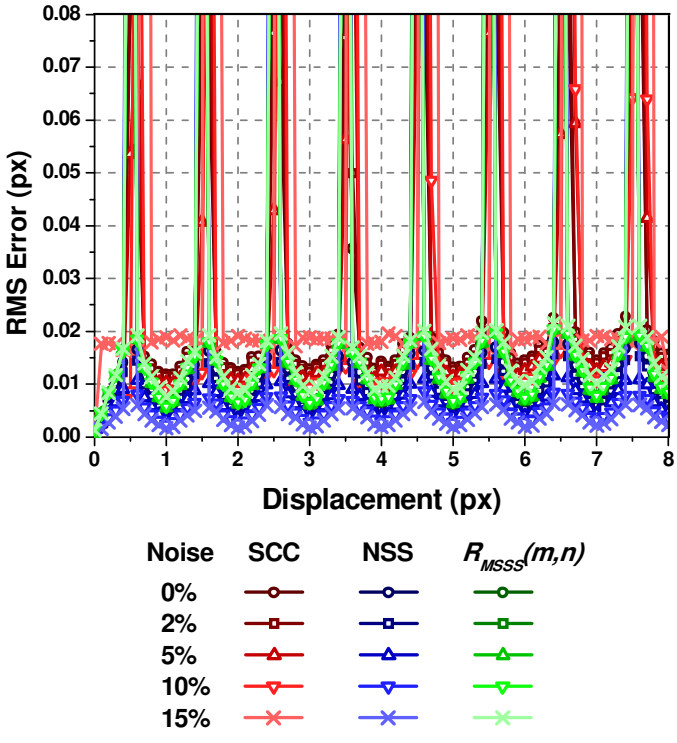

Figure 5.17 Error plots for SCC, NSS and $R_{MSSS}(m,n)$ using the centroid estimator

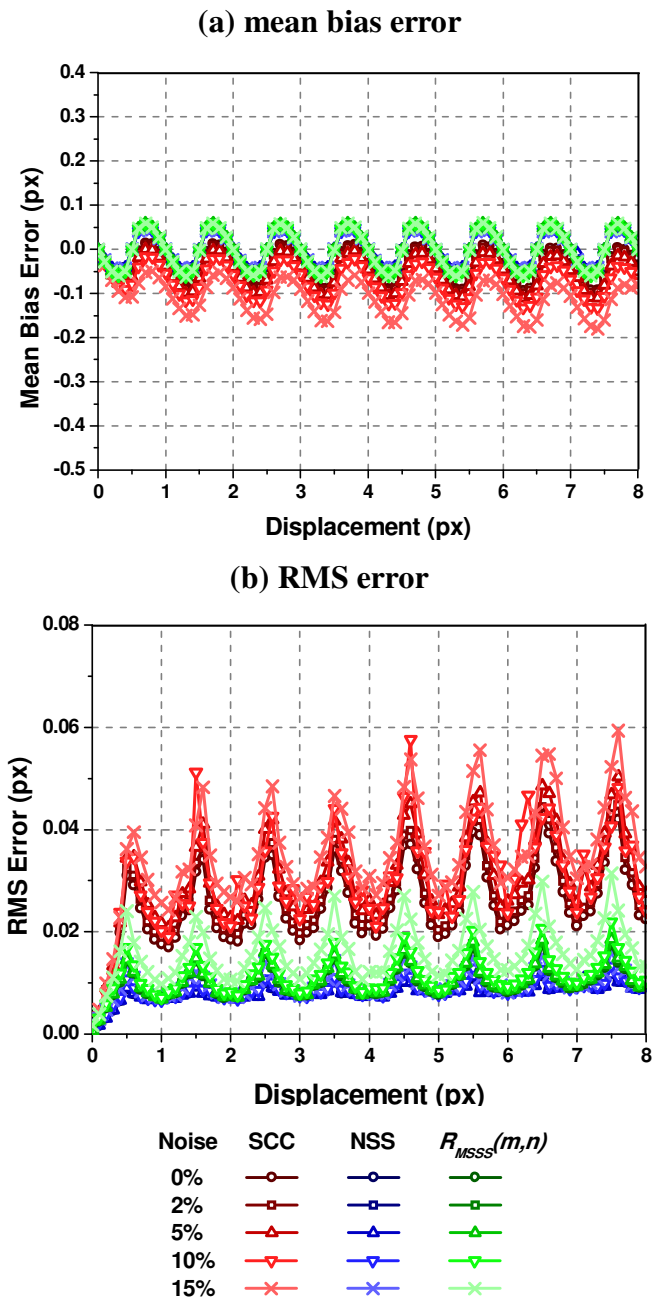

Figure 5.18 Error plots for SCC, NSS and $R_{MSSS}(m,n)$ using the parabolic estimator

Comparing the accuracy metrics from the centroid and parabolic peak estimators (Figure 5.17 and Figure 5.18) with that of the Gaussian sub-pixel estimator (Figure 5.11) it is obvious that the Gaussian sub-pixel provides superior measurements over the other two methods. When investigating the mean bias errors generated through applying the centroid and parabolic peak estimators it is apparent that their results are not as sensitive to the effects of increasing the background noise intensity as the Gaussian estimator. However, overall the two alternative estimators provide worse

estimations as the background noise intensity increases than the Gaussian estimator. On a RMS error basis, the parabolic estimator generates similar results for SCC cross-correlation using the Gaussian sub-pixel estimator, but once the correlation field has been normalised the Gaussian sub-pixel estimator provides superior precision. The RMS errors using the centroid estimator shows a significant increase in magnitude for each $n+0.4$ to $n+0.6$ pixel displacement (where n is the integer pixel displacement). Although the scale of the RMS error plots does not contain these maximum values (the scale is the same for all error plots to maintain continuity and ease of comparison) the maximum RMS values are approximately 0.8 pixels at half-pixel displacements. This identifies that when approaching half-pixel displacements the centroid estimator is unable to correctly resolve these sub-pixel displacements and hence cause measurements to be either greatly overestimated or underestimated. Further evidence of this is shown in the mean bias error plot. Here, at half-pixel displacements the mean bias error is zero, meaning that on average the displacements are not biased. But coupled with a significantly large RMS error identifies that the estimator is unable to resolve these displacements. This is a peak estimator error and its effects are also apparent in parabolic results but to a much lesser extent. Therefore, in order to minimise this effect the Gaussian sub-pixel estimator should be used as an initial estimator. This method generates superior mean bias and RMS error results than the centroid and parabolic estimators over the same displacement data-sets.

5.4 Smaller region measurement errors

When performing DPIV analysis it has become common practice to reduce the interrogation region size in order to increase the velocity vector resolution. Smaller region sizes also allow for flows experiencing strong velocity gradients to be examined (Bolinder, 2000). This avoids the peak splintering effect caused by large displacement gradients across the interrogation region (Keane and Adrian, 1992). This analysis examines the measurement errors generated for a series of uniform displacements using the $R_{MSSS}(m,n)$ algorithm and results are compared to SCC and NSS when each region is reduced to 16 x 16 pixels. This study also continues to examine the effect of increasing the mean background noise intensity on accuracy as the interrogation region size is reduced.

For this study, displacement data-sets containing 300 realisations of 16 x 16 pixel interrogation regions were generated for each uniform displacement. This ranges from zero to 4 pixels at a displacement resolution of one-tenth of a pixel. In order to maintain a constant seeding density ratio per unit area that is consistent with 32 x 32 pixel regions, each 16 x 16 pixel region is randomly populated with 6 particle images each with a diameter of 2.8 pixels. As with the 32 x 32 pixel region study an artificial background noise intensity is added to each data-set using MATLAB. As before, the mean background noise intensities added into each data-set are 2%, 5%, 10% and 15% of the 256 grey-scale value and describe the distribution given in section 3.8 (p.49).

The error plots comparing SCC, NSS and $R_{MSSS}(m,n)$ for a series of uniform displacements and background noise intensities is shown in Figure 5.19. Comparing this with the error plots generated for Figure 5.11 using 32 x 32 pixel interrogation regions, it is evident that SCC results in an increase in the magnitude of the negative mean bias whilst also providing a greater RMS error with increasing displacement. Anandarajah (2005) reasoned that this was because the magnitude of each correlation field value is dependent upon the number of correlated particle images present between the first and second interrogation region. As each region in this study is one-quarter the size of 32 x 32 pixel regions then proportionally fewer intensities contribute to the correlation field. As a consequence of this, the correlation peak height is reduced and

there are large variations in local correlation peak shape resulting in higher RMS errors. Since there are fewer particle images contained within an interrogation region then the increase in partial image error results from a decrease in the number of complete particle images relative to the number of partial images at the edge of a region and hence results in larger mean bias errors.

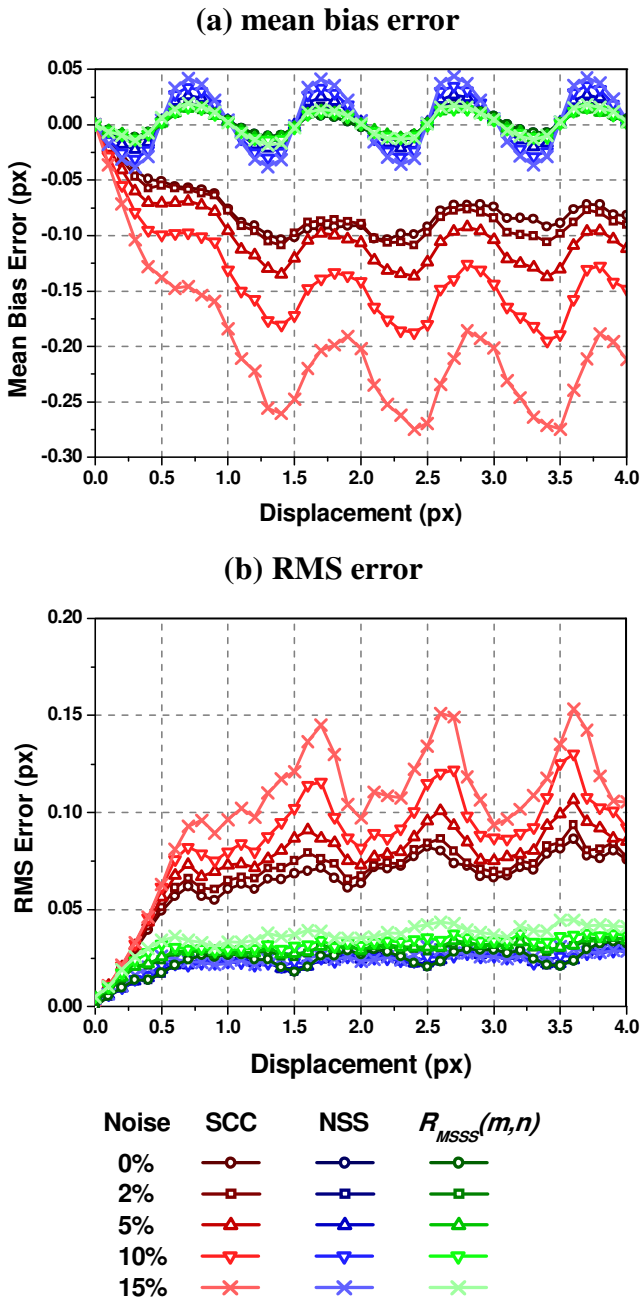

Figure 5.19 Error plots comparing SCC, NSS and $R_{MSSS}(m,n)$ with increasing background noise intensities (16 x 16 pixels)

If the correlation field is normalised by signal strength then both accuracy metrics are improved over the SCC results. This is clear when quantifying the accuracy metrics

from NSS and $R_{MSSS}(m,n)$. The signal strength weighting function compensates for the random distribution of particle images including the effects of partial images. This skews the correlation peak towards the actual displacement to suppress mean bias error and also reduces the local variation in correlation peak shape caused by the cross-correlation of unrelated particle images to suppress RMS error.

When the background noise intensity is increased, Figure 5.19(a) shows that processing with SCC and NSS results in an increase in the magnitude of the mean bias error. This effect was also shown in Figure 4.18(a) for 32 x 32 pixel region processing. The reason for this increase results from a decrease in the ratio between the correlation peak and the two neighbouring values which are used to calculate sub-pixel displacements. The decrease in ratios is caused by an increase in the magnitude of the correlation noise floor as the background noise intensity increases. This occurs because each pixel within a region has a greater intensity value with increasing noise intensity that contributes to each point of the correlation field.

As with 32 x 32 pixel region processing, Figure 5.19(b) shows that there is an increase in RMS error with increasing background noise intensity when processing with SCC. Section 4.5 showed that this is caused by the decrease in the ratios between the three correlation peak values exacerbating the local correlation peak shape and subsequently having a detrimental effect on RMS error.

If the correlation field is normalised by signal strength then the pixel intensities that contribute to each point of the correlation field, including the random distribution of particle images, are compensated for to thereby suppress the local variations between correlation peaks and hence reduce RMS error with increasing background noise intensity.

As with the analysis of 32 x 32 pixel interrogation regions, the $R_{MSSS}(m,n)$ algorithm is again shown to reduce both the mean bias and RMS error. The function is able to suppress background noise intensities to generate accuracy metrics comparable to those generated through NSS processing of 'ideal' regions as the mean background noise intensity increases. This is achieved by suppressing the magnitude of correlation noise

floor that should increases in magnitude as the background noise intensity increases. In doing so, $R_{MSSS}(m,n)$ maintains the ratios between the thee correlation peak values to those provided by 'ideal' region processing. Normalising by the signal strength function subsequently suppresses the other systematic errors prevalent during cross-correlation by compensating for the random distribution of particle images that cause RMS errors and partial images that cause the underestimation of measurements.

5.5 Summary

In summary, this chapter has identified that background noise intensities are systematic to DPIV processing and this affects the accuracy metrics associated to the processing algorithms. Using image enhancement techniques prior to cross-correlation to remove background noise will improve the accuracy metrics but their use is flawed. $R_{MSSS}(m,n)$ is a new, robust processing algorithm that takes advantage of the signal strength function to compensate for the random distribution of particle images across an interrogation region that cause RMS errors, partial images that cause underestimations in measurements and also accounts for background noise intensities including step increases in intensities that also affect measurements. This algorithm thereby suppresses both the mean bias and RMS errors for 32 x 32 pixel regions and smaller and provides accuracy metrics comparable to those generated through 'ideal' artificial region processing using NSS up to a mean background noise intensity of 15% of the 8-bit output. This is achieved by maintaining the ratios between the three central correlation peak values to evaluate the displacement to those provided by NSS processing of 'ideal' regions. The next chapter examines the performance of SCC, NSS and $R_{MSSS}(m,n)$ using iterative correlation techniques.

Chapter 6

Iterative Correlation Methods

6.1 Introduction

This chapter assesses the accuracy metrics generated by two commonly used iterative techniques that were developed to refine measurements using SCC. These techniques are discrete window shifting (DWS) and particle image pattern matching (PIPM). These iterative correlation methods were designed to maintain a constant SNR because concerns were raised that the loss of signal with increasing displacement would affect accuracy.

The objective of this chapter is to review and quantify the measurement errors generated by SCC, NSS and $R_{MSSS}(m,n)$ using DWS and PIPM. This is then extended to study the effect background noise has on the accuracy metrics defined in section 2.4 (p.13).

The error statistics from each algorithm using the iterative methods are presented for a series of uniform particle image displacements. The error plots were calculated using displacement data-sets containing 300 realisations of artificially generated interrogation regions defined using the optimum parameters outlined in section 3.10 (p.64).

6.2 Window shifting

Integer pixel or discrete window shifting (DWS) was proposed by Westerweel et al. (1997) as a way of maintaining a constant SNR with increasing displacement and thereby reducing measurement errors using SCC. As displacement increases the number of related particle image pairs present between sequential regions decreases (Huang et al. 1993a). This is referred to as the out-of-pattern effect and this relationship with displacement is shown in Figure 3.15 (p.60). Previous assumptions have stated that the weighting of the correlation function is responsible for underestimating measurements (Raffel et al. 1998) and hence introduced normalisation by area. It was assumed therefore the out-of-pattern effect causes the signal peak to depreciate and hence cause measurement uncertainties. With these original assumptions it is intuitive to assume that maintaining a constant SNR for all displacements will increase measurement accuracy. However, as was shown in Chapter 4, the cross-correlation of partial images causes the negative bias in measurements, and the cross-correlation of unrelated particle images causes RMS errors and the SCC algorithm does not account for their presence.

The window shifting process occurs in two stages. The first stage estimates the required shift by determining an integer pixel displacement through an initial cross-correlation. Once this displacement is known the second region is remapped within the image in accordance with the integer result. After remapping, the new second region is cross-correlated with the initial region to provide a displacement of less than one pixel determined using a sub-pixel estimator. Therefore the total displacement is composed of the integer pixel shift and the sub-pixel displacement and thereby takes advantage of low sub-pixel displacement errors (Raffel et al., 1998).

To evaluate the measurement error performance of window shifting, error plots are computed for SCC, NSS and $R_{MSSS}(m,n)$ with window shifting and are compared to the results generated when window shifting is not used. The measurement error plots are produced from data-sets of artificial regions modelled using the criteria outlined in section 3.10 (p.64) that do not contain background noise is shown in Figure 6.1.

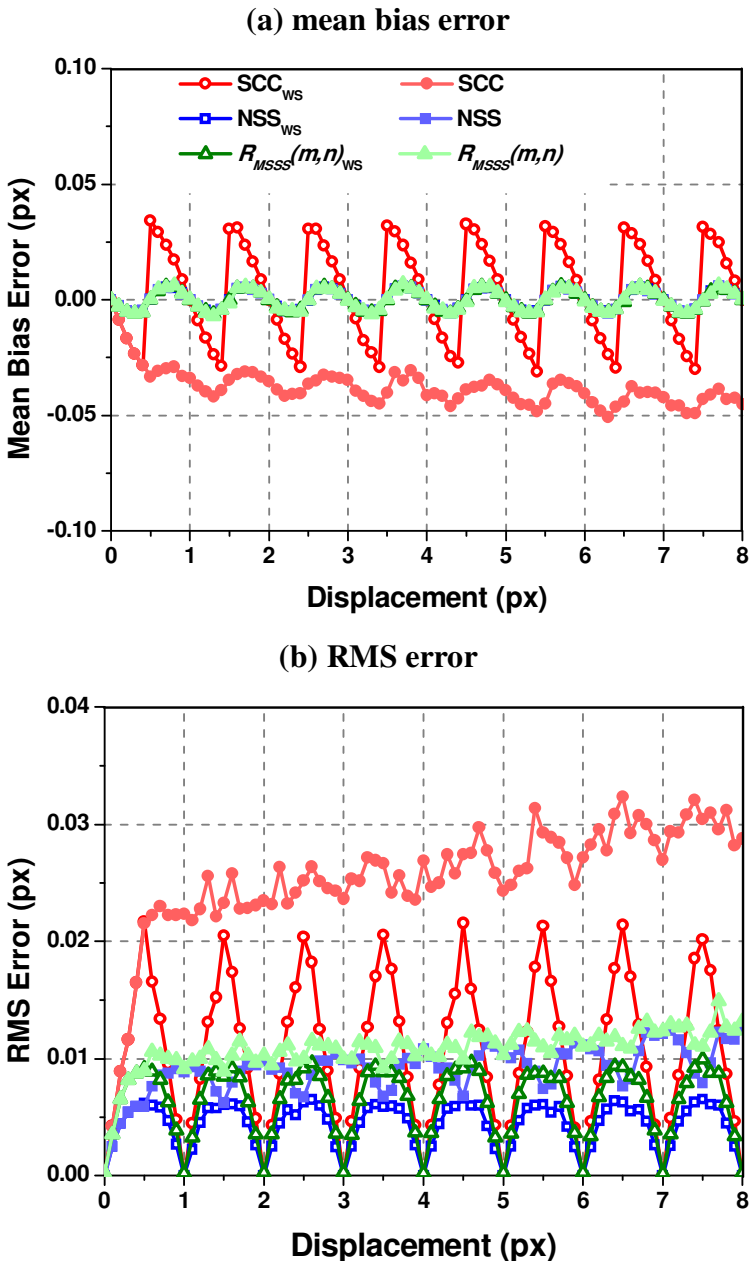

Figure 6.1 Error plots comparing SCC_{WS}, NSS_{WS} and $R_{MSSS}(m,n)_{WS}$ with SCC, NSS and $R_{MSSS}(m,n)$ with no background noise

As with the standard analysis of equal-sized regions, the errors produced by SCC with window shifting (SCC_{WS}) are significantly larger than the NSS_{WS} and $R_{MSSS}(m,n)_{WS}$ results. However, the error plots highlight that DWS with a processing algorithm reduces error analysis to a single pixel displacement cycle. SCC_{WS} however does not account for the random distribution of particle images that affects the underestimation and variations of measurements. This is because partial images will still be present in both regions after DWS and will therefore generate the error plots of Figure 6.1(a). Figure 6.2 shows that although DWS is able to preserve a

constant SNR for SCC over the uniform displacement range, systematic errors caused by the random distribution of particle images still remains in analysis (Figure 6.1).

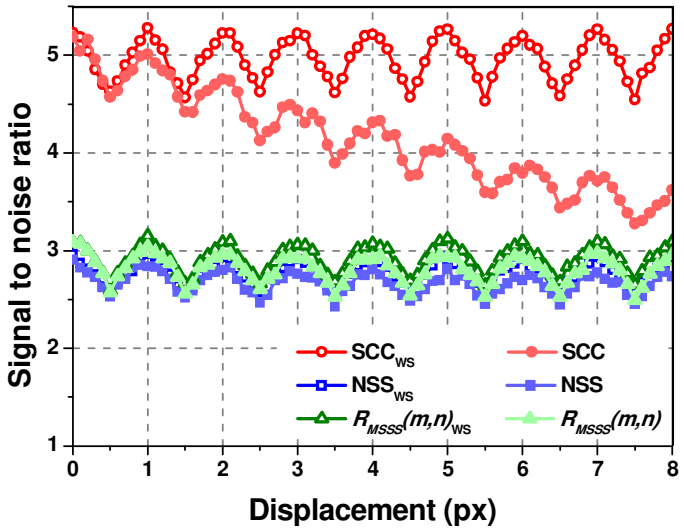

Figure 6.2 SNR for SCC, NSS and $R_{MSSS}(m,n)$ compared with DWS

Comparing the error plots generated for SCC shows that the results for DWS are identical to the non-shifted case for both accuracy metrics up to a ½ pixel displacement. As SCC_{WS} does not account for the random distribution of particle images these results are to be expected. The first and subsequent shifts will initially produce a positive bias as the shift is greater than the particle image displacement, causing an overestimation in measurements. The decline in positive mean bias with increasing displacement is due to a progressive return to a state where both artificial regions have an identical intensity contents. This will only occur at integer pixel displacements. At this point, a symmetric correlation peak is generated; maximising SNR and reducing both accuracy metrics to zero. After an integer pixel displacement the cycle repeats again.

Figure 6.1(a) shows that when normalising the correlation field by signal strength the mean bias error is identical for both the DWS and non-shifted case. As has been established, DWS preserves a constant SNR by maintaining a high number of particle image pairs when processing with a cross-correlation algorithm. However, the number of partial images remains constant with increasing displacement (Figure 4.3, p.70), therefore as has been expressed with the SCC results this will affect the accuracy of measurements. Normalising by signal strength however produces a

mean bias error oscillation which cycles over a pixel displacement when producing error plots from non-shifted regions. The overestimation in measurements shown with SCC after each DWS is subsequently accounted for since the function is able to compensate for the random distribution of particle images.

The processing algorithm also generates a constant SNR both with and without DWS as is shown in Figure 6.2. This occurs because the signal strength function normalises each point of the correlation field by the pixel intensities used to calculate each point. This consequently recovers any signal loss that occurs through the out-of-pattern effect to preserve SNR.

A one pixel displacement cycle pattern identified in the mean bias error plot is also present in Figure 6.1(b) which shows the RMS error plot for SCC_{WS}, NSS_{WS} and $R_{MSSS}(m,n)_{WS}$ with their non-shifted counterparts. For each of the processing algorithms with DWS, the RMS error plot generates measurements with increasing variation up to a ½ pixel displacement and thereby generates error plots typical of sub-pixel displacements. When displacement data-sets exhibiting displacements of ½ pixel or greater are examined a DWS is implemented. For subsequent displacements there is a progressive return to a state where both regions are identical. This occurs at integer pixel displacements. As has been discussed in section 4.3.2 (p.75) the signal strength function accounts for the random distribution of particle images to reduce measurement variations. It is therefore intuitive that normalising the correlation field by signal strength will provide lower RMS errors per pixel displacement over that of SCC_{WS}.

6.2.1 DWS with background noise

When processing 'ideal' artificial regions the NSS and $R_{MSSS}(m,n)$ algorithms both return accuracy metrics with similar results as described in section 5.2.6 (p.125). This occurs during standard processing as well as DWS (Figure 6.1). However, Chapter 5 detailed that the background noise intensity also influences the accuracy of results. Although DWS only provides sub-pixel displacement errors, results processed with SCC or NSS will be affected by background noise. If DWS is used with $R_{MSSS}(m,n)$ background noise intensities and the random distribution of particle

images are accounted for providing robust results that are comparable to the 'ideal' NSS case. This is highlighted in Figure 6.3 which provides the error plots for DWS using SCC, NSS and $R_{MSSS}(m,n)$ as the background intensity increases.

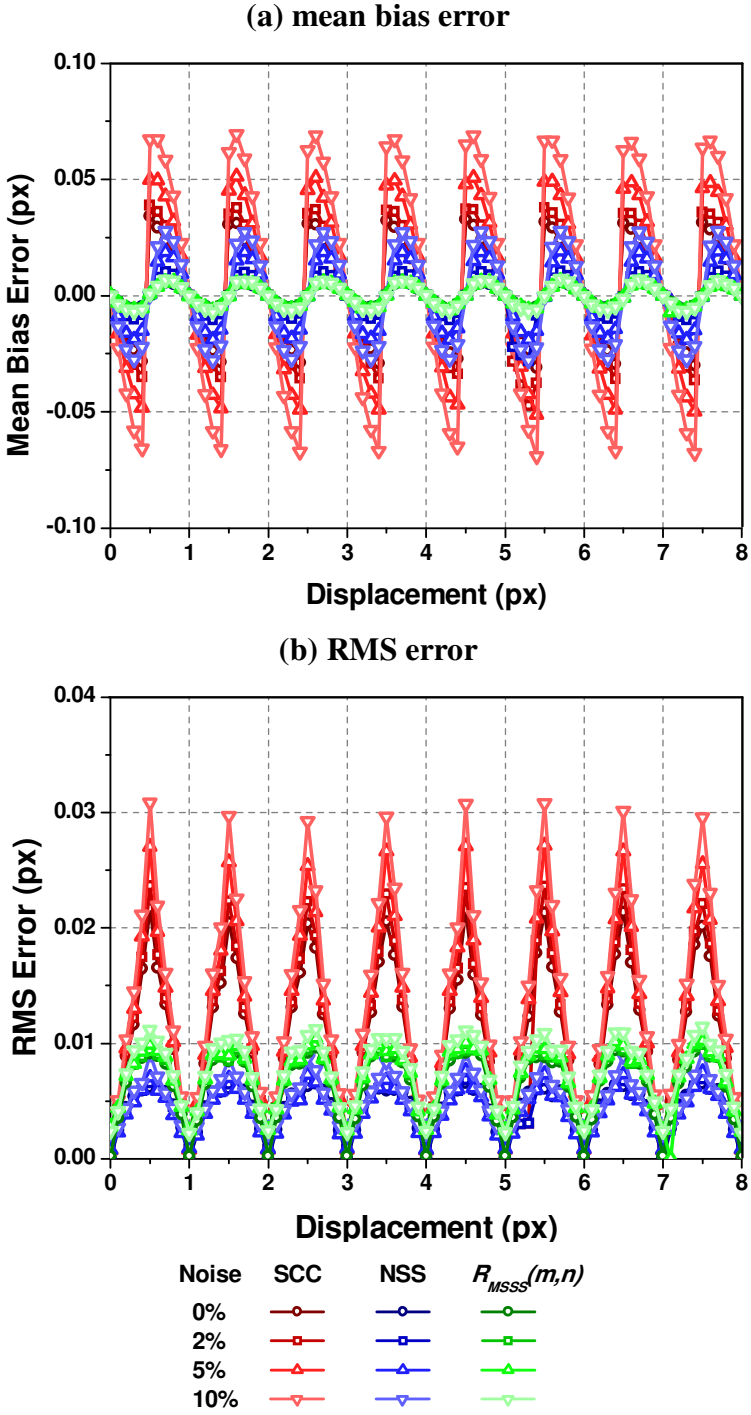

Figure 6.3 Error plots for SCC_{WS}, NSS_{WS} and $R_{MSSS}(m,n)_{WS}$ for increasing background noise intensities (32 x 32 pixels)

As section 4.5 (p.93) explains, the increase in the amplitude mean bias error oscillation for SCC and NSS is caused by a decrease in the ratios between the three

correlation peak values used to calculate the sub-pixel location of the correlation peak. This is caused by an increase to the correlation noise floor as the background noise intensity increases. The $R_{MSSS}(m,n)$ algorithm compensates for background noise intensities thereby suppressing the mean bias error oscillation. The increase in RMS error for SCC with increasing background noise intensity is caused by the decrease in ratio between the correlation peak values coupled with the variations in measurements caused by the cross-correlation of unrelated particle images. As the signal strength function compensates for the random distribution of particle images including partial images across an interrogation region then this subsequently suppresses both mean bias and RMS error.

In summary, DWS was developed to be used in conjunction with SCC to suppress measurement errors. It was assumed that by maintaining a constant SNR with increasing displacement would improve accuracy by taking advantage of low sub-pixel displacement errors. To this extent DWS with SCC does achieve this; improving the accuracy of measurement over the standard case. Nevertheless, the SCC algorithm does not account for the random distribution of particle images and therefore this systematic error remains in measurements. Since the signal strength function compensates for this then there is a reduction in both accuracy metrics when processing 'ideal' artificial regions with either NSS or $R_{MSSS}(m,n)$. In practice background noise intensities will also affect the accuracy of measurements. As was developed and identified in Chapter 5, $R_{MSSS}(m,n)$ is a robust algorithm able to compensate for both background noise intensities and the random distribution of particle images. Therefore this robust algorithm used in conjunction with DWS takes advantage of sub-pixel displacement errors whilst also compensating for the two systematic errors thereby suppressing both accuracy metrics with increasing displacement and background noise intensity.

6.3 Particle image pattern matching

The resolution of the velocity vector field can be enhanced if the size of the regions within the flow image is reduced. However, there is an increase in both mean bias and RMS errors if regions are made smaller. Therefore there is a trade-off between the accuracy of results and the resolution of the vector field. Section 5.4 (p.144) illustrated that decreasing the size of each region results in an increase in both accuracy metrics as a function of displacements. It was demonstrated that reducing the region size decreases the signal available that contributes to the correlation peak. SCC of smaller regions therefore increases sensitivity to partial images resulting in the underestimation of measurements. It also results in large measurement variations compared to SCC of 32 x 32 pixel regions (Figure 5.19, p.145).

Another technique introduced to reduce the mean bias error is to increase the size of the second interrogation region before SCC. Huang et al. (1993a) proposed that the SCC of a smaller first region with a larger second would recover the 'loss-of-signal' with increasing displacement thereby maintaining a constant SNR. This is termed particle image pattern matching (PIPM). The PIPM error plots for SCC, NSS and $R_{MSSS}(m,n)$ using 'ideal' initial regions of 16 x 16 pixels, 24 x 24 pixels and 32x32 pixels cross-correlated with 'ideal' 32 x 32 pixel regions as a function of displacement, is presented in Figure 6.4.

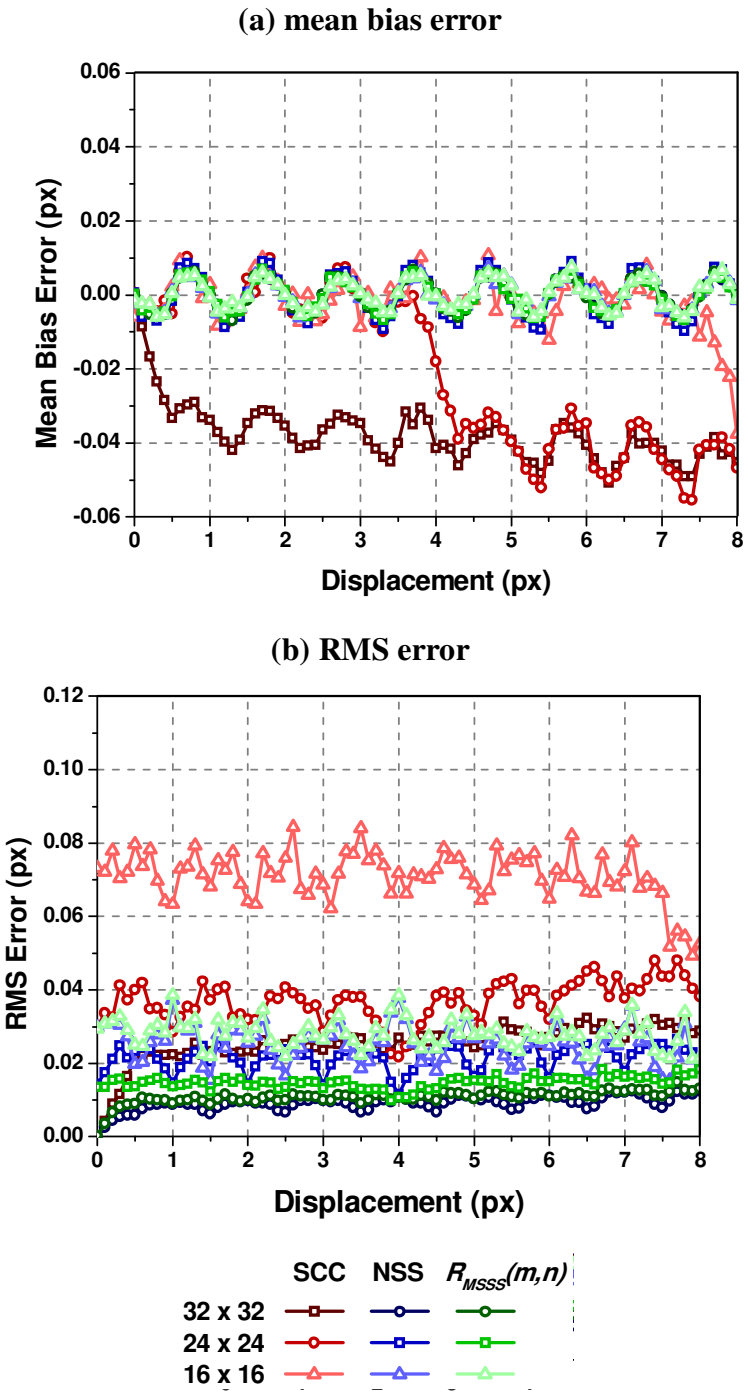

Figure 6.4 Error plots for PIPM of 16 x 16, 24 x 24 and 32 x 32 pixel regions with 32 x 32 pixel regions using SCC, NSS and $R_{MSSS}(m,n)$

On studying Figure 6.4(a) it is clear that when processing with SCC, PIPM results in measurement underestimations when the initial interrogation region is 32 x 32, 24 x 24 or 16 x 16 pixels in size. Yet the displacement at which the underestimation begins is dependent on the size of the initial interrogation region. This underestimation occurs because as the particle image displacement increases the

particle images within the initial region are not present in the second larger region. Therefore PIE is subsequently reintroduced into analysis. Anandarajah (2005) stated that provided the particle images within the first region are present in the second then cross-correlation will result in a correlation peak being either positively or negatively skewed. The skew of the correlation peak is dependent on the random distribution of the particle images within the interrogation regions. It was shown that the cross-correlation of a partial image on the left-hand boundary of the initial region which is subsequently complete in the larger second region will negatively skew the correlation peak. Conversely, the cross-correlation of a partial image on the right-hand boundary of the smaller region with the complete particle image will positively skew the correlation peak. Therefore over a displacement data-set, on average, the skew will be negligible and hence results in the suppression of the mean bias error (Figure 6.4(a)).

Therefore, once the particle images encapsulated in the initial region are not present in the second, measurements begin to be underestimated. In addition to this, the out-of-pattern effect will cause a decline in the magnitude of the signal peak and hence a drop in SNR. This is illustrated in Figure 6.5 which shows the SNR for PIPM using SCC, NSS and $R_{MSSS}(m,n)$.

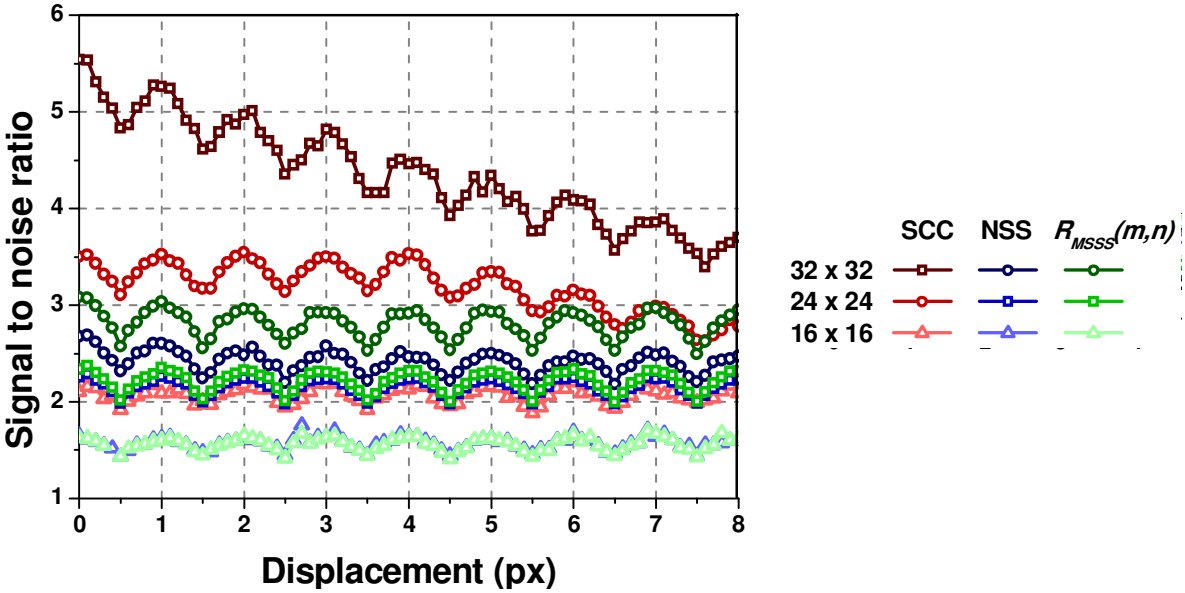

Figure 6.5 SNR plots for PIPM of 16 x 16, 24 x 24 and 32 x 32 pixel regions with 32 x 32 pixel regions using SCC, NSS and $R_{MSSS}(m,n)$

Therefore provided the particle image displacement does not exceed half the difference between the size of the larger second and smaller first region (e.g. if the first region is 24 x 24 pixels and the second region is 32 x 32 pixels then the maximum displacement using SCC before underestimations is 4 pixels) then the measures suggested by Huang et al. (1993a) for suppressing the mean bias error whilst maintaining a constant SNR when processing with SCC holds true. However as Figure 6.4(b) identifies, reducing the size of the first region will affect the variations between measurements. As the size of the first interrogation region decreases fewer pixel intensities are available to contribute to the correlation field; this subsequently reduces magnitude of the correlation peak. The reduced intensity content means that the correlation peak is more sensitive to variations in pixel intensities across the interrogation region than if the first region was larger. This subsequently causes large variations in the shape of the correlation peak and hence results in larger RMS errors. As cross-correlation is a measure of the similarity between the contents of the two regions then reducing the size of the first region in relation to that of the second will inherently result in the cross-correlation of unrelated particle images that contributes to the correlation noise floor. Also, if during cross-correlation a similar pattern of particle images to those contributing to the correlation peak are found else where in the second region then this too will generate a significant noise peak. This, coupled with the decline of the correlation peak height, will subsequently decrease the SNR as is shown in Figure 6.5.

When PIPM is processed with NSS and $R_{MSSS}(m,n)$ the mean bias error remains negligible across the 8 pixel displacement range. This occurs since the signal strength function compensates for the random distribution of particle images across each interrogation region as each intensity contributes to the correlation field. This therefore compensates for the presence of partial images that causes measurement underestimations with SCC. The function also accounts for the asymmetry of the correlation peak caused by the random distribution of particle images to thereby reduce RMS errors when compared with SCC. Furthermore, the signal strength function recovers the signal lost by the out-of-pattern effect to maintain a constant SNR across the 8 pixel displacement range. The magnitude of the SNR however decreases as the first interrogation region reduces in size as less pixel intensities are

available to contribute to the correlation peak and the correlation noise floor increases accordingly.

In summary, PIPM was developed to be used in conjunction with SCC to suppress measurement errors as it was assumed that maintaining a constant SNR with increasing displacement would improve accuracy. To a limited extent PIPM with SCC achieves this, but only for mean bias error; PIPM provides larger RMS errors than the processing of equal sized 32 x 32 pixel interrogation regions. PIPM with SCC generates a negligible mean bias error which is dependent on the particle image displacement and the size of the first interrogation region. If the displacement results in particle images from the first region not being present in the second region then the SCC of partial images causes measurements to be underestimated and hence generates negatively biased mean bias errors. The reduction in the size of the first region also results in large RMS errors. This occurs because fewer intensities are available to contribute to the correlation peak which subsequently means that it is more sensitive to changes in pixel intensities across each interrogation region. A consequence of this is that large variations in the correlation peak shape generates larger RMS errors. When PIPM is used with NSS or $R_{MSSS}(m,n)$ the signal strength function accounts for the random distribution of particle images across each interrogation region therefore accounting for partial images to reduce mean bias and the cross-correlation of unrelated particle images that cause RMS errors. The next section investigates the effect of the addition background noise has on the accuracy of PIPM results.

6.3.1 PIPM with background noise

As Figure 6.4 shows, when processing 'ideal' regions, both the NSS and $R_{MSSS}(m,n)$ algorithm return accuracy metrics with similar results. However, Chapter 5 outlined that the addition of background noise also affected the accuracy of results. If PIPM is used with $R_{MSSS}(m,n)$ Figure 6.6 shows that the background noise intensities and the random distribution of particle images that affect accuracy are account for, thereby providing results for increasing background noise intensities that are comparable to those generated by 'ideal' regions processed using NSS.

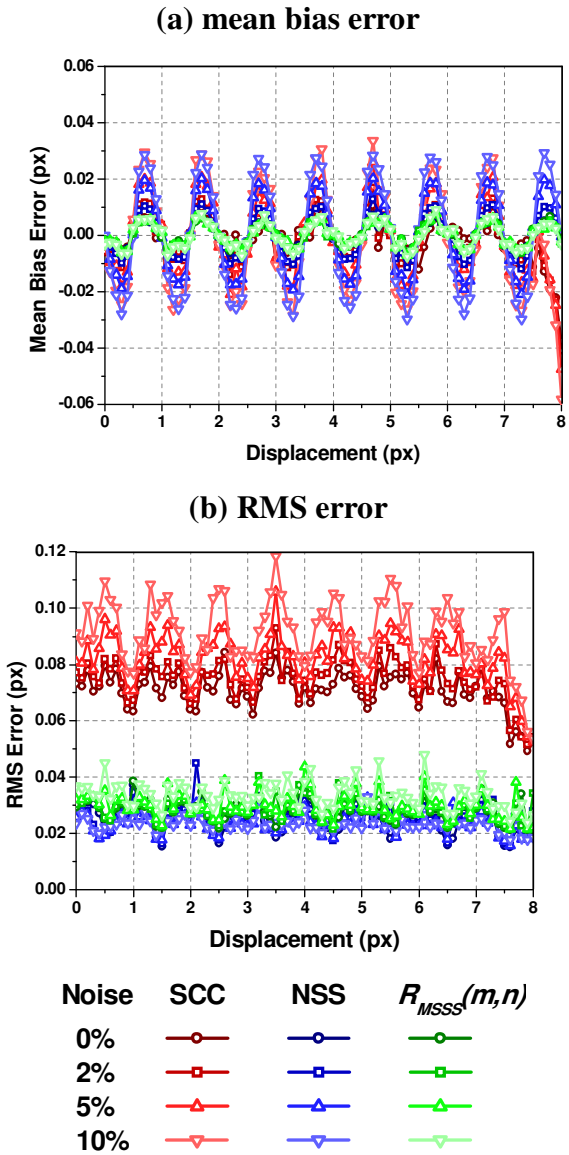

Figure 6.6 Error plots for PIPM of 16 x 16 pixel regions with 32 x 32 pixel regions using SCC, NSS and $R_{MSSS}(m,n)$ for various background noise intensities

Figure 6.6 highlights that as the mean background noise intensity increases the amplitude of the mean bias error oscillation for SCC and NSS increases yet only SCC provides a significant increase in RMS error. The reasons for the changes to the accuracy metrics with increasing background noise intensity is outlined in section 4.5 (p.93).

6.4 Summary

This chapter has reviewed and quantified the measurement errors associated with two iterative techniques intended to improve the accuracy of measurements when processing regions with SCC. Both techniques with SCC provide an improvement in mean bias error over that of the standard procedure whilst also maintaining a constant SNR with increasing displacement. However, the systematic error associated with SCC remains but the random distribution of particle images are accounted for with the signal strength function and background noise intensities are suppressed with $R_{MSSS}(m,n)$.

Section 6.2 highlights that DWS with a cross-correlation algorithm defines the accuracy metrics over sub-pixel displacements. However, it is shown that SCC exhibits significant errors prior to each DWS (Figure 6.1) in comparison to NSS and $R_{MSSS}(m,n)$. The errors incurred before each shift result from a decline in signal contributing to the correlation field coupled with the cross-correlation of partial images which underestimates measurements and unrelated particle images that cause RMS errors. After each shift the particle image displacement is overestimated but the number of particle images contributing the correlation peak increases, re-establishing the relationship where the two interrogation regions are identical; hence no errors are generated at integer pixel displacements.

When unequal sized regions are processed the suppression of the mean bias error with SCC is dependent on the relative sizes of the two interrogation regions (Figure 6.4). The random distribution of particle images within each region will cause a correlation peak to be either positively or negatively skewed and therefore, on average, generate a negligible mean bias error. If the particle images in the first region are not encapsulated in the second after a displacement then underestimations will ensue caused by the cross-correlation of partial images with unrelated particle images. Although PIPM with SCC can provide a negligible mean bias error, the positive or negative skew of the correlation peak leads to significant RMS errors which are also dependent on the relative sizes of the two interrogation regions.

It is demonstrated that when the two iterative techniques are processed with NSS there is an improvement to both mean bias and RMS error. This results because NSS compensates for the cross-correlation of partial images that cause measurement underestimations and the cross-correlation of unrelated particle images that cause asymmetry in correlation peaks which results in RMS errors. It is also clearly shown that NSS generates a negligible mean bias error that is independent of the relative sizes of the two interrogation regions (Figure 6.4(a)).

On processing 'realistic' artificial interrogation regions that contain background noise intensities using the iterative correlation techniques, it is shown that $R_{MSSS}(m,n)$ provides robust accuracy metrics as the background noise intensity increases. The processing algorithm implements the signal strength function to compensate for the random distribution of particle images, thereby reducing mean bias and RMS errors, and also accounts for background noise intensities that also has a noticeable effect on the accuracy of measurements using other processing algorithms (Figure 6.3 and Figure 6.6).

Chapter 7

Experimental Verification

7.1 Introduction

This chapter presents the accuracy metrics generated by SCC, NSS and $R_{MSSS}(m,n)$ processing of interrogation regions recorded during a DPIV experiment, in which the seeding particles of known size are displaced by a controlled distance. The processing of these images provides experimental verifications for the theoretical predictions presented throughout this research. The images used for this verification are provided by the uniform particle image displacement experimental outlined by Anandarajah (2005). The first section briefly describes the experimental set-up and parameter used to generate the DPIV images. The second section details a comparison of the ratio between the three central points of the correlation peak used to define the sub-pixel location of the signal peak for both experimental and theoretical results. This extends to compare the experimental and theoretical signal and noise levels that have been shown to affect accuracy. Following this, the section evaluates the experimental measurement errors produced by the processing routines for a series of uniform particle image displacements using 32 x 32 pixel regions and smaller (i.e. 16 x 16 pixels), discrete window shifting and particle image pattern matching. The error plots generated from each of these processes are compared to their theoretical predictions.

7.2 Experimental set-up and procedure

Experimental images describing a uniform particle image displacement captured by Anandarajah (2005) are used to verify the theoretical predictions that quantify the systematic errors associated with the cross-correlation algorithms. A method of generating a uniform particle image displacement was devised by seeding a glass slide, 60mm x 25mm, with aluminium oxide (Al_2O_3) particles with a mean particle diameter of 0.7µm to 1.2µm. These were passed through a seeded air stream until the slide was covered in randomly distributed particles at the desired density. The slide was then fixed to a 200µm piezo travel traverse with a resolution of 110nm to displace the glass slide over a series of uniform displacements.

A Nd:YAG laser with a wavelength of 532nm and a combination of spherical and cylindrical lenses was used to produce the light sheet used to illuminate the glass slide. A PIVCAM 10-30, with a Nikon Micro-Nikkor 50mm lens was used to capture each image. This is a CCD camera with a resolution of 1000 x 1016 pixels and each pixel is $9\mu m^2$ with an 8-bit pixel output. Each of these were controlled by a TSI commercial system.

The parameters determined for this experiment were a magnification factor, M of 0.75 and f-number, $f^{\#}$ of 11. This was so that each particle image described using equation 3.6 (p.44) has a diameter of between 2.777 and 2.778 pixels and thereby avoiding errors associated to poor particle image resolution. Anandarajah (2005) adjusted the seeding density until, on average, 22 particle images were present in each 32 x 32 pixel interrogation region. This closely replicates the modelling criteria for the artificial interrogation regions discussed in section 3.9 (p.51).

Twin images of the glass slide containing the randomly distributed particle were captured for a series of uniform displacements as the traverse moved through its 200µm range. The displacement was increased between each image pair to provide image pairs experiencing displacements of between zero and 8 pixels at a resolution of one-tenth of a pixel. Once the image pairs for each displacement had been captured each image could then be analysed. This is achieved by dividing each

image into smaller interrogation regions to provide displacements data-sets of 300 realisations for each displacement.

So that experimental and theoretical predictions can be compared both have to contain background noise intensities provided by a similar distribution. The distribution of the experimental images was discussed in section 3.8 (p.49) where it was stated that the background noise measured from these experimental images had a mean pixel intensity of 39 and followed the distribution shown in Figure 3.7 (p.50). This equates to a background noise intensity of 15% of an 8-bit output. Therefore experimental results can be compared to theoretical predictions provided by the data-set containing a mean background noise intensity of 15%.

7.3 Experimental verification of correlation routines

This section presents the accuracy metrics for uniform particle image displacements generated by processing experimental images with SCC, NSS and $R_{MSSS}(m,n)$ algorithms. These are compared to the results achieved by processing artificial regions with a mean background noise intensities of 15%. The correlation field characteristics generated by experimental images and theoretical predictions are presented in section 7.3.1 to show it is reasonable to compare the accuracy statistics. A comparison of the errors generated from processing 32 x 32 pixel regions is presented in section 7.3.2 and smaller region comparisons presented in section 7.3.3. The evaluation of experimental results using the iterative correlation methods of discrete window shifting and particle image pattern matching with the processing algorithms is presented in section 7.3.4 and 7.3.5 respectively.

7.3.1 Correlation field characteristics

Section 4.5.1 (p.95) discussed that maintaining the ratios between the three central points of the correlation peak to those achieved through 'ideal' region processing was critical in suppressing errors associated with the cross-correlation algorithm. It was identified that increasing the magnitude of the correlation noise floor caused the ratios to decline, increasing the error statistics. Figure 7.1 compares the absolute ratio between the adjacent values either side of the SCC, NSS and $R_{MSSS}(m,n)$ correlation peaks as viewed through the x-direction for each displacement data-set between zero and 8 pixels and averaged over 300 realisations for (a) experimental and (b) artificial regions containing a mean background noise intensity of 15%. The absolute ratios for each processing algorithm are computed by calculating the absolute difference between the adjacent values either side of the correlation peak which is then normalised by the central correlation peak value. An average ratio is then computed over the 300 realisations within each data-set for each displacement.

(a) experimental

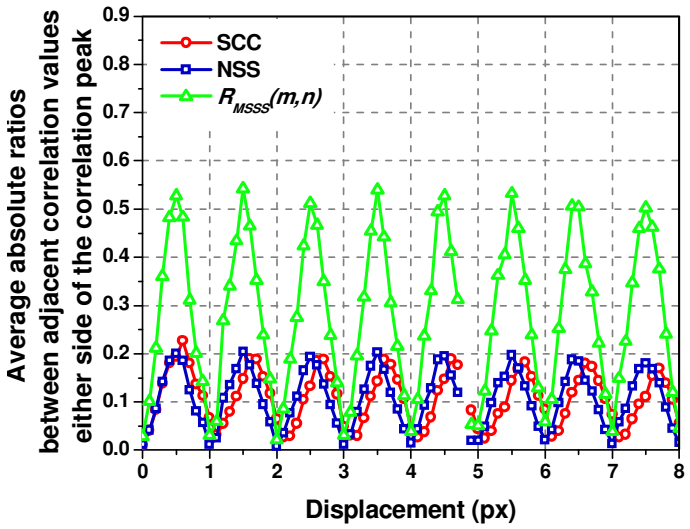

(b) theoretical

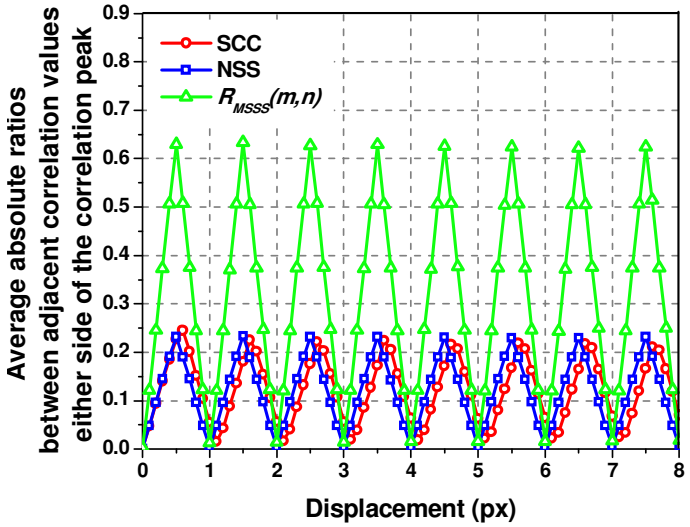

Figure 7.1 Theoretical and experimental comparison of the absolute ratios between adjacent correlation values for SCC, NSS and $R_{MSSS}(m,n)$ (32 x 32 pixels)

When comparing the absolute ratios between adjacent correlation peak points it is evident that experimental results provides lower ratios than the theoretical predictions with the $R_{MSSS}(m,n)$ correlation peaks being affected to the greatest extent. It is also noted that the absolute ratios with the greatest value per displacement provides the most accurate measurements. For example, the small ratio values provided by SCC and NSS shown in Figure 7.1 corresponds to the large mean bias oscillation shown in Figure 5.11 (p.128). Maintaining large values within each ratio per displacement suppresses the mean bias error oscillation as is provided with

$R_{MSSS}(m,n)$ results since this suppresses the background noise intensities that affect measurements as was shown in Figure 5.12 (p. 129). Figure 7.2 shows the average shape of the correlation peak for selected displacements between zero and one pixel. These shapes correspond to the absolute ratios between adjacent correlation values in the x-direction provided in Figure 7.1. A value of zero is provided at integer pixel displacements as each correlation peak is symmetric. The ratio values increase up to half-pixel displacements since the difference between the two adjacent values either side of the correlation peak increases. At half-pixel displacements the difference between the two adjacent points are at a maximum hence a peak is generated in Figure 7.1 at these displacements. After the half-pixel displacement point the difference between the two adjacent points declines as the correlation peak approaches symmetry at integer pixel displacements.

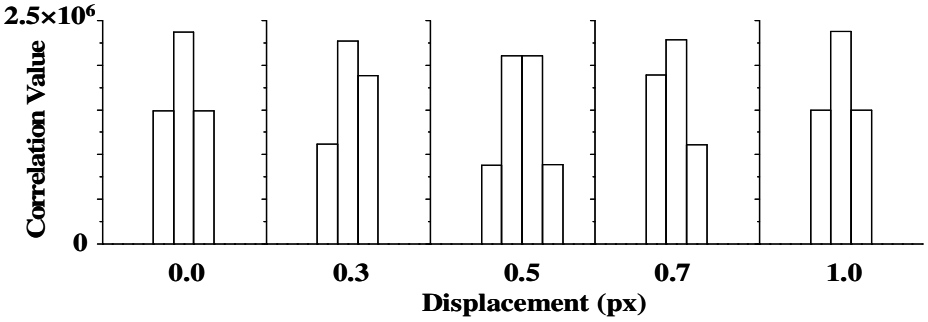

Figure 7.2 The shape of the correlation peak with increasing displacement

When processing with SCC or NSS the shape of the correlation peak remains the same but the cross-correlation of background noise decreases these ratios (Figure 4.19, p.95) which consequently affects the accuracy of measurements (Figure 4.18, p.94). It is also noted that the maximum correlation peak value at integer pixel displacements is greater than that of a correlation peak describing a half-pixel displacement. The decline in peak value occurs at half-pixel displacements because there is a temporary broadening of the correlation peak. This results from the correlation peak being described across two points of the correlation field at these displacements.

To show why there are discrepancies between the ratios provided by theoretical predictions and experimental results, Figure 7.3 presents the average signal and noise magnitude plots for SCC, NSS and $R_{MSSS}(m,n)$ generated from both experimental and

artificially generated correlation fields. The average signal and noise metrics are calculated over 300 realisations for each displacement data-set. The signal magnitude is calculated by computing the height of each correlation peak and the noise magnitude by computing the height of the maximum noise peak.

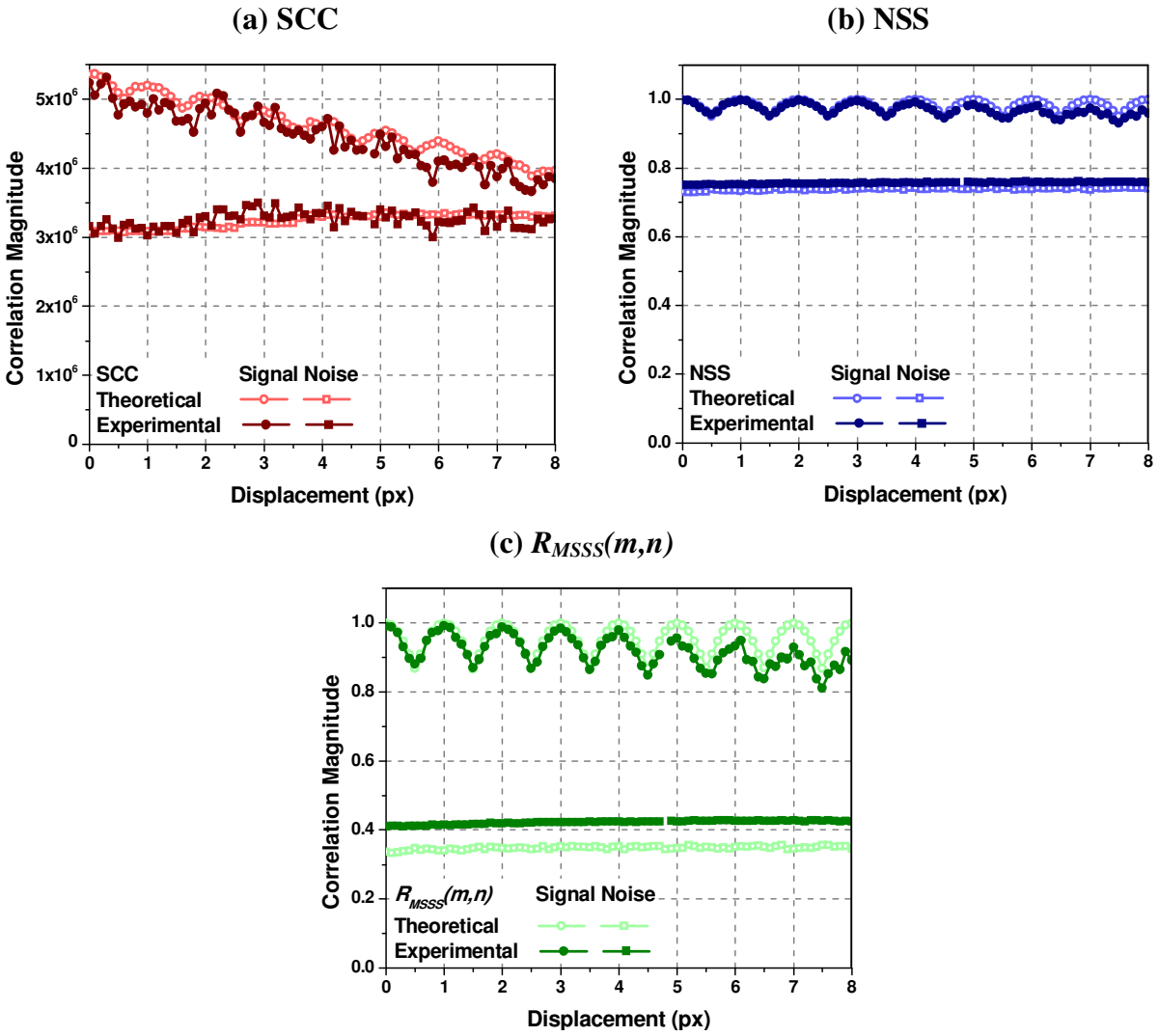

Figure 7.3 Comparison of experimental and theoretical signal and noise plots for SCC, NSS and $R_{MSSS}(m,n)$ (32 x 32 pixels)

Figure 7.3 shows that for each of the processing algorithms the experimental signal magnitude is comparable with theoretical predictions up to a displacement of 4 pixels. Anandarajah (2005) stated that it was difficult to ensure that each 32 x 32 pixel region contains 22 particle images. The decline in signal magnitude beyond 4 pixels displacement corresponds with this statement since it indicates that as the displacement increases fewer particle image pairs are present and able contribute to the correlation peak. The figure also highlights that the addition of background noise

to artificial regions represents most of the noise within the experimental regions. As such, the correlation noise floors generated by each of the processing algorithms using experimental regions are comparable to those produced by the artificial regions. The residual difference between the correlation noise floors generated by theoretical predictions and experimental results can be attributed to variations in pixel intensities within each interrogation region. The cross-correlation of high intensity pixels that are greater than the background noise intensities (see Figure 3.7, p.50) will increase the magnitude of the correlation noise floor. This is evident with Figure 7.3(c); theoretical predictions show that $R_{MSSS}(m,n)$ is able to suppress background noise intensity by subtracting the mean intensity value that contributes to each point of the correlation field to generate robust accuracy metrics comparable to processing 'ideal' regions with NSS (Figure 5.11, p.128). If high intensity pixels are present the background noise intensities will not be fully suppressed thereby increasing the magnitude of the correlation noise floor. Consequently, this will decrease the ratios between the three central points of the correlation peak (Figure 7.1) and will subsequently affect the experimental accuracy metrics.

7.3.2 32 x 32 pixel interrogation region analysis and comparison

The mean bias error plot illustrated in Figure 7.4 provides a comparison between (a) experimental results and (b) theoretical predictions for when the mean background noise intensity is 15% of the maximum pixel 8-bit value. In comparison, the figure demonstrates that the mean bias error generated for SCC of both experimental and artificial regions provides negatively biased results. The magnitude of the mean bias error oscillation is caused by the decrease in the ratios between the three central correlation peak values due to an increase in the magnitude of the correlation noise floor (section 4.5.1, p.95). When normalising the correlation function by signal strength (NSS and $R_{MSSS}(m,n)$) the mean bias error is reduced. This verifies that the signal strength function is able to compensate for the random variations in pixel intensities across an interrogation region which includes the effect of partial images that causes the negative bias in measurements (section 4.2, p.66).

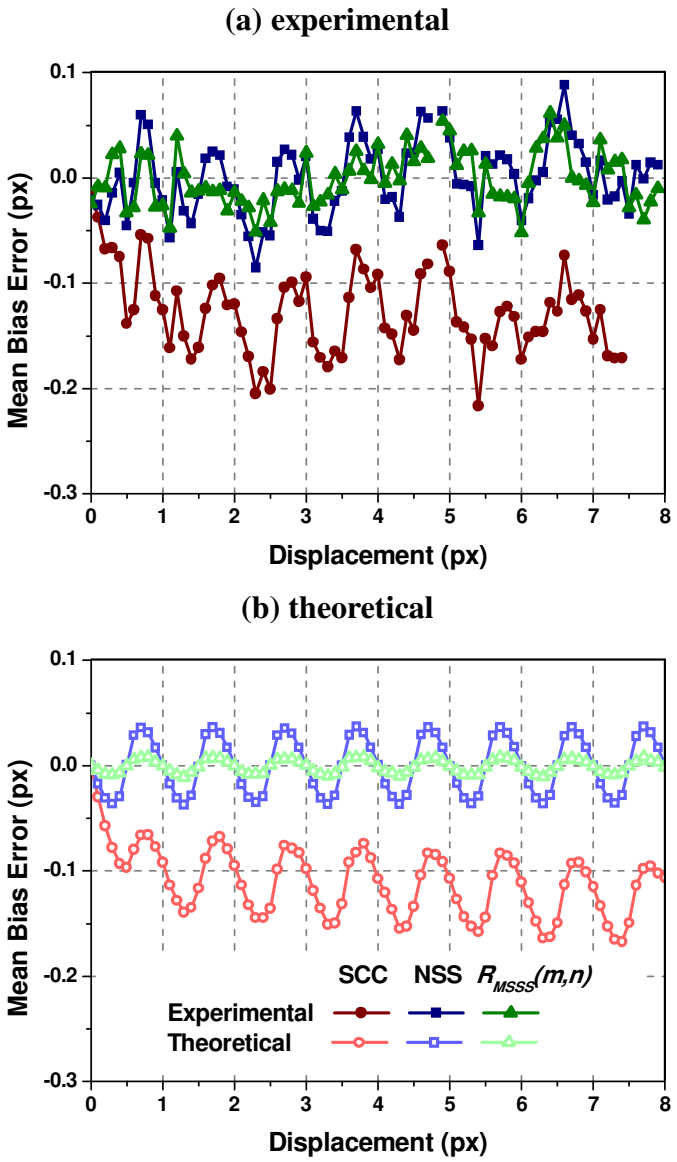

Figure 7.4 Experimental and theoretical mean bias error plot comparison (32 x 32 pixels)

The figure also identifies that on processing with $R_{MSSS}(m,n)$ there is a reduction in the amplitude of the mean bias error oscillation as the algorithm compensates for the background noise intensities which was identified in section 5.2.7 (p.129).

When comparing the RMS error plots in Figure 7.5 for (a) experimental results with (b) theoretical predictions, it is clear that the signal strength function is able to reduce the RMS errors generated by the SCC function. The signal strength function is able to account for local changes in pixel intensities across an interrogation region including those caused by the random distribution of particle images to thereby reduce variations in correlation peak shape and hence suppress RMS error.

(a) experimental

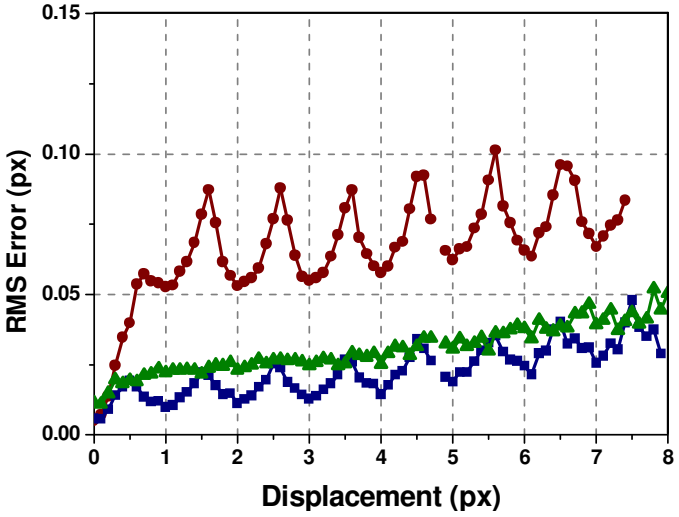

(b) theoretical

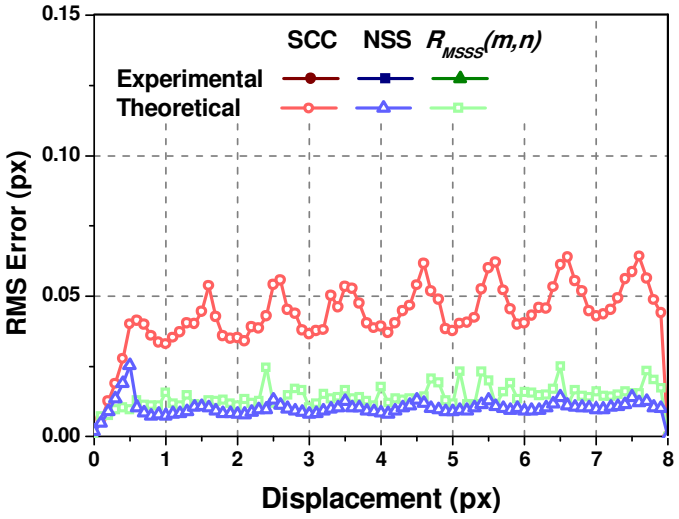

Figure 7.5 Experimental and theoretical RMS error plot comparison (32 x 32 pixel regions)

Both the (a) experimental results and (b) theoretical predictions show that $R_{MSSS}(m,n)$ provides a slightly increased RMS error over that of NSS. This occurs because the mean intensities within the overlapped area prior to cross-correlation are subtracted from each point of the interrogation region. This will affect the Gaussian distribution of each particle image, which, when processing with $R_{MSSS}(m,n)$ will result in a slight increase in RMS error.

As was acknowledged by Figure 4.18 (p.94) and Figure 4.21 (p.98) previous studies by Huang et al. (1997) and Anandarajah (2005) identified a cyclic pattern in the RMS error results produced by the SCC and NSS (Anandarajah, 2005) routines. The

pattern provides errors that are smaller at integer pixel values and higher at half-pixel displacements. It was reasoned that this occurs because at half-pixel displacements the correlation peak is centred directly between two points. The cross-correlation of noise in the image will skew the correlation peak either positively or negatively and thereby generating RMS error peaks at these displacements. As has previously been identified (section 4.5, p. 93) as the correlation noise floor increases with increasing mean background noise intensities the RMS error pattern also increases in magnitude. Therefore, on average, this provides a small mean bias error (i.e. the central point of the mean bias oscillation; this is negatively biased with SCC due to PIE and NSS compensates for the underestimations) but variations between measurements will generate large RMS errors. At integer pixel displacements the correlation peak is centred on one point of the correlation field providing minimum variations. This thereby generates a cyclic pattern in the RMS error.

Since $R_{MSSS}(m,n)$ compensates for the presence of background noise then as Figure 7.5 identifies this algorithm is able to remove the cyclic pattern from the RMS error plot.

Although the experimental verifications for the processing of 32 x 32 pixel interrogation regions are in good agreement with their artificially generated counterparts there are still variations between experimental results and theoretical predictions. These uncertainties can be attributed to changes in particle image seeding density, the accuracy of the actual displacement and changes in pixel intensities between interrogation regions; including particle images and background noise. Anandarajah (2005) stated that variations in particle image size would remain small as the experimental parameters mean that each particle image would have diameters of between 2.777 and 2.778 pixels as each physical particle is between 0.7µm and 1.2µm.

This section has quantified the accuracy metrics generated using the SCC, NSS and $R_{MSSS}(m,n)$ processing algorithms on a series of 32 x 32 pixel experimental regions; these results are compared to those produced by processing artificial interrogation region with background noise. It has been identified that $R_{MSSS}(m,n)$ is the preferred

algorithm when processing 32 x 32 pixel experimental regions since the signal strength function suppresses underestimations caused by partial images; reduces RMS errors that are caused by the cross-correlation of unrelated particle images and suppresses the effects of background noise that also affects measurements. The next section compares the accuracy metrics generated from processing smaller experimental regions (i.e. 16 x 16 pixels) with theoretical predictions.

7.3.3 16 x 16 pixel interrogation region analysis and comparison

This section provides the accuracy metrics generated by the SCC, NSS and $R_{MSSS}(m,n)$ algorithms when processing 16 x 16 pixel regions. The experimental images provided by Anandarajah (2005) from the uniform displacement experiment were divided into 16 x 16 pixel regions. The accuracy metric plots from the processing of the 16 x 16 pixel experimental regions are illustrated in Figure 7.6 and Figure 7.7 respectively and are compared to theoretical predictions.

(a) experimental

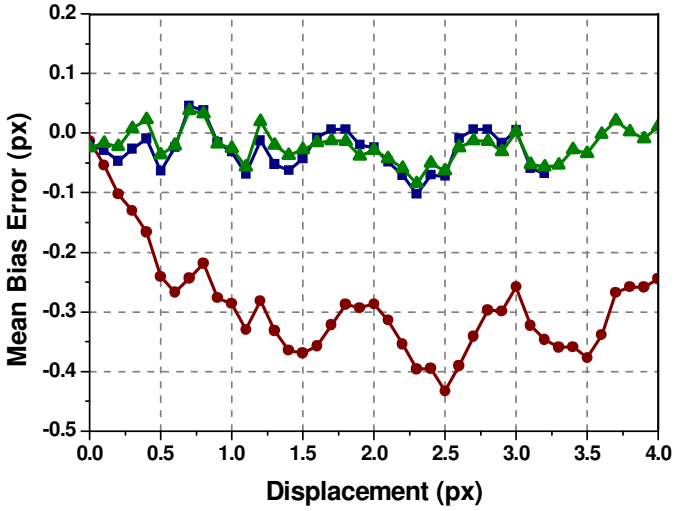

(b) theoretical

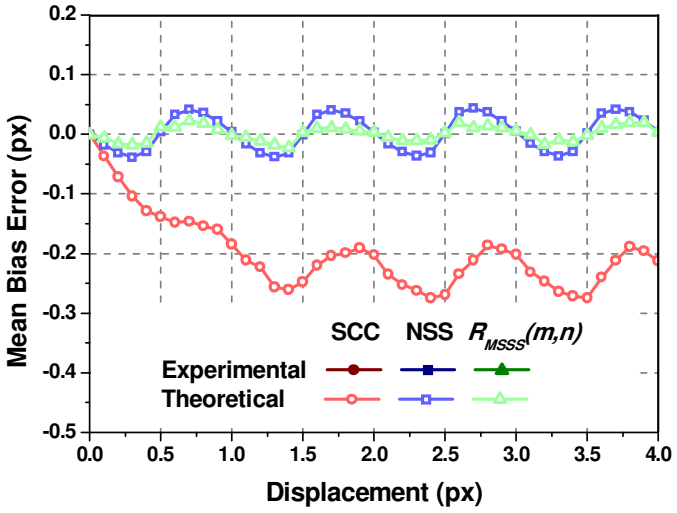

Figure 7.6 Experimental and theoretical mean bias error plot comparison (16 x 16 pixels)

Figure 7.6 illustrates that the mean bias error produced by SCC processing of 16 x 16 pixel interrogation regions is significantly higher than the results generated by

processing 32 x 32 pixel regions (Figure 7.4). This is caused by an increase in PIE whilst processing smaller regions (section 5.4, p.144). When the correlation field is normalised by signal strength, measurement underestimations caused by the cross-correlation of partial images is suppressed. As with the 32 x 32 pixel regions, $R_{MSSS}(m,n)$ also suppresses the effects of background noise to further reduce mean bias error. This is achieved by maintaining the ratio between the three central correlation peak points that are used to define the sub-pixel location of the correlation peak to those achieved with 'ideal' region processing using NSS. The benefits of using the $R_{MSSS}(m,n)$ algorithm over SCC are further demonstrated by Figure 7.7. The figure shows that the experimental RMS error results are comparable to the theoretical predictions. This demonstrates that signal strength function suppresses the asymmetry of the correlation peak caused by the cross-correlation of unrelated particle images that generates variations in measurements thereby suppressing RMS errors.

(a) experimental

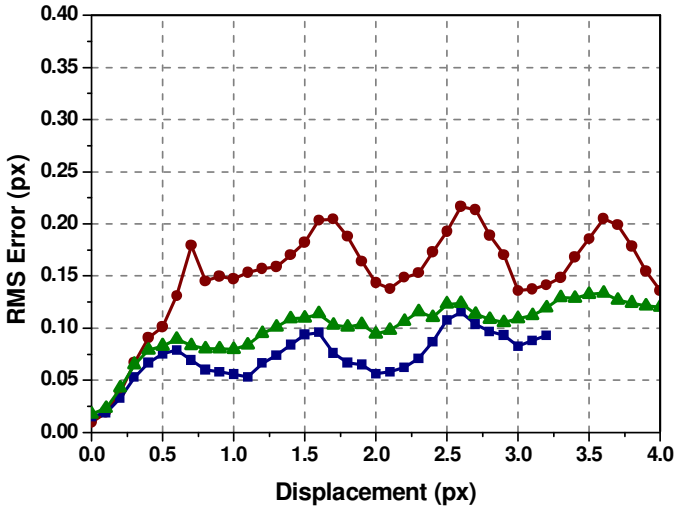

(b) theoretical

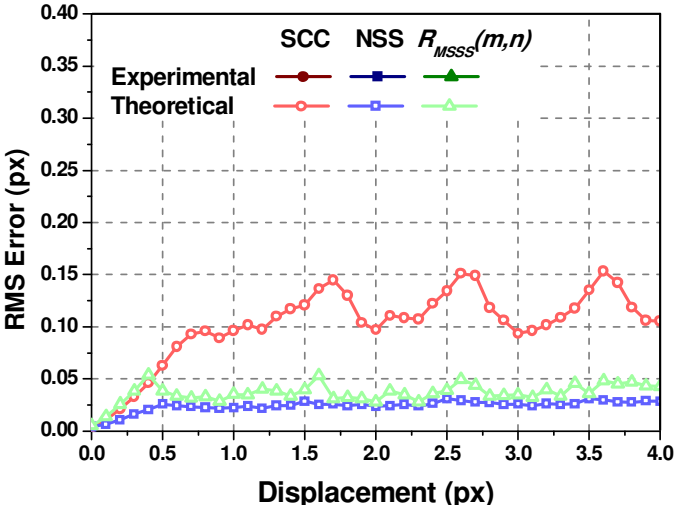

Figure 7.7 Experimental and theoretical RMS error plot comparison (16 x 16 pixel regions)

This section has demonstrated that when processing smaller interrogation regions (e.g. 16 x 16 pixel regions) the $R_{MSSS}(m,n)$ algorithm is preferred. This is because the routine is able to suppress the partial images that cause underestimations in measurements; accounts for the asymmetry of the correlation peak caused by the cross-correlation of unrelated particle images that result in RMS errors and compensates for background noise that also affects measurements.

7.3.4 Window shifting analysis and comparison

In this section, the experimental accuracy metrics generated by SCC, NSS and $R_{MSSS}(m,n)$ with discrete window shifting of 32 x 32 pixel regions are examined and compared to theoretical predictions. The experimental images captured by Anandarajah (2005) were processed using the cross-correlation algorithms and discrete window shifting described in section 6.2 (p.150). The error plots generated by these routines with DWS and the theoretical comparisons are show in Figure 7.8 and Figure 7.9 respectively.

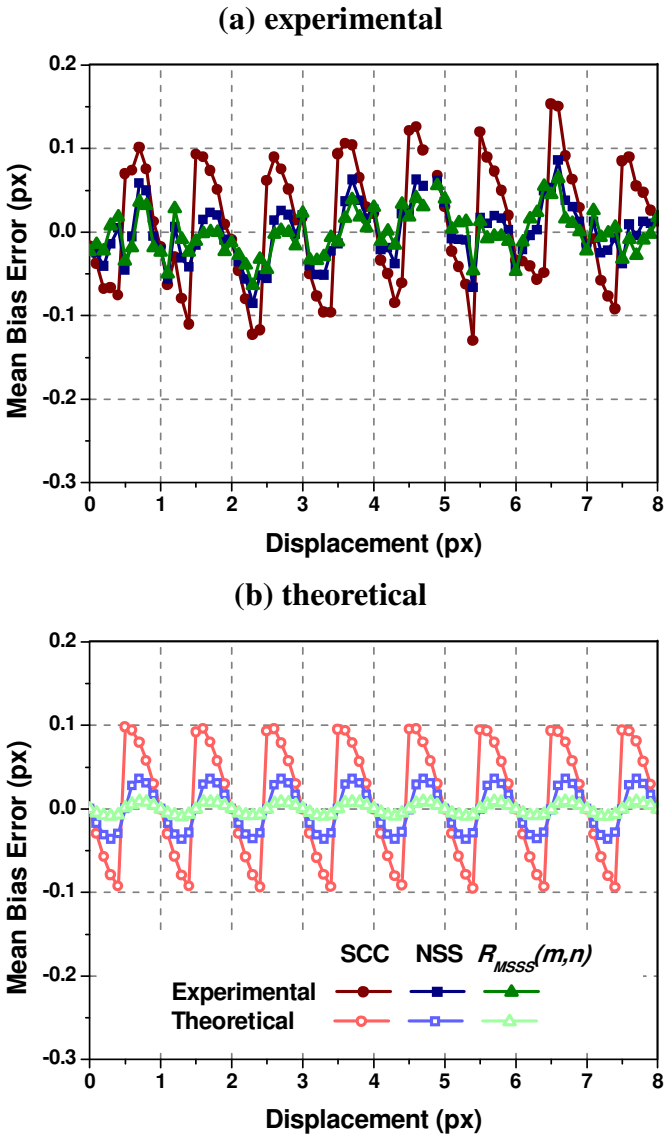

Figure 7.8 Experimental and theoretical mean bias error plot comparison for window shifting (32 x 32 pixels)

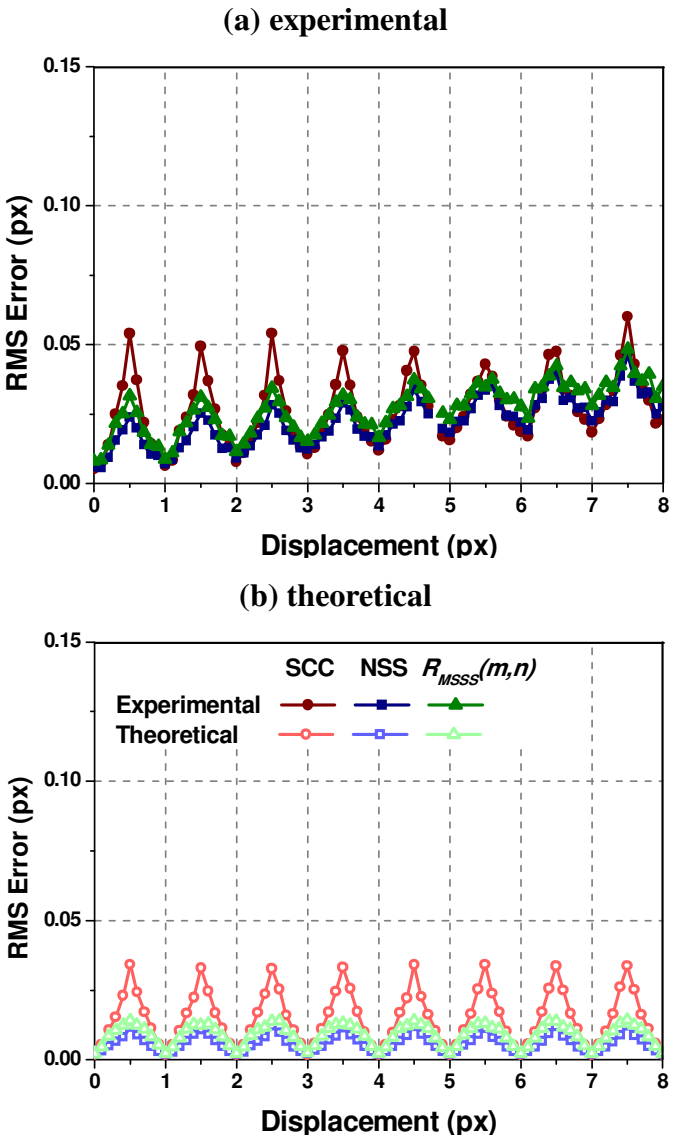

Figure 7.9 Experimental and theoretical RMS error plot comparison for window shifting (32 x 32 pixels)

The figures highlight that the DWS experimental results are in good agreement with theoretical predictions, and shows that DWS reduces measurement errors to sub-pixel displacements as discussed in section 6.2 (p.150).

7.3.5 PIPM analysis and comparison

This section provides the experimental error plots for SCC, NSS and $R_{MSSS}(m,n)$ with PIPM. The first region in each realisation is 16 x 16 pixels and is processed with larger regions of 32 x 32 pixels. Results generated by experimental images are compared to theoretical predictions.

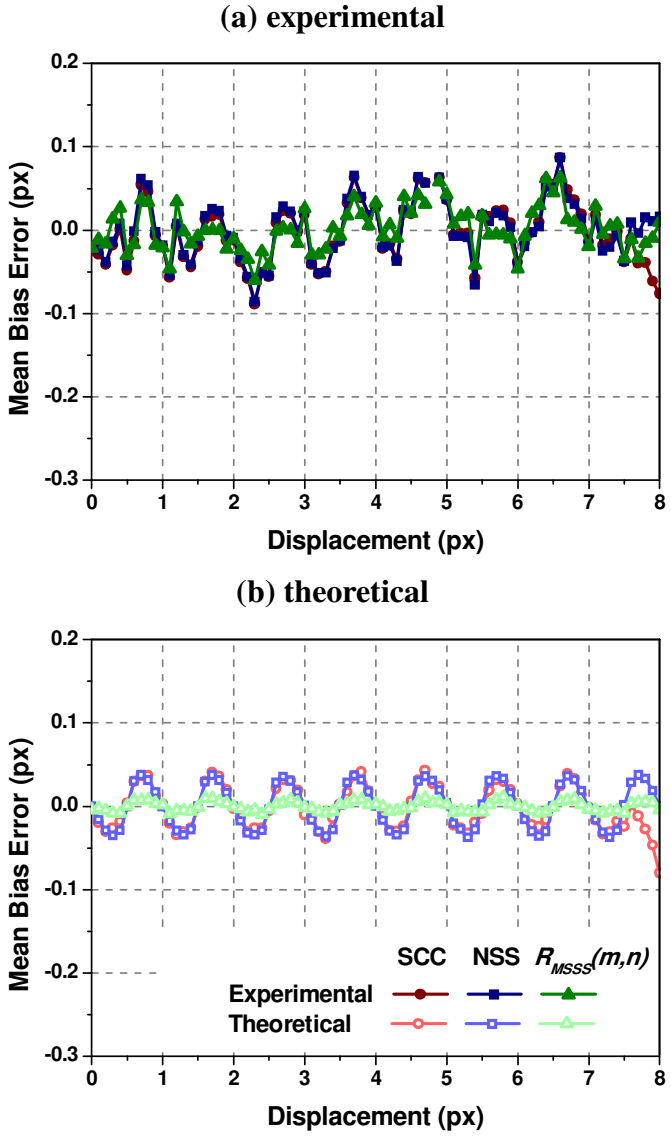

Figure 7.10 Experimental and theoretical mean bias error plot comparison for PIPM (16 x 16 pixel regions with 32 x 32 pixels regions)

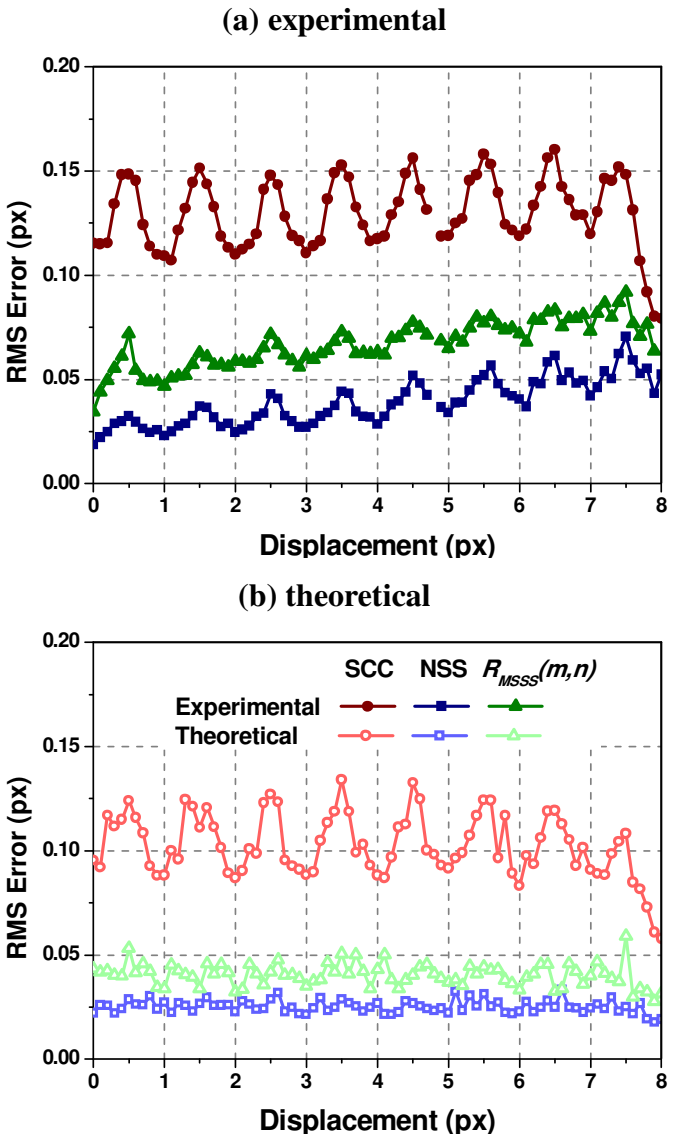

Figure 7.11 Experimental and theoretical RMS error plot for PIPM (16 x 16 pixel regions with 32 x 32 pixels regions)

PIPM results generated through experimental means are also shown to be in good agreement with their theoretical predictions. Figure 7.10 shows that the mean bias error is suppressed for the series of uniform displacements regardless of which processing algorithm is used; an explanation for this is given in section 6.3 (p.156). The RMS error plot generated in Figure 7.11(a) is also comparable to theoretical analysis with SCC generating the highest RMS errors, caused by the cross-correlation of unrelated particle images. The cyclic pattern is identified as being caused by the cross-correlation of background noise. Its effect is utmost at half-pixel displacements as was acknowledged by Figure 4.21 (p.98). With the application of

smaller regions the background noise effect on RMS error becomes more prominent resulting in the cyclic pattern for all processing algorithms.

7.4 Summary

This chapter has compared the accuracy metrics generated from experimental images with theoretical results from interrogation regions that contain mean background noise intensities of up to 15% of the 8-bit output. It has been shown that experimental results are in close agreement with theoretical predictions. When normalising the correlation field by signal strength there was a reduction in both mean bias and RMS error for commonly used interrogation regions of 32 x 32 pixels and smaller as well as for DWS and PIPM. The $R_{MSSS}(m,n)$ algorithm is shown to further suppress measurement errors by accounting for background noise intensities.

Chapter 8

Conclusions

Advances in image capture and laser-based technologies have lead to the development of time-resolved DPIV systems that have the potential to resolve the spatio-temporal dynamics of transient and turbulent flows. Being able to acquire 2D velocity vectors across a global domain that have both high spatial and temporal resolutions has provided fluid dynamic researchers with a technique has the prospect of being used to verify predictive computational models in the real world. However, before drawing any conclusions with regards to the validity and accuracy of DPIV velocity statistics, the systematic errors associated to the cross-correlation techniques have to be quantified. It is therefore essential to minimise these systematic errors in order to accurately resolve flow field measurements.

For this study, the accuracy of measurements is defined using two metrics, which are: mean bias error: describing the closeness an average measured value is to the actual result, and RMS error: which shows the variations in measurements across a data-set of measurements. Both metrics have to be minimised in order to provide accurate measurements.

A measurement evaluation in DPIV processing is typically provided by cross-correlation: using the fast Fourier transform algorithm in the Fourier domain, or digital direct cross-correlation in the spatial domain. Through processing data-sets of artificially generated realisations (Chapter 3, p.36) experiencing a series of known uniform displacements across each region it has been shown that the random distribution of particle images affects measurements when processing with these standard cross-correlation routines (Figure 4.2, p.68). Cross-correlation of clipped particle images (partial images) at the edge of each interrogation region which results from the random distribution across each region will cause measurement underestimations. The cross-correlation of unrelated particle images between

regions will cause variations in the shape of the correlation peak resulting in RMS errors. This clarifies the original findings of Anandarajah (2005) which goes against the previous assumption that the weighting of the correlation function is the contributory factor in providing measurement uncertainties.

Since cross-correlation was first used to quantify measurements (Willert and Gharib, 1991) several techniques developed to refine the accuracy of results. This study identified that discrete window shifting (Westerweel, 1997) with SCC processing takes advantage of sub-pixel displacement accuracy but does not account for the cross-correlation of randomly distributed particle images that cause measurement uncertainties (Figure 6.1, p.151). Likewise, particle image pattern matching (Huang et al., 1993a) that was originally developed to account for the out-of-pattern effect compensates for mean bias errors but cannot suppress RMS error (Figure 6.4, p.157). Suppression of these metrics with PIPM and SCC is dependent on the size of interrogation regions that are processed. This provides further evidence that the cross-correlation of unrelated and randomly distributed particle images affects the accuracy of measurements.

Cross-correlation normalisation functions were also introduced as a means of improving the accuracy of measurements. However, as section 2.8 (p.24) in conjunction with section 4.2 (p.66) identified, normalisation by area (section 4.3.1, p.73) and by variance (section 4.3.4, p.78) only affect the closeness of measurements to the actual value and not variations between individual results. Normalisation by intensity (section 2.8.3, p.28) and mean subtraction prior to cross-correlation (section 4.3.3, p.77) provided no improvement in measurement statistics over standard cross-correlation of 'ideal' interrogation regions. Although these weighting functions are unable to minimise both metrics each function accounts for the condition that was assumed to affect accuracy. Normalisation by area accounts for the non-uniform weighting of the correlation field (Figure 2.7, p.25), normalisation by intensity accounts for variations in correlation peak height. Normalisation by variance accounts for the image quality across and between realisations, and mean intensity subtraction prior to cross-correlation accounts for background noise intensities that will also affect measurements (section 5.2.5, p.120). Section 4.3.2 (p.75) showed

that the signal strength weighting function (NSS) compensated for the underestimations in measurements, caused by cross-correlation of partial images, and variations in the shape of the correlation peak, caused by the cross-correlation of related particle images. This function compensates for these systematic errors by normalising each point of the SCC field by the pixel intensities that are used to calculate each point. This thereby suppresses both the mean bias and RMS error metrics when processing 'ideal' artificial interrogation regions.

This study has demonstrated that although NSS is able to suppress both accuracy metrics when using a Gaussian sub-pixel estimator, the most accurate results are from the evaluation of 'ideal' interrogation regions where no background noise is present. Noise in DPIV analysis manifests as several quantities including: increasing the particle image seeding density per realisation, increasing the effective particle image size and also the addition of background noise that is inherent in experimental images. Each of which will increase the intensity content of an interrogation region. Qualitatively, these are expressed as intensities that contribute to the correlation field and therefore can affect the shape of the correlation peak. Section 3.9 (p.51) addressed the accuracy dependence on image quality by optimising the particle image size and seeding density using the standard cross-correlation algorithm. It has been demonstrated that each region should be populated with 22 particle images each with a diameter of 2.8 pixels, to provide the lowest accuracy metrics whilst using the standard cross-correlation algorithms. This concurs with the parameters stipulated by Huang et al. (1997) and Anandarajah (2005).

The addition of background noise into each displacement data-set provoked an increase in the amplitude of the mean bias error oscillation whilst also introducing a 'beating' effect into RMS error results when processing with both SCC and NSS (Figure 4.18, p.94). This increase in mean bias error amplitude was shown to be caused by a decrease in the ratios between the three points of the correlation peak used to evaluate the sub-pixel displacement during analysis which results from increasing the magnitude of the correlation noise floor. The 'beating' effect for SCC evaluation is caused by the decline in the ratios between the three correlation peak values coupled with variations in the shape of the correlation peak (Figure 4.20, p.

97). This not only contributes to an increase in RMS error as the mean intensity of the background noise increases, but at half-pixel displacements will cause an RMS error peak (Figure 4.18, p.94). This peak occurs because at half-pixel displacements the correlation peak is defined across two points on the correlation field; the addition of background noise will thereby skew the correlation peak and its effects are greatest at half-pixel displacements and hence causes significant variations for these displacements.

Several image enhancement algorithms have been developed to suppress background noise prior to cross-correlation. These are: average image subtraction, image thresholding and mean intensity kernel subtraction prior to cross-correlation (sections 5.2.1 to 5.2.3). However, although this systematic error can be suppressed with these enhancement algorithms SCC does not account for partial images that cause underestimations and the cross-correlation of unrelated particle images that cause measurement variations. Image enhancements with NSS provided a significant improvement over SCC results by accounting for the systematic errors caused by particle images but were unable to supply metrics typical of 'ideal' region analysis.

A robust processing algorithm called mean intensity subtraction prior to $R(m,n)$ cross-correlation normalised by signal strength, $R_{MSSS}(m,n)$ was subsequently introduced. This algorithm was shown to be able to compensate for the systematic errors caused random distribution of particle images across each realisation as well as the addition of background noise (Figure 5.11, p.128). $R_{MSSS}(m,n)$ is able to suppress both metrics as the mean background noise intensity increases because firstly the mean intensity from within the area that contributes to each point of the correlation field is subtracted from each pixel value to suppress background noise (section 5.2.5, p.120). This suppresses an increase in magnitude of the correlation noise floor with increasing background noise intensity and hence maintains the ratios between the three central points of the correlation field (Figure 5.12, p.129) to ratios gathered through 'ideal' region processing. It secondly takes advantage of the signal strength weighting function to compensate for random distribution of particle images across each realisation that includes partial images, by normalising by the pixel intensities that are used to calculate each point on the correlation field. This thereby

suppresses measurement underestimations and measurement variations that are prevalent with SCC. Therefore $R_{MSSS}(m,n)$ provides robust accuracy metrics as the mean intensity of background noise increases.

Results show that processing artificial regions, with additional background noise, using $R_{MSSS}(m,n)$ produces accuracy metrics typical of those generated by the NSS algorithm using 'ideal' images. Comparable results are also generated for equal-sized region cross-correlation (i.e. 32 x 32 pixels and smaller, Figure 5.19, p.145) as well as for the iterative techniques with moderate background noise intensities (Figure 6.3, p.154 for DWS and Figure 6.6, p.161 for PIPM). It has also been demonstrated that $R_{MSSS}(m,n)$ is able to compensate for changes in background intensity across an interrogation region (section 5.2.8, p.138) to provide metrics comparable to 'ideal' NSS analysis. Since $R_{MSSS}(m,n)$ has proven to be a robust algorithm with regards to suppressing background noise intensities it is also able to account for variations in background noise intensity between regions as well. Additionally, prior knowledge of a region's quality before evaluation with $R_{MSSS}(m,n)$ is not required. Typically, an image enhancement algorithm will assess this prior to cross-correlation.

The accuracy metrics predicted by analysis of artificially generated interrogation regions were verified using the controlled experiment described in Chapter 7. The original images were captured by Anandarajah (2005) and processed with NSS. However, the increase in metrics associated with background noise was not addressed. Experimental verifications of $R_{MSSS}(m,n)$ were shown to be in good agreement between theoretical predictions and experimental data. It is shown that $R_{MSSS}(m,n)$ minimises both accuracy metrics on the analysis of equal-sized interrogation regions and the iterative techniques over that of standard cross-correlation results by compensating for the presence of background noise and the random distribution of particle images, both of which are systematic errors in DPIV analysis.

This study has achieved its overall goal of defining the major systematic errors within DPIV processing that are apparent during cross-correlation and has provided a

solution in a robust processing algorithm that is able to suppress their affects. In addition, it has been identified that the three point Gaussian sub-pixel estimator, generally used to define the sub-pixel displacement, is suited to accurately defining measurements provided that there is no background noise, each particle image is the right size and that the systematic errors associated with cross-correlation are suppressed.

References

Adrian, R. J. (1991). "Particle-Imaging techniques for experimental fluid mechanics." Annual Review of Fluid Mechanics **23**: 261-304.

Adrian, R. J. (1995). Limiting resolution of particle image velocimetry for turbulent flow. Advances in Turbulence Research - 1995, POSTECH, Pohang, Korea.

Adrian, R. J. (2005). "Twenty years of particle image velocimetry". Experiments in Fluids. **39**: 159-169.

Anandarajah, K. (2005). Digital Particle Image Velocimetry (DPIV): Limitations to Measurement Accuracy. Ph.D. Thesis, Wolfson School of Mechanical and Manufacturing Engineering, Loughborough University, Loughborough, UK.

Bolinder, J. (2000). In situ estimation of the random error in DPIV measurement. 9th International Symposium on Flow Visualization, Edinburgh, Scotland, UK.

Burt, P. J., C. Yen and X. Xen (1982). Local correlation measures for motion analysis, a comparative study. Proceedings of the conference on pattern recognition and image processing, Las Vegas, NV, USA.

Dellenback, P. A., J. Macharivilakathu and S. R. Pierce (2000). "Contrast enhancement techniques for particle-image velocimetry". Applied Optics **39**(32): 5978-5990.

Drain, L. E. (1980). The Laser Doppler Technique. Chichester, John Wiley and Sons.

Durst, F., A. Melling and J. H. Whitelaw (1976). Principles and practice of laser-Doppler anemometry, Academic Press.

Eckstein, A. (2007). Development of Robust Correlation Algorithms for Image Velocimetry Using Advanced Filtering. Dissertation for Masters of Science in Mechanical Engineering. Department of Mechanical Engineering, Virginia Tech, Blacksburg, VA, USA.

El-Bakry, H. M. and M. Hamada, (2008). A New Implementation for High Speed Normalised Neural Networks in Frequency Space. In: Proceedings of 12th International Conference, KES 2008, Zargreb, Croatia, Part I, LNAI 5177, pp. 33–40.

Fincham, A. M., and G. R. Spedding (1997).”Low cost, High Resolution DPIV for Measurement of Turbulent Flow”. Experiments in Fluids, **23**: 449-462.

Fore, L. B., A. T. Tung, J. R. Buchanan and J. W. Welch (2005). “Nonlinear temporal filtering of time-resolved digital particle image velocimetry data”. Experiments in Fluids **39**:22-31.

Fore, L. B. (2010). “Reduction of peak-locking errors produced by Gaussian sub-pixel interpolation in cross-correlation digital particle image velocimetry.” Measurement Science and Technolgy **21**: 1-6

Gonzales, R. and P. Wintz (1987). Digital Image Processing. New York, Addison-Wesley.

Goodman, J. W. (1968). Introduction to Fourier Optics. San Francisco, McGraw-Hill.

Goodman, J. W. (1996). Introduction to Fourier Optics. New York, McGraw-Hill.

Gui, L., and S. T. Wereley (2002). “A Correlation-based continuous window-shift-technique to reduce the peak-locking effect in digital PIV image evaluation”. Experiments in Fluids. **32**: 506-517.

Hain, R., C. J. Kähler and C. Tropea (2007). "Comparison of CCD, CMOS and intensified cameras" Experiments in Fluids **42**: 403–411.

Hart, D., (1998). The Elimination of Correlation Errors in PIV processing. 9th International Symposium on Applications of Laser Techniques to Fluid Mechanics. Lisbon, Portugal.

Huang, H. and H. E. Fielder (1993a). "Deformed Particle Image Pattern Matching in Particle Image Velocimetry". Applied Scientific Research **51**: 179-183.

Huang, H., H. E. Fielder and J. J. Wang (1993b). "Limitations and improvements of PIV, Part I: Limitations of conventional techniques due to deformation of particle image patterns." Experiments in Fluids **15**: 168-174.

Huang, H., D. Dabiri and M. Gharib (1997). "On errors of digital particle image velocimetry." Measurement Science and Technology **8**: 1427-1440.

Keane, R. D. and R. J. Adrian (1992). "Theory of cross-correlation analysis of PIV images." Applied Scientific Research **49**: 189-190.

Jambunathan, K., X. Ju, B. Dobbins and S. Ashfort-Frost (1997) "An improved cross-correlation technique for particle image velocimetry." Measurement Science and Technology **6**: 507-514.

Lewis, J. P. (1995). Fast Template Matching. Vision Interface 95, Canadian Image Processing and Pattern Recognition Society, Quebec City, Canada. (also see "Fast Normalized Cross-correlation")

Lourenco, L. and A. Krothapalli (1995). "On the accuracy of velocity and vorticity measurements with PIV". Experiments in Fluids **18**: 421-428.

Marxen, M., P. E. Sullivan, M. R. Loewen and B. Jahne (2000). "Comparison of Gaussian particle centre estimators and the achievable measurement density for particle tracking velocimetry." Experiments in Fluids **29**(2): 145-153.

McKenna, S. P. and W. R. McGillis (2002). "Performance of digital image velocimetry processing techniques." Experiments in Fluids **32**(1): 106-115.

Meinhart, C. D., S. T. Wereley and J. G. Santiago (2000), "A PIV algorithm for estimating time-averaged velocity fields", Journal of Fluid Engineering, **122**: 285-289.

Meinhart, C.D. and S. T. Wereley (2003). "The theory of diffraction-limited resolution in microparticle image velocimetry". Measurement Science and Technology, **14**: 1047-1053.

Nobach, H. N. Damaschke and C. Tropea (2004). "High-precision sub-pixel interpolation in particle image velocimetry image processing". Experiments in Fluids **39**: 299-304

Nogueira, J., A. Lecuona and P. A. Rodríguez (1999). "Local field correction PIV: on the increase of accuracy of digital PIV systems." Experiments in Fluids **27**: 107-116.

Nogueira, J., A. Lecuona and P. A. Rodriguez (2001). "Identification of a new source of peak locking, analysis and its removal in conventional and super-resolution PIV techniques." Experiments in Fluids **30**: 309-306.

Prasad, A. K., R. J. Adrian, C. C. Landreth and P. W. Offutt (1992). "Effect of resolution on the speed and accuracy of particle image velocimetry interrogation". Experiments in Fluids **13**: 105-116.

Pust, O (2000). PIV: Direct Cross-Correlation compared with FFT-based Cross-Correlation. In: Proceedings of the 10th International Symposium on Applications of Laser Techniques to Fluid Mechanics, Lisbon, Portugal.

Raffel, M., C. E. Willert and J. Kompenhans (1998). Particle Image Velocimetry: A Practical Guide. First Edition. Gottingen, Springer-Verlag.

Raffel, M., J. Kompenhans, S. T. Wereley and C. E. Willert (2007). Particle Image Velocimetry: A Practical Guide. Second Edition. Gottingen, Springer-Verlag.

Roesgen, T. (2003). "Optimal subpixel interpolation in particle image velocimetry". Experiments in Fluids **35**: 252–256.

Roth, G. and J. Katz (2001). "Five techniques for increasing the speed and accuracy of PIV interrogation" Measurement Science and Technology 12: 238-245.

Scarano, F. and M. L. Riethmuller (2000). "Advances in iterative multigrid PIV image processing." Experiments in Fluids **29**(7): S051-S060.

Scarano, F. (2002). "Iterative image deformation methods in PIV." Measurement Science and Technology **13**: R1-R19.

Shavit, U., R. J. Lowe and J. V. Steinbuck (2006). "Intensity Capping: a simple method to improve cross-correlation PIV results". Experiments in Fluids **42**:225–240.

Tokumaru, P. and P. Dimotakis (1995). "Image correlation velocimetry." Experiments in Fluids **19**: 1-15.

Wernet, M. J. (2005), "Symmetric phase only filtering: a new paradigm for DPIV data processing". Measurement Science and Technology,. **16**(3): 601-618.

Westerweel, J. (1993a). Analysis of PIV interrogation with low pixel resolution. Proceedings of the SPIE-2005. Optical Diagnostics in Fluid and Thermal Flow, San Diego, USA.

Westerweel, J. (1993b). Digital particle image velocimetry: theory and application. Ph.D. Thesis. Delft, Technische Universiteit, Delft, The Netherlands: 231.

Westerweel, J. (1997). "Fundamental of digital particle image velocimetry." Measurement Science and Technology **8**: 1379-1392.

Westerweel, J., D. Dabiri and M. Gharib (1997). "The effect of a discrete window offset on the accuracy of cross correlation analysis of digital PIV recordings." Experiments in Fluids **23**(1): 20-28.

Westerweel, J., P. F. Geelhoed and R. Lindken (2004). "Single-pixel resolution ensemble correlation for micro-PIV applications". Experiments in Fluids **37**:375–384

Westerweel, J. and F. Scarano (2005). "Universal outlier detection for PIV data". Experiments in Fluids 39: 1096-1100.

Willert, C. E. (1996). "The Fully Digital Evaluation of Photographic PIV Recordings". Applied Scientific Research **56**: 79-102.

Willert, C. E. and M. Gharib (1991). "Digital particle image velocimetry." Experiments in Fluids **10**: 181-193.

Williams, T. C., G. K. Hargrave and N. A. Halliwell (2003). "The development of high-speed particle image velocimetry (20 kHz) for large eddy simulation code refinement in bluff body flows." Experiments in Fluids **35**:85-91.

Appendix I - Noise distributions

Although the background noise generated and analysed throughout this thesis has been modelled from experimental images the background noise distribution will vary as different data-sets are analysed. This section provides the SCC error plots when each data-set contains various distributions of Gaussian background noise whilst maintaining the mean intensity at 15% of the total 8-bit output.

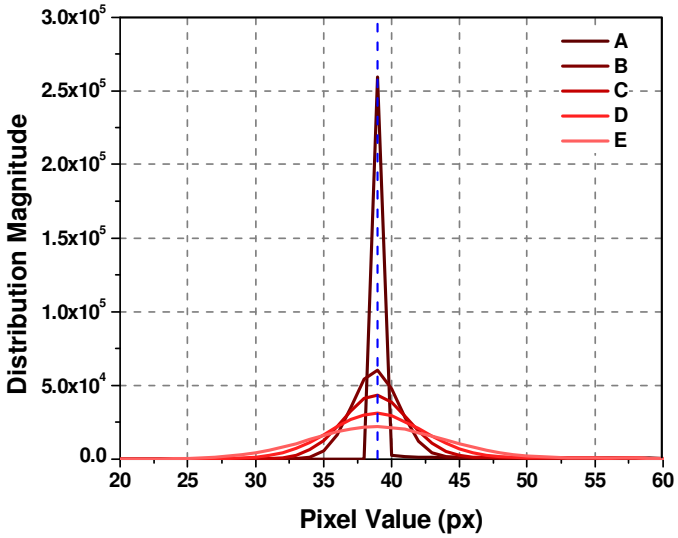

Figure A1.1 Various noise distributions whilst maintaining a mean background noise intensity of 15%

The background noise distributions for this analysis are shown in Figure A1.1 and vary from when there is a uniform magnitude of background noise (**A**) across each interrogation region (i.e. each pixel has a value of 39 grey-scale). For the other four data-sets provided in Figure A1.1, the standard deviation of the distribution is increases accordingly and includes the distribution used throughout this research (**C**).

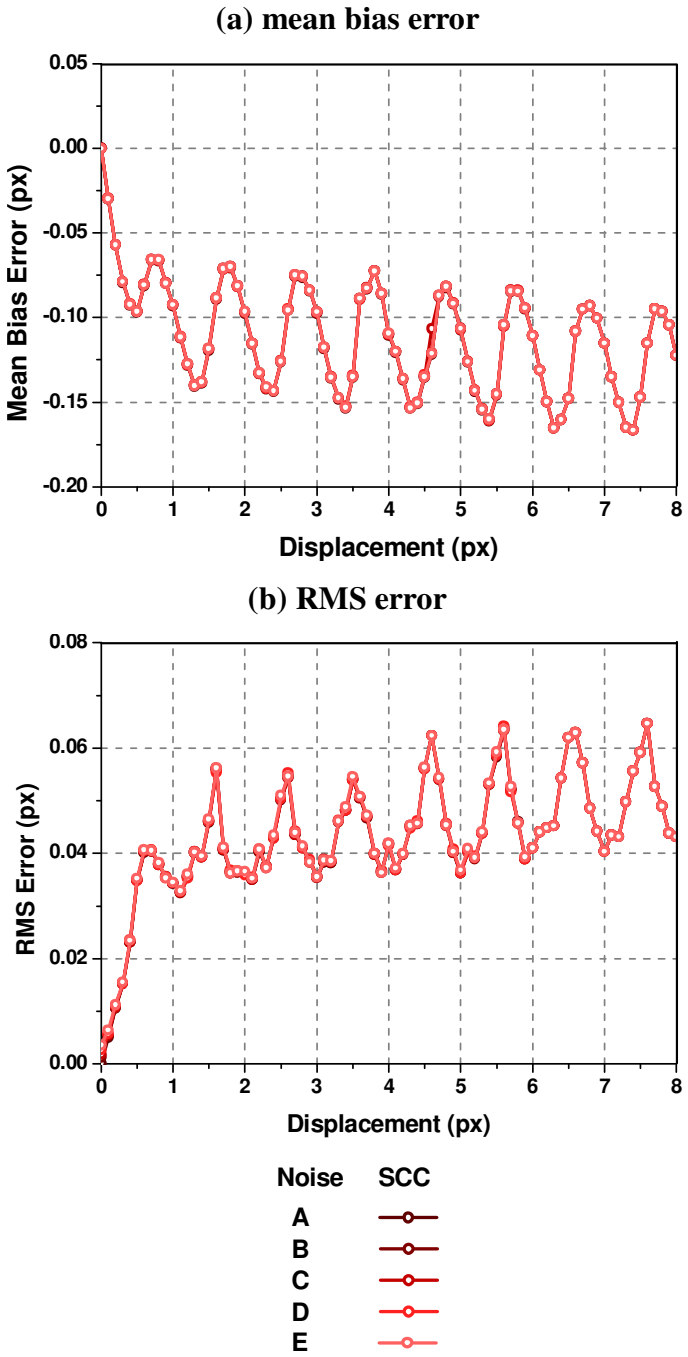

Figure A1.2 Error plots for a mean background noise intensity of 15% for various distributions of noise

Figure A1.2 clearly highlights that the distribution of Gaussian white noise across each interrogation region does not affect the accuracy metrics since the error plots generated from SCC of the five data-sets are identical. These error plots do however demonstrate that it is the mean intensity of the background distribution that affects measurement as was identified in Figure 4.18 (p.94).

Appendix II - Publications

Partial Image Error (PIE) in Digital Particle Image Velocimetry (DPIV), E. Putman, G. K. Hargrave and N. A. Halliwell, Proceedings in the 26th AIAA Aerodynamic Measurement Technology and Ground Testing Conference, Seattle, WA, United States of America, 2008

Partial Image Error (PIE) in Digital Particle Image Velocimetry (DPIV)

E.R.J. Putman[1], G.K. Hargrave[2] and N.A. Halliwell[3]
Wolfson School of Mechanical and Manufacturing Engineering, Loughborough University, Leicestershire, LE11 3TU, United Kingdom.

This paper examines and quantifies Partial Imaging Error (PIE) that is caused when an image is divided up into smaller interrogation regions, cutting particle images at the edge of a region in two. Original investigations have assumed that this source of error is negligible, yet this paper will prove that PIE is in fact a major contributor to measurement error and is more significant that the non-uniform weighting of the correlation function usually associated with measurement discrepancies. Results show that this error is significant for typical seeding densities and commonly used interrogation region sizes. If the correlation of regions that are 16 x 16 pixels or less is attempted PIE can prohibit a meaningful result from being obtained despite there being a valid correlation peak. It will also be highlighted that processes usually associated with improving the accuracy of measurements are unable to account for the effects of PIE and hence this inherent error remains. In order to reduce the effects of PIE and to increase measurement accuracy, it is necessary to normalise the correlation field before using a curve fit estimator on the correlation peak. However, it is shown that normalising by overlapped area, which is typically used as a normalisation function, is able to reduce mean bias error by correcting for the non-uniform weighting of the correlation function yet has no effect on RMS error. To correct for PIE, normalisation of the correlation field by signal strength (NSS) is presented here as an effective means of reducing both the mean bias and RMS error.

Nomenclature

d_a	= Actual particle image displacement
d_b	= Mean bias error
d_m	= Mean measured displacement
DPIV	= Digital Particle Image Velocimetry
FFT	= Fast Fourier Transform
$I(x,y)$	= Two-dimensional Gaussian intensity profile
I_0	= Peak image intensity
$I_1(i,j)$	= First Interrogation region
$I_2(i,j)$	= Second interrogation region
$\hat{I}_1(\xi,\eta)$	= Fourier transform of $I_1(i,j)$
$\hat{I}_2^*(\xi,\eta)$	= Complex conjugate of the Fourier transform of $I_2(i,j)$
NSS	= Normalisation by Signal Strength
PIE	= Partial Image Error
$R(m,n)$	= Direct digital cross-correlation
$R_{OA}(m,n)$	= Normalisation of the $R(m,n)$ correlation field by overlapped area
RMS	= Root mean square
(x_c,y_c)	= Pixel location of the correlation peak
(x_{pk},y_{pk})	= True centre of correlation peak

[1] Ph.D. Student, Student Member, AIAA.
[2] Professor of Optical Diagnostics, Member, AIAA
[3] Professor of Optical Engineering

I. Introduction

Digital Particle Image Velocimetry (DPIV) is an important, whole field measurement technique capable of quantifying two-dimensional velocity fields within a flow. In a typical DPIV experiment, two images of a flow seeded with tracer particles and illuminated by a light sheet are both captured within a short time period. These images are then divided into smaller interrogation regions and corresponding regions from each image are then cross-correlated, typically with a fast Fourier Transform (FFT) algorithm. This generates a correlation field where the position of the highest peak corresponds to the average particle image displacement between the two interrogation regions. The displacement is then enhanced to sub-pixel accuracy by fitting a curve estimator (typically a three point Gaussian) across the signal peak. This process is repeated over the entire image and allows for velocity vectors to be extracted from each region to form a two-dimensional velocity map of the flow under examination.

This work quantifies the inherent errors that occur in a DPIV experiment due to the random distribution of particle images between each region. This random positioning means that a number of complete particle images will sit entirely within a region whilst some will intersect the boundary causing PIE. For an actual displacement of d_a we define a mean displacement d_m and a mean bias error d_b over N measurements by:

$$d_m = \frac{1}{N}\sum_{i=1}^{N} d_i \Leftrightarrow d_b = d_m - d_a \qquad \textbf{(1)}$$

where d_i is the displacement from a single measurement.

In addition, the root mean square (RMS) error which measures the deviation of individual measurements from the mean is defined as:

$$\sigma = \sqrt{\frac{1}{N}\sum_{i=1}^{N}\left(d_i - \bar{d}_i\right)^2} \qquad \textbf{(2)}$$

By calculation the average displacement and the variation from the average means that the inherent measurement errors within a DPIV experiment can be quantified.

II. Processing Methods

The average particle image displacement between two regions is computed using a cross-correlation algorithm. For equal sized interrogation regions (typically 32 x 32 pixels) the favoured cross-correlation routine, used in commercial systems, is the fast Fourier Transform (FFT) preformed in the frequency domain. For a pair of regions $I_1(i,j)$and $I_2(i,j)$their cross-correlation is written as:

$$I_1(i,j) \otimes I_2(i,j) \Leftrightarrow FFT^{-1}\left(\hat{I}_1(\xi,\eta) \times \hat{I}_2^{*}(\xi,\eta)\right) \qquad \textbf{(3)}$$

where $\hat{I}_1(\xi,\eta)$ denotes the Fourier transform of $I_1(i,j)$ and $\hat{I}_2^{*}(\xi,\eta)$ represents the complex conjugate of the Fourier transform of $I_2(i,j)$. The pixel position during correlation is denoted by (i,j). However, if regions are cross-correlated in the spatial domain both equal and non-equal sized regions can be used to determine their respective displacements between regions, this is defined as:

$$R(m,n) = \sum_{i=0}^{M}\sum_{j=0}^{N} I_1(i,j)\, I_2(i-m, j-n) \qquad \textbf{(4)}$$

Computation of the correlation field in the frequency domain defined in Eq. (3) is subjected to an effect referred to as 'wrap around' caused by the assumed periodicity of the signal when FFT is used. This can be avoided if regions are zero-padded[1] before computing with FFT making results equate to those of *R(m,n)* correlation.

A. Location of the correlation peak

Following the computation of the correlation field, the position of the highest peak (the signal peak), is used to determine the average particle image displacement between the two regions. The position of this peak can be located to within ±0.5 pixels yet the accuracy of its location can be enhanced to a sub-pixel position if a curve estimator is fitted across the correlation peak. The most commonly used curve estimator is a three point Gaussian fit and if the pixel location of the signal peak is given as (x_c,y_c) then the sub-pixel peak centre is (x_{pk},y_{pk}) where the three point Gaussian fit[2] is defined as:

$$x_{pk} = x_c + \frac{\log R(x_c - 1, n_c) - \log R(x_c + 1, y_c)}{2(\log R(x_c - 1, y_c) - 2\log R(x_c, y_c) + \log R(x_c + 1, y_c))} \qquad \textbf{(5)}$$

$$x_{pk} = x_c + \frac{\log R(x_c - 1, n_c) - \log R(x_c + 1, y_c)}{2(\log R(x_c - 1, y_c) - 2\log R(x_c, y_c) + \log R(x_c + 1, y_c))}$$

From Eq. (5) it is clear that the central point (x_c,y_c) and the values of the four neighbouring points are of high importance when calculating the sub-pixel position of the correlation peak. For the same velocity measurements, discrepancies in the relative values between subsequent measurements caused by the random distribution of particle images must be normalised before a peak estimator is fitted across the correlation peak in order to reduce the RMS error defined in Eq. (2).

III. Modelling of the Experiment

In order to quantify the inherent errors that occur due to the random positioning of particle images between subsequent measurements a theoretical model of a DPIV experiment was developed, which would not be subject to any form of experimental error.

To a good approximation it can be assumed that an individual particle image can be modelled as a two-dimensional Gaussian intensity profile[3], $I(x,y)$ which is given as:

$$I(x, y) = I_0 \exp\left[\frac{(x - x_0)^2 - (y - y_0)^2}{\sigma_i^2}\right] \qquad \textbf{(6)}$$

Where the centre of the particle image is located at $I(x_0,y_0)$ with the maximum intensity of I_0. The particle image diameter d_i is defined as the $e^{-½}$ intensity value of the Gaussian function.

To evaluate the inherent error caused by the random distribution of particle images a simple uniform flow, moving purely in the *x*-direction, was modelled where the actual displacement between regions could be controlled and ranged between zero and eight pixels whilst also including sub-pixel displacements. To generate the sub-pixel displacements, a 3200 x 3200 pixel interrogation region was populated with 22 randomly distributed high resolution particle images as shown in Fig. 1a). A second high resolution region was then generated by taking the location of each particle image in the first region and displacing each of them by a prescribed amount in the *x*-direction. These high resolution regions were then digitised, based on an 8-bit imaging device (256 grey-scale) to produce two 32 x 32 pixel

regions, one of which is shown in Fig. 1b). The size of region and the 8-bit imaging device is commonly used in commercial DPIV systems. Digitisation also means that the location of each particle image can be determined to within one-hundredth of a pixel.

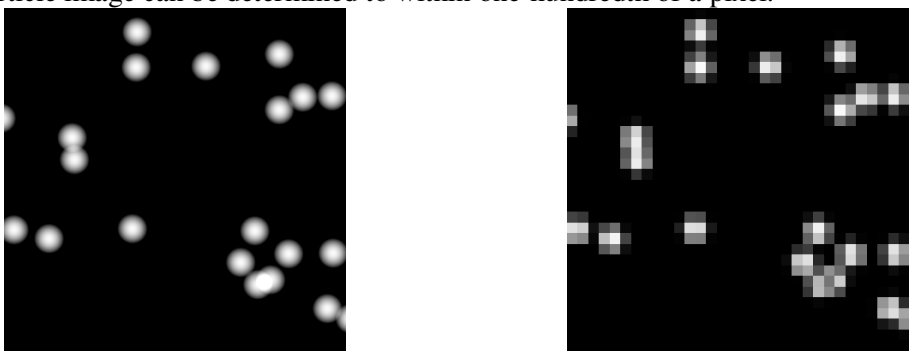

(a) high resolution region (3200 x 3200 pixels) (b) digitised region (32 x 32 pixels)

Figure 1. Particle images distributed within an interrogation region

Each region was populated with 22 particle images each with a digitised diameter of 2.8 pixels as this avoids errors associated with a poor signal-to-noise ratio (SNR) and an inadequate pixel resoltion[3]. A data-set containing 300 realisation were calculated for each displacement. When the measured displacement was calculated for each realisation and then averaged over the number of realisations there are equal numbers of particle images entering into and out of each interrogation region pair, therefore the measurement error relating to the random distribution of particle images can be determined.

IV. Model Predictions

In order to quantify the effect of the correlation noise floor on measured displacement, an average noise floor was calculated for the same displacement data-set for 300 realisations. This was accomplished by computing 300 correlation fields from correlating 300 statistically independent interrogation region pairs where the position of the particle images in the second region are not related to the position of the particle images in the first. Each pair of independent regions were correlated using *R(m,n)* and FFT defined by Eqs. (3) and (4) respectively. The correlation field formed were summed and averaged to generate a mean correlation noise floor for both *R(m,n)* and FFT correlation which can be seen in Figs. 2 and 3 respectively.

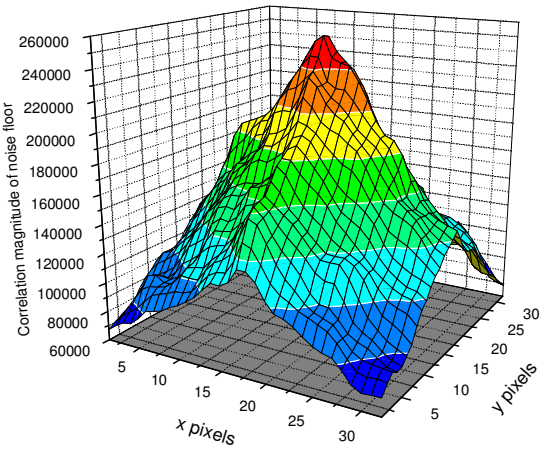

Figure 2. *R(m,n)* correlation noise floor

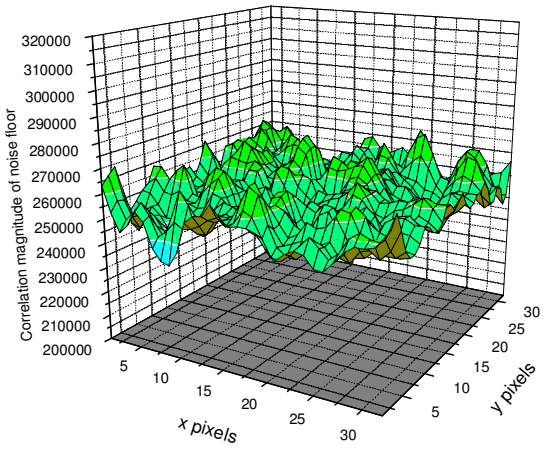

Figure 3. FFT correlation noise floor

The pyramid shaped noise floor developed from *R(m,n)* correlation is due to the change in overlapped area that occurs when each correlation value is calculated. This shape has been

used to explain why the correlation peak is bias toward a smaller displacement value for the correlation of each realisation[4]. This negative bias has been well reported in literature and methods for its avoidance have included using an appropriate weighting function or by the subtraction of the mean intensity value of the interrogation region before correlation commences[5]. FFT correlation, on the other hand, generates a flat noise floor caused by the periodic wrap around effect inherent with the FFT process.

The mean bias error plot shown in Fig 4a) is based on a range of displacements from one to eight pixels and extending through sub-pixel values whilst analysing 32 x 32 pixel interrogation regions using *R(m,n)* and FFT. The negative mean bias results for *R(m,n)* are anticipated due to the assumption that the pyramid noise floor will skew the correlation peak towards smaller displacements. However, the mean bias calculated from FFT correlation follows the same trends as those for *R(m,n)* yet as was shown in Fig. 3, FFT correlation generates a flat noise floor and therefore should not show a bias. This suggests that the correlation noise floor only plays a minor role in error propagation. Fig. 4 also includes the RMS error plot extending over the same displacement range for the correlation of 32 x 32 pixel interrogation regions. The results show there are large variations in measurements between individual realisations that extend over the entire examined range.

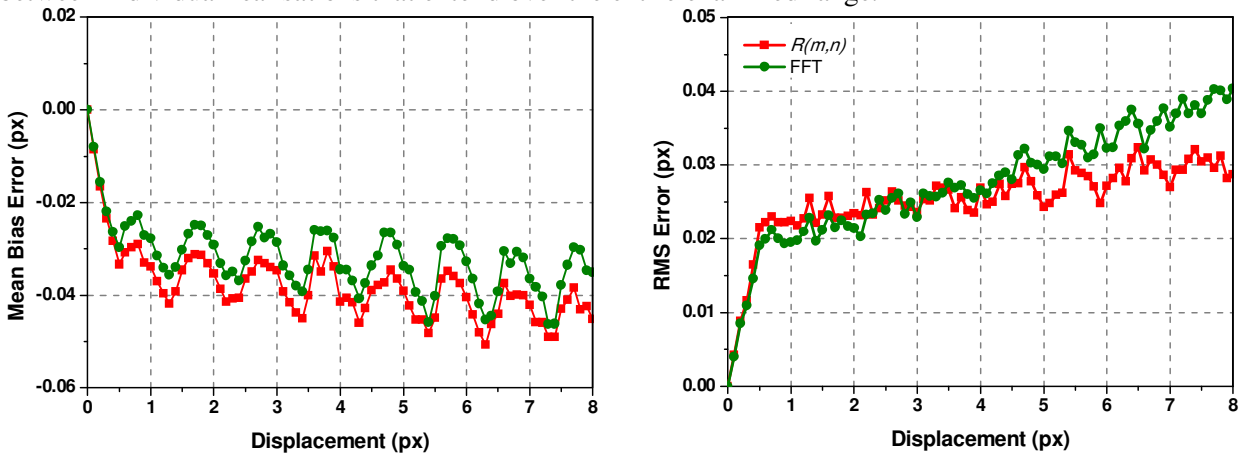

(a) mean bias error – 32 x 32 pixels (b) RMS error – 32 x 32 pixels

Figure 4. Measurement error plots - *R(m,n)* and FFT analysis

It is interesting to consider the equivalent error associated with the correlation of 16 x 16 pixel interrogation regions that are increasingly being used in DPIV analysis. The mean bias and RMS error results are shown in Fig. 5. The latter Fig. 5b) raises serious concerns about experimental accuracy with FFT correlation, which is used in most commercially available PIV systems, to compute the correlation field using the smaller sizes interrogation regions.

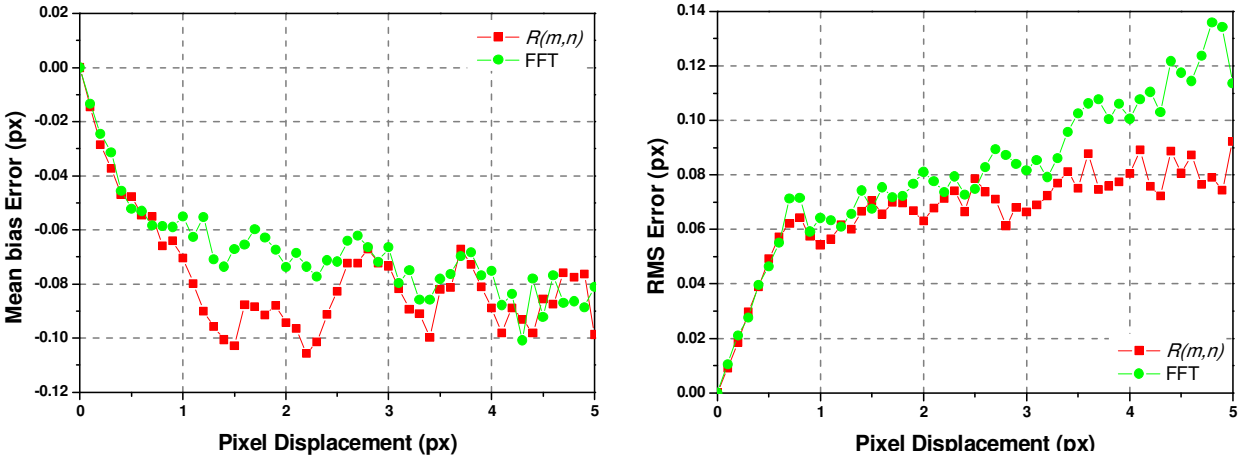

(a) mean bias error – 16 x 16 pixels (b) RMS error – 16 x 16 pixels

Figure 5. Measurement error plots – *R(m,n)* and FFT analysis

In the following section we will show that the negative mean bias which has previously been assumed to be due to the non-uniform weighting of the correlation function is in fact dominated by the effects of partial images found at the boundary of an interrogation region. Initial investigations recognised that partial images were a source of measurement error[6] but their effect were assumed to be negligible. Partial imaging was also recognised by Nogueira et al.[7] as being a major contributor to measurement error and proposed a solution for their removal. This paper will further quantify this error and will highlight that processes assumed to increase the accuracy of measurements as in fact unable to do so due to PIE. An alternative and improved solution is proposed to correct for the inclusion of partial images and therefore reduce both the mean bias and RMS error over a range of displacements.

V. Partial Images

When equal-sized regions are correlated, the signal peak is inherently skewed towards smaller displacement values due to the presence of partial images at the edge of a region. The importance of partial imaging as a source of measurement error can be best explained using a simplified example shown in Fig, 6. Here, two particle images in region $I_1(i,j)$ are displaced by two pixels in the x-direction so that one particle image in the second exposure $I_2(i,j)$ is clipped at the boundary. The corresponding (one-dimensional) correlation signal peak for $R(m,n)$ and FFT is shown in Fig. 7. The value to the left of the correlation peak is larger than that on the right, hence the correlation peak is skewed towards a smaller value.

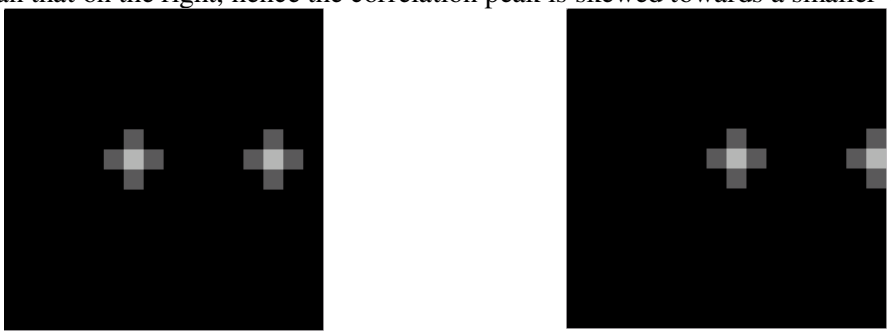

First interrogation region Second interrogation region

Figure 6. Partial image in the second interrogation region

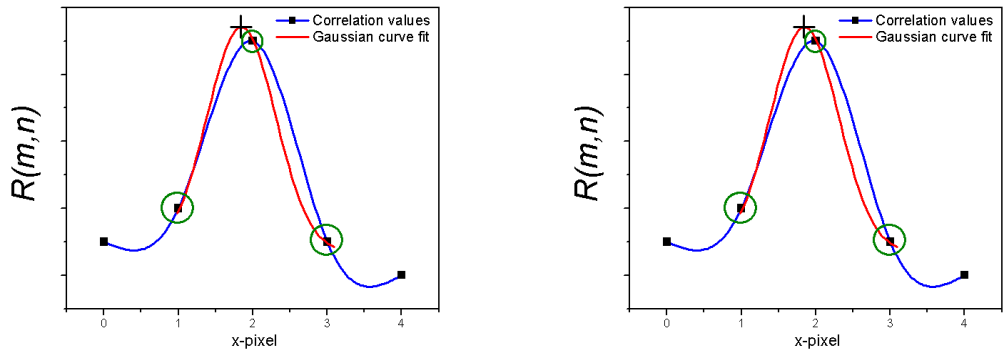

(a) $R(m,n)$ routine (b) FFT routine

Figure 7. Correlation peak for a partial image in the second interrogation region

In contrast, Fig. 8 shows a partial and complete particle image in the first exposure. One again these are subjected to a two pixel shift, forming two complete particle images in the second exposure. Correlation of these two regions still cause a negative skew in results, as is seen in Fig. 9. This inherent bias explains why that even in the presence of a flat noise floor (as with FFT correlation) the negative mean bias results shown in Fig. 4 are produced.

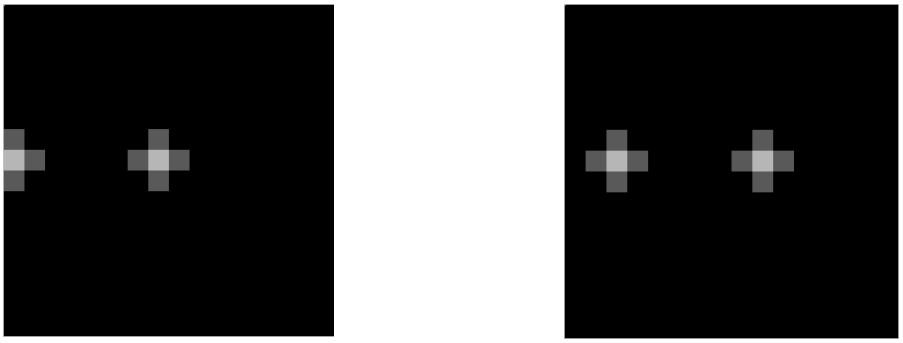

First interrogation region Second interrogation region

Figure 8. Partial image in the first interrogation region

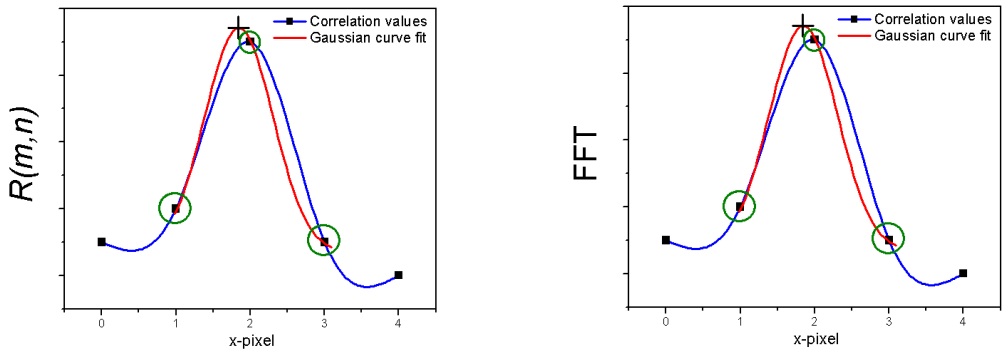

(a) *R(m,n)* routine (b) FFT routine

Figure 9. Correlation peak for a partial image in the first interrogation region

In this simplified example it is fair to assume that window shifting[5] the second region $I_2(i,j)$ by two pixels in order to maintain a high SNR will remove the presence of the partial images and hence restore the symmetry to the correlation peak. However, it should be noted that when the two regions are fully populated with randomly dispersed particle images, the first exposure will always be exposed to the effects of PIE and will also introduce partial images at the boundary of the second region, hence discrete window shifting is unable to account for the effects of PIE on measurements.

A further illustration of the effect of partial imaging is shown in Fig. 10 below. This error plot shows that the mean bias produced when only complete particle images were randomly distributed within each interrogation region, maintaining the seeding density and the particle image diameter as before. These regions were correlated using *R(m,n)* to produce a mean bias error plot that is not influenced by partial imaging. Furthermore, to show that the noise floor has little effect on the overall measurement error, a noise floor was generated in each correlation field by adding six complete but uncorrelated particle images into each interrogation region. For comparison the mean bias plots for the real case consisting of complete and partial images is also shown in the figure.

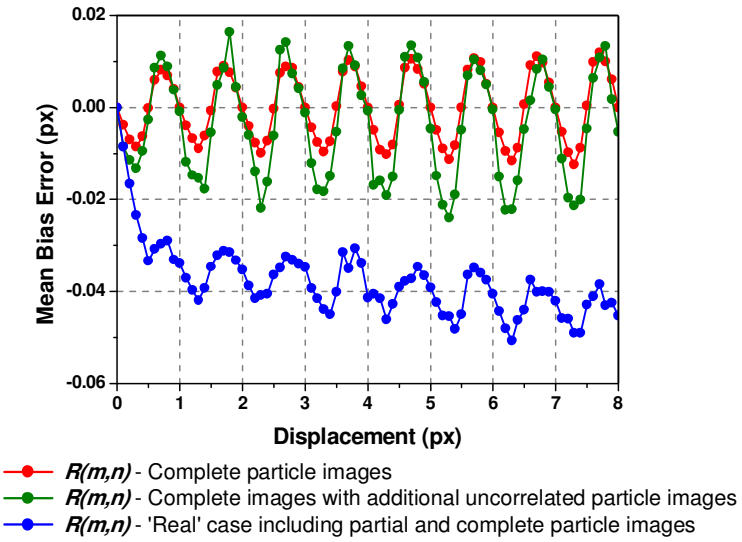

Figure 10. Mean bias error plot for complete and partial images

In the absence of a noise floor, when each interrogation region contains only complete particle images then the two regions of the pair are identical albeit for a uniform shift, therefore cross-correlation will produce a mean bias plot influenced by the digitisation effect which is shown as the oscillation in results. The addition of a noise floor to the correlation field by adding six complete, but uncorrelated particle images to each region has a negligible effect on the overall mean bias error. The inclusion of partial images in the real case however has the greatest effect on the mean bias as at small displacements there is a significant increase in negative mean bias which is maintained as the displacement is increased. It is clear from this example that partial images and not the non-uniform weighting of the correlation function has a major influence of measurement error.

VI. PIE Reduction

When an image of a flow is divided into interrogation regions, the random distribution of particle images within each region will result in come particle images being clipped at the boundary forming partial images. Correlation of these partial images causes an asymmetry in the correlation peak, skewing it towards smaller displacement values. As has been shown, partial images have a major influence on measurement error and it is therefore necessary to correct for partial images during DPIV analysis. Processes usually associated with improving the accuracy of measurements such as window shifting and particle image pattern matching[3] do not account for the effects of PIE and hence this inherent error remains.

As has been stated previously, discretely window shifting the second region is able to preserve a high SNR and also maintain the signal peak around the centre of the correlation field. With previous measurement error assumptions, holding the signal peak high on the pyramid noise floor during $R(m,n)$ correlation would have meant that the signal peak would not be skewed towards smaller measured displacement values. However, as has been shown, partial imaging has a greater influence of measurement error so when interrogation regions are fully populated with particle images the first region will always be subjected to the influences of PIE, so shifting the second region will introduce partial images into the second region hence window shifting is unable to account for the effects of PIE on measurement error. Nevertheless, when particle images are subjected to a integer pixel displacement coupled with a discrete window shift the particle images in the second region $I_2(i,j)$ are identical in their position and intensity to those in the first and when identical regions are correlated a symmetric correlation peak results and hence zero measurement errors are produced at these displacements.

To increase the resolution of velocity vectors the size of interrogation regions under examination are decreased. Smaller interrogation regions will however be greatly effected by factors that contribute to measurement error. As the particle image displacement between the two exposures is increased there is a decrease in the number of correlating particle images between the two regions. Decreasing the interrogation region size will also increase correlation sensitivity to partial imaging which is a significant contributor to measurement error.

Reaffirming the SNR lost through the lack of particle image correlation can be improved by properly choosing the size of the interrogation region to suit the displacement. It was proposed that correlation of a smaller first region with that of a larger second would result in all the correlation particle images remaining in the larger second region. This process is known as particle image pattern matching (PIPM).

When correlating a smaller first region $I_1(i,j)$ with a larger second $I_2(i,j)$ which are fully populated with randomly distributed particle images means that the distribution of particle images and the location of the partial images will influence whether the correlation peak is skewed positively or negatively, therefore, on average, will produce a negligible means bias error over the entire displacement range. Smaller region sensitivity to partial imaging and particle image distribution does however lead to variations in the correlation peak shape and therefore the RMS error remains in measurements.

In fact, all processes that involve cross-correlation of interrogation regions including iterative methods are subjected to the effects of PIE, thereby causing a negative bias in measurements.

B. Normalising by Overlapped Area

The asymmetry of the correlation peak has to be corrected before a curve peak estimator is applied to the signal peak to determine the displacement. Previous investigations have centred on normalising the correlation field by overlapped area. This normalisation function is able to compensate for the non-uniform weighting of the correlation function by skewing the correlation peak back towards the actual displacement and can therefore reduce mean bias error. However, this method is unable to compensate for the random distribution of particle images across an interrogation region that cause partial images and therefore shows no signs of correcting for the asymmetry caused by PIE, hence the RMS error remains.

Fig. 11(a) and 11(b) compares the mean bias and RMS errors computed for $R(m,n)$ and $R_{OA}(m,n)$ correlation for 32 x 32 pixel interrogation regions over a range of displacements from zero to eight pixels and extending to sub-pixel displacements. In this figure, $R_{OA}(m,n)$ denotes the errors from the correlation routine due to normalising by overlapped area. Fig 11(a) shows there is a significant reduction in mean bias error with $R_{OA}(m,n)$ when compared to $R(m,n)$ correlation. However, normalising by overlapped area is unable to compensate for changes in the seeding distribution across an interrogation region which cause partial images and results in large variations in the shape of the correlation peak generating RMS errors equivalent to that of standard $R(m,n)$ correlation.

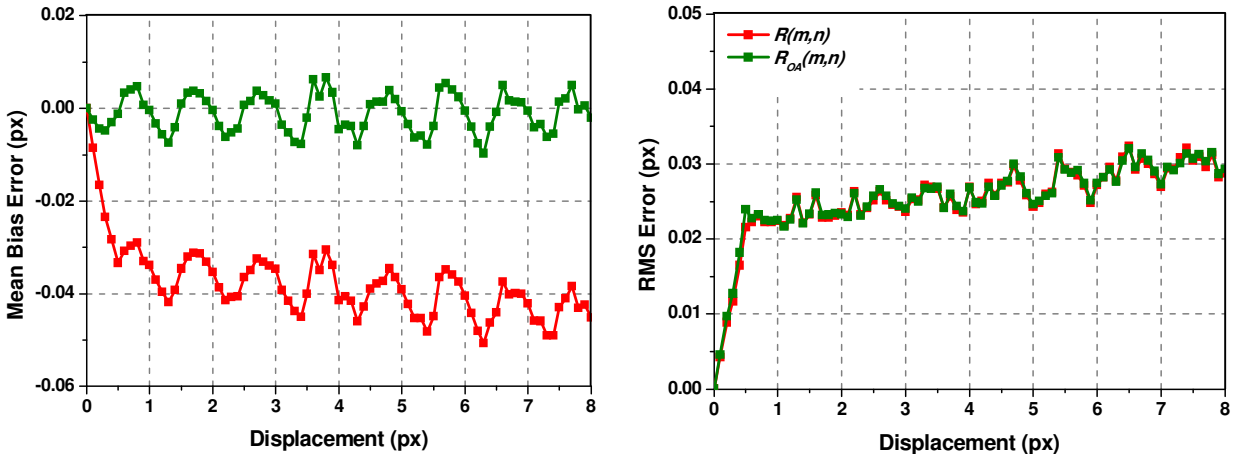

(a) mean bias error – 32 x 32 pixels (b) RMS error – 32 x 32 pixels

Figure 11. Measurement error plots – *R(m,n)* and $R_{OA}(m,n)$ analysis

C. Normalisation by Signal Strength

As has been shown, particle images that intersect the boundary of an interrogation region cause an asymmetry in the correlation peak skewing the measured displacement towards smaller values. Furthermore, for the same actual displacement there can be large variations between measurement values caused by the asymmetry in individual correlation peaks which is defined as the RMS error. It is necessary therefore to correct for this asymmetry by normalising the correlation peak. PIE can be significantly reduced if the *R(m,n)* correlation field is normalised by signal strength in the overlapped area (NSS)[6], which is defined as:

$$NSS = \frac{R(m,n)}{Signal\ Strength} = \frac{\sum_{i=0}^{M}\sum_{j=0}^{N} I_1(i,j)\, I_2(i-m, j-n)}{\left[\sum_{i,j\in A} I_1^2(i,j) \times \sum_{i,j\in A} I_2^2(i,j)\right]^{1/2}} \qquad (7)$$

If the correlation field for the simplified particle image examples in Fig. 6 and 8 are computed using NSS the asymmetry in the correlation peak is corrected for. This result is shown in Fig. 12.

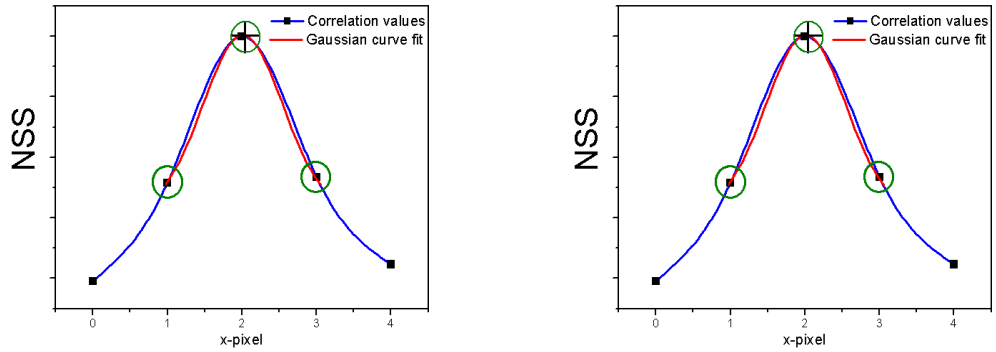

(a) *R(m,n)* routine (b) FFT routine

Figure 12. NSS correlation peak for a partial image in a) the second region and b) the first region

Normalising by signal strength is able to compensate for changes in particle image seeding density across the interrogation region since the correlation field is normalised by the signal used to compute each point in the correlation field and can thereby correct for the random positioning of particle images and significantly reduce both the mean bias and RMS errors over a broad range of displacements. Measurement error plots produced when each

correlation field is normalised by signal strength is shown in Fig. 13 andfor comparison, results for *R(m,n)* and FFT correlation are also included in the figure

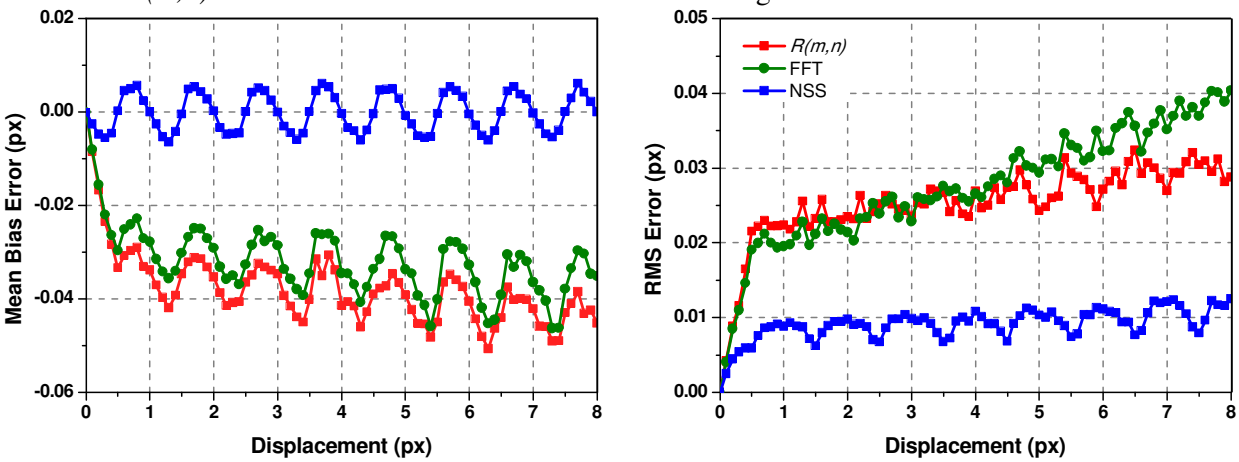

(a) *R(m,n)* routine (b) FFT routine

Figure 13. Measurement error plots – *R(m,n)*, FFT and NSS analysis

As has been shown, partial imaging has a significant influence on measurement error causing the correlation peak to be skewed towards smaller displacement values. It is therefore necessary to correct for their presence and thereby restore the symmetry to the correlation peak. Normalisation by signal strength here is highlighted as being an effective method of correcting for partial imaging to reduce both the mean bias and RMS error as shown in Fig. 13.

Conclusions

This paper has identified partial images found at the boundary of an interrogation region as being a major source of error in DPIV analysis regardless of the size of interrogation region used in analysis.

It has become common practice to reduce the interrogation region size to increase the spatial resolution, yet it is partial image error that can preclude a meaningful result from being obtained. The correlation of interrogation regions that are 32 x 32 pixels or smaller increases the sensitivity to PIE. An example of this is the correlation of 16 x 16 pixel regions that are analysed using FFT, which is common is commercially available DPIV systems. PIE has a significant contribution on the overall measurement error producing a mean bias and RMS error that are both 7% respectively for a mean displacement of only one pixel. This paper has shown that the negative mean bias previously associated with the non-uniform weighting of the correlation function is in fact due to the presence of partial images and so their influence will always be present in DPIV analysis.

PIE can be significantly reduced if the correlation field is normalised by signal strength before the sub-pixel position of the correlation peak is determined with a curve estimator. If the correlation field is normalised by area the non-uniform weighting of the correlation function is corrected for and therefore mean bias error is reduced. However, this approach has no effect on reducing the variation in correlation peak shape between measurements and therefore RMS error remains. Normalisation by signal strength (NSS) is able to correct for the random positioning of particle images within and at the boundary of an interrogation region and so is able to correct for the skew in the correlation peak as well as reducing the variation in the correlation peak shape between subsequent realisations thereby resulting in a significant reduction in both mean bias and RMS error when interrogation regions that are 32 x 32 pixel or less are correlated.

Reference

[1]McKenna, S. P., and McGillis, W. R., "Performance of digital image velocimetry processing techniques", *Experiments in Fluids*, Vol. 32, No.1, 2002, pp. 106-115.

[2]Willert, C. E., and Gharib, M., "Digital particle image velocimetry", *Experiments in Fluids*, Vol. 10. No. 4, 1991, pp. 181-193.

[3]Huang, H., D. Dabiri and M. Gharib. "On errors of digitial particle image velocimetry". *Measurement Science and Technology*, Vol 8, No 12, 1997, pp. 1427-1440.

[4]Raffel, M., Willert, C., and Kompenhans, J., *Particle Image Velocimetry: A Practical Guide*, 1st ed., Springer-Verlag, New York, 1998, Chap. 5.

[5]Westerweel, J., "Fundamentals of digital particle image velocimetry", *Measurement Science and Technology*, Vol. 8, No 12, 1997, pp. 1379-1392.

[6]Westerweel, J., "Digital Particle Image Velocimetry: Theory and Application", Ph.D. Disseration, Mechanical Engineering Dept., Delft University of Technology, The Netherlands, 1993.

[7]Nogueira, J., Lecuona, A., and Rodriguez, P. A., "Identification of a new source of peak locking, analysis and its removal in conventional and super-resolution PIV techniques", *Experiments in Fluids*, Vol. 30, No. 3, 2001, pp. 309-316.

[8]Anandarajah, K., "Digital Particle Image Velocimetry: Limitations to Measurement Accuracy", Ph.D. Disseration, Wolfson School of Mechanical and Manufacturing Engineering, Loughborough Univeristy, UK, 2005.